# Growth and Chemical Functionalization of SiC Nanowires for Biomedical Applications in Cardiology and Oncology

**Martina Quaretti**




**University of Cape Town**

**November 2018**

I declare that **“Growth and Chemical Functionalization of SiC Nanowires for Biomedical Applications in Cardiology and Oncology”** is my own work. All sources of information used are cited, acknowledged and completely referenced.

Signed by candidate

# Growth and Chemical Functionalization of SiC Nanowires for Biomedical Applications in Cardiology and Oncology

Thesis presented for the degree of

**Doctor of Philosophy**

by


## Martina Quaretti

Department of Chemistry

University of Cape Town


Supervisors: Assoc. Prof. G. S. Smith
Dr.ssa Laura Lazzarini
Dr.ssa Francesca Rossi

November 2018

*To my family & Ga*

# Contents

# Abstract

The current leading causes of death in the world are cardiovascular diseases (in particular myocardial infarctions) and cancer. In Italy in 2016 almost 400,000 people died because of these two pathologies.

Despite the great progress made by medicine in recent decades, the road to cure these diseases is still long, and cancer and cardiac diseases remain a serious socio-economic problem for our society.

For this reason, this PhD research focuses on these two main topics; called in the thesis the *oncology project* and the *cardiology project*.
Both projects were devoted to the synthesis of Silicon Carbide Nanowires (SiC NWs), aiming to devise their new possible biomedical applications in the field of oncology and cardiology.

This PhD, funded by Cariparma Crédit Agricole, is part of a *Bilateral Agreement for Joint Philosophy Doctor (PhD) Degrees* between the University of Parma and CNR-IMEM with the University of Cape Town.

The synthesis of compounds for potential applications in cancer treatment was the main research topic of the *oncology project* during the period spent abroad in South Africa.

Modern anti-tumor therapies are very invasive for the patient and often based on the administration of drugs, generally cisplatin derivatives, very cytotoxic and harmful to the human body. Furthermore, such treatments are often not fully selective and kill the diseased but also the healthy cells of the organism.

Therefore, the aim of many scientists in the world is to design and synthesize new molecules with excellent anticancer properties but with fewer side effects compared to the drugs already currently in use, for example, less toxicity and greater selectivity for the cancer cells.

Thiosemicarbazones (TSCs) are Schiff bases which in recent years have attracted considerable attention thanks to their promising anticancer properties. These compounds are very active also in the fight against malaria, moreover they are used as antifungal and antibacterial agents.

TSCs are widely documented in literature, and a correlation has often been found between the efficacy of the antitumor activity of the molecule and the presence of aromatic groups in its structure. Furthermore, exploiting the presence in the TSCs of a set of donor atoms (N and S) able to coordinate various types of metal ions to form the related complexes, many studies emphasize the importance of the presence of metal ions bound to the molecule to further increase the antitumor efficacy.

Unfortunately, TSCs have poor solubility in aqueous matrices. This behavior can make their administration as drugs more complex and create possible problems of precipitation (due to the insolubility) or accumulation inside the human body.

For this reason, in the *oncology project* of this PhD research a series of aromatic-TSCs were synthetized and then anchored on the chemically modified surface of SiC NWs, employed as carriers. According to previous results obtained by my research group at IMEM-CNR, these SiC-based NWs are biocompatible and can be conjugated with several organic molecules (e.g. porphyrins).
The target of these new nanomaterial-drug systems are solid tumors, e.g. affecting breast, lungs, pancreas and liver, where they can be injected and be active to reduce the tumor mass in view of later surgical removal.

To anchor these thiosemicarbazones to the nanowires, SiC NWs coated with a thin external layer of silica (nanomaterials called core-shell SiC/$SiO_2$ NWs) were chosen. In fact, this external layer of silica can be chemically functionalized by appropriate silane linkers.

The silane linkers used are (*3-aminopropyl)triethoxysilane* (APTES) and *triethoxy(3-isothiocyanatopropyl) silane* (Si-NCS). These alkoxysilanes react with the silica surface and covalently bind to the NWs. Thus, it was possible introduce on the NWs surface amino or isothiocyanate groups, able to react with proper TSCs in the anchoring step.

To conjugate the NWs with TSCs, it was required the synthesis of thiosemicarbazones having suitable functional groups able to react with the groups present on NWs surface. In this way thiosemicarbazone molecule was anchored by covalent bonds to the surface of the nanowires.

During the time spent at the University of Cape Town, working on the *oncology project,* various TSCs-metal complexes were prepared and successively anchored to NWs previously decorated with amino groups.

Literature is rich in examples of platinum (and related metals) complexes with excellent anticancer activity. Therefore, reactions between the TSCs bound to the NWs surface and platinum, ruthenium and rhodium salts were carried out to obtain NWs functionalized with these complexes.

Unfortunately, it was observed that this approach has a drawback due to the ability of the amino groups to give competitive complexes with transition metals.

Therefore, the attention of the *oncology project* was focused on a specific thiosemicarbazone compound (Triapine), on a way to find a new procedure to anchor it to NWs and subsequently on the evaluation of the antitumor activity of this new nano-system by *in vitro* tests.

Triapine is an α-(N)-heterocyclic thiosemicarbazone, which successfully passed Phase II of Clinical Trial. Currently, Triapine is tested as an anticancer drug in human patients.

The precursor of Triapine was synthetized, with a suitable functional group able to react with the Si-NCS linker anchored to the NWs. In this way the NWs surface was covered by Triapine molecules connected to the SiC/$SiO_2$ structure through a carbon chain as linker.

Then, the anchored Triapine was used as a ligand to coordinate metal ions; specifically copper, a metal with low toxicity to the human body.
Subsequently, these nano-systems (NWs-Triapine and NWs-Triapine-Cu complex) and the free molecules (Triapine and Triapine-Cu complex without NWs) were tested on A549 human lung adenocarcinoma cell line to evaluate their antitumor efficacy.

The free molecules showed good $IC_{50}$ values – in the micromolar range - with greater antitumor activity of the free complex compared to the free ligand in the first 24 h, but situation reversed in the subsequent 48 h and 72 h.
Vice versa, about the compounds anchored to the NWs, only the NWs-complex has proved active, suggesting that the free molecules and the molecules anchored to the NWs have different mechanisms of action and different interactions with cancer cells. The mechanisms of action were better investigated studying the cell cycle.

Regarding the other research topic of this PhD thesis, the problem of myocardial infarction has been addressed in the *cardiology project*.

Infarction is the death (necrosis) of part of the heart muscle tissue (myocardium) due to the lack of adequate oxygenation by the arterial blood flow (ischemia). After the infarction, the affected area is no longer able to contract due to the death of cardiomyocytes, the cardiac cells responsible for the generation and transmission of the electro-cardiac pulse.

The dead cardiac cells cannot be regenerated and are replaced by a fibrous connective tissue (collagen fibers) that forms a scar area in which the electrical pulse is no longer able to be diffused. Therefore, an insulating area is generated in the heart, with drastic consequences for the health of the organ and for the correct cardiac functioning.

Previous *in vitro* experiments on cardiomyocytes had shown that SiC NWs (semiconductive nanowires, without the external shell of silica) were able to connect two distant cardiac cells, previously isolated from each other. Thanks to the presence of SiC NWs, the two cells, previously silent, were able to propagate the electric pulse to each other and to synchronize their action potential.

Based on these results, in collaboration with a medical research team of the University of Parma, in this *cardiology project* SiC NWs were tested *in vivo* on infarcted rats' hearts, to verify if the SiC NWs semiconductive properties were able to restore, even partially, the normal propagation of the cardiac electrical pulse, interrupted after the infarction in the ischemic tissues area.

For this purpose, in ten rats the myocardial infarction was induced by creating an ischemic zone in the left ventricle through three different protocols: injection of formaldehyde solution at different concentrations (4% and 38%), deposition of a drop of formaldehyde 38% solution on the heart surface and cryoinjury (creation of a necrotic area by selective burning of cardiac tissues using a metal tip cooled by liquid nitrogen).

Before and after the infarction the electro-cardiac activity was monitored with a special high-resolution electrode grid.
This accurate epicardial mapping of the affected area showed important changes in the values related to the EGs parameters (waves and intervals) and in the isochrone maps (velocity and direction of propagation of the pulse wavefront) before and after the infarction.
These data also allowed to understand that cryoinjury was the best technique in creating an effective ischemic zone, with well-defined edges, easily reproducible in rats.

Subsequently, a saline solution containing SiC NWs was injected into the infarcted area and the cardiac signals were collected and analyzed.

The aim of this *cardiology project* is to compare the cardiac functioning after the injection of semiconductive SiC NWs with the pre-infarction conditions to evaluate whether the use of SiC NWs helps restore normal cardiac functioning, lost as a result of a myocardial infarction.

Based on preliminary data, in some rats after the injection of SiC NWs some important physioelectric parameters show promising changes compared to the values recorded after the infarction, returning similar to the normal pre-infarction conditions.

However, the absence of significant statistical series makes it difficult to assert more specific statements.

# 1. Nanomedicine

## 1.1 Definition and brief history of Nanomedicine

Defining the term Nanomedicine may sound simple, but an official definition does not currently exist. In literature there are several "internationally acceptable" definitions and the most complete two are given below.

The Medical Standing Committee of the European Science Foundation (ESF) defined the term Nanomedicine as “the science and technology of diagnosing, treating, and preventing disease and traumatic injury, of relieving pain, and of preserving and improving human health, using molecular tools and molecular knowledge of the human body”. (*European Science Foundation, ESF Forward Look on Nanomedicine, November 2005, retrieved December 15, 2005*).

For the National Institutes of Health Roadmap for Medical Research, Nanomedicine is "an offshoot of nanotechnology, [which] refers to highly specific medical interventions at the molecular scale for curing disease or repairing damaged tissues, such as bone, muscle, or nerve". (*National Institutes of Health. National Institute of Health Roadmap for Medical Research: Nanomedicine, 2006*).

Both reports emphasize that Nanomedicine is a young interdisciplinary science focused on the applications of nanotechnology in clinical use. In order to interact with human body (atomic, molecular or macromolecular levels) the length scale of nanomaterials employed is nano size, generally less than 100 nm.
To better understand the size of these objects, look at the Figure 1.1 in which the dimensional range of the Nanoworld is highlighted.

In 2011, the European Commission adopted the following definition of nanomaterial:

"A natural, incidental or manufactured material containing particles, in an unbound state or as an aggregate or as an agglomerate and where, for 50% or more of the particles in the number size distribution, one or more external dimensions is in the size range 1 nm – 100 nm."[1]

In 2015, the International Organization for Standardization (ISO) provided a more general definition: "Material with any external dimension in the nanoscale or having internal structure in the nanoscale." [2]

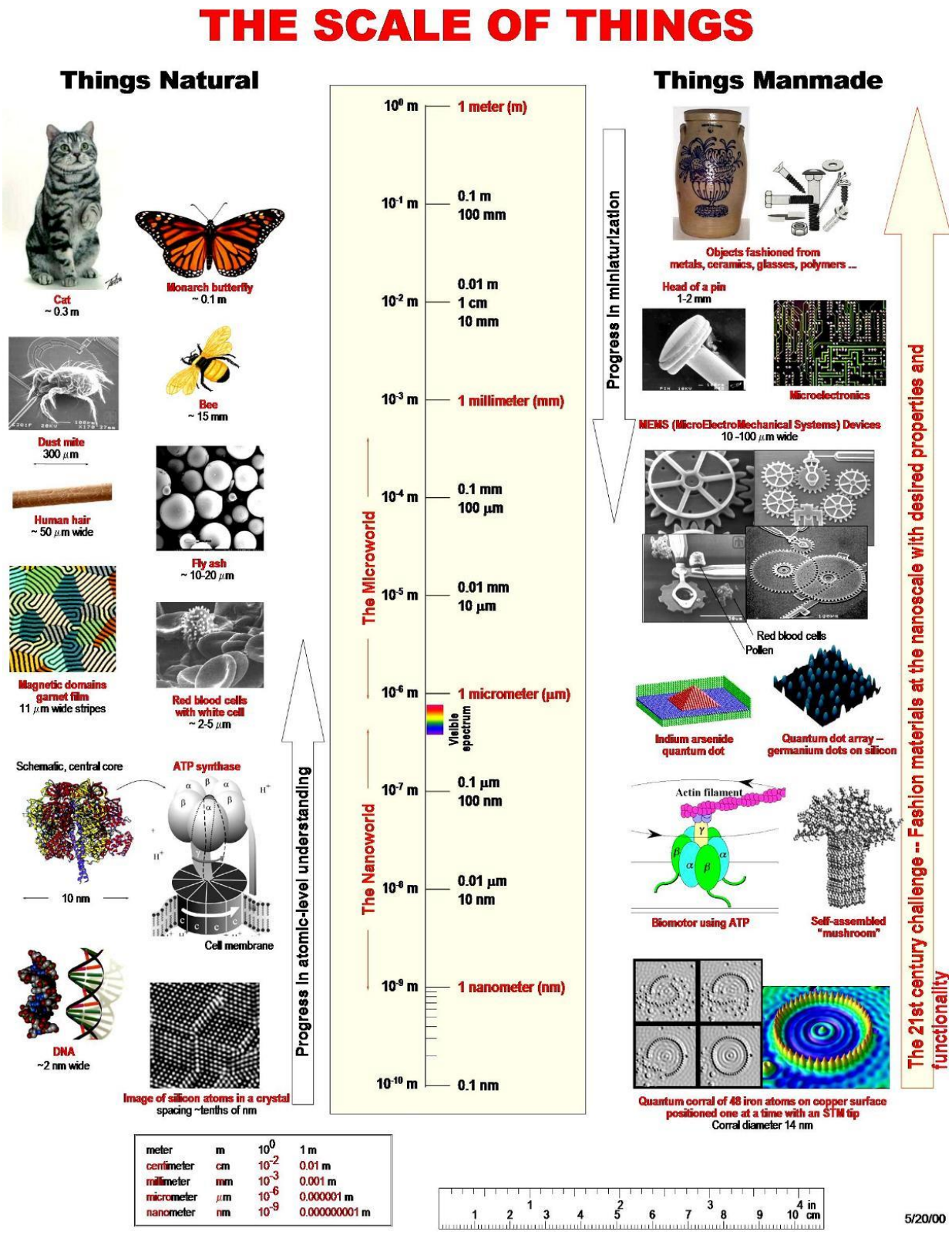


*Figure 1.1: The scale of things. Nanomaterials are the materials with nano and under micron size. Credits: Triton World-The scale of things.*

Nanomedicine is a new science with very recent origins.

In 1959 the physicist Richard Feynman in his lecture *There's Plenty of Room at the Bottom. An invitation to enter a new field of physics* suggested that it should be possible to make machine at the nanoscale able to "*arrange the atoms the way we want*" and carry on chemical synthesis using mechanical manipulation:

*"A friend of mine (Albert R. Hibbs) suggests a very interesting possibility for relatively small machines. He says that, although it is a very wild idea, it would be interesting in surgery if you could swallow the surgeon. You put the mechanical surgeon inside the blood vessel and it goes into the heart and "looks" around. [...] It finds out which valve is the faulty one and takes a little knife and slices it out. Other small machines might be permanently incorporated in the body to assist some inadequately-functioning organ. Now comes the interesting question: How do we make such a tiny mechanism? I leave that to you."*

*"We can arrange the atoms the way we want; the very atoms, all the way down! What would happen if we could arrange the atoms one by one the way we want them."* [3]

This lecture was the birth of the idea of nanotechnology, a sort of manifesto.

The term "Nanotechnology" was coined in 1974 by Norio Taniguchi, and its definition is still valid even today: "*[...], nanotechnology mainly consists of the processing of separation, consolidation and deformation of materials by one atom or one molecule.*" [4]

However, the term Nanotechnology acquired its current meaning only in the late 80's with Dr. K. Eric Drexter. He promoted the nanoworld through two main books: *Engines of Creation: The Coming Era of Nanotechnology* (1986), where he proposed the notion of cell repair machines for damaged DNA, organelles and other cellular structures, and *Nanosystems: Molecular Machinery, Manufacturing and Computation* (1992).

In 2003, the European Science Foundation (ESF) launched the *Forward look on Nanomedicine* aiming to provide a reference for the future research. European Medical Research Councils (EMRC) identified Nanomedicine as a scientific field that is rapidly evolving, gaining both momentum and importance within the medical community.

In 2004, the US National Institute of Health (NIH) released their first roadmap on Nanomedicine. In the same year, the National Cancer Institute (NCI) launched the Cancer Nanotechnology Plan with the aim of exploiting nanotechnologies in clinical oncology.

In 2005, a group of 53 European industrial and academic experts established the European Technology Platform on Nanomedicine (ETP Nanomedicine). The first task was to write a document on the future of nanotechnologies in the health care, assuming the needs and possibilities up to 2020.

In 2007, the European Foundation for Clinical Nanomedicine (CLINAM) was established in Basel, Switzerland. The goal of the CLINAM is to contribute to the benefit of patients and society by exploring and translating leading edge technologies towards clinical application, with an emphasis on Nanomedicine, Targeted Medicine and Precision Medicine.

The timeline of Nanomedicine is shown schematically in Figure 1.2.

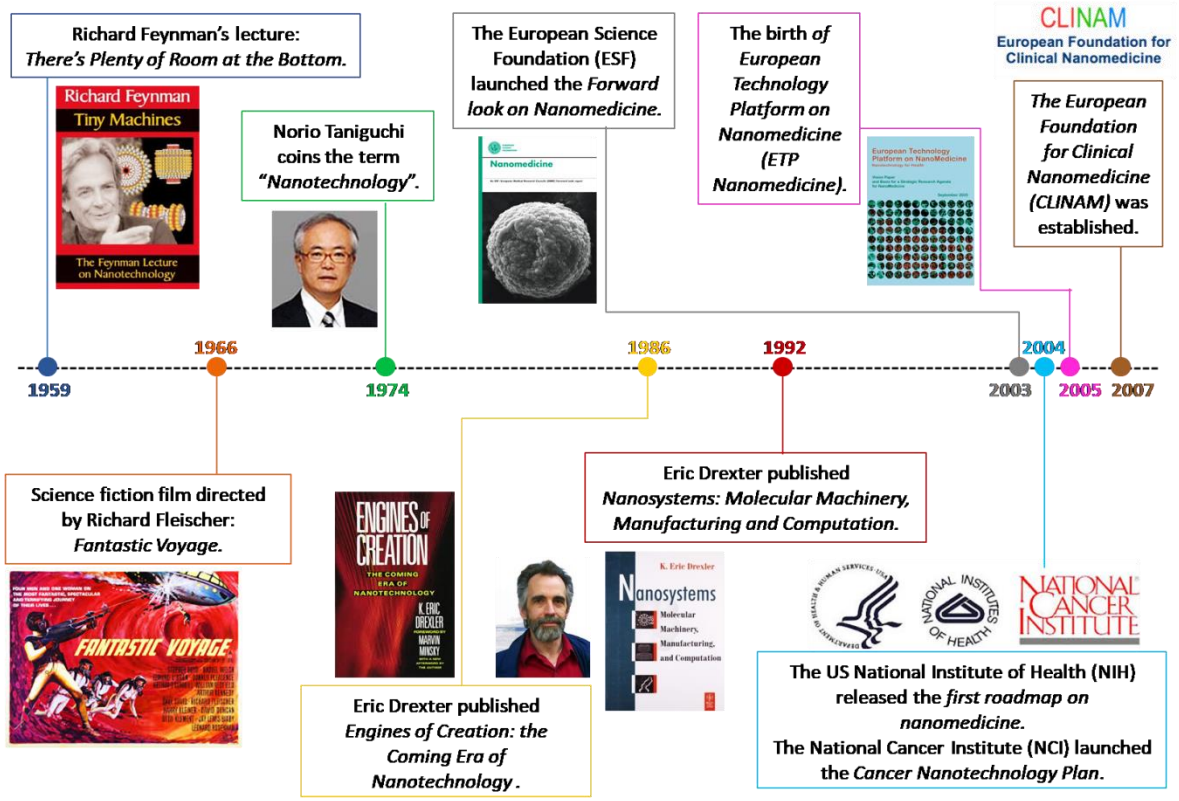


*Figure 1.2: The Nanomedicine timeline.*

A curiosity about how nanotechnologies became part of the collective imagination of ordinary people. In 1966, Richard Fleischer directed a science-fiction movie entitled *Fantastic Voyage*.
The brilliant scientist Jan Benes develops a way to miniaturize humans and objects for brief periods of time. Unfortunately, Benes has an accident and slips into an inoperable coma. To save him, a team of doctors inside a nuclear submarine are reduced to microscopic size and injected into Benes bloodstream. In this way, the miniaturized crew is able to remove the clot in his brain using a mini-laser.

As mentioned previously, Nanomedicine is a recent science and its birth is largely due to some important inventions and scientific discoveries that have allowed scientists all over the world to investigate and better understand the world of infinitesimally small.

During the 30's, microscopy made enormous progress. In 1931 Max Knoll and Ernst Ruska developed the transmission electron microscope (TEM), with significantly better resolution in comparison to the light microscopes conventionally used until then. In 1936 Erwin Müller discovered the field ion microscope (FIM), with which in 1951 physicists saw for the first time the individual atoms and their arrangement on a surface. This innovative microscopy, applied to biology, allowed to discover the cell structures and its constituents.

In 1947, the invention of voltage clamp allowed to study the cell membrane, the diffusion processes, the systematic cell communication, receptors and antibodies. In the following years, the scientists managed to explain the role of enzymes, proteins and the immune system.
In the 50's and the 60's the DNA and RNA were studied and described.

In the 80's Nanomedicine arose. In these years, it was possible to explore and manipulate the nanoworld through the development of the scanning tunneling microscope (STM) (Gerd Binnig and Heinrich Rohrer, 1981) and the first atomic force microscope (AFM) (Gerd Binnig, 1986).

The main discoveries were made during this period (Figure 1.3, purple dots): polymers, dendrimers, fullerenes, magnetic nanoparticles, carbon nanotubes, quantum dots... but Nanomedicine started to grow only at the beginning of 21$^{th}$ century with the applications of nanotechnology in the clinical use (orange dots). Currently several nano-products can be utilized for medical use or are commercially available (light blue dots).

Nanomedicine has the potential to revolutionize medicine and improve the health of humanity. However, these new prospects are also associated with several risks and social-ethical questions which should not be ignored.

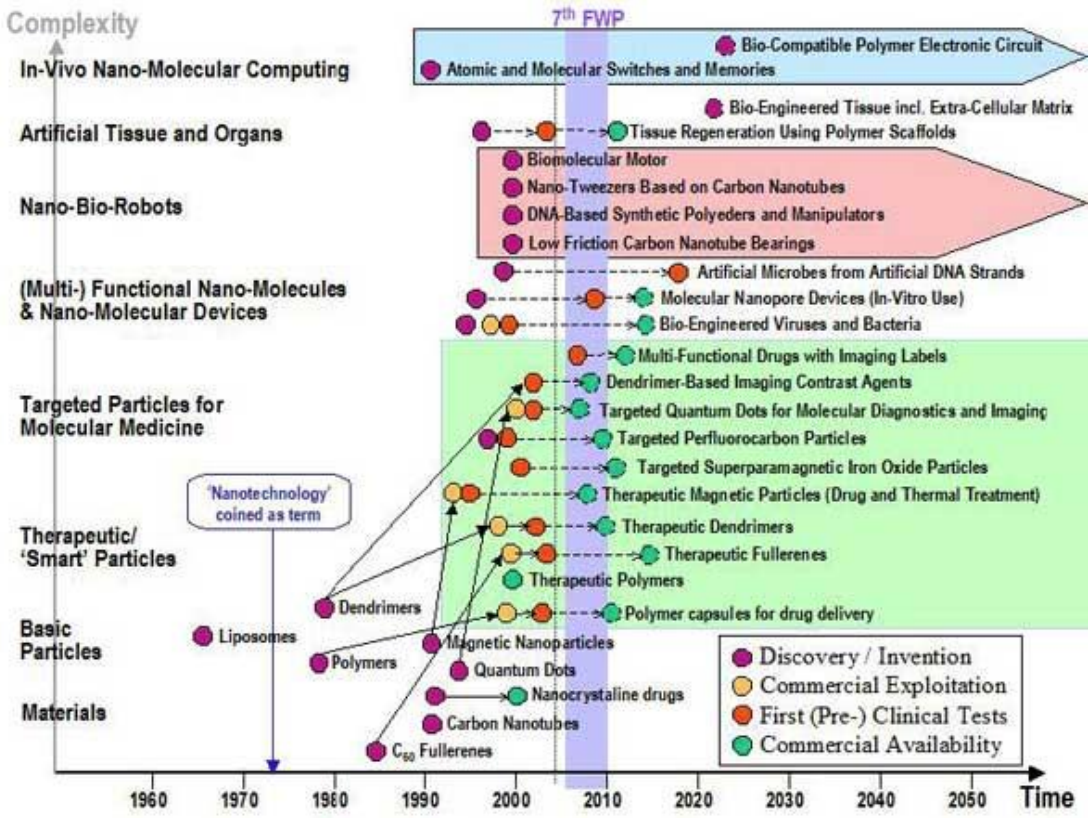


*Figure 1.3: Timeline of discoveries and inventions. The diagram indicates what has already been achieved and the future prospects for Nanomedicine. Source: Philips Medical Systems (7$^{th}$ FWP refers to the European Union's Seventh Framework Program).*

## 1.2 Applications of Nanomedicine

Nanomedicine is a recent, interdisciplinary science which covers a wide range of applications. The diagram in Figure 1.4 highlights the most important fields in which Nanomedicine is divided.

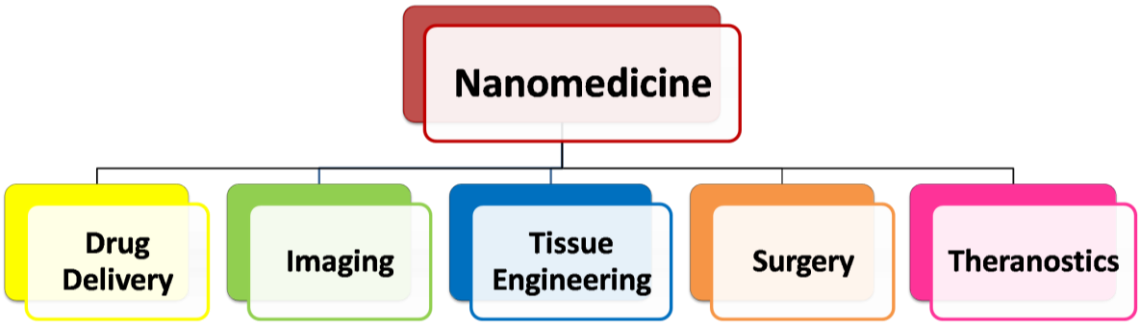


*Figure 1.4: Diagram of the different applications in Nanomedicine.*

- **Drug Delivery**
  The drug delivery technique is a method to deliver drugs or pharmaceuticals into specific sites of the human body controlling the rate, the time and the place of release. Whit this approach the medicine is more effective and less harmful to the other parts of the body. Other advantages are the possibility to increase the drug solubility by encapsulation, limiting systemic toxicity, increasing the bioavailability and improving the cellular up-take bypassing several biological barriers.[5]
  The most interesting drug delivery nanomaterials are nanoparticles[6,7], dendrimers[8], and liposomes[9,10].

- **Imaging**
  The Imaging is process of producing an image of a part of the body by radiographic techniques. Some nanomaterials can be used as non-invasive contrast agents. In particular, metal oxide nanoparticles are good candidates as marker for biological structure to improve the contrast and the biodistribution.[11]
  An example of imaging is the visualization of small tumors by magnetic resonance imaging (MRI) using magnetic iron oxide nanoparticles.[12]
  Other contrast agents are dendrimers[13] and quantum dot nanocrystals (i.e. nano cadmium and nano zinc)[14].

- **Tissue Engineering**
  Damaged tissues and organs need to be replaced by artificial substitutes or be regenerated. Biocompatible nanomaterials can be able to improve interface properties, adhesion, durability and lifespan of these new implants. For examples some nanopolymers are used to coat implantable devices[15] in contact with blood to avoid or prevent the formation of clots. They are used for artificial hearts, vascular grafts, catheters, etc.

- **Surgery**
  Minute surgical instruments and nanorobots can be used to perform precise and accurate microsurgeries on a focused part of the body, instead of damaging the whole areas. Nanosensors and nanocameras, controlled by computer, help to monitor the medical process reducing errors or accidents.[16]

- **Theranostics**
  The term "Theranostics" comes from the fusion of the words thera(py) + (diag)nostics. This new medical field combine simultaneously diagnosis (the ability to define a disease status) and therapeutics (the ability to affect therapy or treat a disease).
  A theranostic agent provides rapid and accurate feedback on the performance of a specific drug since in a single formulation there are both the pharmaceuticals and the imaging agent.[11]
  For example the combination of drug delivery and molecular imaging can be used for image-guided therapy in cancer treatment.[17,18] In real time we are able to evaluate how the tumor responses to therapies.

Currently, the main efforts made by Nanomedicine are focused in the fight against cancer[19] (specially to find more effective treatment methods than those used today and with fewer undesirable effects for patients) and in the fight against cardiovascular diseases[20] (first and foremost infarction). These two pathologies, which are the basis of this thesis, will be discussed in more detail in Chapters 3 and 6.

## 1.3 Nanostructures in Nanomedicine

As mentioned before, Nanomedicine can be defined as the clinical application of suitable nanostructures to the prevention and treatment of disease in the human body.
For this reason, the nanostructures morphology plays a key role on the interaction between the nanodevice and the biological system. The size and the shape of these nanostructures have a crucial role on the cell fate and greatly influence the cellular up-take.

In this paragraph, the effect of morphology of different nanomaterials is briefly discussed.

### 1.3.1 Unique properties at the nanoscale

The interest of nanotechnology derives from the properties that these materials show compared to their bulk counterparts. From the chemical point of view nanomaterials have the same composition of the corresponding bulk materials, but due to their reduced size, they give rise to different properties. Fundamental electronic, magnetic, optical, chemical properties changed at the nanoscale.

Nanoscale materials differ from macroscale objects in four important ways: dominance of electromagnetic forces, greater surface to volume ratio, quantum mechanics effects appear and significant random molecular motion.

- **Dominance of electromagnetic forces:** At the nanoscale the gravitation forces become negligible: the materials mass is small, and the gravitation force is very week between nanosized particles. The electromagnetic forces (not affected by mass) are very strong and begin to dominate the gravitational forces. For example, electromagnetic forces between two protons are $10^{36}$ times stronger than gravitational forces!

- **Surface to volume ratio:** The surface area increases significantly, and a greater amount of a substance comes in contact with surrounding materials. This process positively influences the reactivity, which is very important in catalysis.

- **Quantum mechanics effects:** The classical mechanics explains phenomena at the macroscale, but this model often break down at the nanoscale. Phenomena like discreteness of energy, wave-particle duality and quantum tunneling find explanation with quantum mechanics. A fascinating quantum effects is the "tunability" of properties. By changing the size of the material, it is possible to optimize the property of interest. Another effect is the "tunneling", a quantum mechanical phenomenon in which a particle tunnels through a barrier that could not be classically overcome.

- **Significant random molecular motion:** The random motion at the macroscale is very small in comparison to the size of the objects, but at the nanoscale is very large compared the size of the material. If we consider tiny particles (like dust) move randomly, at the macroscale we can barely see this movement, but at the nanoscale these particles are moving wildly compared to the size of the objects.

Another feature to remember is that only nano-sized objects can interact with the biological environment and directly interface with the cells.

### 1.3.2 Nanomaterials classification

Nanomaterials can be categorized using different methods. Below, the two most common classifications.

According to their origin, nanomaterials are divided into two very broad classes:

- **Natural nanomaterials:** Nanomaterials which exist in nature. For example, mineral such as clays, natural colloids like milk or blood, fog (aerosol type), gelatin (gel type), mineralized natural materials like shells or corals, volcanic ash, ocean spray, etc.

- **Artificial nanomaterials:** Nanomaterials prepared through a mechanical or chemical fabrication process. Examples include nanoparticles, carbon nanotubes, nanowires, etc.

The dimensional classification is more specific and detailed. This type of classification is based on the number of dimensions D (x, y, z) which are not confined to the nanoscale range (<100 nm).
We can divide nanostructures into four main classes.

A summary diagram is shown in Figure 1.5.

| CLASSIFICATION | DIMENSION < 100 nm | EXAMPLES |
|---|---|---|
| 0-D | x, y, z |  Nanoparticles Fullerenes |
| 1-D | x, y |  Nanowires Nanorods Carbon Nanotubes |
| 2-D | x | 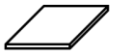 Nanofilms Nanocoating Graphene |
| 3-D | / |  Nanocomposite Bulk |

*Figure 1.5: Summary diagram of the dimensional classes of nanostructures.*

- **0-Dimensional Nanomaterials (0-D):** Materials wherein all the dimensions are measured within the nanoscale (no dimensions are larger than 100 nm). Examples are nanoparticles and fullerenes.

- **1-Dimensional Nanomaterials (1-D):** Materials with two dimensions (x, y) smaller than 100 nm and one dimension (z) outside the nanoscale. One-dimensional nanostructures are nanowires (NWs), nanorods and carbon nanotubes.

- **2-Dimensional Nanomaterials (2-D):** Materials with one dimension (x) at nanoscale and the other two dimensions (y, z) larger than 100 nm. Examples are nanofilms, nanocoating and graphene.

- **3-Dimensional Nanomaterials (3-D):** Materials with all dimensions outside the nanometer range. Three-dimensional nanomaterials are bulk materials, composite materials containing a dispersion of nanomaterials (nanoparticles, bundles of nanowires, nanotubes) or nanocomposite thick films.

### 1.3.3 The most used nanomaterials in Nanomedicine

This paragraph briefly summarizes the most used 0-D and 2-D nanomaterials in Nanomedicine.

- **Nanoparticles (NPs):** Nanoparticles are 0-D structures which can be synthesize using different material in order to obtain several compositions: metal NPs (in particular gold, silver and transition metals, etc.)[21,22], magnetic NPs (like iron oxide or $MFe_2O_4$ where M is Zn(II), Mn(II), Co(II), Ni(II), etc)[23,24] and polymeric NPs (usually inorganic compounds encapsulated in polymeric nanospheres.[25,26] An interesting aspect of these nanostructures is the possibility to conjugate them with antibodies, suitable ligands, fluorescent markers or drugs. Thus opening up a wide range of potential applications in nanomedicine, in particular targeted drug delivery and diagnostic imaging.[27]

- **Fullerenes**

  A fullerene is a 0-D carbon based nanostructure in the form of a hollow sphere or ellipsoid in which the carbon atoms are interconnected in pentagonal and hexagonal rings. Fullerenes have been used for several biomedical applications, including the design of high-performance MRI contrast agents, X-Ray imaging contrast agents, photodynamic therapy, and drug delivery.[28,29]

- **Carbon Nanotubes (CNTs)**

  Carbon Nanotubes are 1-D structures composed of one or more sheets of carbon atoms wound on themselves forming a tube whit a diameter of between 0.6 and 10 nm.

  These nanostructures are being extensively investigated for biomedical applications[30] due to their large inner volume and the possibility to functionalize their internal and external surfaces in different ways.[31] A drawback of this nanostructures is the high toxicity of CNTs to the human body.[32]

- **Nanowires**

  Nanowires (NWs) are 1-D structures, explained in detail in the next Chapter.

## References


1 European Commission, *COMMISSION RECOMMENDATION of 18 October 2011 on the definition of nanomaterial (2011/696/EU)*, Official Journal of the European Union, 2011.

2 International Organization for Standardization (ISO), ISO/TS 80004-2:2015-Nanotechnologies-Vocabulary-Part 1.

3 Richard Feynman, Caltech Engineering and Science, Pasadena, *29 December* 1959.

4 N. Taniguchi, in *International Conference on Production Engineering - Japan Society of Precision Engineering*, Tokio, 1974, 18–23.

5 A. R. Bilia, V. Piazzini, C. Guccione, L. Risaliti, M. Asprea, G. Capecchi and M. C. Bergonzi, *Planta Med.*, 2017, **83**, 366–381.

6 T. C. Yih and M. Al-Fandi, *J. Cell. Biochem.*, 2006, **97**, 1184–1190.

7 T. M. Allen and P. R. Cullis, *Science*, 2004, **303**, 1818–22.

8 H. Yang, S. T. Lopina, L. P. DiPersio and S. P. Schmidt, *J. Mater. Sci. Mater. Med.*, 2008, **19**, 1991–1997.

9 T. M. Allen and P. R. Cullis, *Adv. Drug Deliv. Rev.*, 2013, **65**, 36–48.

10 J. M. Caster, A. N. Patel, T. Zhang and A. Wang, *WIREs Nanomed Nanobiotechnol*, 2016, **9**, 1416–1434.

11 D. Cassano and V. Voliani, *Bioconjug. Chem.*, 2018, **29**, 4–16.

12 R. Thomas, I. K. Park and Y. Y. Jeong, *Int. J. Mol. Sci.*, 2013, **14**, 15910–15930.

13 M. Longmire, P. L. Choyke and H. Kobayashi, *Curr. Top. Med. Chem. (Sharjah, United Arab Emirates)*, 2008, **8**, 1180–1186.

14 B. Dubertret, P. Skourides, D. J. Norris, V. Noireaux, A. H. Brivanlou and A. Libchaber, *Sci. (Washington, DC, United States)*, 2002, **298**, 1759–1762.

15 N. M. Alves, I. Pashkuleva, R. L. Reis and J. F. Mano, *Small*, 2010, **6**, 2208–2220.

16 J. Wang and W. Gao, *ACS Nano*, 2012, **6**, 5745–5751.

17 Z.-R. Lu, F. Ye and A. Vaidya, *J. Control. Release*, 2007, **122**, 269–77.

18 A. M. E. Abdalla, L. Xiao, M. W. Ullah, M. Yu and C. Ouyang, *Theranostics*, 2018, **8**, 533–549.

19 L. P. Balogh, *Nanomedicine in cancer*, 2017.

20 V. Margarita, M. Giménez, D. E. Kassuha and W. Manucha, *Ther. Adv. Cardiovasc. Dis. Rev.*, 2017, **11**, 133–142.

21 G. Merga, N. Saucedo, L. C. Cass, J. Puthussery and D. Meisel, *J. Phys. Chem. C*, 2010, **114**, 14811–14818.

22 J. H. Fendler, *Adv. Mater. (Weinheim, Ger.)*, 2002, **14**, 1006.

23 Z. Surowiec, M. Budzynski, K. Durak and G. Czernel, *Nukleonika*, 2017, **62**, 73–77.

24 M. Kooti and A. N. Sedeh, *J. Mater. Sci. Technol. (Shenyang, China)*, 2013, **29**, 34–38.

25 A. Harguindey, D. W. Domaille, B. D. Fairbanks, J. Wagner, C. N. Bowman and J. N. Cha, *Adv. Mater.*, 2017, **29**, 213-221.

26 P. Dutta, S. Shrivastava and J. Dey, *Macromol. Biosci.*, 2009, **9**, 1116–1126.

27 R. Mout, D. F. Moyano, S. Rana and V. M. Rotello, *Chem. Soc. Rev.*, 2012, **41**, 2539–2544.

28 C. Kepley and A. Dellinger, in *Nanosci. Nanoeng.*, CRC Press, 2014, pp. 147–164.

29 P. Chawla, V. Chawla, R. Maheshwari, S. A. Saraf and S. K. Saraf, *Mini-Reviews Med. Chem.*, 2010, **10**, 662–677.

30 A. Liu and H. Qiu, in *Graphene, Carbon Nanotubes, Nanostruct.*, CRC Press, 2013, pp. 169–210.

31 I. T. Kim, G. A. Nunnery, K. Jacob, J. Schwartz, X. Liu and R. Tannenbaum, *J. Phys. Chem. C*, 2010, **114**, 6944–6951.

32 M. Bottini and N. Bottini, *Proc. SPIE*, 2012, **8462**, 84620T/1-84620T/11.

# 2. Nanowires: growth, characterization and applications

## 2.1 Nanowires: a brief overview

Nanowires (NWs) are 1-D structures with two dimensions in the nanometer range and the third (length) in the micron range. Usually the ratio of the length to width is greater than 1000.

The first successful growths of 10 nm nanowires dates to the late 90's, using a Vapor-Liquid-Solid (VLS) method.
Back in the 1960s, the VLS method was successfully employed by Wagner to grow silicon microwires (whiskers), with a diameter greater than 0.1 μm. These whiskers were the first evidence that it was possible to scale the dimensions of semiconductors at the submicronscale.[1]
However, nanometer scale nanowires were obtained only in 1998, about twenty-five years later. Morales and coworkers employed laser ablation to generate the source of vapor needed for VLS growth and grew the first single-crystalline Si and Ge nanowires.[2]
Soon the process was improved and VLS become the dominant method for nanowire growth, due to its excellent control over many aspects of the synthesis process.

As mentioned in the previous Chapter, nanowires have physico-chemical properties totally different from those of the corresponding bulk material. This behavior is typical for all nanostructures.
For example, below defined critical dimensions and with a very high surface to volume ratio, some nanowires can present the phenomenon of quantum confinement. In this case we call these structures quantum wires.[3]

Nanowires are generally used to build nano-electronic devices (e.g. nano field-effect transistors[4]), nano-electromechanical systems able to operate even in harsh environments[5], nano-sensors and nano-probes for biological systems.[6,7]

## 2.2 VLS growth and CVD technique

Nanowires can be produced with two different approaches: the "top-down" technique and the "bottom-up" technique:

- **Top-down**

This technique uses sculpting or etching to carve structures from a larger piece of material in a subtractive fashion. In this way NWs are synthesized by etching out crystals planes from the substrate.[8] One example is photolithography technique.

- **Bottom-up**

This technique assembles the final structure by adding sub-components to the substrate. The nanostructures are synthesized onto the substrate by stacking atoms onto each other, producing new crystal planes. Later, crystal planes stack onto each other, resulting in the synthesis of the nanostructures. The VLS process is one of the most widely used bottom-up growth technique. The name derives from the nature of the three phases present in the growth interface: vapor, liquid and solid phases. This method is used in various vapor-phase

growth techniques, such as chemical vapor deposition (CVD), laser ablation and molecular beam epitaxy (MBE).

Figure 2.1 shows the schematic mechanism of the VLS growth.

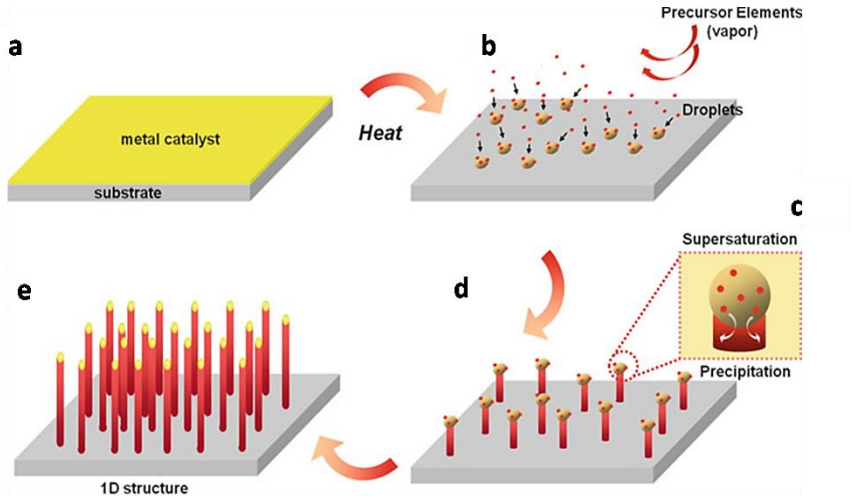


*Figure 2.1: Growth of NWs by VLS mechanism. a) A thin layer of metal catalyst (yellow layer) covers the growth substrate (grey layer). b) Dewetting phase and formation of eutectic alloy droplets in presence of gaseous precursor elements. c) Droplets supersaturation and material precipitation. d) NWs formation by precipitation. e) Platelet with nanowires.*

The VLS process is assisted by a metal catalyst. The metal is deposited on the substrate as a thin metal layer. Iron, gold and nickel are the most common catalysts. (Figure 2.1 a)

During the growth the system is heated up and the catalyst forms a liquid eutectic alloy with the material of the substrate (usually a semiconductor). Subsequently, the phenomenon of "dewetting" occurs: the liquid-alloy aggregates forming droplets on the substrate surface, due to its surface tension. (Figure 2.1 b)

At high temperature, the eutectic alloy continues to incorporate materials through the vapor-liquid interface thanks to the presence of suitable precursor elements in the vapor phase. In a short time, the alloy is supersaturated. Inside each droplet the concentration of the material becomes higher than the equilibrium point. (Figure 2.1 c)

The material begins to precipitate at the liquid-solid growth interface. This precipitation continues as long as the vapor components are supplied. (Figure 2.1 d)

The metal catalyst remains on the tip of the nanowire while the nanowire grows below, at the liquid-solid interface. At the end of the process, the NW diameter is proportional to the initial size of the catalyst drop, and its length is determined by many factors, e.g. growth time and precursor elements rate flow. (Figure 2.1 e)

Briefly, in summary, the NWs growth process is based on three main steps: (Figure 2.2)

- Metal-substrate liquid alloy droplets formation.
- Gaseous precursors decomposition at the vapor-liquid interface and diffusion through the alloy droplets.
- Nucleation at the growth interface: the NWs growth occurs between the solid phase and the liquid phase, along a single direction. For instance, single-dimensional structures(1D) are originated.

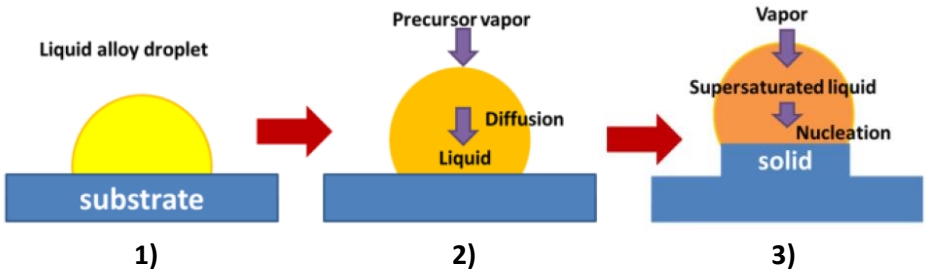


*Figure 2.2: Enlarged view illustrating the three main steps of NWs growth.*

The role of the metal catalyst is twofold. First, the metal catalyst is used to form small drops of eutectic metal-substrate alloy during the dewetting phase. (Figure 2.3 a, c)
The eutectic temperature is much lower than the melting temperature of the single compounds, as shown in Figure 2.3 b. For this reason, VLS growth can be carried out at lower temperature.
Secondly, the metal assists the diffusion and incorporation of the species from gaseous precursors, promoting the nucleation and allowing to obtain nanowires with a fixed elemental composition and uniform growth over the whole substrate.

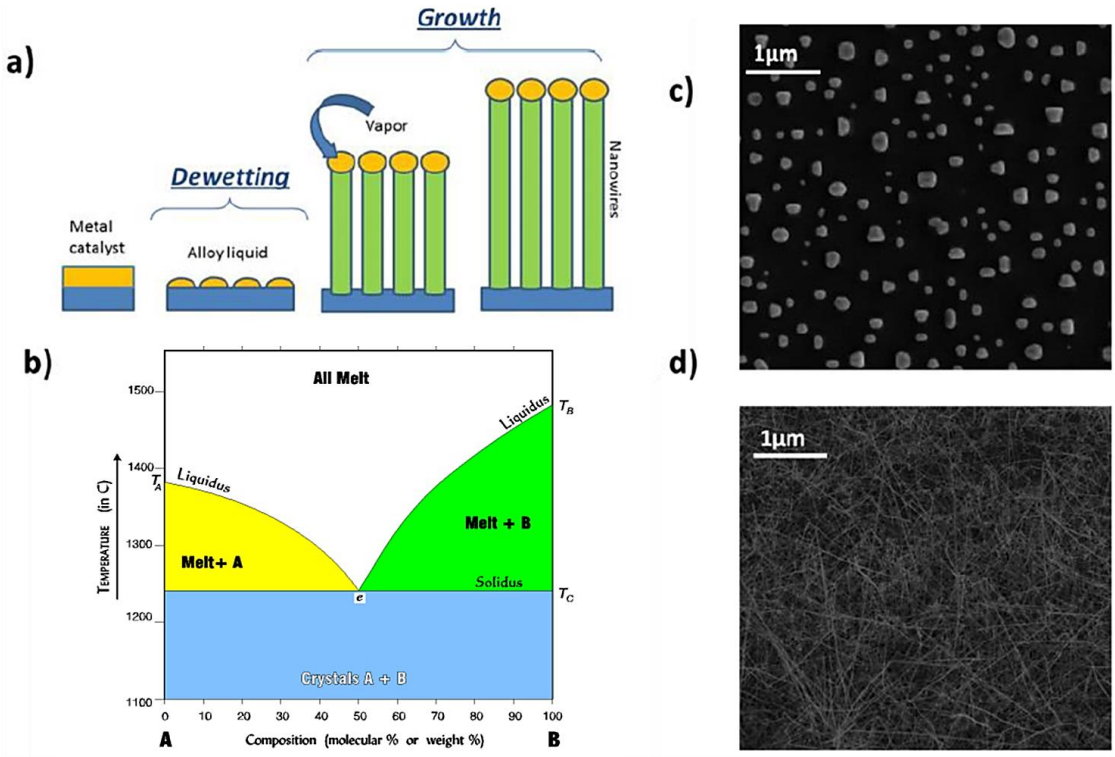


*Figure 2.3: a) Schematic representation of VLS process. b) Binary phase diagram for a Metal-Substrate system (elements A and B in the graph); the eutectic point "e" is a function of the temperature in which the system is located and of the percentage composition of A and B in the system. (c) SEM image of dewetting phase. (d) SEM image of NWs.*

The VLS process is employed for the growth of different types of NWs, especially elemental semiconductors (Si,Ge,B)[9,10], III-V semiconductors (GaN, GaAs, GaP, InP, InAs)[11,12,13], II-VI semiconductors (ZnS, ZnSe, CdS, CdSe)[14,15] and metal oxides (ZnO, MgO, CdO, $TiO_2$, $SnO_2$, $In_2O_3$, $Ga_2O_3$)[16,17].

The NWs treated in this thesis are silicon-based NWs, in particular silicon carbide NWs (SiC), silicon oxide NWs ($SiO_2$), core-shell silicon carbide-silicon oxide NWs ($SiC/SiO_2$) and silicon oxycarbide NWs ($SiO_xC_y$), which will be described in detail in following paragraphs.

These nanowires have been grown using the hot wall-open tube CVD technique, exploiting the classic VLS process. The growth apparatus used was designed by Dr. Giovanni Attolini at IMEM-CNR Institute of Parma.

The CVD technique is a synthesis process that allows the precursors deposition on a solid substrate. The precursor is introduced in a gaseous form in presence of a carrier gas (e.g. argon, hydrogen or nitrogen). The carrier gas carries the precursor flow into the growth chamber, where the precursors decompose on the substrate surface, and removes gaseous byproduct from the system.

The CVD machine consists of the system for the gas supply controlled by mass flow controllers, the purge system, the growth chamber, the furnace and the aspiration tool for the removal of reaction byproducts. (Figure 2.4)

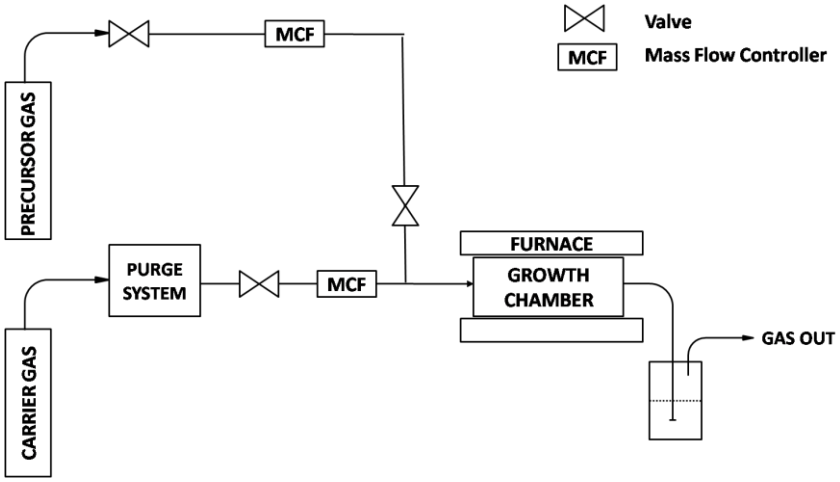


*Figure 2.4: CVD system block diagram.*

The growth chamber is "hot wall" type (it is surrounded by a tubular furnace, therefore the substrate and the reactor walls have the same temperature, as shown in Figure 2.5) and "open tube" (the growth occurs in continuous gas flow at atmospheric pressure). The carrier gas used is nitrogen.

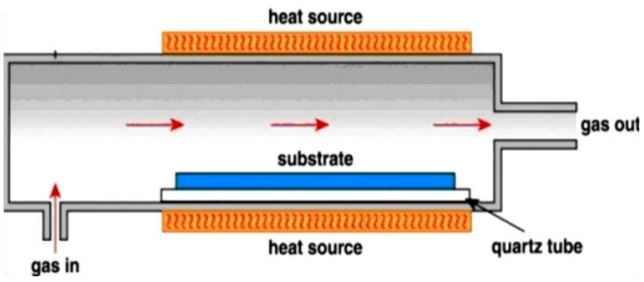


*Figure 2.5: A schematic representation of hot wall CVD reactor. The blue layer is the substrate for the growth of nanowires.*

## 2.3 Silicon-based Nanowires

IMEM-CNR has developed the preparation and the characterization of different classes of nanowires, in particular silicon carbide NWs (SiC), silicon oxide NWs ($SiO_2$), core-shell silicon carbide-silicon oxide NWs ($SiC/SiO_2$) and silicon oxycarbide NWs ($SiO_xC_y$).
As mentioned before, all these structures are obtained using hot wall-open tube CVD technique.

### 2.3.1 Silicon Carbide Nanowires (SiC)

Silicon carbide (SiC) is a semiconductor composed of silicon and carbon. This material is mostly synthesized industrially through various processes.[18]

High band gap semiconductors, such as SiC, have shown thermal properties (thermal conductivity and high temperature resistance) and electrical properties far superior to those of conventional semiconductors.
In addition, SiC has a strong resistance to chemical attacks (both acidic and basic), wear and corrosion. This behavior makes it suitable for use in harsh environments, such as body fluids, even for a prolonged period of time. Furthermore, its chemical inertia, low thermal expansion and high biocompatibility make SiC a perfect candidate for biomedical applications.[19,20]

Silicon carbide is also extensively used in the aerospace industry as low density refractory material for high temperatures, as abrasive and in many mechanical applications due to its high hardness, strength, low friction coefficient and its high Young's modulus.[21]

Table 2.1 shows some structural and physical properties of silicon carbide in comparison to pure silicon.

*Table 2.1: Structural and physical properties of silicon and silicon carbide polytypes 3C-SiC, 4H-SiC, 6H-SiC.*[21]

| | **Si** | **3C-SiC** | **4H-SiC** | **6H-SiC** |
|---|---|---|---|---|
| **Density ($g/cm^3$)** | 2.33 | 3.21 | - | 3.21 |
| **Lattice (Å)** | 5.43 | 4.36 | 3.07 | 3.08 |
| **Hardness ($Kg/mm^2$)** | 1000 | 2600 | 2600 | 2600 |
| **Band Gap (eV) at 300K** | 1.12 | 2.39 | 3.26 | 3.02 |
| **$T_{max}$ (K)** | 600 | 1200 | - | 1580 |
| **Thermal conductivity ($W/cm^1K^1$)** | 1.45 | 4.9 | 3.7 | 4.9 |
| **Dielectric constant** | 11.9 | 9.7 | 10.1 | 9.66 |
| **Electron mobility ($cm^2/Vs$)** | 1400 | 1000 | 460 | 600 |
| **Hole mobility ($cm^2/Vs$)** | 600 | 40 | 115 | 50 |

As shown in Table 2.1, SiC presents a monodimensional polymorphism, called polytypism.

Polytypes are a special case of polymorphs, where multiple close-packed crystal structures differ in only one dimension. Polytypes have identical close-packed planes, but different stacking sequence in the third dimension perpendicular to these planes.

Silicon carbide has more than 200 known polytypes.[22]

The most technologically relevant forms of SiC polytypes are 3C-SiC, 4H-SiC and 6H-SiC, shown in Figure 2.6. In any structure, all SiC crystals are formed via bilayers of C and Si atoms, covalently bonded to form a tetrahedron. Four carbon atoms are covalently bonded with a silicon atom in the center, and conversely four Si atoms are covalently bonded with a C atom. This tetrahedral subunits are the building block of all SiC materials.[23,24]

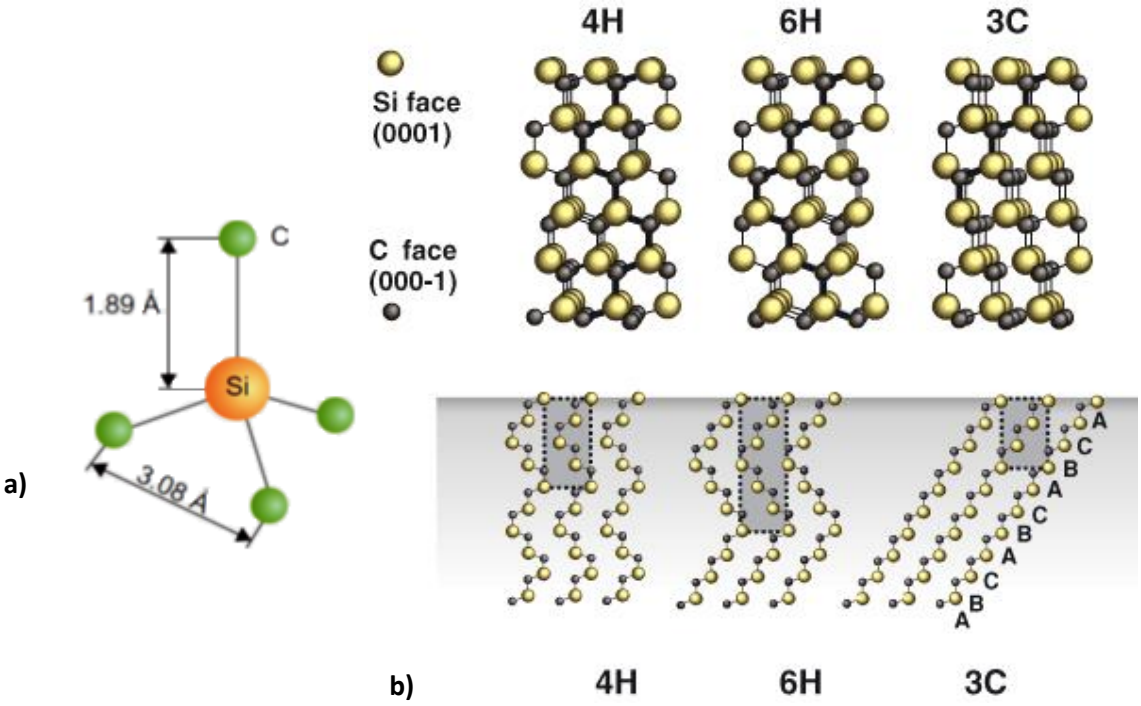


*Figure 2.6: a) The tetrahedral subunits of C (green sphere) and Si (orange sphere)[23]. b) The atomic stacking sequence of the three most relevant SiC polytypes: 4H-SiC (ABCB), 6H-SiC (ABCACB), and 3C-SiC (ABC). The letters "H" and "C" denote the lattice: Hexagonal and Cubic. The numbers "4, 6 and 3" indicate that 4, 6 or respectively 3 bilayers of Si-C are needed to form the basic structure of the solid.*[24]

These polytypes of SiC have different applications: 4H-SiC, which has the highest band gap, is used to build electronic devices, while 6H-SiC is employed for blue ray technology and solid-state lighting (LEDs), as its lattice constant is close to the GaN family of alloys.[25]

This thesis research is focus only on the cubic phase 3C-SiC, also known as β-SiC. This specific polytype presents great structural symmetry, the highest electronic mobility and it can be grown on a silicon substrate (100) using the CVD technique.
Therefore, in this thesis, the term "SiC" will refer exclusively to the 3C-SiC polytype.

The SiC NWs are obtained by chemical etching of the core shell SiC/$SiO_2$ NWs by removing of the shell. (The growth procedure of core-shell NWs is explained in the next section).
A conventional HF etching does not completely remove the shell.[13] Therefore, several etching steps are mandatory to obtain bare SiC NWs.

In the first step, the platelet with the grown core-shell NWs are dept in a RCA clean ($H_2O$ : $NH_4OH$ : $H_2O_2$ = 5 : 1 : 1), in order to eliminate all the organic contaminants on the silicon substrate.[26]
The second step removes part of the oxide layer by using a solution of $H_2O$ : HF = 50 : 1 and the third step is necessary to eliminate ionic contaminants with a solution of $H_2O$ : HCl : $H_2O_2$ = 6 : 1 : 1.
The fourth chemical treatment is a Piranha solution ($H_2SO_4$ : $H_2O_2$ = 3 : 1), followed by an etching in a solution HCl : $H_2O$ = 2 : 1. The last step is in a solution $H_2O$ : HF = 50 : 1 again.[27]

This procedure allows to obtain bare crystalline SiC NWs with a diameter of about 20 nm. (Figure 2.7)[28]

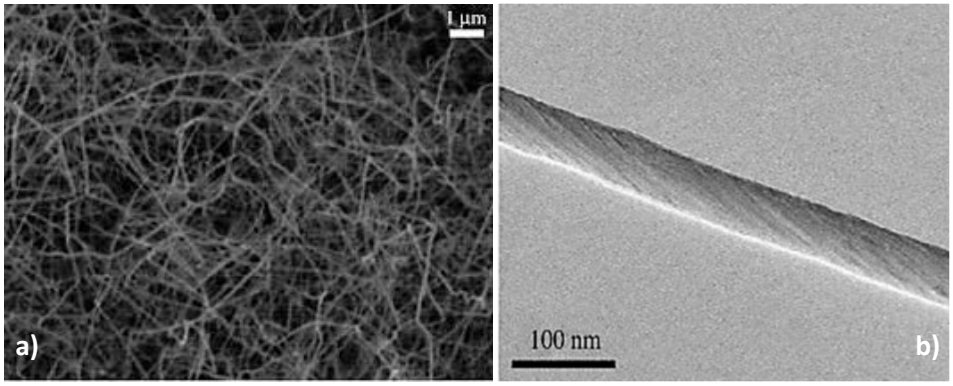


*Figure 2.7: a) SEM image of SiC NWs. b) Low-magnification TEM image of a single SiC NW.*[28]

### 2.3.2 Core-shell Silicon Carbide-Silicon Oxide Nanowires (SiC/$SiO_2$)

The core-shell NWs are structures composed by a continuous crystalline core encapsulated in a sheath of a different material. SiC/$SiO_2$ NWs are characterized by an inner core made of silicon carbide and an external shell made of silicon oxide.[29,30] (Figure 2.8)
The presence of the thin layer of silica (insulating material) makes the core-shell NWs less conductive than SiC NWs.

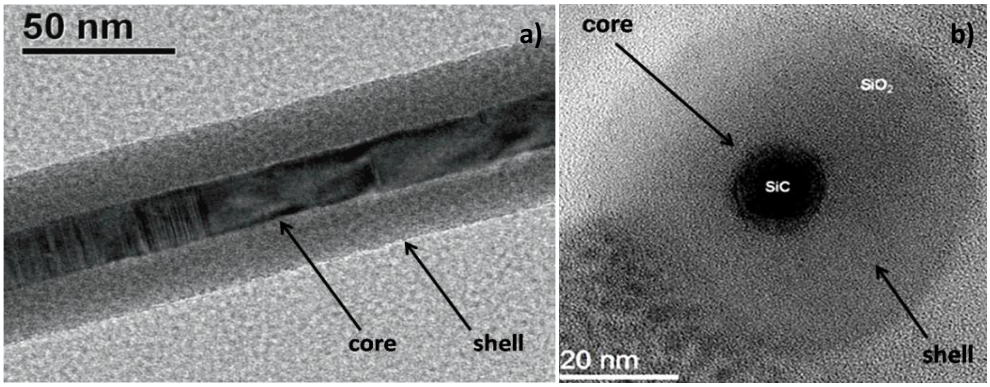


*Figure 2.8: a) Zero-loss image of core-shell SiC/$SiO_2$NW by TEM. b) TEM image of NW section.*

Figure 2.9 shows the band structure of a SiC/$SiO_2$ NW. The greater band gap of the silica shell allows the formation of a quantum well (type I).[31]

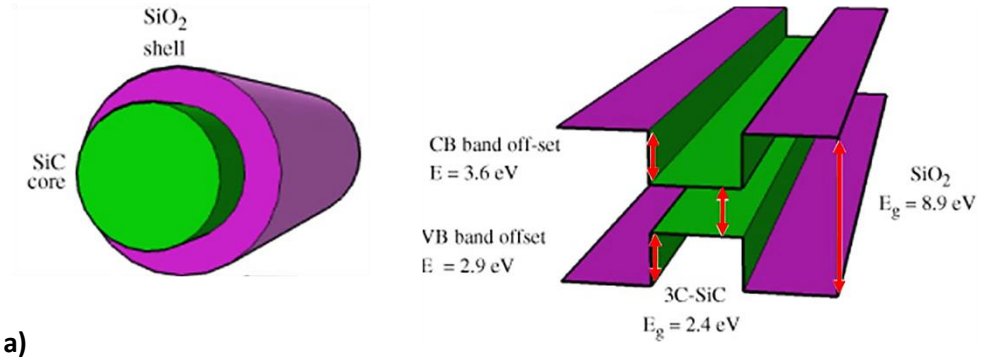


*Figure 2.9: a) The structure of a SiC/$SiO_2$ nanowire: the core of SiC is represented in green, the shell of $SiO_2$ in violet. b) The alignment of the bands inside the structure.*

This feature, combined with the resulting light emission, finds an important application in photodynamic therapy. This technique involves the use of chemically selective photosensitive agents for diseased cells, which can induce cellular necrosis with light irradiation. This therapy is generally used for the treatment of not surgically removable skin tumors.[32]
Another approach is to functionalize the surface of NWs with photosensitive compounds (for example porphyrin) for X-ray excited photodynamic therapy.[33]

Core-shell SiC/$SiO_2$ nanowires are synthesized on a silicon substrate <100> by hot wall-open tube CVD technique, using carbon monoxide (CO) as gaseous precursor. The mass flow controller (MCF, in Figure 2.4) allows the control of the precursor flow and its concentration in time. The growth temperature is set at 1100 °C.
The process is metal assisted. Nickel based compounds (e.g. nickel nitrate $Ni(NO_3)_2$) perform as the most effective catalysts, but safety standards for applications in biological environment require to minimize the employment of nickel, which can stimulate neoplastic transformations.[34,35]
Therefore, an iron catalyst (ferric nitrate $Fe(NO_3)_3$), more suitable for biomedical applications, was chosen.[36,37]

The substrate is cleaned by ultrasonic bath in acetone and then in deionized water. The superficial oxide layer, which is naturally formed, is removed by an etching in concentrated hydrofluoric acid.
The catalyst $Fe(NO_3)_3$ is dissolved in ethanol. To obtain a uniform nanowires growth, a non-ionic surfactant (oleylamine: *cis*-1-amino-9-octadecene) is added to the ethanol solution. The presence of surfactant improves the wetting of the substrate surface.[38]
The catalyst solution is drop-casted on the silicon platelet. The ethanol is slowly evaporated in controlled humidity chamber (less than 10%) at room temperature.

Afterwards, the sample is loaded in the growth chamber of the CVD system, purged with $N_2$ to remove oxygen. The temperature is raised to 1100 °C and the precursor gas CO is introduced (the concentration is about 0.4%, $P_{CO}$: 400 Pa) using $N_2$ as carrier gas. The growth lasts 30 minutes. Then the growth chamber is cooled down to room temperature, in nitrogen atmosphere.

The typical morphology of the NWs over the growth substrate is a dense network of long interwoven fibers. The average core diameter is around 20 nm, while the shell thickness can be tuned from about 20 nm (standard) to about 100 nm, depending on the growth conditions.

### 2.3.3 Silicon oxycarbide NWs ($SiO_xC_y$)

$SiO_xC_y$ NWs are grown by a hot wall-open tube CVD technique on Si substrates, with the same setup described before for the core-shell NWs. The temperature is fixed at 1050 °C but, in this process, carbon monoxide acts as dopant precursor. We obtain carbon-doped under-stoichiometric silicon dioxide NWs.[39]
X-Ray Photoemission Spectroscopy (XPS) measurements of NWs surface indicates that carbon content is about 13%, silicon 36%, oxygen 51%.
The typical $SiO_xC_y$ NW length is several tens of μm: the dense bundle of NWs interwoven fibers cover the whole sample surface (Figure 2.10 a). In comparison to the other silicon-based nanowires, the average diameter is slightly larger, approximately 80 nm. (Figure 2.10 b)[39]

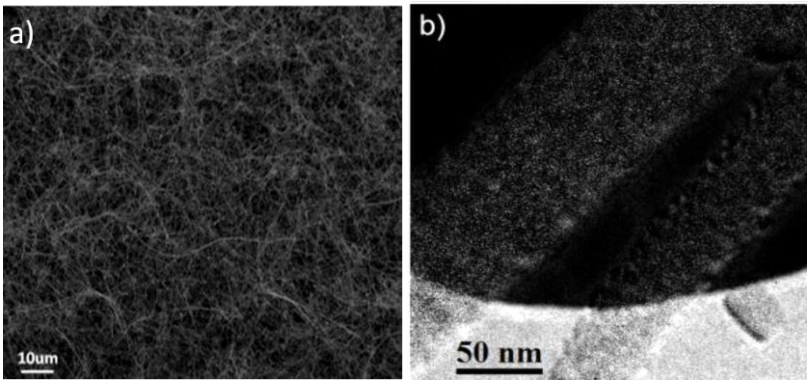


*Figure 2.10: a) SEM image of $SiO_xC_y$ NWs bundle. b) Carbon map obtained with energy filtered TEM of two single $SiO_xC_y$ NWs. (White area corresponds to the carbon support film of the TEM grid).*

Silicon oxycarbide NWs present high elastic modulus, bending strength, hardness, chemical durability in aggressive environments and high temperature stability.[40,41]
Furthermore, $SiO_xC_y$ NWs can be easily engineered through chemical functionalization and decoration with macro-molecules and nanoparticles, which makes these structures ideal candidates for several biomedical experiments, thanks to their high biocompatibility.[42,43,44]

### 2.3.4 Silicon Oxide Nanowires ($SiO_2$)

Silicon oxide NWs are nanostructures mainly composed of silica.
The growth process is similar to that of silicon oxycarbide NWs, but the CO flow is drastically reduced in order to obtain a final percentage of C very low. Therefore, with good approximation, it can be stated that the silica NWs are composed almost exclusively of $SiO_2$.
The presence of silica makes these wires easily chemically functionalizable and biocompatible.[44] Moreover, they possess excellent insulating properties.

## 2.4 Characterization Techniques for Nanowires

All NWs described in the previous paragraph are studied and characterized at IMEM-CNR Institute.

The main techniques of analysis used to investigate the morphology of these structures are scanning electron microscopy (SEM), conventional bright-field and high-resolution transmission electron microscopy (HR-TEM), high angle annular dark field imaging in scanning mode (HAADF-STEM) and energy dispersive X-Ray Spectroscopy TEM (EDX-TEM).

Figure 2.11 shows some examples of these different techniques of characterization.

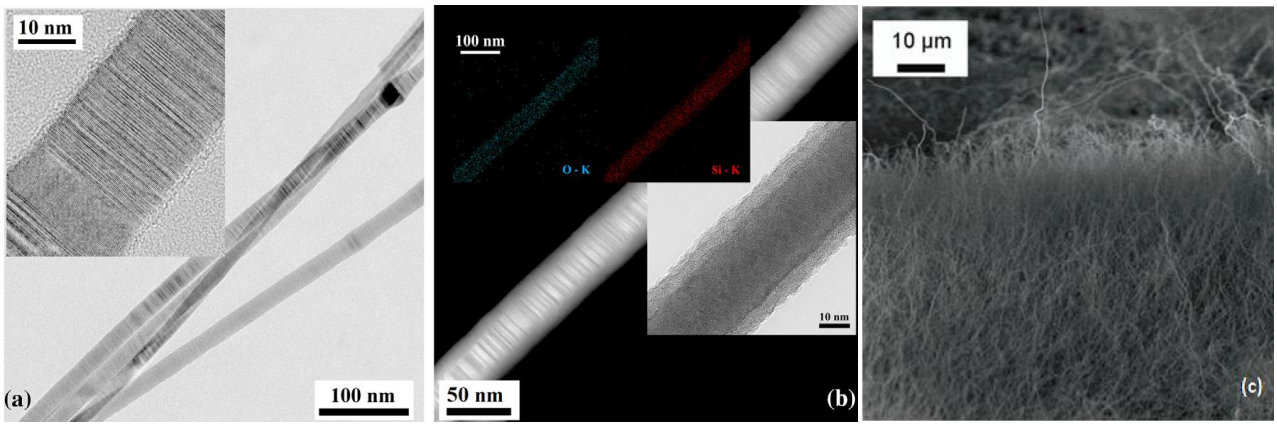


*Figure 2.11: (a) Bright-field TEM image of chemically etched NWs. The insert shows the HR-TEM image of a NW segment, where a residual amorphous layer is detected. b) STEM-HAADF image of a single NW, after chemical etching and thermal re-oxidation. The bright-field TEM image of a NW segment is reported as lower insert. EDX elemental maps of oxygen (blue) and silicon (red) are reported as upper inserts. c) 45° tilted SEM secondary electron image of core-shell SiC/$SiO_2$ NWs.*

## 2.5 Nanowires in Nanomedicine: the biocompatibility

In this section the biocompatibility of core-shell SiC/$SiO_2$ NWs and SiC NWs will be briefly discussed.
The NWs were evaluated detached from the growth substrate, as free nanostructures.

The *in vitro* tests on different cells lines showed that silicon-based NWs do not release cytotoxic agents. Therefore, they are cytocompatible and suitable for biomedical applications.

Hemocompatibility tests with platelet-rich plasma and kinetic blood coagulation tests showed that SiC NWs are hemocompatible.[45] These results indicate that the analyzed NWs are promising as biomaterials to design implantable biomedical devices for brain-machine interface or cardiovascular field, based on bare SiC NWs, or for bone implants and tissue regeneration, based on core-shell NWs.[23]

### 2.5.1 Nanowires and cytotoxicity

Any innovative nano/bio-material in contact with animal and human cells or tissues must be cytocompatible. For applications, i.e. drug delivery, requiring internalization of the material into the target cells, the analysis of the interaction between nanomaterials and intracellular components of different cell lines is very important.[46]

The silicon-based NWs were studied after the detachment from the silicon substrate, through ultrasonic bath. The NWs were suspended in water and in cell culture medium (RPMI 1640 medium), in order to study their behavior.

The first experiment was based on the registration of the Z potential. The Z potential values obtained were -(37 ± 3) mV in water and +(12 ± 2) mV in cell culture medium (RPMI). These data indicated that the nanowires have a negative surface charge in water and a good stability. In cell culture medium the Z potential value is smaller and changes sign. This fact suggests that the medium components (e.g. proteins, vitamins, lipid, growth factors) can interact with the NWs and cover their surface causing a different charge compensation.[45]

- **Core-shell SiC/$SiO_2$ NWs**

*In vitro* cytocompability studies[45,47] were performed on normal cell line as non-cancer control cells (human-derm fibroblasts, HuDe) and three human cancer cell lines: lung adenocarcinoma alveolar basal epithelial cells (A549), breast cancer cells (MCF-7), and the monocytic cell line derived from acute monocytic leukemia (THP-1).

The analysis of the cell cycle progression shows that in all the cellular lines the NWs do not cause any perturbation, and do not induce apoptosis, as proved by morphological analyses: absence of changes typical of cell apoptotic death (nuclear condensation and apoptotic bodies) and no sub-$G_0/G_1$ peak, (corresponding to apoptotic cells) are detected in the cytograms.
Oxidative stress was evaluated through quantification of Reactive Oxygen Species (ROS), Thiobarbituric Acid Reactive Substances (TBARS) and carbonyl groups levels.
These results indicate that the intracellular presence of NWs does not cause cytotoxic activity leading to irreversible cellular damages or death.
NWs cytocompatibility on the cellular lines A549, MCF-7 and HuDe was also tested on a long-time scale (10 days), with the aim of simulating real biological interactions.
No significant reduction is observed after 10 days, confirming that the core-shell SiC/$SiO_2$ NWs do not cause cytotoxic activity.
TEM and SEM analysis confirmed that the NWs did not induce alterations in cell morphology (shape, size, etc.) or alterations in the nucleus/cytoplasm ratio.

- **Silicon Carbide NWs**

As with $SiC/SiO_2$ NWs, the analysis focus on how SiC NWs can influence cell morphology, cell cycle progression and oxidative stress. Also in this case the results confirmed the total cytocompatibility of the SiC NWs.[45,23]

*In vitro* tests were performed on a cardiac muscle cell line, designated HL-1, from the AT-1 mouse atrial cardiomyocyte tumor lineage.
The analysis of the cell cycle progression shows that the SiC NWs do not induce any perturbation. No sub-$G_0/G_1$ peak (corresponding to apoptotic cells) is detected in the cytograms.
Oxidative stress was evaluated by Thiobarbituric Acid Reactive Substances (TBARS) and reactive oxygen species generation was not detected.[45]

### 2.5.2 Nanowires and cells: the UP-TAKE

The cell is surrounded by a selectively permeable membrane: the plasma membrane. Its purpose is to delimit the boundary of the cell structure and maintain intracellular environment.

Small and non-polar molecules, such as $O_2$ or $CO_2$, can diffuse across the lipid bilayer. Conversely, polar molecules or ions are unable to cross the membrane.
For this reason, important biological ions or nanometer-sized proteins are transported across the lipid bilayer through specialized membrane-transport protein channels.[48]

The same happens for macromolecules at the nanoscale, molecular assemblies and nanomaterials. These structures are internalized through endocytosis. This process consists in the absorption of macromolecules into cells through membrane enclosed vesicles confinement, in contact with the cell membrane. [49]

There are three types of endocytosis:

- **Phagocytosis:** is a process of transporting a solid substance into the cell. The contact between the solid substance and the cell membrane causes a folding of the membrane and the formation of pseudopodium. In this way the cell membrane surrounds the solid substance. When the cell membrane completely encloses the solid, it breaks down to form a vacuole, which separates from the membrane. (Figure 2.12 a)

- **Pinocytosis:** is a process of transporting liquid material inside the cell. The mechanism follows the same principle of phagocytosis. (Figure 2.12 b)

- **Receptor-mediated endocytosis:** is a type of endocytosis in which specific molecules on the external substances surface combine with the cell membrane receptor proteins. To enter the cell, all substances must first bind to receptor proteins. Then there is the formation of a vesicle covered by a layer of proteins. (Figure 2.12 c)

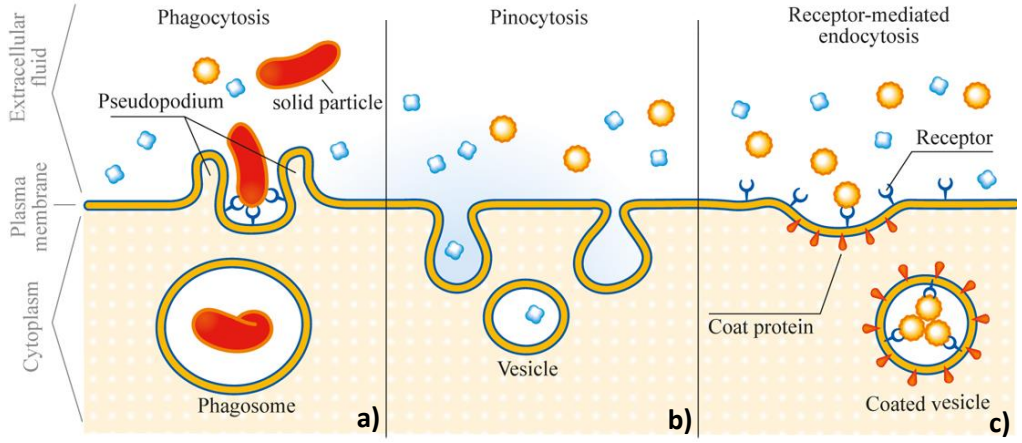


*Figure 2.12: Basic principles of endocytosis: a) phagocytosis, b) pinocytosis and c) receptor-mediated endocytosis. Credit: Pinterest.com.*

Typically, nanomaterial interactions with cell membranes are dictated by the chemical functionalities on the surface, in addition to their dimensions. In fact, the shape and size of nanostructures has been found to greatly influence the cellular up-take.

In the case of nanowires, the cells use cytoplasmic protrusions to surround the nanowire and trap it in a large vesicle. These vesicles are predominantly localized near the plasma membrane and the NWs are never inside the nucleus.[47]
The pictures of NWs internalization are shown in Figure 2.13.

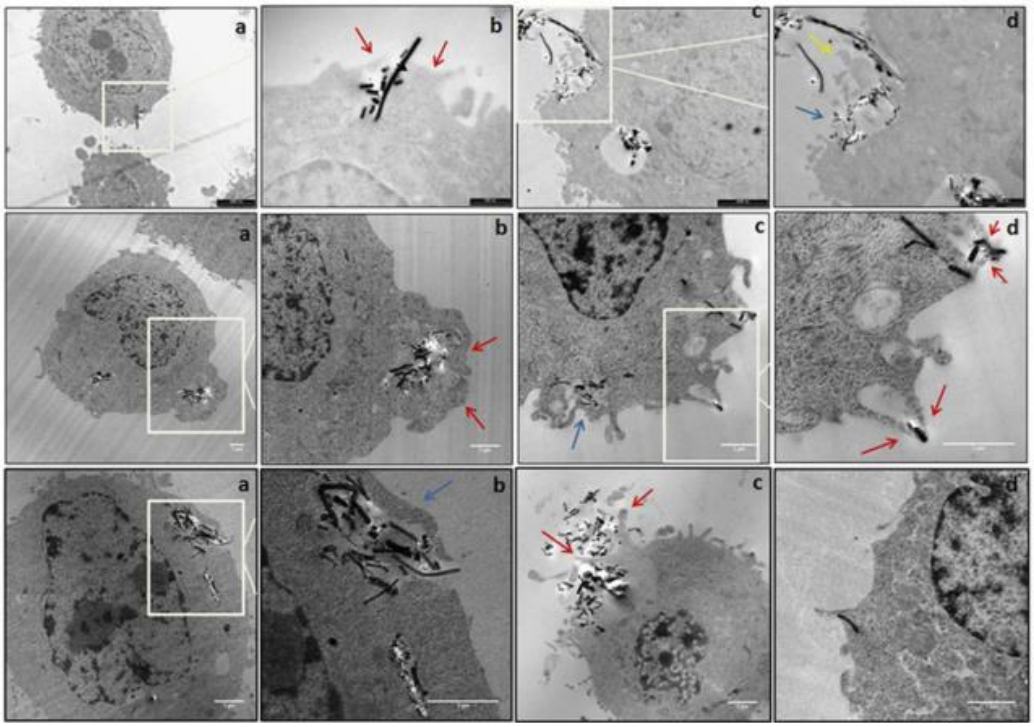


*Figure 2.13: NWs internalization analyzed by TEM in A549 cells (first line), MCF-7 cells (second line), and HuDe cells (third line).*[47]

## References


1 R. S. Wagner and W. C. Ellis, *Appl. Phys. Lett.*, 1964, **4**, 89–90.
2 C. M. Morales, A.M and Lieber, *Science*, 1998, **279**, 208–11.
3 P. Cheyssac, M. Sacilotti and G. Patriarche, *J. Appl. Phys.*, 2006, **100**, 044315/1-044315/12.
4 J. H. Zhao, *MRS Bull.*, 2005, **30**, 7–8.
5 H. Wingbrant, H. Svenningstrop, P. Salomonsson, P. Tengström, I. Lundström and A. L. Spetz, *Sensors Actuators, B Chem.*, 2003, **93**, 295–303.
6 W. E. Svendsen, M. Jørgensen, L. Andresen, K. B. Andersen, M. B. B. Larsen, S. Skov and M. Dimaki, *Procedia Eng.*, 2011, **25**, 288–291.
7 B. Tian and C. M. Lieber, *Pure Appl. Chem.*, 2011, **83**, 2153–2169.
8 H. D. Tong, S. Chen, W. G. van der Wiel, E. T. Carlen and A. van den Berg, *Nano Lett.*, 2009, **9**, 1015–1022.
9 T. I. Kamins, X. Li, R. S. Williams and X. Liu, *Nano Lett.*, 2004, **4**, 503–506.
10 J. Westwater, *J. Vac. Sci. Technol. B Microelectron. Nanom. Struct.*, 1997, **15**, 554-563.
11 S. Bhunia, T. Kawamura, Y. Watanabe, S. Fujikawa and K. Tokushima, *Appl. Phys. Lett.*, 2003, **83**, 3371–3373.
12 X.-Y. Bao, C. Soci, D. Susac, J. Bratvold, D. P. R. Aplin, W. Wei, C.-Y. Chen, S. A. Dayeh, K. L. Kavanagh and D. Wang, *Nano Lett.*, 2008, **8**, 3755–3760.
13 H. M. Lin, Y. L. Chen, J. Yang, Y. C. Liu, K. M. Yin, J. J. Kai, F. R. Chen, L. C. Chen, Y. F. Chen and C. C. Chen, *Nano Lett.*, 2003, **3**, 537–541.
14 X. T. Zhang, Z. Liu, Y. P. Leung, Q. Li and S. K. Hark, *Appl. Phys. Lett.*, 2003, **83**, 5533–5535.
15 C. J. Barrelet, Y. Wu, D. C. Bell and C. M. Lieber, *J. Am. Chem. Soc.*, 2003, **125**, 11498–11499.
16 H. K. Park, B. Yang, S. W. Kim, G. H. Kim, D. H. Youn, S. H. Kim and S. L. Maeng, *Phys. E Low-Dimensional Syst. Nanostructures*, 2007, **37**, 158–162.
17 P. C. Chang, Z. Fan, D. Wang, W. Y. Tseng, W. A. Chiou, J. Hong and J. G. Lu, *Chem. Mater.*, 2004, **16**, 5133–5137.
18 R. Regonini, C. Pelosi, B. E. Watts and F. Leccabue, *Epitassial growth of Silicon Carbide*, vol. 102.
19 X. Li, X. Wang, R. Bondokov, J. Morris, Y. H. An and T. S. Sudarshan, *J. Biomed. Mater. Res. - Part B Appl. Biomater.*, 2005, **72**, 353–361.
20 R. Yakimova, R. M. Petoral, G. R. Yazdi, C. Vahlberg, A. Lloyd Spetz and K. Uvdal, *J. Phys. D. Appl. Phys.*, 2007, **40**, 6435–6442.
21 J. D. Parsons, R. F. Bunshah and O. M. Stafsudd, *Solid State Technol.*, 1985, **133**, 1536–1548.
22 J. A. Powell, P. Pirouz and W. J. Choyke, in *Semicond. Interfaces, Microstruct. Devices*, Inst. Phys., 1993, 257–293.
23 S. E. Saddow, *Silicon carbide biotechnology : a biocompatible semiconductor for advanced biomedical devices and applications*, Elsevier, 2012.
24 A. Winkelmann, B. Schröter and W. Richter, *J. Phys. Condens. Matter*, 2004, **16**, S1555–S1578.
25 M. E. (Mikhail E. Levinshteĭn, S. L. Rumyantsev and M. Shur, *Properties of advanced semiconductor materials : GaN, AlN, InN, BN, SiC, SiGe*, Wiley, 2001.
26 W. Kern and J. E. Soc, *J. Electrochem. Soc.*, 1990, **137**, 1887–1892.
27 F. Fabbri, F. Rossi, P. Lagonegro, M. Negri, J. S. Ponraj, M. Bosi, G. Attolini and G. Salviati, *J. Phys. D. Appl. Phys.*, 2014, **47**, 394006/1-394006/7.
28 G. Attolini, F. Rossi, F. Fabbri, M. Bosi, B. E. Watts and G. Salviati, *Mater. Lett.*, 2009, **63**, 2581–2583.
29 G. Attolini, F. Rossi, F. Fabbri, G. Salviati, M. Bosi and B. E. Watts, *Mater. Sci. Forum*, 2012, **711**, 75–79.
30 S. C. Dhanabalan, M. Negri, F. Rossi, G. Attolini, M. Campanini, F. Fabbri, M. Bosi and G. Salviati, *Mater. Sci. Forum*, 2013, **740–742**, 494–497.
31 F. Fabbri, F. Rossi, G. Attolini, G. Salviati, S. Iannotta, L. Aversa, R. Verucchi, M. Nardi, N. Fukata, B. Dierre and T. Sekiguchi, *Nanotechnology*, 2010, **21**, 1-7.
32 P. Juzenas, W. Chen, Y.-P. Sun, M. Alvaro Neto Coelho, R. Generalov, N. Generalova and I. L. Christensen, *Adv. Drug Deliv. Rev.*, 2008, **60**, 1600–1614.
33 F. Rossi, E. Bedogni, F. Bigi, T. Rimoldi, L. Cristofolini, S. Pinelli, R. Alinovi, M. Negri, S. C. Dhanabalan,

G. Attolini, F. Fabbri, M. Goldoni, A. Mutti, G. Benecchi, C. Ghetti, S. Iannotta and G. Salviati, *Sci. Rep.*, 2015, **5**, 7606-7613.
34 J. D. Burch, G. R. Howe, A. B. Miller and R. Semenciw, *JNCI, J. Natl. Cancer Inst.*, 1981, **67**, 1219–1224.
35 E. Pedersen, A. C. Hogetveit and A. Andersen, *Int. J. cancer*, 1973, **12**, 32–41.
36 M.-M. Song, W.-J. Song, H. Bi, J. Wang, W.-L. Wu, J. Sun and M. Yu, *Biomaterials*, 2010, **31**, 1509–1517.
37 M. Mahmoudi, a Simchi and M. Imani, *J. Iran. Chem. Soc.*, 2010, **7**, 1–27.
38 F. M. Fowkes, Ed., *Contact Angle, Wettability, and Adhesion*, American Chemical Society, Washington D.C., 1964, vol. 43.
39 F. Fabbri, F. Rossi, M. Negri, R. Tatti, L. Aversa, S. Chander Dhanabalan, R. Verucchi, G. Attolini and G. Salviati, *Nanotechnology*, 2014, **25**, 1-8.
40 P. Du, X. Wang, I.-K. Lin and X. Zhang, *Sensors Actuators, A Phys.*, 2012, **176**, 90–98.
41 A. V Vasin, A. V Rusavsky, D. V Kysil, S. Prucnal, Y. P. Piryatinsky, S. P. Starik, I. Nasieka, V. V Strelchuk, V. S. Lysenko and A. N. Nazarov, *J. Lumin.*, 2017, **191**, 102–106.
42 A. Tamayo, J. Rubio, F. Rubio, J. L. Oteo and R. Riedel, *J. Eur. Ceram. Soc.*, 2011, **31**, 1791–1801.
43 S. Onclin, B. J. Ravoo and D. N. Reinhoudt, *Angew. Chem. Int. Ed. Engl.*, 2005, **44**, 6282–6304.
44 P. Lagonegro, F. Rossi, C. Galli, A. Smerieri, R. Alinovi, S. Pinelli, T. Rimoldi, G. Attolini, G. Macaluso, C. Macaluso, S. E. Saddow and G. Salviati, *Mater. Sci. Eng. C Mater. Biol. Appl.*, 2017, **73**, 465–471.
45 P. Lagonegro, *Study of interaction between Si(O,C) nanowires and biological systems*, Università degli Studi di Parma, 2016.
46 J. Coty and C. Vauthier, *J. Control. Release*, 2018, **275**, 254–268.
47 A. Cacchioli, F. Ravanetti, R. Alinovi, S. Pinelli, F. Rossi, M. Negri, E. Bedogni, M. Campanini, M. Galetti, M. Goldoni, P. Lagonegro, R. Alfieri, F. Bigi and G. Salviati, *Nano Lett.*, 2014, **14**, 4368–4375.
48 E. Nogueira, C. F. Cruz, A. Loureiro, P. Nogueira, J. Freitas, A. Moreira, A. M. Carmo, A. C. Gomes, A. Preto and A. Cavaco-paulo, *Biochim. Biophys. Acta*, 2016, **1858**, 163–167.
49 G. Sahay, D. Y. Alakhova and A. V Kabanov, *J Control Release*, 2010, **145**, 182–195.

# 3. Cancer

## 3.1 Cancer: a brief introduction

### 3.1.1 What is cancer?

Cancer is described as a disease caused by uncontrolled growth and reproduction of abnormal cells.[1]
When healthy cells grow old or become damaged, they die, and new cells take their place.
When cancer develops, this orderly process breaks down: when a cell become cancerous, old or damaged this cell survives instead of dying.
Cancer cells lose their normal control mechanisms. They are able to expand continuously, invade adjacent tissues, migrate to distant parts of the body, and promote the growth of new blood vessels to obtain more nourishment.

Cancerous cells can develop from any tissue within the body and they are less specialized than normal cells: whereas healthy cells mature with specific functions, cancer cells do not.
Therefore, cancer cells continue to divide without stopping because they can ignore signals that normally order cells to stop dividing or start the process of programmed cell death (apoptosis). (Figure 3.1)
Furthermore, cancer cells are often able to evade the immune system or are able to "hide" from the removal of damaged or abnormal cells from the body.

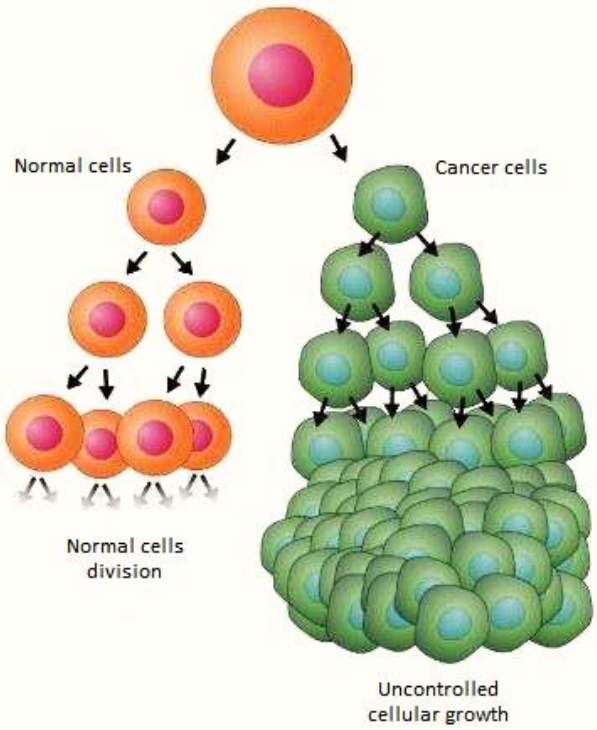


*Figure 3.1: Schematic mechanism of cell division in normal cells and in cancer cells. Credits: SlideShare, Liam Arnade-Colwill.*

### 3.1.2 Types of cancer and statistic

Cancer is a genetic disease: it is caused by changes in genes that control the cells functioning, particularly growth and division.

The most common origins of cancer are the inheritance of this disease from our parents, or during person's lifetime the result of errors in cells division, or the damage to the cell's DNA caused by environmental exposures and radiation, such as the chemicals in tobacco smoke or carcinogenic compounds of chemical industries, ultraviolet rays from the sun, high-energy radiation (X-rays or gamma rays), radon gas, etc.[2,3,4]

Tumors are divided into benign and malignant:

- **Benign tumors**
  Benign tumors are classified as non-cancerous. A benign tumor is not able to spread to adjacent tissues or to distant sites through the bloodstream or the lymphatic system. This type of tumor can usually be removed and is rarely a threat to the patient life.

- **Malignant tumors**
  Malignant tumors are classified as cancerous. A malignant tumor can invade and damage the nearby tissues and organs. This type of tumor is a serious threat to the patient life because cancer cells break away from the malignant tumor original site and enter the bloodstream or the lymphatic system to form secondary tumors in other parts of the body. This transport mechanism is called metastasis.

The name of a malignant tumor is assigned based on the site of primary origin: the organs or tissues in which cancer begins. For example, lung cancer starts in the lung cells while brain cancer starts in the cells of the brain.
However, cancer can spread from the point of origin to other parts of the body through blood system, lymphatic system and/or cerebrospinal fluid.
Even in these cases, cancer derives its name from the original starting point, and not from the point of arrival. Therefore, a cancer that originates in the colon and spread to the liver, is called colon cancer that has metastasis to the liver, and not liver cancer.

Below, the main types of cancer and their respective cancer ribbons, the international symbols for cancer awareness, are listed. (Table 3.2)[5]


*Figure 3.2: Cancer awareness colors for different types of cancer.*
*Credits: Asian Fund for Cancer Research (AFCR).*

Cancer is one of the main public health problem worldwide. The most recent cancer data available lags 2 to 5 years behind the current year (2018) due to the time required for data collection, compilation, control, and dissemination.

There were an estimated 14.1 million cancer cases around the world in 2012, of these 7.4 million cases were in men and 6.7 million in women. The number of cancer deaths in 2012 was 8.2 million and in 2015 8.8 million. The data of new cancer cases expected to be diagnosed in 2030 is 21.7 million with 13 million of deaths.[6,7]

In Figure 3.3, the world map shows the estimated age-standardized mortality rates in 2018.

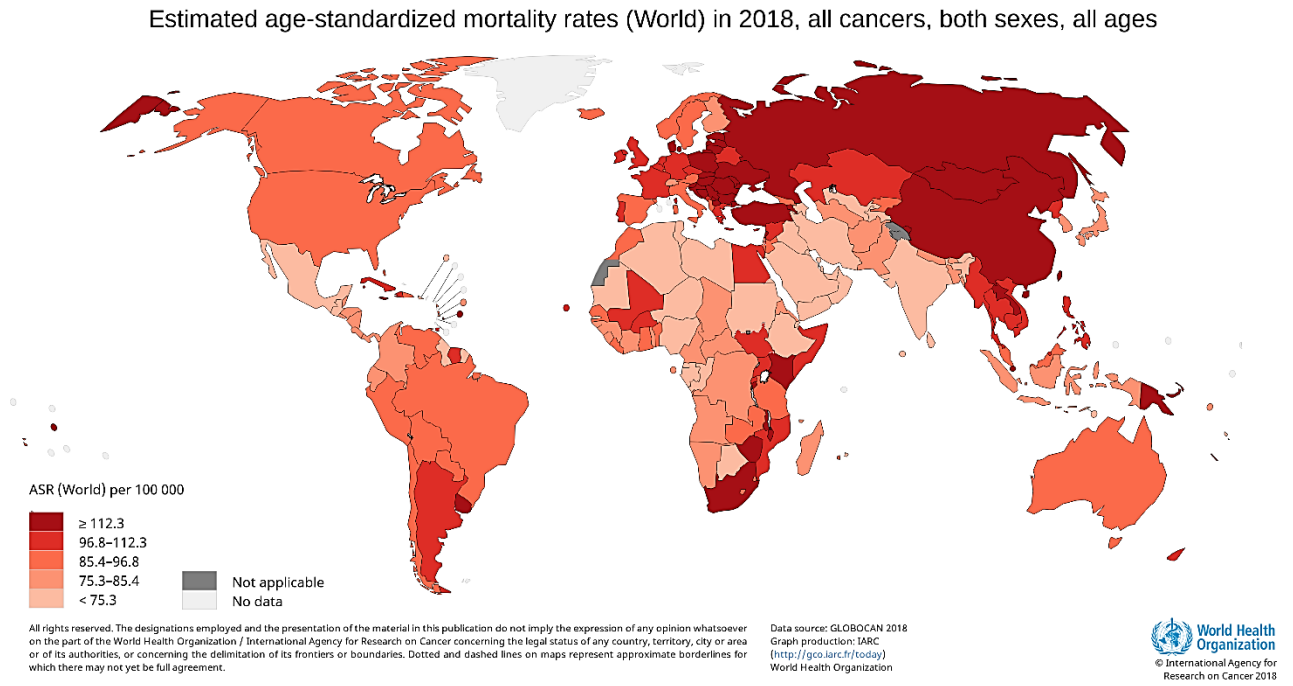


*Figure 3.3: Estimated age-standardized rates (World) of deaths, all cancers, both sexes, all ages, worldwide in 2018.[8] Credits: GLOBOCAN 2018.*

## 3.2 A general overview of cancer treatments

Given the serious gravity of the problem, the fight against cancer has become one of the major priorities for the modern medicine.
Currently the main techniques for treating malignant tumors are surgery, radiotherapy and chemotherapy.[9,10,11]

The advent of anesthesia in the middle of 19$^{th}$ century made the use of surgery to remove tumors possible.
This technique is still widely used but has some disadvantages. In fact, it is effective only for i) small solid tumors or tumors in the early stages of the disease; ii) is an invasive technique for the patient; iii) if the carcinogenic tissue is not completely removed it can give rise to relapses, metastases and new tumors.

Radiotherapy is a technique born in the early 1900s, after the discovery of X-rays and the properties of the radio.
This technique exploits high-energy radiation to destroy the DNA of diseased cells and block their process of uncontrolled division.
The disadvantage of radiotherapy is that radiation affects both cancer cells to healthy cells, causing serious side effects in the patient. For this reason, radiotherapy cannot be used for spread tumors. Furthermore, an excessive or too prolonged dose of radiation leads to the appearance of new tumors.

Chemotherapy is the most recent technique, born in the early 40s, with the discovery of the anticancer properties of nitrogen mustard, a derivative of mustard gas employed during the World War I.
For the first time, a tumor has regressed thanks to the administration of drugs, since then called chemotherapeutic agents.
This sensational discovery has opened the door to the search for new, more effective and selective chemotherapy drugs in the fight against cancer.

The main findings are reported in chronological order in Figure 3.4. Over time, awareness of the cancer problem has taken place. This led to the emergence of scientific associations and new regulations on drugs and therapies.

The advantage of chemotherapy is that it can, in principle, affect all the tumor cells that are spread in the body, even if they are very distant from each other (for example in case of diffuse metastases). Furthermore, it is also a non-invasive therapy as the drugs are administered intravenously or orally.

But the greatest improvements came from the combination of surgery with a set of drugs aimed at different specific targets.

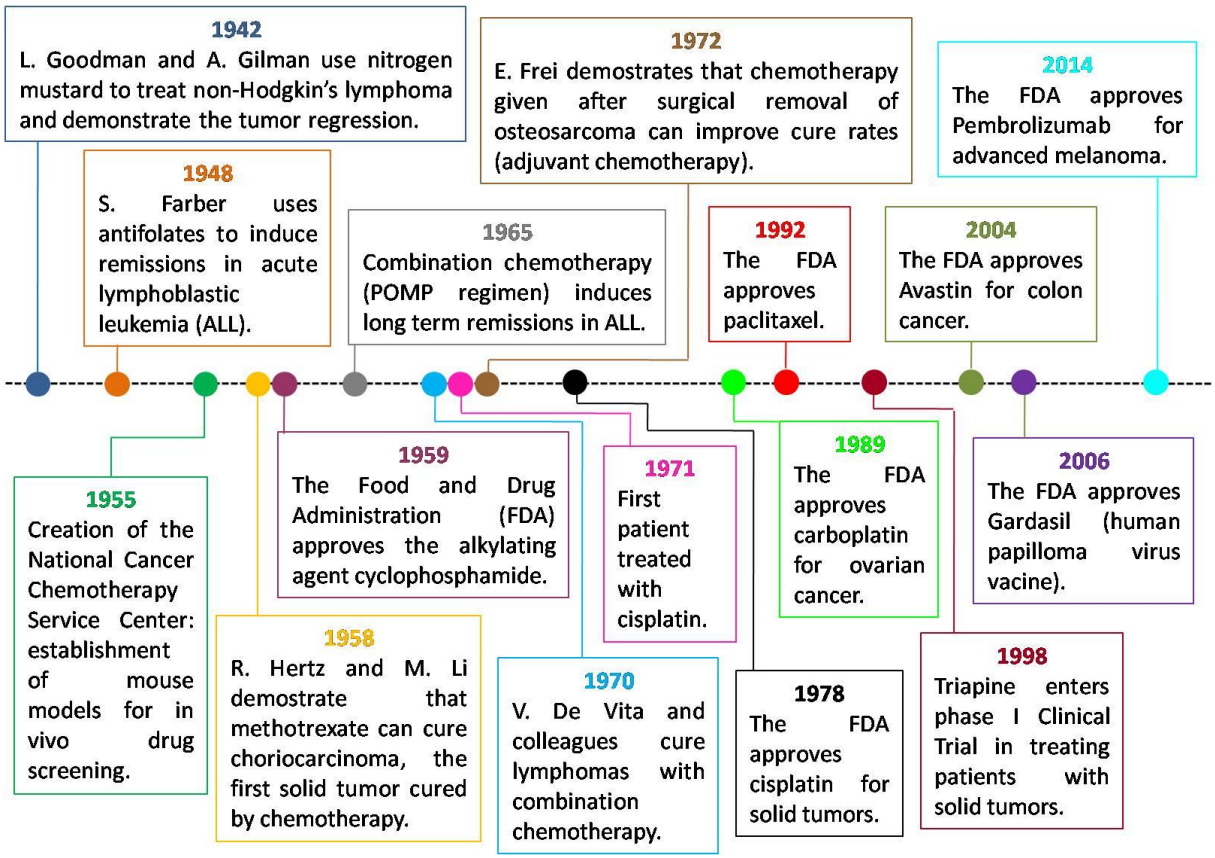


*Figure 3.4: Timeline of the main discoveries and events related to the world of anticancer medicine (years: 1940-2014)*

Among the most active anticancer agents, there are compounds containing metals. The pioneer of such classes of drugs is cisplatin, used for the first time in the early 70s.
After the discovery of the efficacy of cisplatin, many structural analogues were synthesized and tested.

An example of second-generation platinum-based compounds are carboplatin and oxaliplatin. (Figure 3.5)

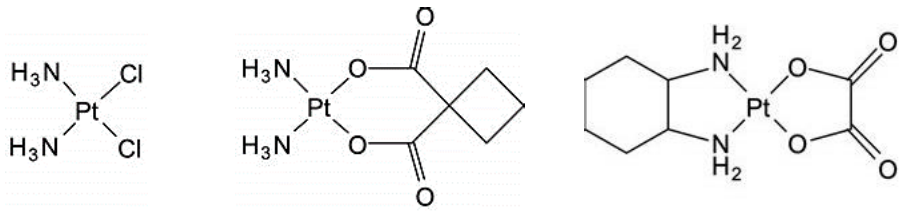


*Figure 3.5: Chemical structure of cisplatin, carboplatin and oxaliplatin.*

Platinum-based drugs are still among the main chemotherapeutic agents in use, but they have the disadvantage of having a biological toxicity.[12] In addition, some tumor cell lines have become resistant to platinum-based drugs treatment.[13]

For all these reasons, scientists all over the world are looking for valid alternatives to these drugs, following very different ideologies.

Many researchers have tried or are trying to replace platinum with related metals (such as Pd and Ru)[14,15] or with biologically present metals in the human body, more biocompatible, such as Cu, Zn, Fe, etc.

Another very broad line of research has instead focused on the study of completely new chemical compounds, sometimes with very complex structures.

The latter category includes thiosemicarbazones, a family of compounds that has shown promising antineoplastic properties. Moreover, their nature of ligands makes them suitable for complexations with various types of metals, such as Pt and similar (Pd and Ru) or more biocompatible metals such as Cu, Fe, Zn, etc.

The next Chapter will describe in more detail the thiosemicarbazones and their complexes.

The nanotechnology applications in cancer treatment are relatively new and constantly evolving.
Most recent allies in the fight against cancer are some nanomaterials used as drugs carriers. In particular liposomes[16,17], nanoparticles[18], dendrimers[19,20] or nanomicelles[21].

The advantages of using a nanomaterial as drugs carrier are: i) the possibility of increasing the water solubility of the drugs and protecting them improving the pharmacokinetic and pharmacological properties; ii) the ability to target the drugs release in specific tissues or cells, reducing the spread around and increasing the therapeutic efficacy; iii) the possibility to decorate nanomaterials with more chemically or physically active components: different types of drugs, imaging agents, antibodies, markers, etc.

While the main disadvantages in the use of nanomaterials are their potential biological toxicity and the risks of possible accumulation of material in organs such as kidney, liver, spleen, etc.

## References


1 National Cancer Institute (NIH), Understanding Cancer, https://www.cancer.gov/about-cancer/understanding/what-is-cancer.

2 J. D. Burch, G. R. Howe, A. B. Miller and R. Semenciw, *JNCI, J. Natl. Cancer Inst.*, 1981, **67**, 1219–1224.

3 E. Pedersen, A. C. Hogetveit and A. Andersen, *Int. J. cancer*, 1973, **12**, 32–41.

4 L. A. Torre, F. Bray, R. L. Siegel, J. Ferlay, J. Lortet-Tieulent and A. Jemal, *CA. Cancer J. Clin.*, 2015, **65**, 87–108.

5 Asian Fund for Cancer Research, Every Shade of Cancer, https://afcr.org.hk/en/content/help-us-find-cure-every-shade-cancer.

6 L. Torre and A. J. Rebecca Siegel, American Cancer Society. Global Cancer Facts & Figures 3rd Edition. Atlanta: American Cancer Society; 2015.

7 National Cancer Institute (NHI), Cancer Statistics, https://www.cancer.gov/about-cancer/understanding/statistics.

8 J. Ferlay, F. Bray, E. Steliarova-Foucher and D. Forman, *Cancer Incidence in Five Continents*, IARC Scientific Publications, Lyon, 2018.

9 F. F. Becker, *Cancer: A Comprehensive Treatise, Vol. 6: Radiotherapy, Surgery and Immunotherapy.*, Plenum, 1977.

10 S. K. Carter, M. T. Bakowski and K. Hellmann, *Chemotherapy of Cancer. 2nd Ed.*, Wiley, 1981.

11 J. Egawa, *Manual of Cancer Radiotherapy.*, Chugai Igaku Co., Ltd., 1989.

12 M. Markman, *Expert Opin. Drug Saf.*, 2003, **2**, 597–607.

13 L. P. Martin, T. C. Hamilton and R. J. Schilder, *Clin. Cancer Res.*, 2008, **14**, 1291–1295.

14 A. Matilla, J. M. Tercero, J. Niclós-Gutiérrez, N.-H. Dung, B. Viossat, J. M. Pérez, C. Alonso and J. D. Martín-Ramos, *J. Inorg. Biochem.*, 1994, **55**, 235–247.

15 G. Zhao, H. Lin, Y. Ping, H. Sun, S. Zhu, S. Xuncheng and Y. Chen, *J. Inorg. Biochem.*, 1999, **73**, 145-149.

16 Y. Gao, J. Chen, H. Jiang, Y. Wu and Y. Li, *Drug Des. Devel. Ther.*, 2015, **9**, 2265-2278.

17 Z. Liu, M. Xiong, J. Gong, Y. Zhang, N. Bai, Y. Luo, L. Li, Y. Wei, Y. Liu, X. Tan and R. Xiang, *Nat. Commun.*, 2014, **5**, 4280.

18 C. Sanchez, P. Belleville, M. Popall and L. Nicole, *Chem. Soc. Rev.*, 2011, **40**, 696-705.

19 N. Malik, E. G. Evagorou and R. Duncan, *Anticancer. Drugs*, 1999, **10**, 767–776.

20 K. T. Al-Jamal, W. T. Al-Jamal, J. T.-W. Wang, N. Rubio, J. Buddle, D. Gathercole, M. Zloh and K. Kostarelos, *ACS Nano*, 2013, **7**, 1905–1917.

21 S. Biswas, P. Kumari, P. M. Lakhani and B. Ghosh, *Eur. J. Pharm. Sci.*, 2016, **83**, 184–202.

# 4. The oncology project: Thiosemicarbazones (TSCs)

The research project on thiosemicarbazones and their antitumor properties started in 2016, during the period spent abroad as researcher at the University of Cape Town, South Africa.

Thanks to the *Bilateral Agreement for Joint Philosophy Doctor (PhD) Degrees* between the University of Parma and the University of Cape Town, I had the pleasure of working with the research group of Professor G. Smith, at the Department of Chemistry of University of Cape Town (UCT).

Almost the whole Chapter is the result of the work done at the University of Cape Town.

## 4.1 Brief general overview

In recent years, chemotherapy has achieved important results in the fight against cancer.
However, there are still many tumors resistant to this technique that are not effectively eradicated using the most common anticancer drugs, such as cisplatin and derivatives.

To try to solve this problem, scientists around the world are focusing their attention on the design of new anticancer agents with a mechanism of action different from that of cisplatin. Of particular interest are compounds targeting ribonucleotide reductase (RR).

RR is a heteromeric enzyme consisting of two R1 and R2 subunits, which catalyzes the reductive conversion of RNA building blocks to DNA building blocks for DNA replication and repair. RR is fundamental for all living cells because it controls cell proliferation and maintains genomic stability.[1,2]
Since tumor cells proliferate much faster than normal healthy cells, selectively blocking the enzyme RR of the diseased cells through appropriate inhibitors could be the solution to hit all the tumors, even the most resistant ones.

Thiosemicarbazones (TSCs) are strong metal N,S-chelating agents and have been reported to be among the most effective RR inhibitors yet identified.[3]

Observing the structural characteristics, TSCs are Shiff bases containing a rich set of donor atoms (N and S) which makes them excellent chelating agents. (Figure 4.1

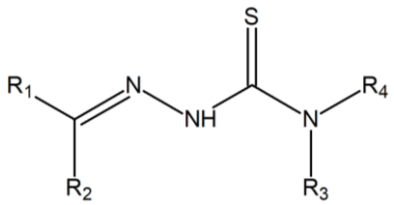


*Figure 4.1: General structure of thiosemicarbazone. $R_1$, $R_2$, $R_3$, $R_4$ = H, or any organic substituent.*

TSCs may exist as thione/thiol tautomeric forms due to proton transfer. (Figure 4.2)

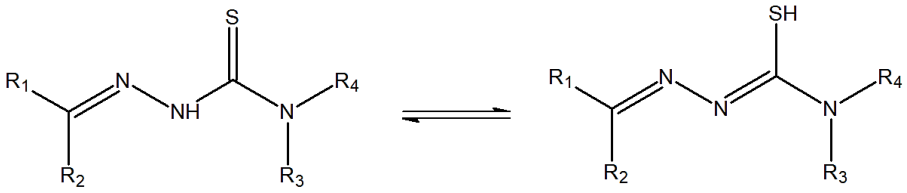


*Figure 4.2: Tautomeric forms of thiosemicarbazones: thione and thiol.*

The most common synthetic route to obtain TSCs is the condensation of a ketone or aldehyde with a thiosemicarbazide in environmental conditions. This synthesis presents low cost and high atoms economy since all the atoms from the reagents (except water released in the condensation) are present in the final molecule.

The TSCs are great ligands and can coordinate a metal ion in neutral or anionic forms. This behavior is due to the presence of tautomerism and the anionic form is generated by the loss of N-NH proton of the thione form or the SH proton of the thiol form.
Their ability to coordinate metal ions can be further increased if the aldehyde or ketone used as a reagent in the synthesis contains an additional functional group in a position suitable for chelation, like X atom in Figure 4.3.

The most common coordination modes (**I-IV**) are shown in Figure 4.3. [4]

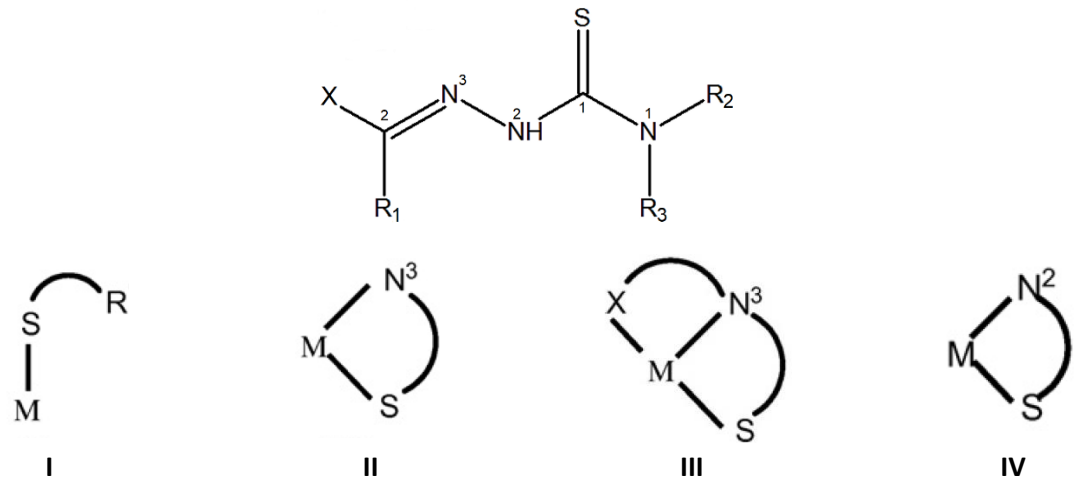


*Figure 4.3: Most common coordination modes for neutral and anionic TSCs. The X atom connected with $C^2$ represents a generic donor atom like N, O.*

In neutral and anionic forms, the metal (M) binding can occur via only S atom in $\eta^1$-S (**I**)[5] and $\eta^2$-$N^3$,S-chelation (**II**)[6]. If the substituent at $C^2$ has a donor atom X, and engages in bonding, the additional bonding modes observed is $\eta^3$-X,$N^3$,S-chelation (**III**). [7]
In addition, only for the anionic form a $\eta^2$-$N^2$,S-chelation (**II**) exists. [8]

Despite the promising antitumor activity of TSCs, these compounds show an extremely low water solubility[9] and tend to precipitate[10] rapidly in the culture medium, making their administration as anticancer drugs sometimes problematic.
As already explained in Chapter 3.2, the possibility of anchoring TSCs to carriers, such as nanowires, would solve the problem of the poor hydrophilicity of these molecules and/or avoid the uncontrolled dispersion within the body.

The most active TSCs against various types of tumors are TSCs that present in their structure at least one aromatic ring in position $R_1$ or $R_2$.[11,12]
Moreover, the efficacy of the antitumor activity is often related to the presence of metal ions chelated to the structure of TSCs.[13,14]
Compounds containing in position $R_1$ or $R_2$ substituents such as ferrocene widely increase the metallic percentage and they proved to be very biologically active against various diseases. In addition to their antitumor properties, ferrocene-TSCs play an important role in the fight against malaria.[15,16,17]

For this reason, thiosemicarbazones with aromatic substituents or ferrocene in $R_1$ position were synthetized. Once the thiosemicarbazones were anchored on the surface of the NWs through a suitable molecular linkers, these N,S-donor ligands were complexed with heavy metal ions, often used in the biomedical field in the fight against tumors for their anticancer properties. [18]
Of course, also other metal ions (i.e. copper, gold, iron, etc.) were reported in the literature. [19,20,21]

## 4.2 Choice of the linkers and the three anchoring methods

As already explained above, the simplest synthetic route to obtain a generic thiosemicarbazone is the condensation reaction between an aldehyde or ketone with a thiosemicarbazide.

However, to anchor the synthesized thiosemicarbazone molecule on the surface of nanowires it is essential that the thiosemicarbazone has an appropriate functional group able to react with the functional group of a selected linker, to form an NW-linker-thiosemicarbazone connection. (Figure 4.4)


*Figure 4.4: Schematic diagram of the connection between NW (in red), linker (in green) and thiosemicarbazone (in blue). The three elements are represented as pieces of a puzzle.*

The NWs used are core-shell, so they have an outer layer of silica. Unlike SiC, silicon oxide is much more reactive and can be easily functionalized through various chemical processes.

The reactions of functionalization can occur on NWs anchored to the growth substrate (reactions involving the use of the whole platelet immersed in a solvent) and on nanowires detached from the growth substrate (reactions on nanowires no longer anchored to the platelet and dispersed in a solvent).

To differentiate the two types of process, in the reaction figures the image of a gray platelet with a red arrow and a gray nanowire will be used to indicate the reactions occurring on the platelet, while for the reactions occurring on detached NWs the image of the platelet will be omitted and only the image of the nanowire will be present.

An example of a reaction that occurs on a platelet is the surface activation reaction.
To optimize the reactivity of the silica layer, the platelet of NWs is put in concentrated HCl (37%) and the system is heated to about 80 degrees for at least 2 hours. The acidic environment and the high temperature activate the surface, making it more chemically reactive. This mechanism is shown in Figure 4.5. For visual simplicity, the NW active surface was drawn rich in -OH groups.
In Figure 4.6 the platelet before and after the surface activation: before the acid treatment the platelet is dark gray, while after HCl the surface is light gray.

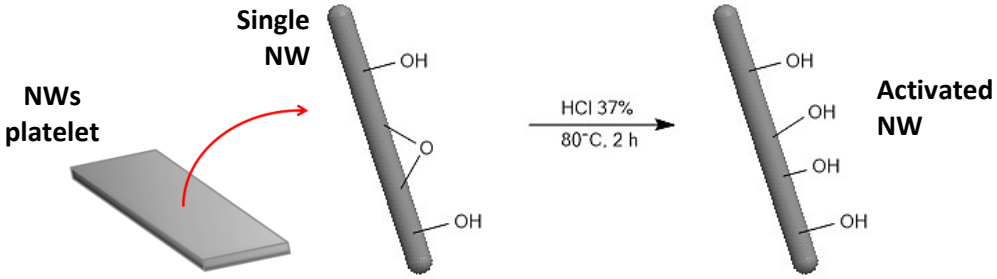


*Figure 4.5: NWs surface activation step with concentrated HCl (37%). To indicate that the reaction takes place on the NWs anchored on the growth substrate there is an image of a gray platelet and a red arrow on the left of the reaction image. The activated NW has the surface covered of free -OH groups.*

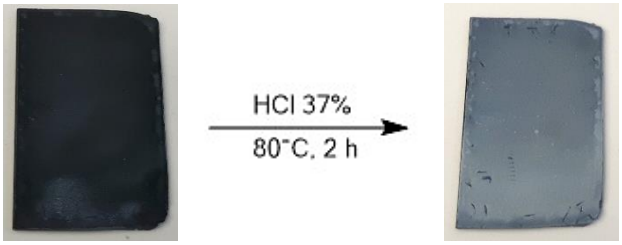


*Figure 4.6: NWs platelet before the surface activation (left) and after the acid treatment (right).*

For the choice of the most appropriate linker to use, molecules having a chemical composition as similar as possible to the chemical composition of NWs (predominantly silicon, oxygen and carbon) were searched.

The most obvious choice fell on the family of silanes, already widely used in literature to functionalize different types of surfaces.[22,23] and previously for the functionalization of silica in the preparation of supported catalyst.[24]

Silanes containing -OH groups (silanols) or -OR (alkoxysilanes) bound to the silicon atom can react with various materials through the hydroxyl groups present on the material surface.

Although the exact mechanism for the formation of the surface coating is not yet fully understood. Probably, the silanes react with the surface hydroxy groups by eliminating a water (or ROH) molecule to be permanently bonded to the surface through new Si-O bonds.

Once anchored on the surface, silanes can polymerize internally with each other to form Si-O-Si bonds (siloxane bond).
In this thesis the degree of polymerization that occurs between the various silanes or how they are anchored to the surface of nanowire have not been analyzed. The chosen linker is a silane terminating with three -OR groups to maximize the interactions with the surface of the NWs.

Hypothetically, each Si-O-R arm can react with the -OH groups present on NWs; therefore, the anchoring can occur through 1, 2 or all 3 arms. (Figure 4.7).

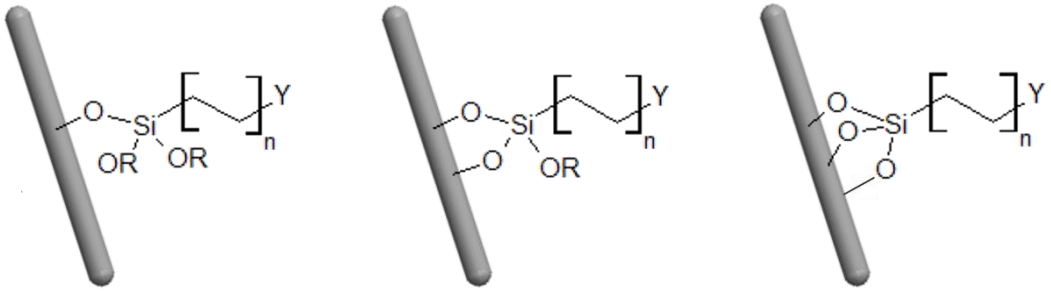


*Figure 4.7: Image that visually describes the anchoring of silane to the surface of the nanowire through 1, 2 or 3 Si-O-R arms. The fourth arm is composed of a chain of n carbon atoms and ends with a generic Y functional group.*

On the basis of results reported on silica functionalization with trialkoxysilanes, which evidenced that on average the condensation involved two alkoxy groups, in this thesis the silane will be depicted anchored to the nanowire through two arms.

As seen in Figure 4.7, the silicon atom in addition to the three alkoxy groups has a longer arm, terminating with a generic functional group Y.
In order to successfully anchor thiosemicarbazones to the nanowire it is essential that the length of this arm allows the functional group Y to react with thiosemicarbazone without being excessively hindered by the solid body of the nanowire. On the other hand, chains that are too long could fold in on itself and bring the Y group close to the surface, making it less accessible. As a compromise between the two options a linker with a chain of three C atoms linked to the silicon atom was chosen.

The choice of the functional group Y was mainly determined by the following reasons: i) Y was to be a reactive group and at the same time chemically stable in various conditions (high temperatures, aqueous environments, presence of oxygen, etc.); ii) Y had to react with thiosemicarbazone creating a new covalent bond; iii) in the anchoring process the specific structure of thiosemicarbazone has to be respected by maintaining the bonds $R_2C{=}NNHC(=S)NR_2$.

Following in the text, the three different anchoring approaches on the NWs surface will be described in the bulleted list with the titles: 1st Anchoring Method, 2nd Anchoring Method and 3rd Anchoring Method.
At the end of the discussion, on page 51, there is a summary table (Table 4.4) of these three anchoring approaches used, the various chemical reaction steps and the problems encountered.
For greater clarity for the reader, it can already anticipate that the best anchoring approach will be the 3rd Anchoring Method.

- **1st Anchoring Method: APTES**

In order to respect the third point, APTES *(3-aminopropyl)triethoxysilane* was selected as linker. (Figure 4.8)

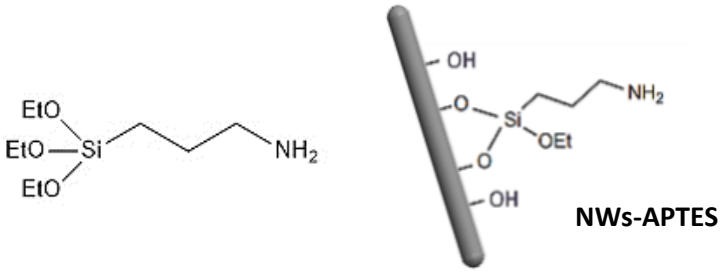


*Figure 4.8: Left, structure of (3-aminopropyl)triethoxysilane (APTES). Right, a NW functionalized with APTES (NWs-APTES).*

The functionalization of the NWs with APTES generates nanowires whose surface is covered by free amino groups.
Therefore, to anchor the thiosemicarbazone to the NWs it will be necessary to use a thiosemicarbazone precursor with a specific functional group able to react with the -$NH_2$ group of the linker anchored to the nanowires. The reaction between the amino group of the linker and the functional group of the thiosemicarbazone precursor will form the complete structure of the desired thiosemicarbazone, anchored to the NWs.

The thiosemicarbazones precursors (generically represented as compound **2** in Figure 4.9 and called in the text simply "thiosemicarbazone precursor") were obtained from the reaction between a S-methyl dithiocarbazate (Figure 4.9, **1**) and an aldehyde or ketone.
From the reaction between the HN(S=)C-$SCH_3$ precursors functional group and the amino group of APTES the thiourea group HN(S=)C-NHR is generated (Figure 4.9, **3**) and the thiosemicarbazone is formed.

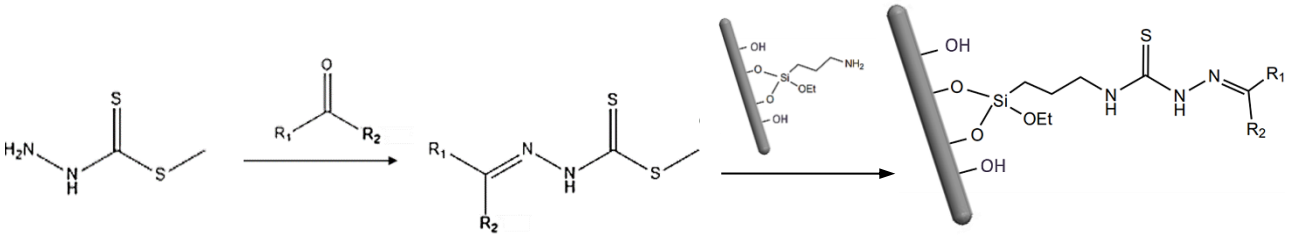


**1** **2** **3**

*Figure 4.9: Example of reaction between a S-methyl dithiocarbazate (**1**) with an aldehyde or ketone to obtain a thiosemicarbazone precursor (**2**). Precursor **2** can react with the -$NH_2$ group of the APTES linker (NWs-APTES) and generate the anchored thiosemicarbazone **3**.*

### 4.2.1 Synthetized thiosemicarbazones precursors for NWs-APTES

The first step in the synthesis of thiosemicarbazones precursors was the synthesis of the S-methyl dithiocarbazate. The reaction scheme is shown below, while details are given in the Experimental Section at the end of the Chapter.

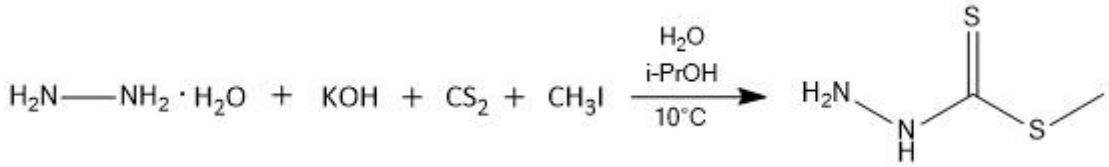


**1**

Compound **1** can react with suitable aldehydes and ketones to generate various thiosemicarbazones precursors. To obtain thiosemicarbazones containing aromatic groups, aromatic aldehydes and ketones were chosen as starting reagents.

The scheme in Figure 4.10 shows the various reagents used in the reaction with compound **1** and the related precursors of the thiosemicarbazones obtained: in the diagram above the ferrocene-TSCs precursors (**2** and **3**) while in the diagram below the aromatic TSCs precursors with different substituents on the ring (**4**-**7**).

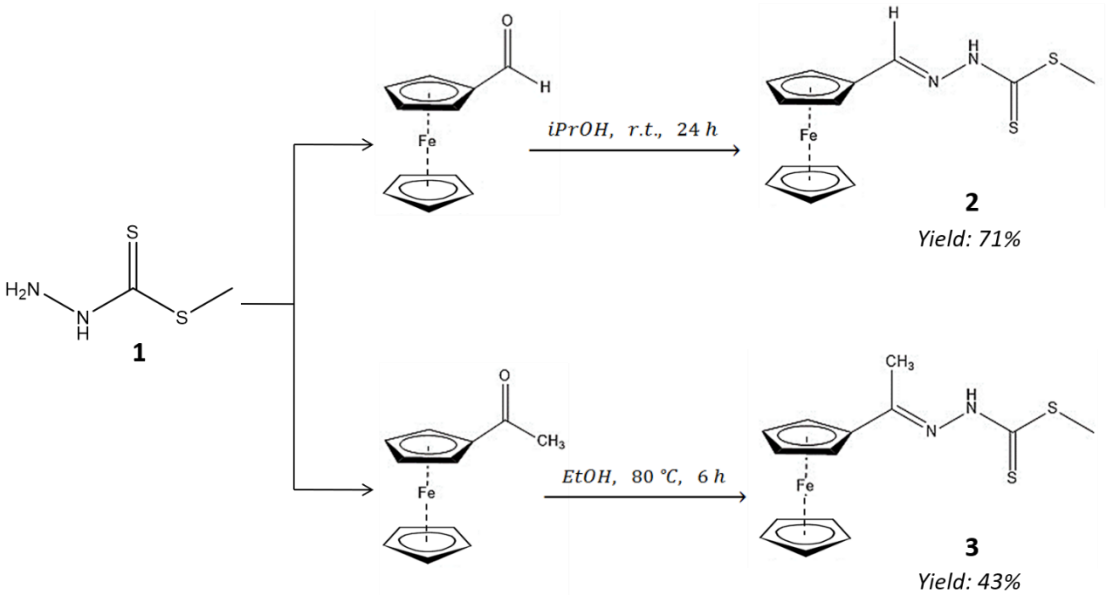

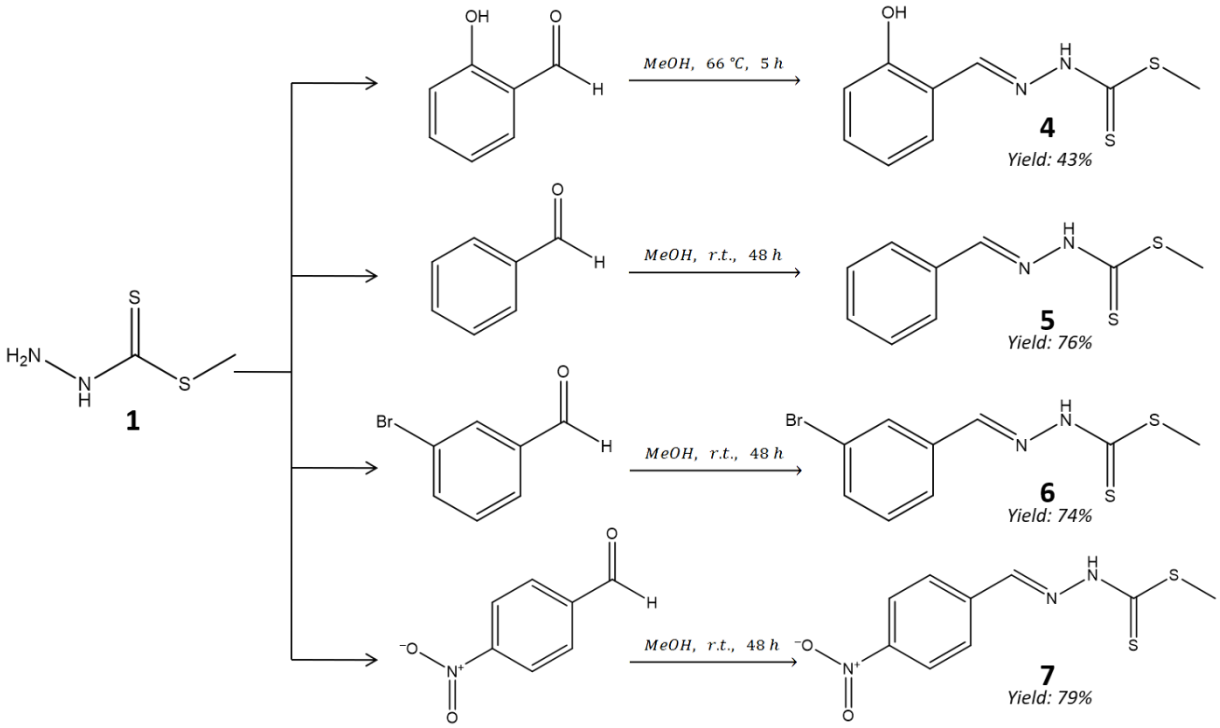


*Figure 4.10: Scheme of the reactions of compound **1** with aromatic aldehyde and ketone to obtain compounds **2-7**.*

Compounds **2-7** were characterized by $^{1}$H-NMR and FT-IR spectroscopy.

In Figure 4.11 the $^{1}$H-NMR spectrum of compound **5**. The N-NH proton peak is visible at 13.29 ppm, followed by the HC=N proton signal at 8.26 ppm. The aromatic protons are in the area between 7.80 and 7.40 ppm, while the S-$CH_3$ signal is at about 2.50, superimposed on the DMSO signal.

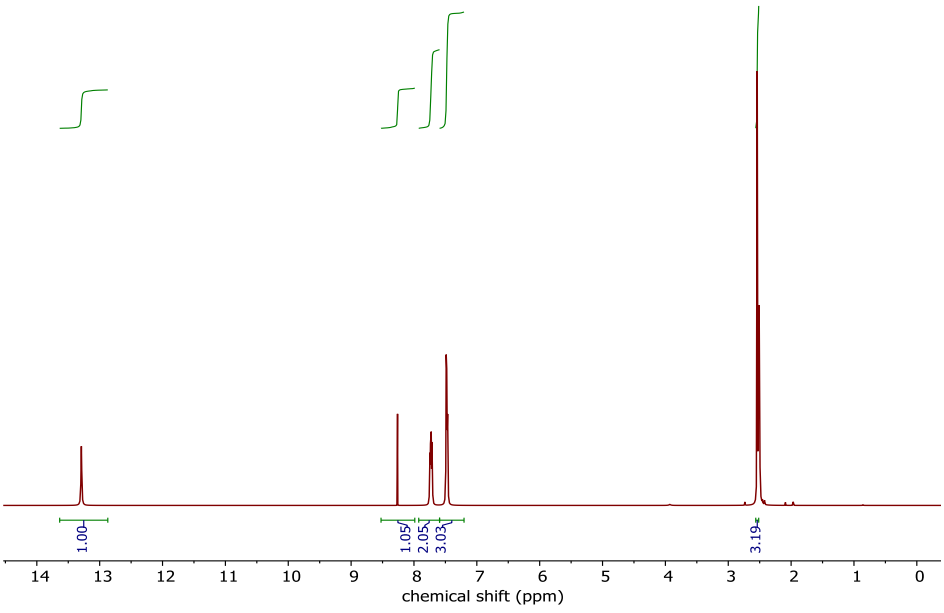


*Figure 4.11: $^{1}$H-NMR spectrum of compound **5** in DMSO-$d_6$.*

To attach the TSCs precursors to nanowires, the preliminary functionalization step of the NWs surface with APTES is necessary.
After the activation in concentrated HCl (37%), the platelet is reacted with APTES in toluene, as shown below, to obtain NWs-APTES.

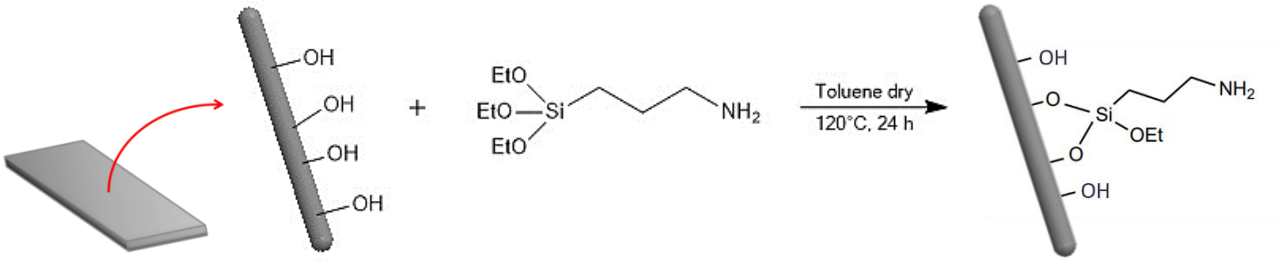


Subsequently the NWs-APTES, detached from the growth substrate by sonication in a bath at 59 MHz, can react with the various precursors of the thiosemicarbazones.

The general reaction is drawn below.

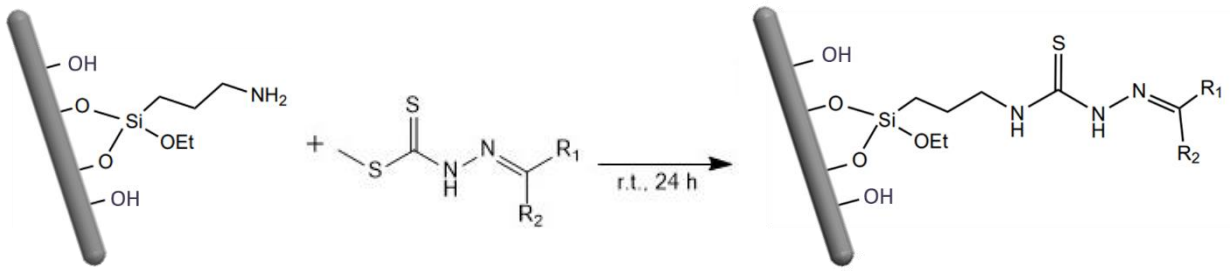


The result is the anchoring of thiosemicarbazones on the surface of nanowires. The table below shows all the compounds obtained on NWs (**8-13**). (Table 4.1)

*Table 4.1: Thiosemicarbazones obtained (**8-13**) anchored on NWs surface.*

***8***

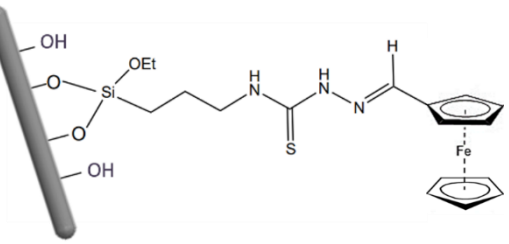


***11***

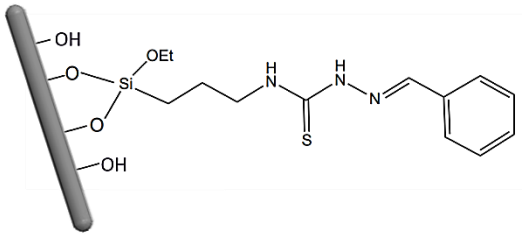


***9***

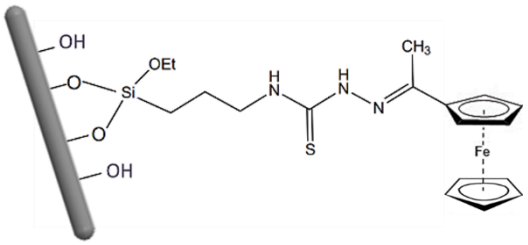


***12***

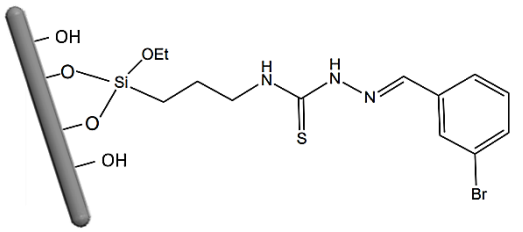


***10***

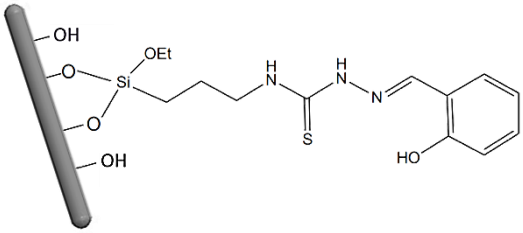


***13***

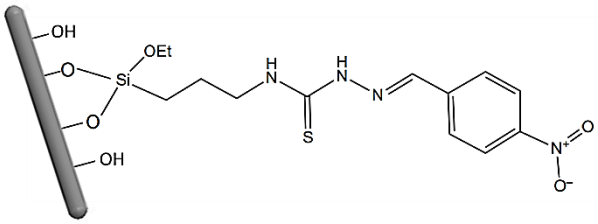


Compounds **8-13** were analyzed using FT-IR, SEM microscopy, TEM microscopy and EDX technique.

Figure 4.12 shows the EDX-TEM characterization performed on compound **9**. From the images, the functionalization of the NWs surface with the precursor **3** occurred with good yields: the presence of S (in yellow) and Fe (in light green) are the demonstration.

In fact, both these two elements are not naturally present on the NWs surface and arise from the molecular structure of the precursor **3**. This means that the precursor reacted with the APTES anchored to NWs and the surface is covered by the relative thiosemicarbazone **9**.

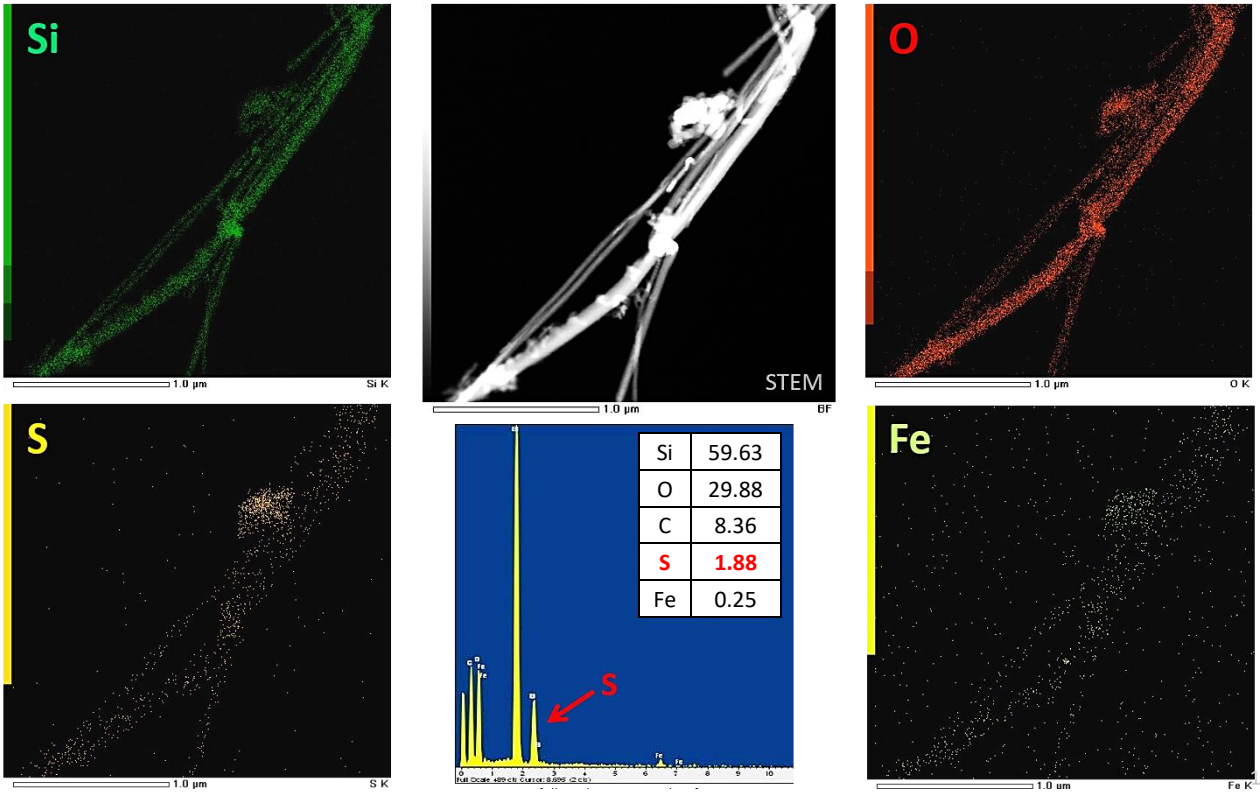


*Figure 4.12: EDX-TEM analysis on compound **9**. The presence of sulfur is highlighted by the red arrow in the elemental spectrum, while in the elemental maps: silicon is green, oxygen is red, sulfur is yellow, and iron is light green.*

As mentioned before, thiosemicarbazone are very good N,S-ligand. Therefore, also the thiosemicarbazones anchored on NWs can react with several metal ions to form the related anchored complexes (NWs-complexes).

As starting metal salts $K_2[PtCl_4]$, $[(Cp^*)Rh(\mu\text{-}Cl)Cl]_2$ and $[Ru(\eta^6\text{-}p\text{-}Cymene)Cl]_2$ were selected.

The complexes obtained (**14-18**) are shown in Table 4.2. Initially it was decided to give priority only to the thiosemicarbazones able to chelate the metal through the two N and S atoms.
For this reason, thiosemicarbazone **10** was not involved in complexation reactions, because due to the presence of the -OH group in the aromatic ring it would give a tridentate chelation.

*Table 4.2: Anchored thiosemicarbazone metal complexes obtained.*

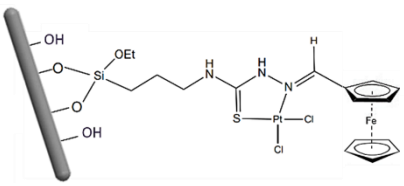

**14a**

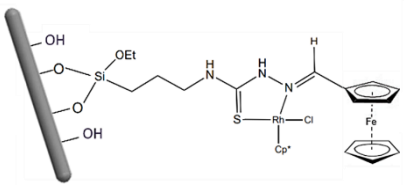

**14b**

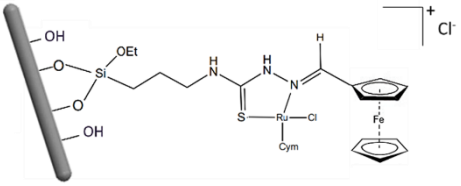

**14c**

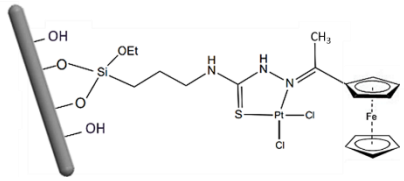

**15a**

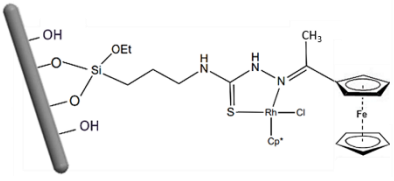

**15b**

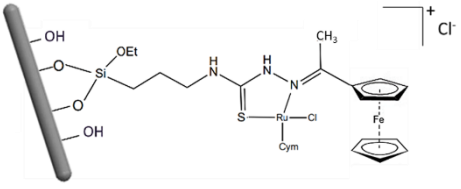

**15c**

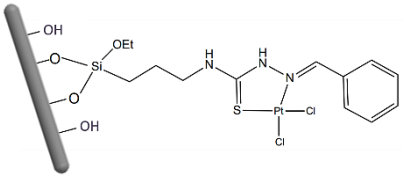

**16a**

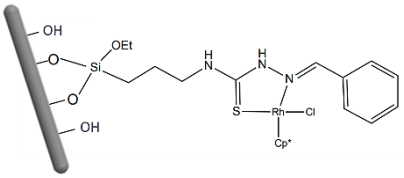

**16b**

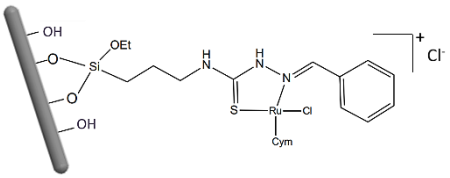

**16c**

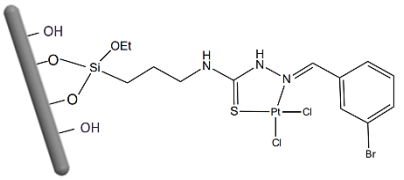

**17a**

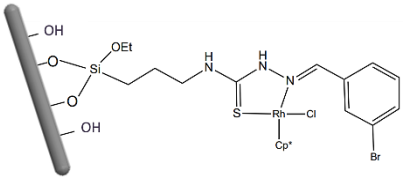

**17b**

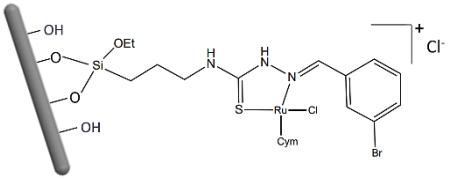

**17c**

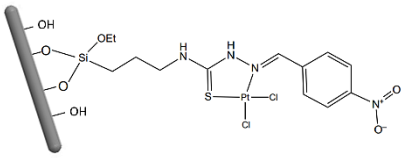

**18a**

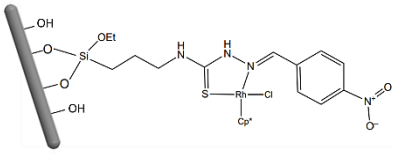

**18b**

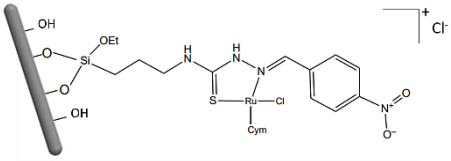

**18c**

EDX-TEM analyses were performed on the various NWs-complex samples to verify the successful chelation of the metal ions to the thiosemicarbazone ligand.

In Figure 4.13 and 4.14 some images of the EDX NWs surface mappings of compound **14a** and compound **14c** are reported.

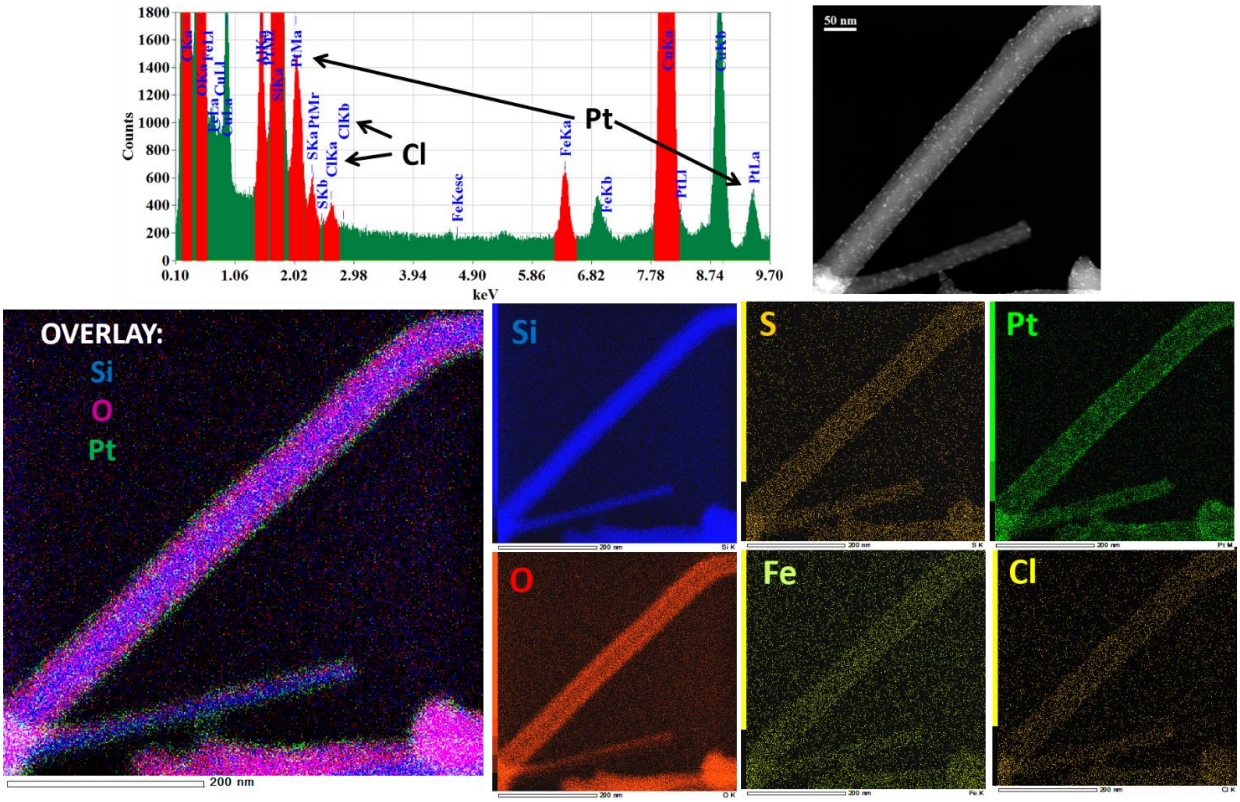


*Figure 4.13: EDX-TEM analysis of compound **14a**. The presence of Pt and Cl is highlighted by the black arrows in the elemental spectrum (image in the upper left corner). The elemental maps show the presence of silicon in blue, oxygen in red, sulfur in orange, iron in pale yellow, platinum in green and chlorine in yellow. On the left, the overlap of Si, O and Pt maps on the NWs surface.*

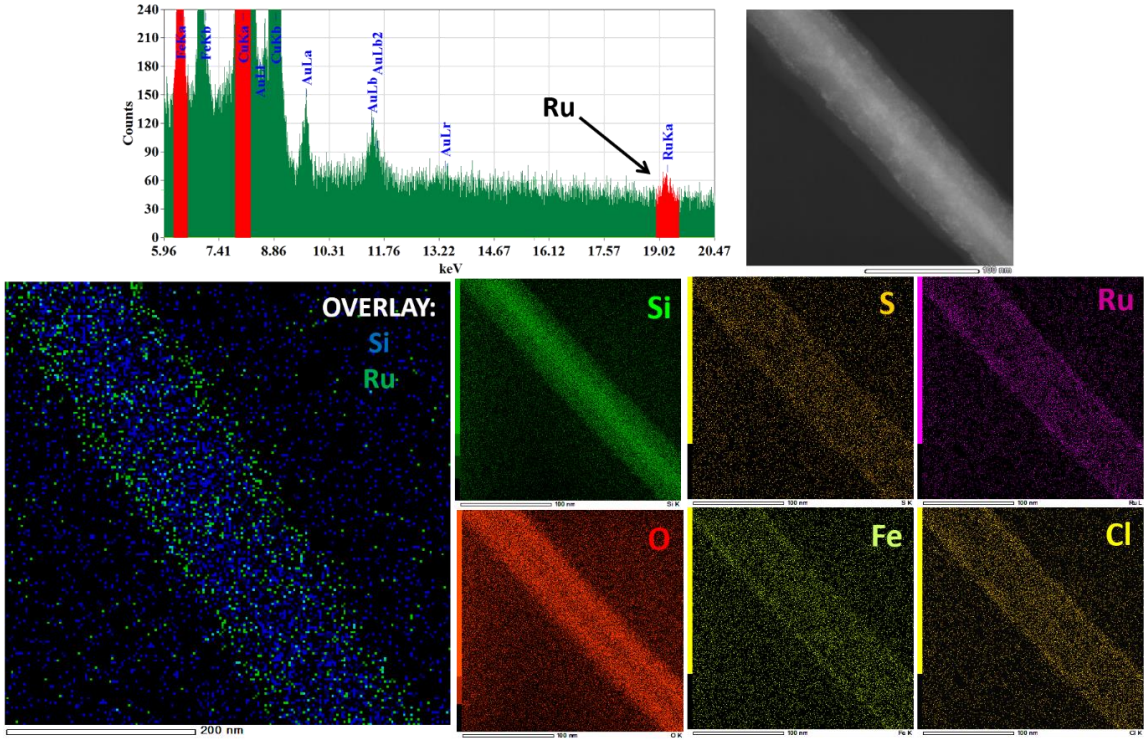


*Figure 4.14: EDX-TEM analysis of compound **14c**. The presence of Ru is highlighted by the black arrows in the elemental spectrum (image in the upper left corner). The elemental maps show the presence of silicon in green, oxygen in red, sulfur in orange, iron in pale yellow, ruthenium in purple and chlorine in yellow. On the left, the overlap of Si and Ru maps on the NW surface.*

The percentage composition data obtained from the mapping of the NWs surface, show in all samples a percentage of metal ions higher than the percentage of sulfur.

Since every single thiosemicarbazone anchored on NWs can bind a single metal ion because the chelation ratio is 1:1, the data should have highlighted the same 1 to 1 ratio in the percentage composition values of the S (diagnostic to identify the presence of thiosemicarbazone on NWs) and the metal ions.

For example, Table 4.3 shows the results for compounds **14a-c**. The sulfur and metal composition percentages are framed in red.

*Table 4.3: Percentage composition values of compounds **14a-c**. Framed in red the S and M data.* (*The value of % Other mainly includes the values of carbon, iron and chlorine).*

| | **14a** | **14b** | **14c** |
|---|---|---|---|
| **% Si** | 37,27 | 38,26 | 36,96 |
| **% O** | 31,01 | 31,74 | 34,40 |
| **% S** | **0,76** | **0,68** | **0,65** |
| **% M** | **4,34** (Pt) | **3,01** (Rh) | **1,74** (Ru) |
| **% Other** | 26,62 | 26,31 | 26,25 |

The excess of Pt, Rh and Ru cannot be attributed to the formation of insoluble metal clusters that remain trapped between the NWs. In fact, SEM and TEM analyzes do not show the presence of foreign bodies trapped on the surface or between the NWs.

The very lower percentage of sulfur suggested the possibility that the reaction between the precursors of thiosemicarbazone (**2-7**) and the APTES anchored to NWs occurs with low yields, leaving on the nanowires surface some free APTES -$NH_2$ terminal groups.

The free amino groups may be able to react with the metal ions in solution, competing with the thiosemicarbazone ligands, increasing the percentage of detected metal. To verify if in addition to thiosemicarbazones also the -$NH_2$ groups of APTES are able to sequester metal ions, the following experiment was carried out.

Nanowires functionalized with APTES were reacted with a solution containing dissolved $K_2[PtCl_4]$ salt. The sample was analyzed with SEM and TEM techniques to verify if N-Pt coordination occurred.

The EDX results highlighted the presence of Pt and Cl, as shown in Figure 4.15, therefore the amino group of unreacted APTES anchored to NWs is able to compete with thiosemicarbazone in the complexation of platinum.
This behavior explains why a greater percentage of metal is detected compared to the sulfur percentage of thiosemicarbazone: platinum can be linked to both APTES and thiosemicarbazone and in both ways covers the surface of the NWs.

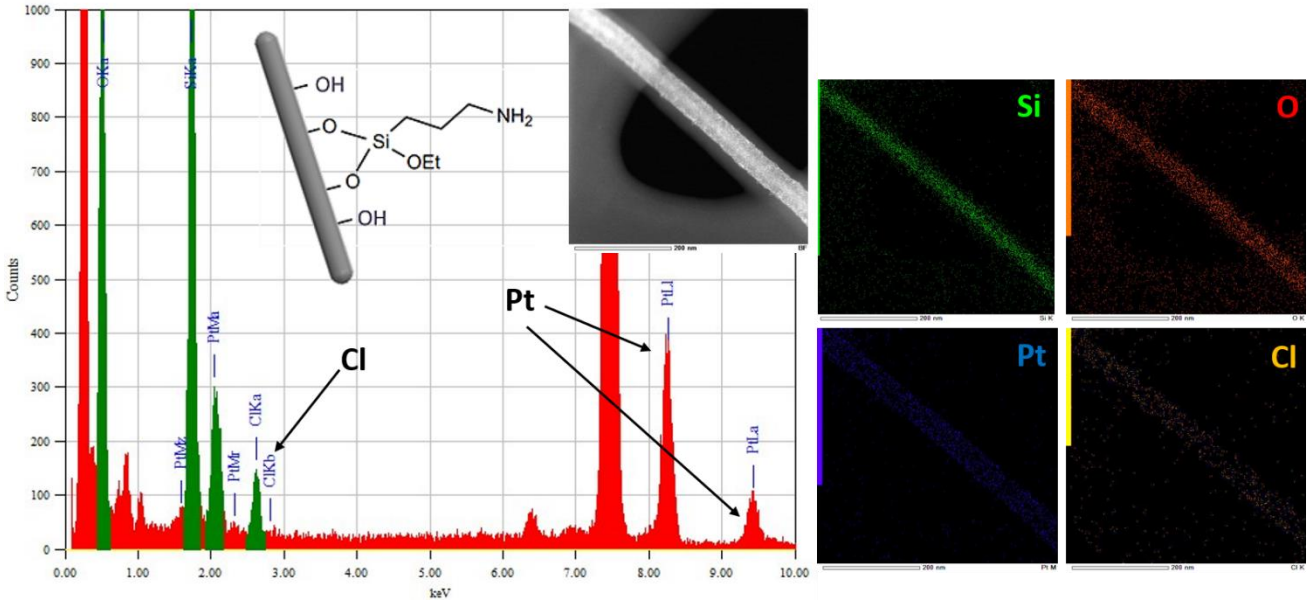


*Figure 4.15: EDX-TEM analysis of NWs functionalized with APTES and reacted with $K_2[PtCl_4]$ solution. The presence of Pt and Cl is highlighted by the black arrows in the elemental spectrum (left). The elemental maps show the presence of silicon in green, oxygen in red, platinum in blue and chlorine in yellow.*

Therefore, to avoid the presence of unreacted APTES on the surface of nanowires, a new anchoring method was adopted.

(A schematic representation of the 1st Anchoring Method approach and its disadvantages is present on page 51, Table 4.4)

- **2nd Anchoring Method**

This new approach is based on the reversal of the 1st Anchoring Method reaction steps order.

Instead of reacting the APTES functionalized nanowires with the precursors of thiosemicarbazones, the thiosemicarbazones precursors were reacted with free APTES molecules and then, just at the end, these products (precursor+APTES) were anchored on the surface of NWs.

Precursor **6** was used as reagent in the test reaction. (Figure 4.16)

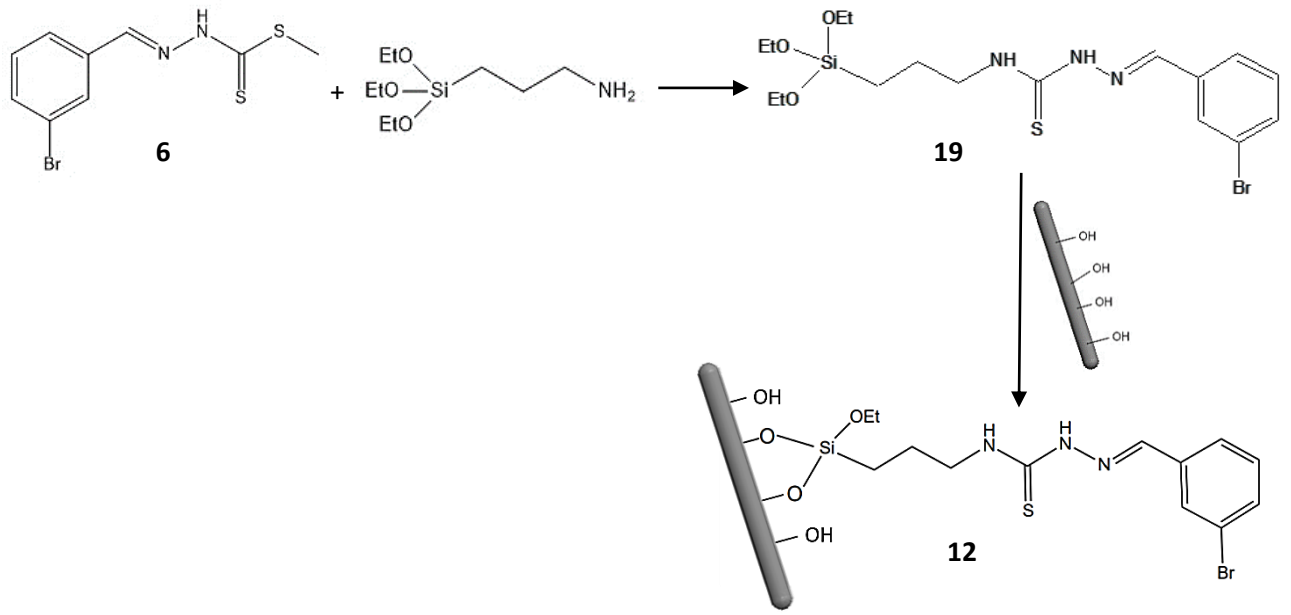


*Figure 4.16: Scheme of reaction. Step I: the reaction between thiosemicarbazone precursor **6** and APTES. Step II: anchoring reaction between compound **19** and the HCl activated NWs to bind thiosemicarbazone on NWs surface.*

The $^{1}$H-NMR analysis shows that compound **19** tends to hydrolyze quickly and is not stable over time.

Even if the subsequent anchoring reaction on HCl activated NWs is carried out immediately, TEM-EDX results show poor surface functionalization, determined by a low sulfur percentage.
Even by repeating the NWs functionalization reaction twice using fresh reagent, the final coverage of the nanowires surface remained poor. (Figure 4.17)

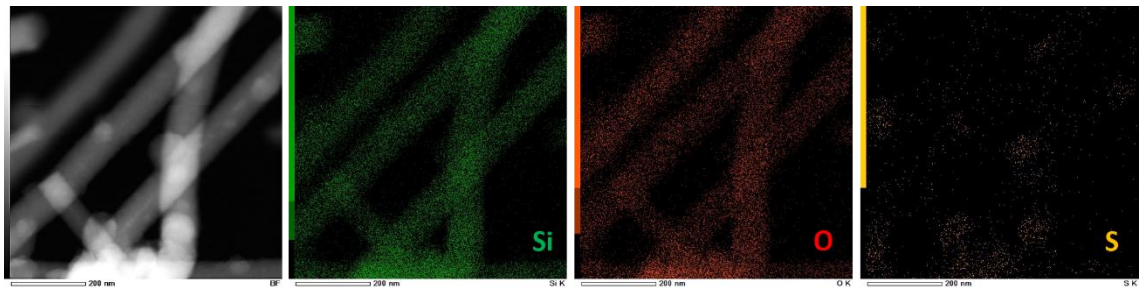


*Figure 4.17: EDX-TEM analysis of compound **12** obtained with 2nd Anchoring Method. The elemental maps show a good presence of silicon in green, oxygen in red, and a poor surface functionalization of sulfur in yellow.*

Also this anchoring method did not lead to expected results. (See Table 4.4 on page 52)

- **3rd Anchoring Method**

The 3rd Anchoring Method is similar to the first approach used (1st Anchoring Method): before the NWs surface functionalization with a linker and then the attack of thiosemicarbazone precursors.

Instead of APTES triethoxy(3-isothiocyanatopropyl)silane (Si-NCS, a very similar linker from a structural point of view) was used, but with an isothiocyanate group in place of the amino group. (Figure 4.18)

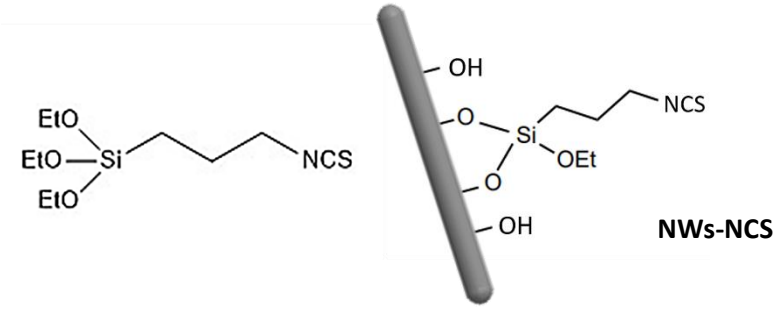


*Figure 4.18: Left, structure triethoxy(3-isothiocyanatopropyl)silane (Si-NCS). Right, a NW functionalized with Si-NCS (NWs-NCS).*

To verify if the isothiocyanate group was able to compete with the anchored thiosemicarbazones in the coordination of metal ions in solution, the same test done for NWs-APTES was performed to the NWs-NCS.

NWs functionalized with Si-NCS were dispersed in a solution containing dissolved $K_2[PtCl_4]$ salt in water. The reaction mixture was heated, and the NWs remained in the solution for 5 hours and for more than 48 hours. Then, EDX-TEM analyzes were performed on nanowires surface, to check the presence of platinum.

In the EDX map obtained (Figure 4.19) the signals relating to C, O, Si and S are observed, while the platinum signal is missing. The -NCS group does not coordinate the metal in solution and is therefore the ideal candidate as a linker for the nanowires.

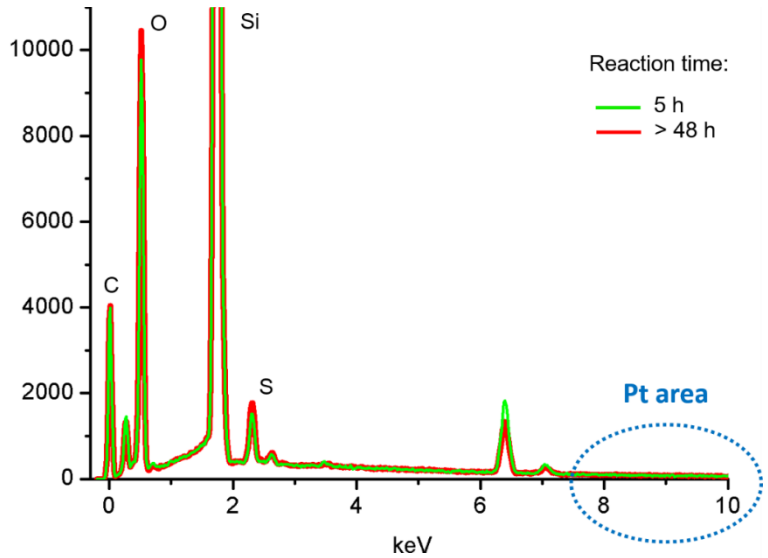


*Figure 4.19: EDX-TEM analysis of NWs functionalized with Si-NCS and reacted with $K_2[PtCl_4]$ solution. The absence of Pt is highlighted by the blue dotted circle at about 9 keV.*

The 3rd method is the method that gave the best results and will be used as the only method of the NWs functionalization from now on.

Obviously, the change of the linker functional group (-NCS and no more the APTES -$NH_2$) will require the synthesis of a new thiosemicarbazone precursor with a suitable functional group able to react with the isothiocyanate, for example amines or hydrazines.

For greater clarity, the diagram below reports the three different Anchoring Methods discussed in the previous sections, also with the three different synthetic approaches used to functionalize the NWs surface with the corresponding problems encountered. (Table 4.4)

*Table 4.4: Summarizing diagrams of the three Anchoring Methods, the various steps of the chemical functionalizations and the problems encountered. The 3rd Anchoring Method showed the most promising results and therefore will be the only method of functionalization used henceforth.*

<table>
<tr><th colspan="3">1st Anchoring Method</th></tr>
<tr><th>Linker used</th><th>NWs functionalization steps</th><th>Problems</th></tr>
<tr>
<td> 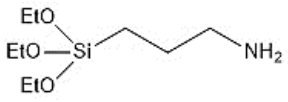

APTES</td>
<td>1. Reaction between free APTES molecules and HCl activated NWs (on platelet) to obtain NWs-APTES:<br> 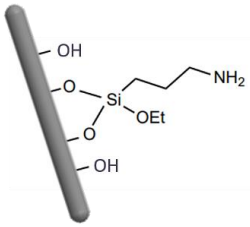

<br>2. Reaction between NWs-APTES and a general thiosemicarbazone precursor<br>(in the text compounds 2-7):<br> 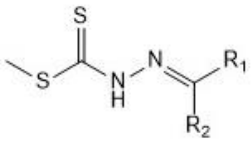

<br>to obtain NWs functionalized with thiosemicarbazones (in the text compounds 8-13):<br> 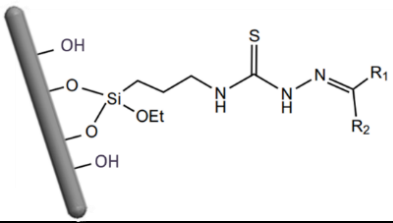
</td>
<td>Unreacted anchored APTES on NWs surface is present after the reaction with thiosemicarbazone precursor (NWs functionalization step 2).<br> 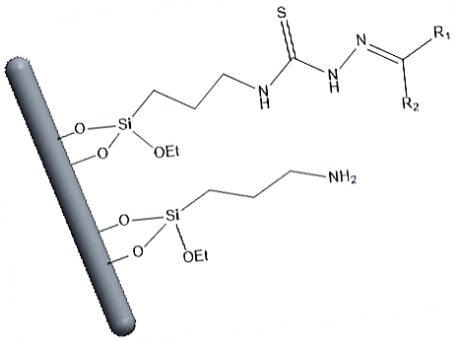

<br>This unreacted APTES can interact with metal ions in solution and can compete in chelation with the thiosemicarbazones anchored on NWs surface.<br><br>X Method <u>not</u> used.</td>
</tr>
</table>

# 2nd Anchoring Method

| Linker used | NWs functionalization steps | Problems |
|---|---|---|
| 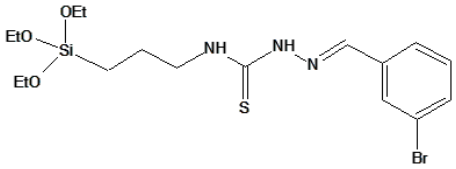 <br>Thiosemicarbazone Precursor + APTES<br>(Compound **19**) | 1. Reaction between free APTES molecules and thiosemicarbazone precursor (compound **6**) to obtain the linker (compound **19**).<br> 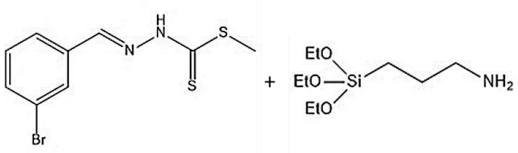 <br>2. NWs surface functionalization with the linker to obtain compound **12**:<br> 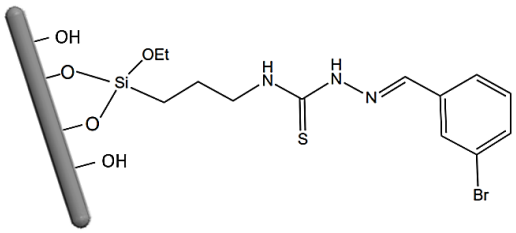 | The linker (compound **19**) is not stable over time and tends to hydrolyze. Moreover, TEM-EDX results show poor NWs surface functionalization, determined by a low sulfur percentage.<br><br>**X Method <u>not</u> used.** |

# 3rd Anchoring Method

| Linker used | NWs functionalization steps | Problems |
|---|---|---|
| 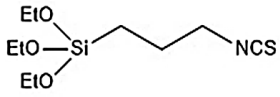 <br>**Si-NCS** | 1. Reaction between free Si-NCS molecules and HCl activated NWs (on platelet) to obtain NWs-NCS:<br> 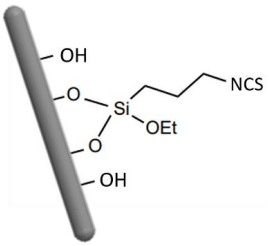 <br>2. Reaction between NWs-NCS and a suitable thiosemicarbazone precursor with a proper functional group able to react with the -NCS group of the anchored linker to obtain NWs functionalized with thiosemicarbazones:<br> 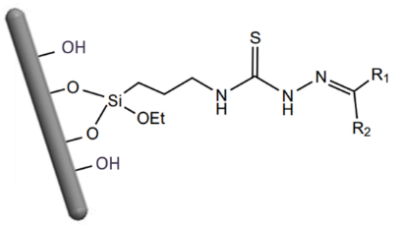 | NO PROBLEMS,<br>Good NWs surface functionalization.<br>The -NCS group does not coordinate metal ions in solution.<br><br>**√ Method used** |

## 4.3 Reactions on nanowires surface and Model Reactions in solution

Working with nanomaterials is not as simple as working with chemical compounds.

In fact, chemical compounds can: i) be dissolved in a wide range of solvents; ii) be purified using chromatographic techniques or recrystallizations; iii) be easily characterized by studying them in solution through several techniques ($^1$H-NMR, UV-Vis, MS, ESI-MS, etc.); iv) be treated using the main laboratory instruments (rotavapor, mechanical pumps for vacuum-nitrogen cycles, etc.)

Vice versa, nanomaterials do not dissolve in any solvent; they disperse creating a heterogeneous mixture, often turbid, and sometimes this behavior makes their study in solution difficult.

Therefore, to characterize nanomaterials, it is necessary to use appropriate techniques; some of them, such as TGA/DTG, and atomic absorption for loading determination, require some amount of not recoverable samples, others require not easily accessible instruments, e.g. diffuse reflectance UV–Vis spectrophotometer, TEM and SEM microscopes.
However, such analyses are often very effective in characterizing the material from a physical-structural point of view, but less efficient in giving evidences of chemical reaction with new bond formation Therefore, studying the chemical functionalizations that occur on the surface of the NWs is not always simple.

Another important information difficult to obtain in the surface functionalization reactions is the coverage yield (which represent the reaction yield). With chemical compounds, verify the success of a reaction and calculate its yield are simple operations, but for nanomaterials is more complicated and sometimes requires destructive analysis techniques that do not allow the sample to be re-used for other experiments, such as atomic absorption or thermogravimetric analyses.

To better understand the reactions occurring on the NWs surface, it is useful to simulate these reactions using model reactions in solution. Such model reactions have the same reaction conditions of the reaction carried out on NWs, but occur between free molecules dissolved in solution, having similar structure and reactivity to the molecules anchored to NWs.

The difference is that in the reactions carried out on NWs surface (called Reactions on nanowires surface) at the end I obtain functionalized nanomaterials, while in the model reactions the final products are free molecules dissolved in solution. For this reason, these reactions will be called Model Reactions in solution.

Figure 4.20 shows an example of the difference between Reaction on NWs surface and Model Reaction in solution.

In both cases the reactions occur between a generic benzylidenehydrazine (a generic thiosemicarbazone precursor) and a -NCS group (highlighted by a green circle).

In the Reaction on NWs surface the -NCS group is anchored to the nanostructure (first red arrow) and the reaction product is a thiosemicarbazone anchored to the nanowire (second red arrow).
In the Model Reaction in solution the -NCS group belongs to butylisothiocyanate molecule that is not anchored to any nanowires (no red arrows) and is dissolved in solution. The final product is a free thiosemicarbazone molecule in solution.

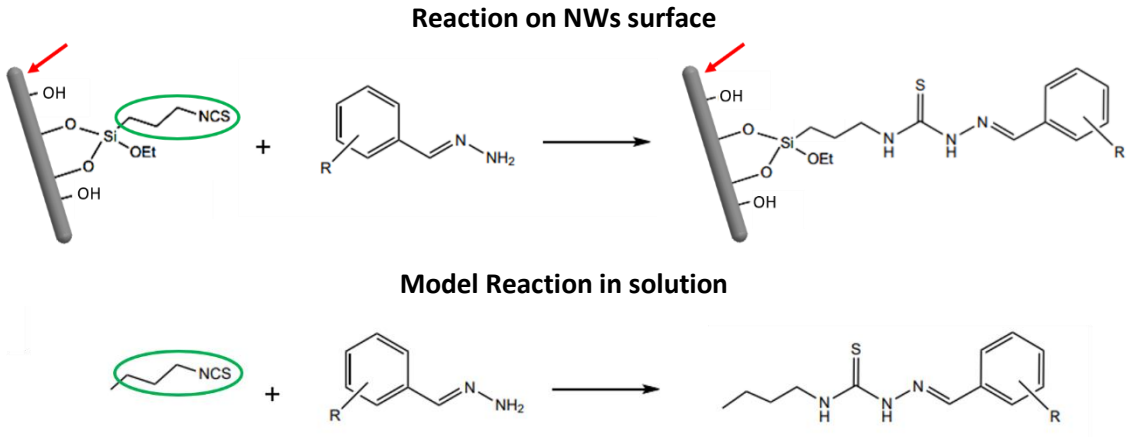


*Figure 4.20: Example of Reaction on NWs surface and Model Reaction in solution: the two reactions are almost identical, but in the first reaction the -NCS group is anchored to the surface of the nanowire, whereas in the second reaction the -NCS group belongs to a dissolved molecule structurally similar to the Si-NCS linker.*

Using free molecules dissolved in solution, simulating the molecules anchored on NWs, gives the possibility to study such molecules with various easily accessible characterization techniques (such as NMR, ESI-MS or UV-Vis) and to obtain valuable chemical information about the reaction: yields, product purity, stability of compounds, possible reactivity problems, etc.

In this way it was possible to study and optimize the reaction conditions of each step and better predict what will happen in the reactions that will occur on the NWs surface.

As already mentioned before, using a linker with a -NCS group requires a new thiosemicarbazone precursor with a suitable functional group.

Among all thiosemicarbazones, Triapine proved to be the best candidate as anticancer drug, passing phase II of clinical trial.
For this reason, Triapine was chosen as reference molecule for future experiments on NWs. The next Chapter will be entirely dedicated to Triapine, its anchoring on nanowires surface and its complexation.

## 4.4 Experimental Section

### 4.4.1 Activation of NWs surface

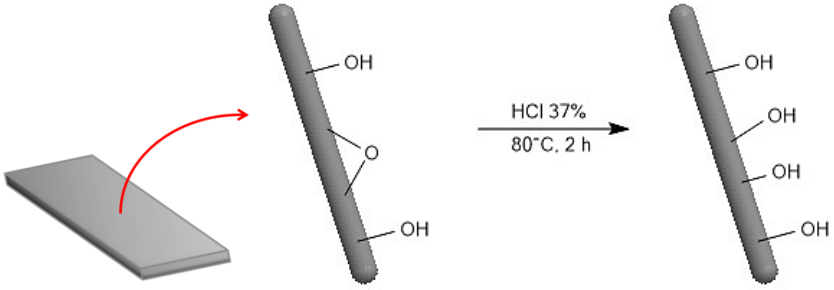


A platelet of SiC nanowires was placed in a 25 mL round-bottom flask and covered with 8 mL of HCl 37%. The system was heated to 80 °C for two hours.
On top of the refrigerant was placed a trap containing a solution of NaOH, to neutralize the HCl vapors. At the end of the reaction the platelet was washed thoroughly with water, making sure that the pH was returned to neutral and acetone. The final platelet appeared light gray.

### 4.4.2 Functionalization with (3-aminopropyl)triethoxysilane (APTES)

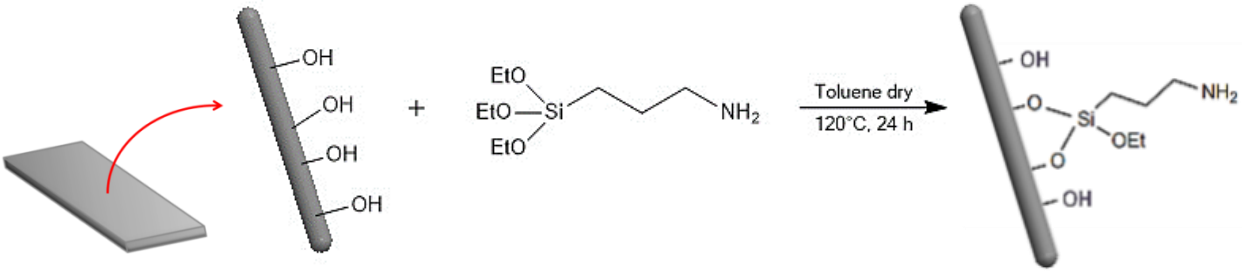


The activated platelet was placed in a 25 mL two-neck round-bottom flask, after vacuum-nitrogen cycles to obtain an anhydrous environment. The platelet was covered with 8 mL of toluene dry. A 6.5 M solution of APTES [(3-aminopropyl)triethoxysilane] (1.52 mL, 6.50 mmol) in dry toluene (1 mL) was prepared. 15 µL of this solution were added to the round-bottom flask, under nitrogen flux. The reaction was stirred and heated at 120 °C (reflux using a glycerin trap at the end of the refrigerant) for 24 h. Once the solution has cooled the platelet was removed and washed with toluene. After the functionalization the platelet color was lighter, almost gray-white.

### 4.4.3 Synthesis of S-methyl dithiocarbazate (1)

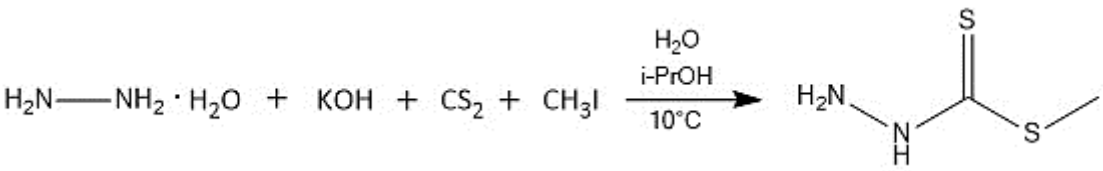


A cooled solution of KOH (10 g) in water (12 mL) and isopropanol (10 mL) was treated with hydrazine monohydrate (13 mL, 267 mmol). Cold $CS_2$ (11 mL, 178 mmol) was added drop-wise to the stirred solution

maintaining the temperature below 10°C. After 2.5 hours, cold $CH_3I$ (11 mL, 178 mmol) was added over 2 hours. After further 90 minutes the white precipitate formed was filtered, washed with cold water and recrystallized from DCM to give the desired product as white needles.[16] The reaction was monitored with TLC (diethyl ether: petroleum ether 66.6% : 33.3%, $R_f$=0.53). The final yield was 49%.

**$^1$H NMR** (300 MHz, DMSO-$d_6$) δ 10.77 (1H, 1s, NH), 5.06 (2H, s, $NH_2$), 2.39 (3H, 1s, $CH_3$).

### 4.4.4 Synthesis of ferrocenemethylidene hydrazinecarbothioate (2)

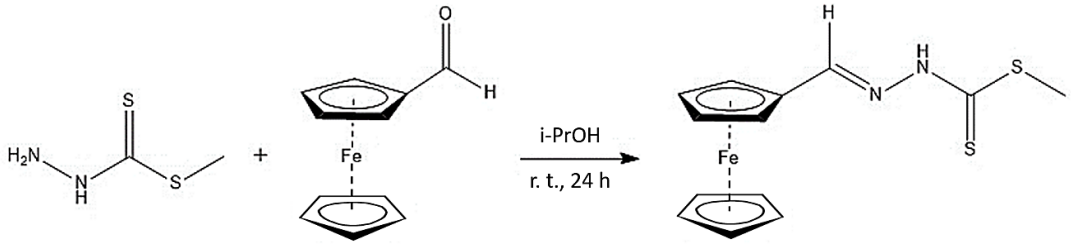


A suspension of S-methyl dithiocarbazate (0.100 g, 0.818 mmol) in i-PrOH (5 mL) was treated with ferrocenecarboxaldehyde (0.175 g, 0.818 mmol) at ambient temperature. The mix was stirred for 24 h accompanied by the formation of a precipitate. The precipitate was filtered and washed with i-PrOH. The crude was recrystallized by n-pentane, producing a red powder. The desired product was dried under vacuum.[17] The final yield was 63%.

**$^1$H NMR** (300 MHz, DMSO-$d_6$) δ 13.00 (1H, s, NH), 8.12 (1H, s, CH=N), 4.67 (2H, t, *J* = 1.9 Hz, H substituted Cp), 4.51 (2H, t, *J* = 1.9 Hz, H substituted Cp), 4.24 (5H, s, H unsubstituted Cp), 2.50 (3H, s, $SCH_3$).
**FT-IR (cm$^{-1}$):** 3115m-3079m (N-H), 3000m-2953m-2848m (CH), 1680w (CH aromatic), 1597s (C=N), 1520s(NH)- 1407m (CH aliphatic), 1333s, 1308s, 1250s-1207m (C-C-N), 1092s (C=S), 1030s-1018s-998s (C= C aromatic), 930s, 840s (C-S), 812s, 786s, 638m.

### 4.4.5 Synthesis of methyl-3-(ferrocenyl)hydrazine-carbothioate (3)

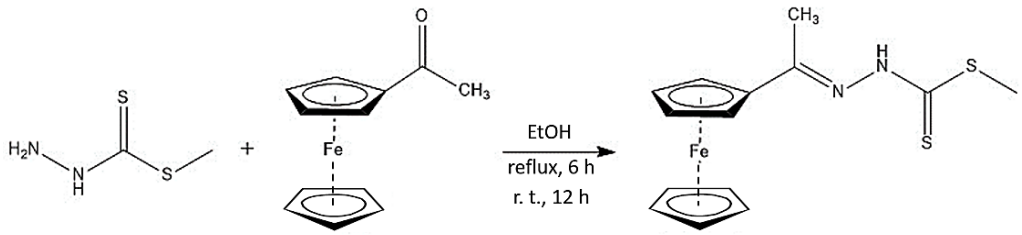


A suspension of S-methyl dithiocarbazate (0.100 g, 0.818 mmol) in ethanol (7 mL) was treated with acetylferrocene (0.187 g, 0.818 mmol). The solution was stirred 6 hours at reflux, then was cooled and stirred at room temperature for 12 hours. The volume of the solvent was reduced, and 3 mL of water was dropped in the flask. The solution became cloudy and after 30 minutes a red-brown solid precipitated. The product was filtered and washed with water, then dried under vacuum.[18] The final yield was 59%.

**$^1$H NMR** (300 MHz, DMSO-$d_6$) δ 12.15 (1H, s, NH), 4.72 (2H, t, *J* = 1.9 Hz, H substituted Cp), 4.45 (2H, t, *J* = 1.9 Hz, H substituted Cp), 4.21 (5H, s, H unsubstituted Cp), 2.49 (3H, s, $SCH_3$), 2.27 (3H, s, $CH_3$).

**FT-IR (cm$^{-1}$):** 3404m-3186m-3091m (N-H and CH), 2956w-2905w (CH), 1657w (CH aromatic), 1593m (C=N), 1496s (NH), 1419s (CH aliphatic), 1310s, 1284s-1258s (C-C-N), 1103s (N-N) 1068s (C=S), 1036s-1017s-996s (C= C aromatic), 957s,885s, 837s (C-S), 810s, 794s, 737s.

### 4.4.6 Synthesis of methyl (*E*)-2-(2hydroxxybenzylidene)hydrazine-1-carbothioate (4)

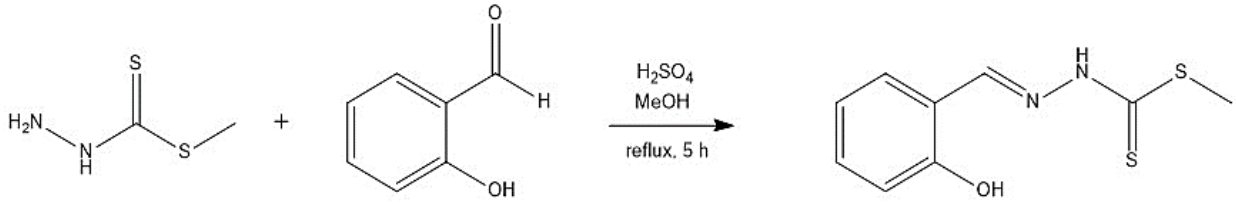


A suspension of S-methyl dithiocarbazate (0.100 g, 0.818 mmol) in methanol (15 mL) was treated with salicylaldehyde (85 µL, 0.818 mmol). To this mixture catalytic amount of concentrated sulfuric acid was added and refluxed for 5 hours. The reaction mixture turned yellow as the methyl hydrazinecarbodithioate dissolved and the yellow product began to precipitate. The product was filtered, washed with MeOH and dried under vacuum. The final yield was 57%.

**$^1$H NMR** (300 MHz, DMSO-$d_6$) δ 13.32 (1H, s, NH), 10.21 (1H, s, OH), 8.54 (1H, s, CH=N), 7.67 (1H, dd, *J* = 7.8, 1.7 Hz, H arom), 7.32 (1H, ddd, *J* = 8.7, 7.3, 1.8 Hz, H arom), 6.98 – 6.86 (2H overlap, m, H arom), 2.55 (3H, s, $SCH_3$).
**FT-IR (cm$^{-1}$):** 3103m-2960m-2869m-2821m (OH/CH/NH), 1619s-1601s-1569s (C=N), 1522s-1488s-1464s (NH), 1266s (C=S), 1103s (C-O), 1042s-1030s-967s-943s (C=C), 901s (C-S).

### 4.4.7 Synthesis of methyl-2-benzylidenehydrazine-1-carbodithioate (5)

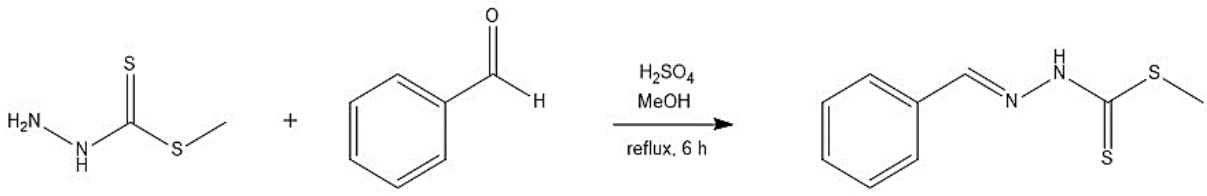


S-methyl dithiocarbazate (0.100 g, 0.82 mmol) was suspended in methanol (8 mL) and benzaldehyde (83 µL, 0.82 mmol) was added. To this mixture, catalytic amount of concentrated sulfuric acid was added, and the reaction was stirred at reflux for 6 hours. The reaction was monitored with TLC (diethyl ether: petroleum ether 66.6% : 33.3%, $R_f$=0.84). The reaction mixture turned yellow, as methyl hydrazinecarbodithioate dissolved, and the yellow product began to precipitate. The solid obtained was filtered and washed with toluene. Then the product was dried under vacuum. The obtained yield was 78%.

**$^1$H NMR** (300 MHz, DMSO-$d_6$) δ 13.29 (1H, s, NH), 8.26 (1H, s, CH=N), 7.78 – 7.66 (2H, m, H arom), 7.53 – 7.39 (3H, m, H arom), 2.54 (3H, s, $SCH_3$).

### 4.4.8 Synthesis of methyl-2-(3-bromobenzylidene)hydrazine-1-carbodithioate (6)

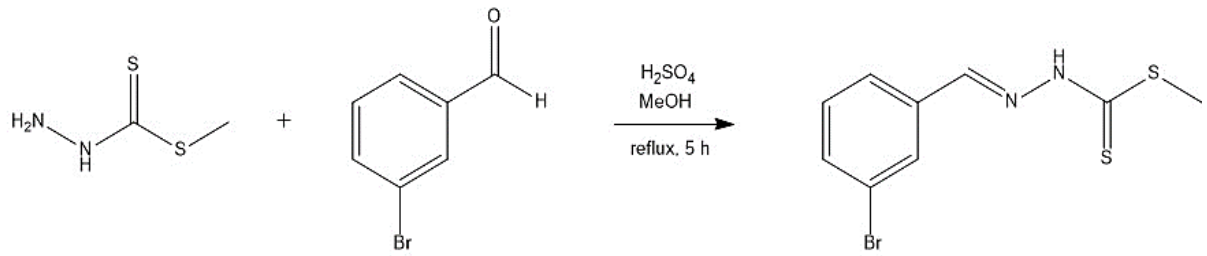


S-methyl dithiocarbazate (0.100 g, 0.82 mmol) and 3-bromobenzaldehyde (95 µl, 0.82 mmol) were dissolved in methanol (8 mL). To this mixture, catalytic amount of concentrated sulfuric acid was added, and the reaction was stirred at reflux for 5 hours. The reaction was monitored with TLC (diethyl ether: petroleum ether 66.6% : 33.3%, $R_f$=0.72). The reaction mixture turned white, as the first reagent dissolved, and the white product began to precipitate. The solid obtained was filtered, washed with cold MeOH and dried under vacuum. The yield is 86%.

**$^1$H NMR** (300 MHz, DMSO-$d_6$) δ 13.39 (1H, s, NH), 8.22 (1H, s, CH=N), 7.91 (1H, t, *J* = 1.8 Hz, H arom), 7.72 (1H, dt, *J* = 7.8, 1.3 Hz, H arom), 7.67 (1H, ddd, *J* = 8.0, 2.0, 1.0 Hz, H arom), 7.44 (1H, t, *J* = 7.9 Hz, H arom), 2.54 (3H, s , $SCH_3$).

### 4.4.9 Synthesis of methyl-2-(4-nitrobenzylidene)hydrazine-1-carbodithioate (7)

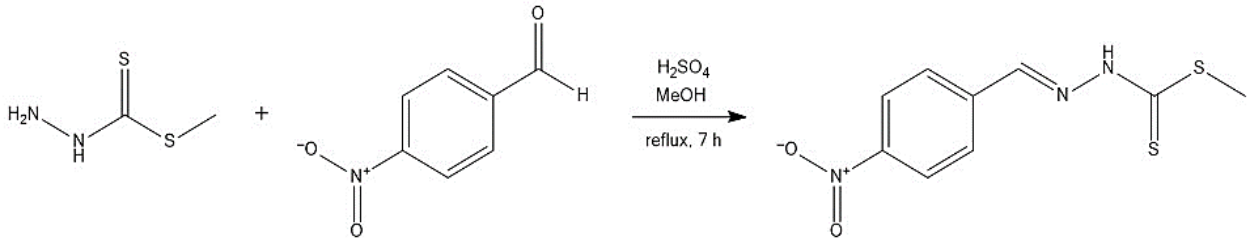


S-methyl dithiocarbazate (0.100 g, 0.82 mmol) was suspended in methanol (10 mL) and 4-nitrobenzaldehyde (0.125 g, 0.82 mmol) was added. To this mixture, catalytic amount of concentrated sulfuric acid was added, and the reaction was stirred at reflux for 7 hours. The reaction was monitored with TLC (diethyl ether: petroleum ether 66.6% : 33.3%, $R_f$=0.55). The reaction mixture turned yellow and the yellow product began to precipitate. The solid obtained was filtered, washed with n-pentane and dried. The final yield was 88%.

**$^1$H NMR** (300 MHz, DMSO-$d_6$) δ 13.53 (1H, s, NH), 8.33 (2H, d, *J* = 5.0 Hz, H arom), 8.30 (1H, s, CH=N), 7.98 (2H, d, *J* = 8.8 Hz, H arom), 2.56 (3H, s, $SCH_3$).

### 4.4.10 NWs functionalization with ferrocenemethylidene hydrazinecarbothioate (8)

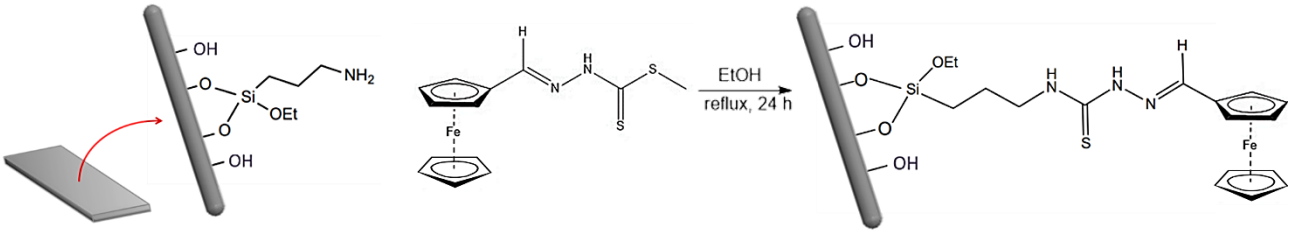


The platelet supporting APTES-functionalized NWs was placed in a 25 mL two-neck round-bottom flask, after vacuum-nitrogen cycles to obtain an anhydrous environment. The platelet was covered with 8 mL of ethanol. Ferrocenemethylidene hydrazinecarbothioate (9.5 mg, 0.030 mmol) was added. The stirred solution was heated at reflux for 24 h. The platelet, washed with fresh ethanol, appeared reddish in color and not grey as before the functionalization.

**FT-IR ($cm^{-1}$):** 3690w-3655w-3619w (OH or NH), 2960m-2925m-2853m ($CH_2$ and $CH_3$), 1730w (NH), 1639w (C=N), 1450w (C=C), 1258s (C=S), 1151m-1026s-1008s (Si-O NWs), 793s-689m (Si-C NWs).
**SEM-EDX:** verified the presence of sulfur and iron.

### 4.4.11 NWs functionalization with methyl-3-(ferrocenyl)hydrazine-carbothioate (9)

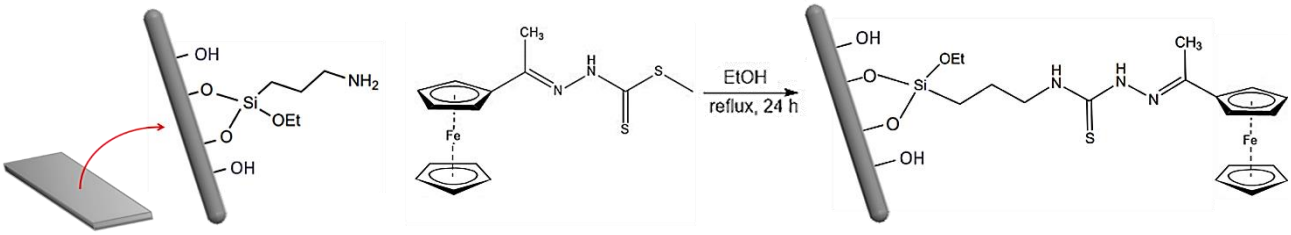


The platelet supporting APTES-functionalized NWs was placed in a 25 mL two-neck round-bottom flask, after vacuum-nitrogen cycles to obtain an anhydrous environment. The platelet was covered with 8 mL of ethanol. Ferrocenemethylidene hydrazinecarbothioate (9.5 mg, 0.030 mmol) was added. The stirred solution was heated at reflux for 24 h. The platelet, washed with fresh ethanol, appeared reddish in color and not grey as before the functionalization.

**FT-IR ($cm^{-1}$):** 3678w-3658w-3621w (OH or NH), 2966m-2915m-2864m ($CH_2$ and $CH_3$), 1732w (NH), 1649w (C=N), 1444w (C=C), 1241s (C=S), 1130m-1041s-1015s (Si-O NWs), 788s-672m (Si-C NWs).
**SEM-EDX:** verified the presence of sulfur and iron.

### 4.4.12 NWs functionalization with methyl (*E*)-2-(2hydroxxybenzylidene)hydrazine-1-carbothioate (10)

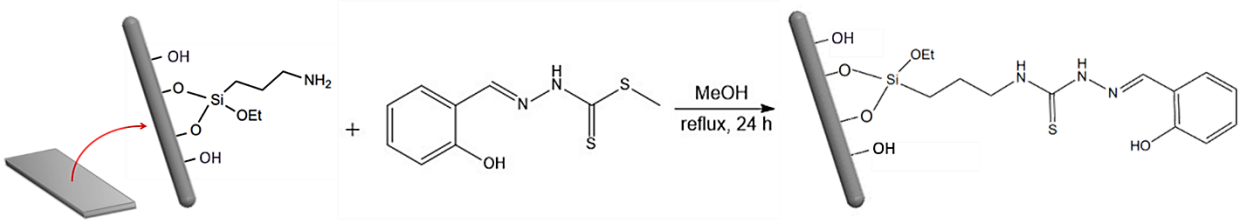


The platelet supporting APTES-functionalized NWs was placed in a 25 mL two-neck round-bottom flask, under nitrogen flux. The platelet was covered with 8 mL of methanol. Methyl (*E*)-2-(2hydroxxybenzylidene) hydrazine-1-carbothioate (8.5 mg, 0.038 mmol) was added. The stirred solution was heated at reflux for 24 hours. The platelet, washed with fresh methanol, appeared grey and opaque once dried.

**FT-IR ($cm^{-1}$):** 3327s-3281s (OH), 2953s-2915s-2869s-2840s (CH and NH), 1629m (aromatic ring), 1545w (NH), 1453s ($CH_2$ aliphatic), 1233w-1201w (C-C-N), 1155s (C=S), 1051s (Si-O-Si), 1030s (C=C aromatic), 783s (Si-C).
**SEM-EDX:** verified the presence of sulfur.

### 4.4.13 NWs functionalization with methyl-2-benzylidenehydrazine-1-carbodithioate (11)

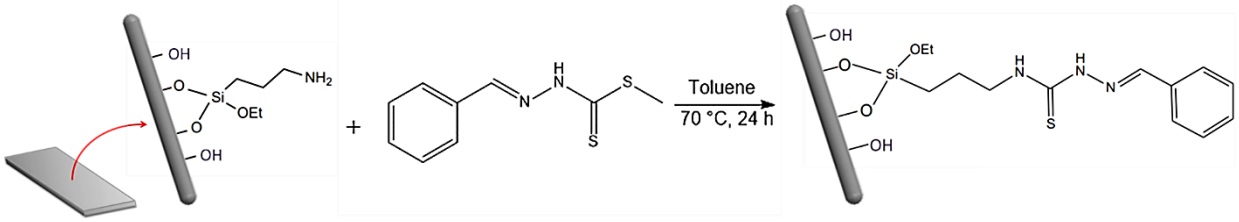


The platelet supporting APTES-functionalized NWs was placed in a 25 mL two-neck round-bottom flask, under nitrogen atmosphere. The platelet was covered with 8 mL of toluene. Methyl-2-benzylidenehydrazine-1-carbodithioate (9.8 mg, 0.047 mmol) was added. The solution was stirred at 70 °C for 24 hours. The platelet, washed with fresh toluene, appeared light grey and opaque once dried.

**FT-IR ($cm^{-1}$):** 3333s-3297s (OH), 2948s-2920s-2873s (CH and NH), 1622m (aromatic ring), 1544w (NH), 1448s ($CH_2$ aliphatic), 1238w-1222w (C-C-N), 1147s (C=S), 1057s (Si-O-Si), 1033s (C=C aromatic), 784s (Si-C).
**SEM-EDX:** verified the presence of sulfur.

### 4.4.14 NWs functionalization with methyl-2-(3-bromobenzylidene)hydrazine-1-carbodithioate (12)

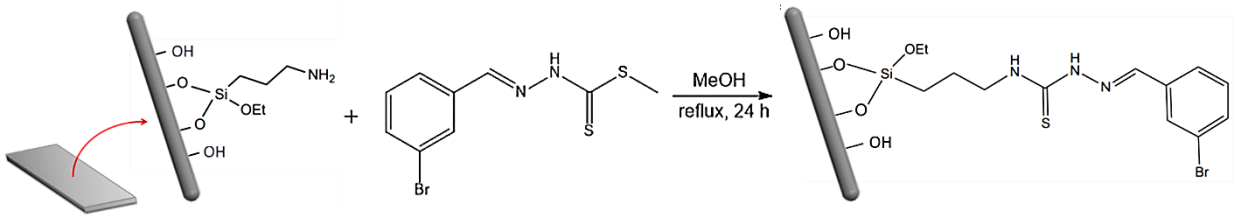


The platelet supporting APTES-functionalized NWs was placed in a 25 mL two-neck round-bottom flask, under nitrogen atmosphere. The platelet was covered with 8 mL of methanol. Methyl-2-(3-bromobenzylidene)

hydrazine-1-carbodithioate (9.3 mg, 0.032 mmol) was added. The solution was stirred under reflux for 24 hours. The platelet, washed with fresh methanol, appeared white-light grey and opaque once dried.

**FT-IR ($cm^{-1}$):** 3328s-3301s (OH), 2940s-2910s-2888s-2871s (CH and NH), 1623m (aromatic ring), 1554w (NH), 1433s ($CH_2$ aliphatic), 1223w-1214w (C-C-N), 1140s (C=S), 1051s (Si-O-Si), 1027s (C=C aromatic), 779s (Si-C).
**SEM-EDX: SEM-EDX:** verified the presence of sulfur.

### 4.4.15 NWs functionalization with methyl-2-(4-nitrobenzylidene)hydrazine-1-carbodithioate (13)

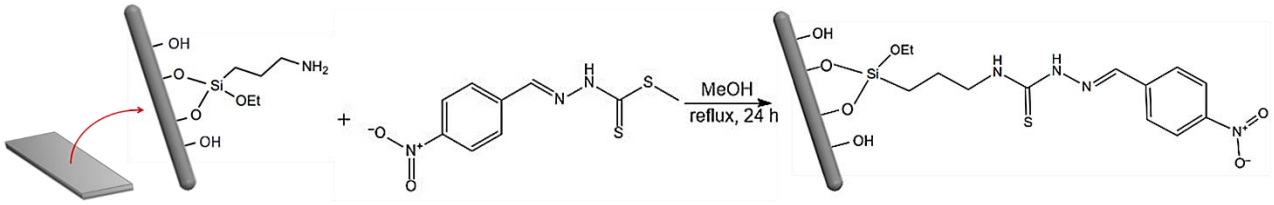


The platelet supporting APTES-functionalized NWs was placed in a 25 mL two-neck round-bottom flask, under nitrogen atmosphere. The platelet was covered with 8 mL of methanol. Methyl-2-(4-nitrobenzylidene) hydrazine-1-carbodithioate (10.5 mg, 0.041 mmol) was added. The solution was stirred at reflux for 24. The platelet, washed with fresh methanol, appeared grey and opaque once dried.

**FT-IR ($cm^{-1}$):** 3330s-3312s (OH), 2966s-2935s-2878s-2841s (CH and NH), 1630m (aromatic ring), 1534w (NH), 1460s ($CH_2$ aliphatic), 1241w-1209w (C-C-N), 1149s (C=S), 1044s (Si-O-Si), 1021s (C=C aromatic), 785s (Si-C).
**SEM-EDX:** verified the presence of sulfur.

### 4.4.16 NWs complexation of (2*E*)-2-(ferrocenylmethylidene)-*N*-propylhydrazinecarbothioamide-NWs with $K_2[PtCl_4]$ (14a)

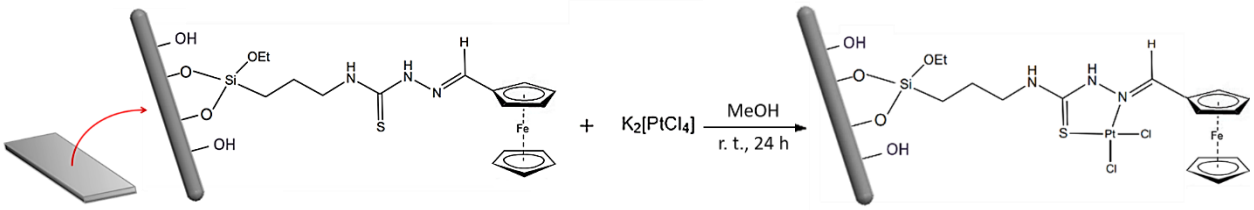


The platelet supporting (2E)-2-(ferrocenylmethylidene)-N-propylhydrazinecarbothioamide-NWs was placed in a 50 mL round-bottom flask and covered with 8 ml of MeOH. 6.5 mg of $K_2[PtCl_4]$ were added to the round-bottom flask. The reaction was stirred at room temperature for 24 hours. Then the platelet, washed with fresh MeOH, appeared white-gray and opaque.

**FT-IR ($cm^{-1}$):** 3328s-3279s (OH), 2944s-2925s-2863s (CH and NH), 1634m (aromatic ring), 1538w (NH), 1462s ($CH_2$ aliphatic), 1231w-1202w (C-C-N), 1148s (C=S), 1056s (Si-O-Si), 1043s (C=C aromatic), 791s (Si-C).
**SEM-EDX:** verified the presence of sulfur, iron, platinum and chlorine.

### 4.4.17 NWs complexation of (2*E*)-2-(ferrocenylmethylidene)-*N*-propylhydrazinecarbothioamide-NWs with $[(Cp^*)Rh(\mu\text{-}Cl)Cl]_2$ (14b)

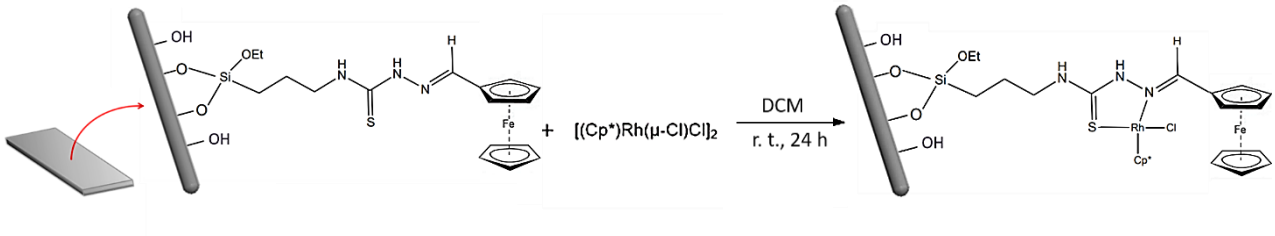


The platelet supporting (2E)-2-(ferrocenylmethylidene)-N-propylhydrazinecarbothioamide-NWs was placed in a 50 mL round-bottom flask and covered with 8 ml of DCM. 6.0 mg of $[(Cp^*)Rh(\mu\text{-}Cl)Cl]_2$ were added to the round-bottom flask. The reaction was stirred at room temperature for 24 hours. The platelet, washed with fresh DCM, appeared reddish-gray and opaque.

**FT-IR ($cm^{-1}$):** 3334s-3322s (OH), 2870s-2861s (CH and NH), 1635m (aromatic ring), 1548w (NH), 1463s ($CH_2$ aliphatic), 1239w-1217w (C-C-N), 1156s (C=S), 1040s (Si-O-Si), 1032s (C=C aromatic), 787s (Si-C).
**SEM-EDX:** verified the presence of sulfur, iron, rhodium and chlorine.

### 4.4.18 NWs complexation of (2*E*)-2-(ferrocenylmethylidene)-*N*-propylhydrazinecarbothioamide-NWs with $[Ru(\eta^6\text{-p-cymene})(\mu\text{-}Cl)Cl]_2$ (14c)

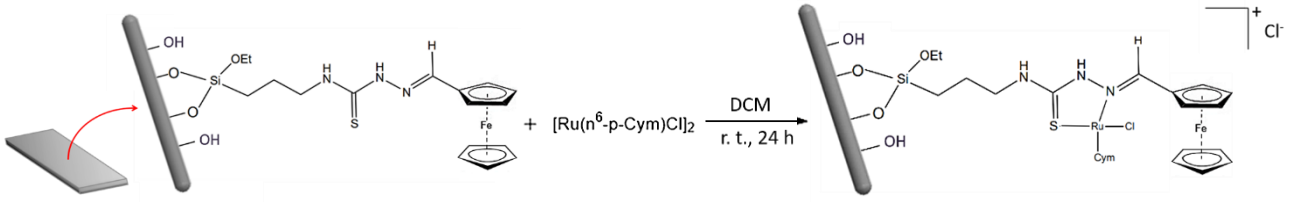


The platelet supporting (2E)-2-(ferrocenylmethylidene)-N-propylhydrazinecarbothioamide-NWs was placed in a 50 mL round-bottom flask and covered with 8 ml of DCM. 9.8 mg of $[Ru(\eta^6\text{-p-cymene})(\mu\text{-}Cl)Cl]_2$ were added to the round-bottom flask. The reaction was stirred at room temperature for 24 hours. The platelet, washed with fresh DCM, appeared light reddish and opaque.

**FT-IR ($cm^{-1}$):** 3338s-3331s (OH), 2879s-2865s (CH and NH), 1631m (aromatic ring), 1547w (NH), 1459s ($CH_2$ aliphatic), 1234w-1220w (C-C-N), 1159s (C=S), 1043s (Si-O-Si), 1027s (C=C aromatic), 791s (Si-C).
**SEM-EDX:** verified the presence of sulfur, iron, ruthenium and chlorine.

### 4.4.19 NWs complexation of (2E)-2-(1-ferrocenylethylidene)-N-propylhydrazinecarbothioamide-NWs with $K_2[PtCl_4]$ (15a)

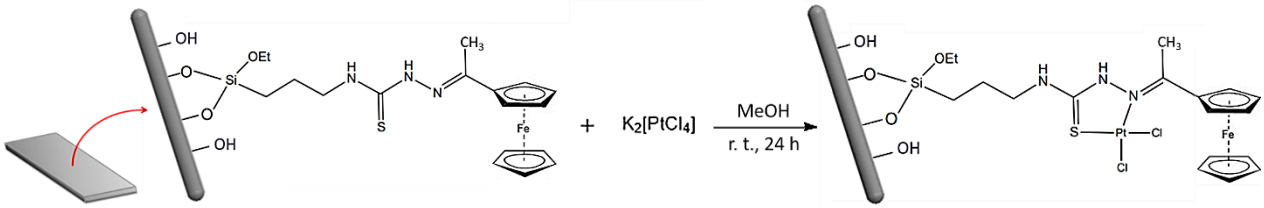

The platelet supporting 2E)-2-(1-ferrocenylethylidene)-N-propylhydrazinecarbothioamide-NWs was placed in a 50 mL round-bottom flask and covered with 8 ml of MeOH. 6.4 mg of $K_2[PtCl_4]$ were added to the round-bottom flask. The reaction was stirred at room temperature for 24 hours. Then the platelet, washed with fresh MeOH, appeared white-gray and opaque.

**FT-IR ($cm^{-1}$):** 3338s-3277s (OH), 2943s-2935s-2854s (CH and NH), 1641m (aromatic ring), 1542w (NH), 1460s ($CH_2$ aliphatic), 1233w-1212w (C-C-N), 1145s (C=S), 1060s (Si-O-Si), 1051s (C=C aromatic), 793s (Si-C).
**SEM-EDX:** verified the presence of sulfur, iron, platinum and chlorine.

### 4.4.20 NWs complexation of (2E)-2-(1-ferrocenylethylidene)-N-propylhydrazinecarbothioamide-NWs with $[(Cp^*)Rh(\mu\text{-}Cl)Cl]_2$ (15b)

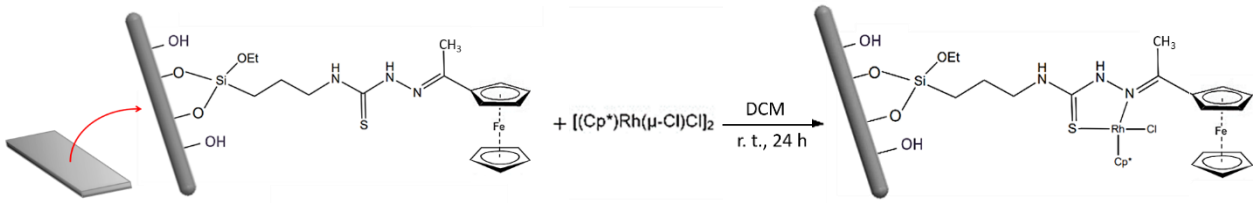


The platelet supporting 2E)-2-(1-ferrocenylethylidene)-N-propylhydrazinecarbothioamide-NWs was placed in a 50 mL round-bottom flask and covered with 8 ml of DCM. 5.9 mg of $[(Cp^*)Rh(\mu\text{-}Cl)Cl]_2$ were added to the round-bottom flask. The reaction was stirred at room temperature for 24 hours. The platelet, washed with fresh DCM, appeared grayish yellow and opaque.

**FT-IR ($cm^{-1}$):** 3331s-3324s (OH), 2878s-2865s (CH and NH), 1633m (aromatic ring), 1541w (NH), 1458s ($CH_2$ aliphatic), 1231w-1207w (C-C-N), 1152s (C=S), 1048s (Si-O-Si), 1027s (C=C aromatic), 777s (Si-C).
**SEM-EDX:** verified the presence of sulfur, iron, rhodium and chlorine.

### 4.4.21 NWs complexation of (2E)-2-(1-ferrocenylethylidene)-N-propylhydrazinecarbothioamide-NWs with $[Ru(\eta^6\text{-p-cymene})(\mu\text{-}Cl)Cl]_2$ (15c)

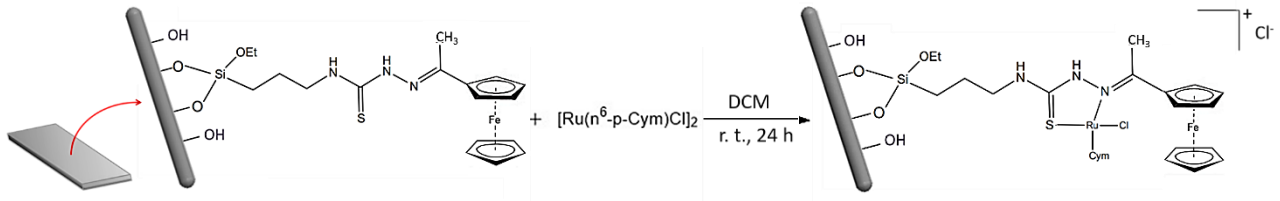


The platelet supporting 2E)-2-(1-ferrocenylethylidene)-N-propylhydrazinecarbothioamide-NWs was placed in a 50 mL round-bottom flask and covered with 8 ml of DCM. 9.9 mg of $[Ru(\eta^6\text{-p-cymene})(\mu\text{-}Cl)Cl]_2$ were added to the round-bottom flask. The reaction was stirred at room temperature for 24 hours. The platelet, washed with fresh DCM, appeared light orange-gray and opaque.

**FT-IR ($cm^{-1}$):** 3435s (OH), 2880s-2874s-2852s (CH and NH), 1642m (aromatic ring), 1555w (NH), 1462s ($CH_2$ aliphatic), 1230w-1226w (C-C-N), 1160s (C=S), 1036s (Si-O-Si), 1030s (C=C aromatic), 786s (Si-C).
**SEM-EDX:** verified the presence of sulfur, iron, ruthenium and chlorine.

### 4.4.22 NWs complexation of (2*E*)-2-benzylidene-*N*-propylhydrazinecarbothioamide-NWs with $K_2[PtCl_4]$ (16a)

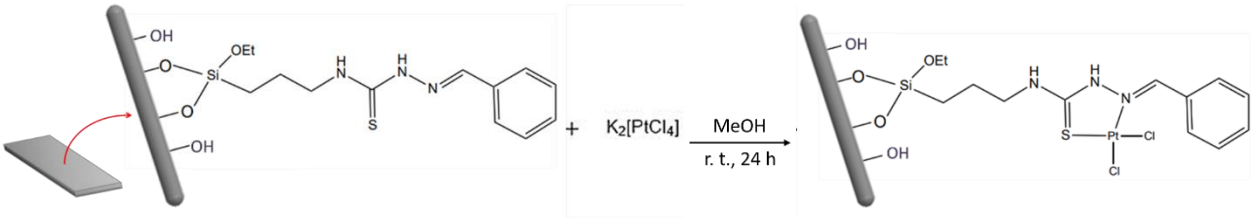


The platelet supporting (2E)-2-benzylidene-N-propylhydrazinecarbothioamide-NWs was placed in a 50 mL round-bottom flask and covered with 8 ml of methanol. 6.4 mg of $K_2[PtCl_4]$ were added to the round-bottom flask. The reaction was stirred at room temperature for 24 hours. Then the platelet, washed with fresh MeOH, appeared white-gray.

**FT-IR ($cm^{-1}$):** 3339s-3302s (OH), 2954s-2925s (CH and NH), 1633m (aromatic ring), 1538w (NH), 1451s ($CH_2$ aliphatic), 1229w-1209w (C-C-N), 1140s (C=S), 1066s (Si-O-Si), 1045s (C=C aromatic), 788s (Si-C).
**SEM-EDX:** verified the presence of sulfur, platinum and chlorine.

### 4.4.23 NWs complexation of (2*E*)-2-benzylidene-*N*-propylhydrazinecarbothioamide-NWs with $[(Cp^*)Rh(\mu\text{-}Cl)Cl]_2$ (16b)

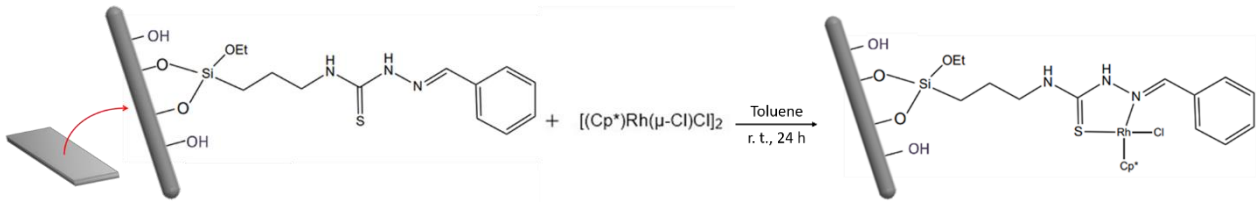


The platelet supporting (2E)-2-benzylidene-N-propylhydrazinecarbothioamide-NWs was placed in a 50 mL round-bottom flask and covered with 8 ml of toluene. 6.2 mg of $[(Cp^*)Rh(\mu\text{-}Cl)Cl]_2$ were added to the round-bottom flask. The reaction was stirred at room temperature for 24 hours. The platelet, washed with fresh toluene, appeared gray and opaque.

**FT-IR ($cm^{-1}$):** 3329s (OH), 2967s-2947s (CH and NH), 1636m (aromatic ring), 1549w (NH), 1466s ($CH_2$ aliphatic), 1235w-1231w (C-C-N), 1138s (C=S), 1051s (Si-O-Si), 1035s (C=C aromatic), 782s (Si-C).
**SEM-EDX:** verified the presence of sulfur, rhodium and chlorine.

### 4.4.24 NWs complexation of (2*E*)-2-benzylidene-*N*-propylhydrazinecarbothioamide-NWs with $[Ru(\eta^6\text{-}p\text{-cymene})(\mu\text{-}Cl)Cl]_2$ (16c)

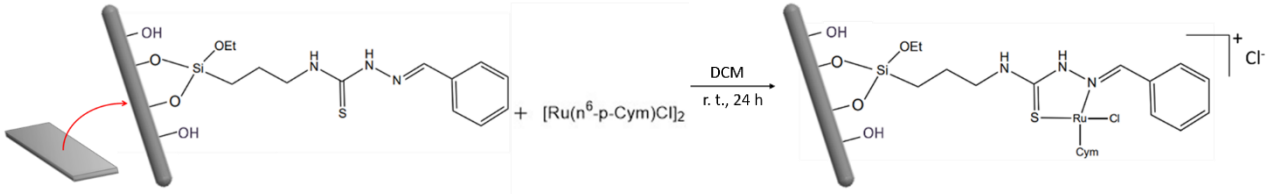


The platelet supporting (2E)-2-benzylidene-N-propylhydrazinecarbothioamide-NWs was placed in a 50 mL round-bottom flask and covered with 8 ml of DCM. 10 mg of $[Ru(\eta^6\text{-p-cymene})(\mu\text{-}Cl)Cl]_2$ were added to the

round-bottom flask. The reaction was stirred at room temperature for 24 hours. The platelet, washed with fresh DCM, appeared reddish-gray.

**FT-IR ($cm^{-1}$):** 3434s-3331s (OH), 2871s-2867s (CH and NH), 1633m (aromatic ring), 1544w (NH), 1466s ($CH_2$ aliphatic), 1238w-1223w (C-C-N), 1154s (C=S), 1038s (Si-O-Si), 1031s (C=C aromatic), 786s (Si-C).
**SEM-EDX:** verified the presence of sulfur, ruthenium and chlorine.

### 4.4.25 NWs complexation of (2E)-2-(3-bromobenzylidene)-N-propylhydrazinecarbothioamide-NWs with $K_2[PtCl_4]$ (17a)

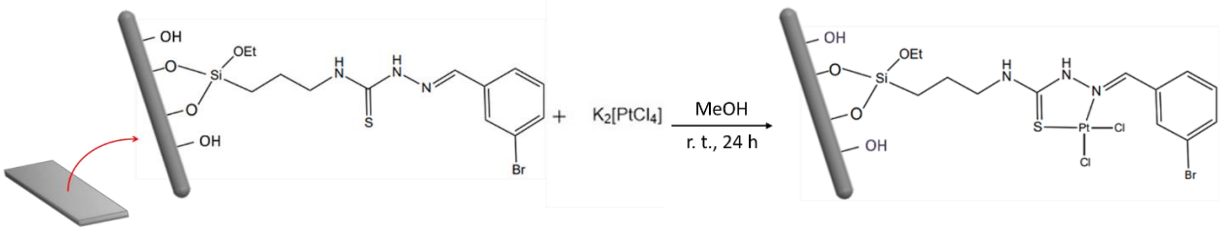


The platelet supporting (2E)-2-(3-bromobenzylidene)-N-propylhydrazinecarbothioamide-NWs was placed in a 50 mL round-bottom flask and covered with 8 ml of MeOH. 6.5 mg of $K_2[PtCl_4]$ were added to the round-bottom flask. The reaction was stirred at room temperature for 24 hours. Then the platelet, washed with MeOH and acetone, appeared white-yellow and opaque.

**FT-IR ($cm^{-1}$):** 3620w-3428w-3398w (OH or NH), 2950m-2912m ($CH_2$ and $CH_3$), 1721w (NH), 1636w (C=N), 1444w (C=C), 1257s (C=S), 1141m-1028s-1018s (Si-O NWs), 798s-683m (Si-C NWs).
**SEM-EDX:** verified the presence of sulfur, platinum and chlorine.

### 4.4.26 NWs complexation of (2E)-2-(3-bromobenzylidene)-N-propylhydrazinecarbothioamide-NWs with $[(Cp^*)Rh(\mu\text{-}Cl)Cl]_2$ (17b)

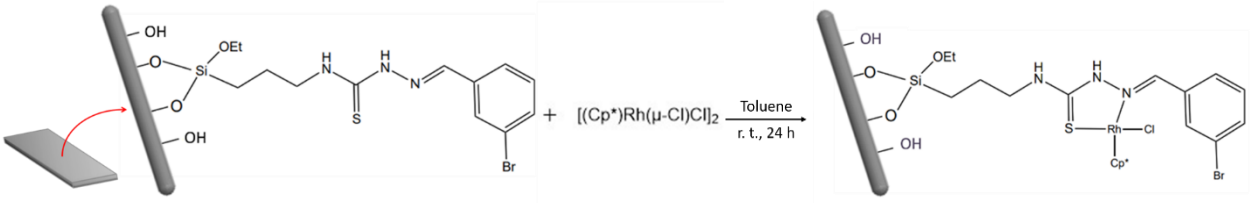


The platelet supporting (2E)-2-(3-bromobenzylidene)-N-propylhydrazinecarbothioamide-NWs was placed in a 50 mL round-bottom flask and covered with 8 ml of toluene. 6.0 mg of $[(Cp^*)Rh(\mu\text{-}Cl)Cl]_2$ were added to the round-bottom flask. The reaction was stirred at room temperature for 24 hours. The platelet, washed with fresh toluene, appeared dark red.

**FT-IR ($cm^{-1}$):** 3327s-3284s (OH), 2963s-2918s-2869s-2842s (CH and NH), 1623m (aromatic ring), 1541w (NH), 1450s ($CH_2$ aliphatic), 1237w-1211w (C-C-N), 1150s (C=S), 1054s (Si-O-Si), 1033s (C=C aromatic), 789s (Si-C).
**SEM-EDX:** verified the presence of sulfur, rhodium and chlorine.

### 4.4.27 NWs complexation of (2E)-2-(3-bromobenzylidene)-N-propylhydrazinecarbothioamide-NWs with $[Ru(\eta^6\text{-p-cymene})(\mu\text{-Cl})Cl]_2$ (17c)

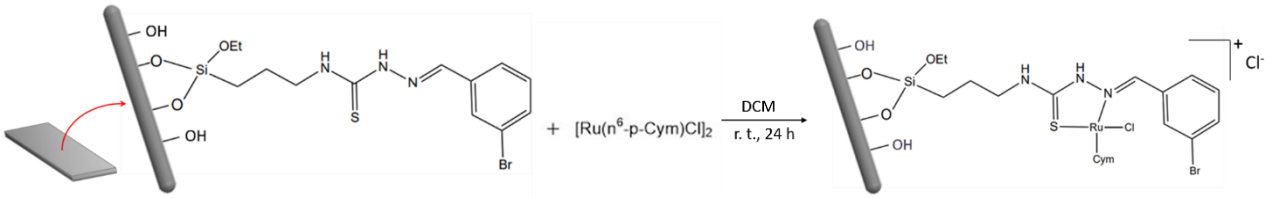


The platelet supporting (2E)-2-(3-bromobenzylidene)-N-propylhydrazinecarbothioamide-NWs was placed in a 50 mL round-bottom flask and covered with 8 ml of DCM. 9.8 mg of $[Ru(\eta^6\text{-p-cymene})(\mu\text{-Cl})Cl]_2$ were added to the round-bottom flask. The reaction was stirred at room temperature for 24 hours. The platelet, washed with fresh DCM, appeared light reddish and opaque.

**FT-IR ($cm^{-1}$):** 3671w-3653w-3631w (OH or NH), 2964m-2863m ($CH_2$ and $CH_3$), 1741w (NH), 1645w (C=N), 1448w (C=C), 1239s (C=S), 1128m-1012s (Si-O NWs), 789s-677m (Si-C NWs).
**SEM-EDX:** verified the presence of sulfur, ruthenium and chlorine.

### 4.4.28 NWs complexation of (2E)-2-(4-nitrobenzylidene)-N-propylhydrazinecarbothioamide-NWs with $K_2[PtCl_4]$ (18a)

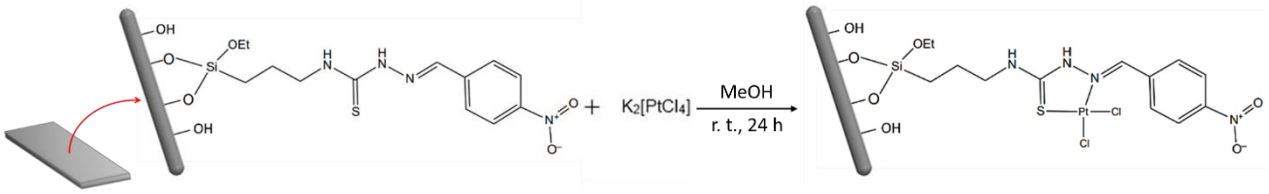


The platelet supporting (2E)-2-(4-nitrobenzylidene)-N-propylhydrazinecarbothioamide-NWs was placed in a 50 mL round-bottom flask and covered with 8 ml of MeOH. 6.4 mg of $K_2[PtCl_4]$ were added to the round-bottom flask. The reaction was stirred at room temperature for 24 hours. Then the platelet, washed with fresh MeOH, appeared white-gray and opaque.

**FT-IR ($cm^{-1}$):** 3332s-3312s (OH), 2954s-2915s (CH and NH), 1634-1628m (aromatic ring), 1528w (NH), 1454s ($CH_2$ aliphatic), 1223w-1202w (C-C-N), 1137s (C=S), 1061s (Si-O-Si), 1035s (C=C aromatic), 793s (Si-C).
**SEM-EDX:** verified the presence of sulfur, platinum and chlorine.

### 4.4.29 NWs complexation of (2E)-2-(4-nitrobenzylidene)-N-propylhydrazinecarbothioamide-NWs with $[(Cp^*)Rh(\mu\text{-Cl})Cl]_2$ (18b)

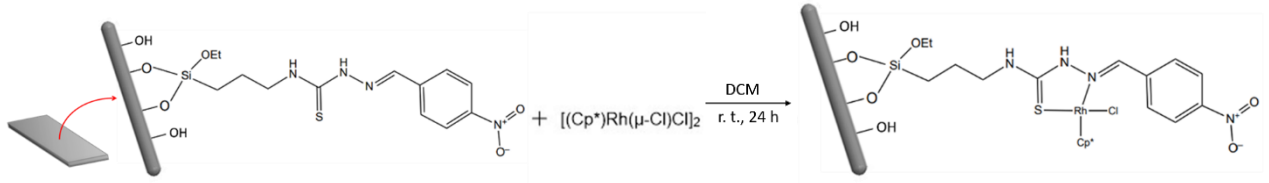


The platelet supporting (2E)-2-(4-nitrobenzylidene)-N-propylhydrazinecarbothioamide-NWs was placed in a 50 mL round-bottom flask and covered with 8 ml of DCM. 6.3 mg of $[(Cp^*)Rh(\mu\text{-Cl})Cl]_2$ were added to the

round-bottom flask. The reaction was stirred at room temperature for 24 hours. The platelet, washed with fresh DCM, appeared grayish yellow and opaque.
**FT-IR ($cm^{-1}$):** 3326s-3283s (OH), 2962s-2914s (CH and NH), 1626m (aromatic ring), 1538w (NH), 1454s ($CH_2$ aliphatic), 1231w-1221w (C-C-N), 1147s (C=S), 1050s (Si-O-Si), 1027s (C=C aromatic), 777s (Si-C).
**SEM-EDX:** verified the presence of sulfur, rhodium and chlorine.

### 4.4.30 NWs complexation of (2E)-2-(4-nitrobenzylidene)-N-propylhydrazinecarbothioamide-NWs with $[Ru(\eta^6\text{-p-cymene})(\mu\text{-Cl})Cl]_2$ (18c)

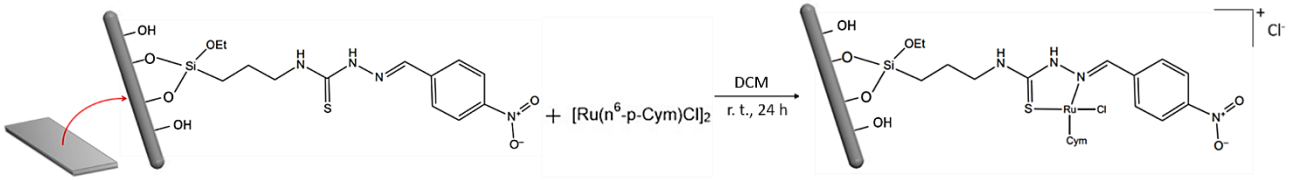


The platelet supporting (2E)-2-(4-nitrobenzylidene)-N-propylhydrazinecarbothioamide-NWs was placed in a 50 mL round-bottom flask and covered with 8 ml of DCM. 9.6 mg of $[Ru(\eta^6\text{-p-cymene})(\mu\text{-Cl})Cl]_2$ were added to the round-bottom flask. The reaction was stirred at room temperature for 24 hours. The platelet, washed with fresh DCM, appeared light reddish and opaque.

**FT-IR ($cm^{-1}$):** 3534s-3430s (OH), 2881s-2877s (CH and NH), 1638m-1627m (aromatic ring), 1541w (NH), 1456s ($CH_2$ aliphatic), 1238w (C-C-N), 1150s (C=S), 1036s (Si-O-Si), 1026s (C=C aromatic), 786s-780s (Si-C).
**SEM-EDX:** verified the presence of sulfur, ruthenium and chlorine.

### 4.4.31 NWs complexation of (3-aminopropyl)triethoxysilane (APTES) functionalized NWs with $K_2[PtCl_4]$ and NWs complexation of triethoxy(3-isothiocyanatopropyl)silane (Si-NCS)

The platelet with NWs functionalized with (3-aminopropyl)triethoxysilane (APTES) or triethoxy(3 isothiocyanatopropyl)silane (Si-NCS) was placed in a 25 mL round-bottom flask and covered with 5 ml of water. 6 mg of $K_2[PtCl_4]$ were added. The reaction was stirred at room temperature for 5 h and for at least 48 h.

**TEM-EDX:** the EDX maps are shown in the text.

### 4.4.32 2nd Anchoring Method: step I (19)

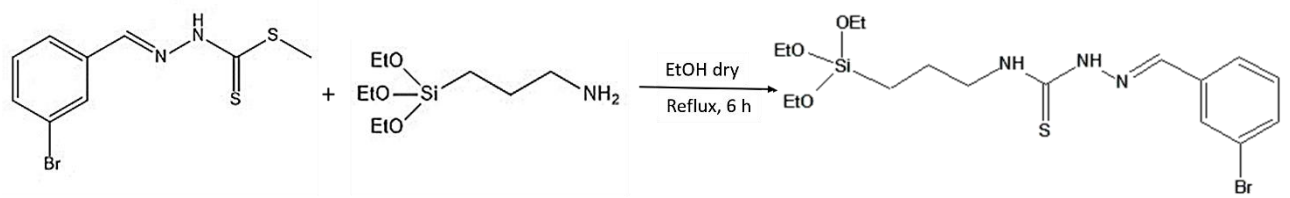


Methyl-2-(3-bromobenzylidene)hydrazine-1-carbodithioate (0.300 g, 1.05 mmol) and (3-Aminopropyl) triethoxysilane (APTES) (260 µl, 1.05 mmol) were dissolved in dry ethanol (12 mL) in a 25 mL two-neck round-bottom flask, after vacuum-nitrogen cycles to obtain an anhydrous environment. The reaction was stirred at

reflux for 6 hours. The solvent was removed, and the yellow solid was dried under vacuum. The yield was 78%.

**$^1$H NMR** (300 MHz, $CDCL_3$) δ 10.00 (1H, s, NH), 7.86 (1H, s, HC=N), 7.62-7.35 (4H, H arom), 3.86 (6H, q, *J* = 7.0 Hz, $OCH_2$), 3.76 (2H, td, *J* = 7.2, 5.9 Hz, $NCH_2$), 1.85 (2H, tt, *J* = 8.0, 6.5 Hz, $SiCH_2$), 1.25 (9H, t, *J* = 7.0 Hz, $CH_3$), 0.82 – 0.64 (2H, m, $CH_2$).

### 4.4.33 2nd Anchoring Method: step II

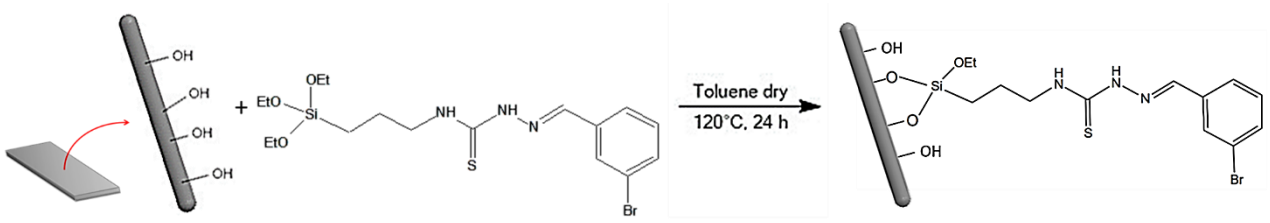


The activated platelet was placed in a 25 mL two-neck round-bottom flask, after vacuum-nitrogen cycles to obtain an anhydrous environment. The platelet was covered with 8 mL of toluene dry. Compound 19 (10 mg, 0.035 mol) was added. The reaction was stirred at reflux for 24 h. Then the platelet, washed with fresh toluene, appeared light gray and opaque.

**TEM-EDX:** the EDX maps are shown in the text.

### 4.4.34 NWs functionalization with triethoxy(3-isothiocyanatopropyl)silane (Si-NCS)

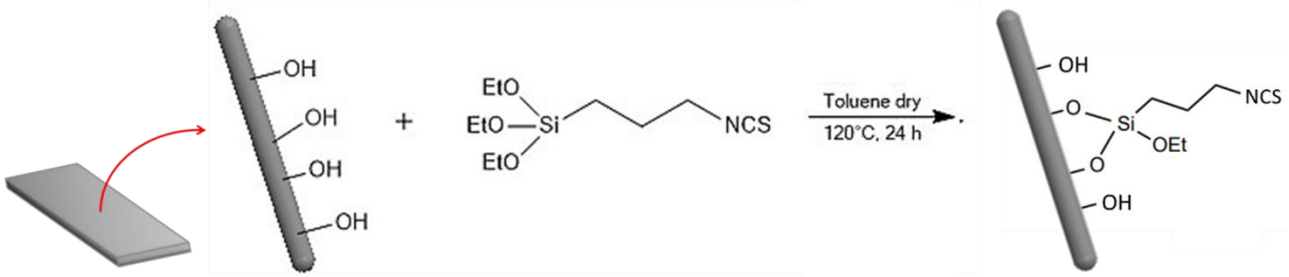


The activated platelet was placed in a 25 mL two-neck round-bottom flask, after vacuum-nitrogen cycles to obtain an anhydrous environment. The platelet was covered with 8 mL of dry toluene. 15 µL of triethoxy(3-isothiocyanatopropyl)silane (Si-NCS) was added to the round-bottom flask, under nitrogen flux. The reaction was stirred and heated at reflux for 24 h. Once the solution was cooled to r.t. the platelet was washed with toluene. After the functionalization the platelet color was lighter, almost gray-white.

**TEM-EDX:** the EDX maps are shown in the text.

## References


1 P. Nordlund and P. Reichard, *Annu. Rev. Biochem.*, 2006, **75**, 681–706.
2 J. Shao, X. Liu, L. Zhu and Y. Yen, *Expert Opin. Ther. Targets*, 2013, **17**, 1423–1437.
3 A. C. Sartorelli, *Some Approaches to the Therapeutic Exploitation of Metabolic Sites of Vulnerability of Neoplastic Cells1*, 1969, vol. 29.
4 T. S. Lobana, R. Sharma, G. Bawa and S. Khanna, *Coord. Chem. Rev.*, 2009, **253**, 977–1055.
5 Y. P. Tian, W. T. Yu, C. Y. Zhao, M. H. Jiang, Z. G. Cai and H. Kun Fun, *Polyhedron*, 2002, **21**, 1217–1222.
6 S. Padhyé, B. G. Kauffman and A. Introduction, *Coord. Chem. Rev.*, 1985, **63**, 127–160.
7 J. S. Casas, M. S. García-Tasende and J. Sordo, *Coord. Chem. Rev.*, 2000, **209**, 197–261.
8 T. S. Lobana, G. Bawa, R. J. Butcher, B. J. Liaw and C. W. Liu, *Polyhedron*, 2006, **25**, 2897–2903.
9 R. J. Glisoni, D. A. Chiappetta, A. G. Moglioni and A. Sosnik, *Pharm. Res.*, 2012, **29**, 739–755.
10 R. J. Glisoni, D. A. Chiappetta, L. M. Finkielsztein, A. G. Moglioni Bc and A. Sosnik, *New J. Chem.*, 2010, **34**, 2047–2058.
11 M. Serda, M. W. Anna, J. Jampilek, M. Pesko, K. Kralova, M. Vejsova, R. Musiol, A. Ratuszna and J. Polanski, *Molecules*, 2012, **17**, 13483–13502.
12 A. Y. Lukmantara, D. S. Kalinowski, N. Kumar and D. R. Richardson, *Org. Biomol. Chem*, 2013, **11**, 6414–6425.
13 J. Chen, Y.-W. Huang, G. Liu, Z. Afrasiabi, E. Sinn, S. Padhye and Y. Ma, *Toxicol. Appl. Pharmacol.*, 2004, **197**, 40–48.
14 L. Saryan, E. Ankel, C. Krishnamurti, D. Petering and H. Elford, *J. Med. Chem.*, 1979, **22**, 1218–1221.
15 C.-M. Sandra, K. Elena, F.-A. Marcos, M.-K. Elena, R.-R. Arturo, R. Teresa and M.-G. Marcos, *Anticancer. Agents Med. Chem.*, 2014, **14**, 459–465.
16 N. Baartzes, T. Stringer, J. Okombo, R. Seldon, F. Warner, C. De Kock, P. J. Smith and G. S. Smith, *J. Organomet. Chem.*, 2016, **819**, 166–172.
17 R. Arancibia, A. H. Klahn, M. Lapier, J. D. Maya, A. Ibañez, M. T. Garland, S. Carrère-Kremer, L. Kremer and C. Biot, *J. Organomet. Chem.*, 2014, **755**, 1–6.
18 N. Farrel, *Metal Complexes as Drugs and Chemotherapeutic Agents*, Richmond, VA, USA, 2003, vol. 9.
19 M. Frezza, S. Hindo, D. Chen, A. Davenport, S. Schmitt, D. Tomco and P. Q. Dou, *Curr Pharm Des.*, 2013, **16**, 1813–1825.
20 R. W. Sun, D. Ma, E. L. Wong, C. Che, D. Ma, E. L. Wong and C. Che, *Dalt. Trans.*, 2007, **3**, 4884–4892.
21 K. M. Deo, B. J. Pages, D. L. Ang, C. P. Gordon and J. R. Aldrich-wright, *Int. J. Mol. Sci.*, 2016, **17**, 1–17.
22 A. Sarkar, T. Daniels-Race, A. Sarkar and T. Daniels-Race, *Nanomaterials*, 2013, **3**, 272–288.
23 A. Hasan, V. Saxena and L. M. Pandey, *Lagmuir*, 2018, **34**, 3494–3506.
24 F. Bigi, A. Corradini, C. Quarantelli and G. Sartori, *J. Catal.*, 2007, **250**, 222–230.

# 5. The oncology project: Triapine and C-Triapine

## 5.1 Brief introduction

In the family of thiosemicarbazones, α-(N)-heterocyclic thiosemicarbazone ((N)-TSCs) are the compounds that have proved to be the most active as inhibitors of ribonucleotide reductase (RR).[1,2]

(N)-TCSs are compounds in which the thiosemicarbazone side-chain is attached in α position to a N-heterocyclic ring.
(N)-TSCs are excellent ligands, with conjugated NNS donors set that promote the coordination with metal ions, forming two 5-member chelation rings, with a partially conjugated character.

The (N)-TSC that has shown the greatest *in vitro* activity against various human cancer cells lines, especially solid tumors[3], is Triapine (3-aminopyridine-2-carboxaldehyde-thiosemicarbazone).[4,5] (Figure 5.1 a)

Triapine is currently completing phase II of clinical trial: it is tested *in vivo* as single agent and/or in combination with other chemotherapeutic drugs on human patients.[6,7]

The excellent antineoplastic properties of Triapine have prompted many scientists to try to create new structurally similar molecules in an attempt to obtain even more effective anticancer drugs.

To modify the structure of Triapine, and more generally the structure of (N)-TSCs, mainly three points can be changed, illustrated in Figure 5.1 b: i) the heterocyclic ring (green circle); ii) the substituents linked to the nitrogen of the thiosemicarbazone side-chain (blue circles); iii) the nature of the chelating metal ions (red circle).

Different structures generate thiosemicarbazones with totally different biological properties and activities.

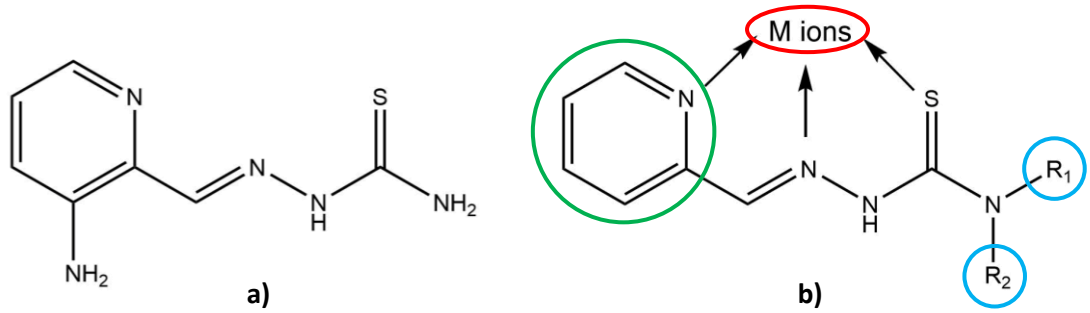


*Figure 5.1: a) The structure of Triapine. b) General α-(N)-heterocyclic thiosemicarbazone. The structure can be modified in the three circled points: the heterocyclic ring (green), the terminal nitrogen of the thiosemicarbazone side-chain (blue) and the metal ions for the chelation (red).*

The most common practice is to synthesize a structure with a selected (N)-heterocycle and then modify the various $R_1$ and $R_2$ groups of the terminal nitrogen of the thiosemicarbazone chain. (In Triapine $R_1$=$R_2$=H).
This process is called terminal (di)methylation, because usually one or both H are substituted with one or two methyl groups.
Further, methyl groups instead of hydrogen atoms are present in the imine group (C=N) and/or in amino group bound to the heterocycle.

In this way it is possible to obtain a set of products having the same structural skeleton, but a different terminal methylation.
Subsequently these compounds can give various metal complexes, using different metal salts.
Usually, the set of free ligands and the set of metal complexes are then tested on various cancer cells lines and the results are compared.

In the literature there are many papers that show that the (di)methylation of thiosemicarbazones with a structure similar to Triapine greatly increases the cytotoxic and antitumor properties of these compounds. This behavior was observed for both the free ligands of the corresponding metal complexes. Particular attention has been given to complexes with non-toxic and biocompatible metals, such as copper, zinc, iron, etc. [2,8,9,10]

However, in the case of Triapine this topic is more complicated. In literature there are conflicting opinions on the effective increase of the anti-tumor properties after the (di)methylation. Some scientists argue that (di)methylation is effective only in structures without amino groups on the heterocycle[9], while others believe that the (di)methylation of Triapine leads to significant changes in the drug's action mechanism and in its cellular interaction. This trend has also been reported for metal complexes.[11,12,13]

Another remarkable aspect is that (di)methylation consists in the substitution of a proton with a methyl group, and not with generic alkyl groups or long aliphatic chains.

This fact is mainly due to the already poor water solubility of thiosemicarbazones: the addition of long aliphatic chains would make them even more hydrophobic, making it difficult to administer as drugs. Vice versa, the increase in lipophilicity could make these compounds more similar to the cell membranes of the diseased cells, improving their up-take and therefore their antitumor efficacy.

As already explained in the previous Chapter, using nanowires as carriers solves the problem of poor solubility of thiosemicarbazones and allows to freely modify the structure of Triapine, even introducing a long terminal aliphatic chain.

Therefore, a derivative of Triapine was synthetized, adding a tail of four carbon atoms to the terminal nitrogen. (Figure 5.2)
For convenience, this synthetic derivative will be called C-Triapine (with the initial letter C indicating the presence of a carbon atom chain), to distinguish it from the original Triapine. This nomenclature will be used throughout the thesis.

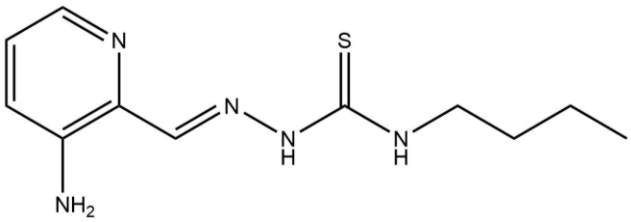


*Figure 5.2: Structure of C-Triapine: (E)-2-((3-aminopyridin-2-yl)methylene)-N-butylhydrazine-1-carbothioamide.*

This compound was then tested *in vitro* on A549 cancer cell lines both as “free” molecules (free ligand and free copper complex), and as molecules anchored to the nanowires (NWs+ligand and NWs+ complex).

## 5.2 Model Reactions in solution: C-Triapine and copper complex

As already explained in the previous Chapter, the Model Reactions are reactions that simulate in solution the reactions that occur on the nanowires allowing to monitor each step and to evaluate the individual yields obtained.

Below, the synthetic scheme followed is reported. The 3rd Anchoring Method was adopted, which first involves the synthesis of the C-Triapine precursor and then the reaction with the Si-NCS linker anchored on NWs.

The detailed description of the individual steps and the product characterization are reported in the Experimental Section at the end of the Chapter.

### 5.2.1 C-Triapine Precursor Synthesis

- **Reaction 0:**

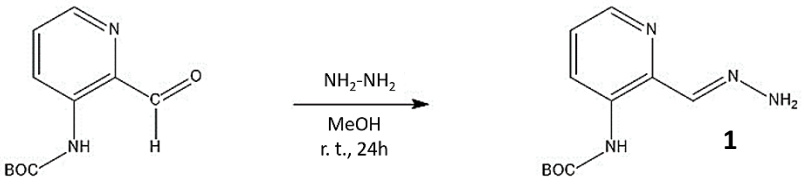


- **Model Reaction 1:**

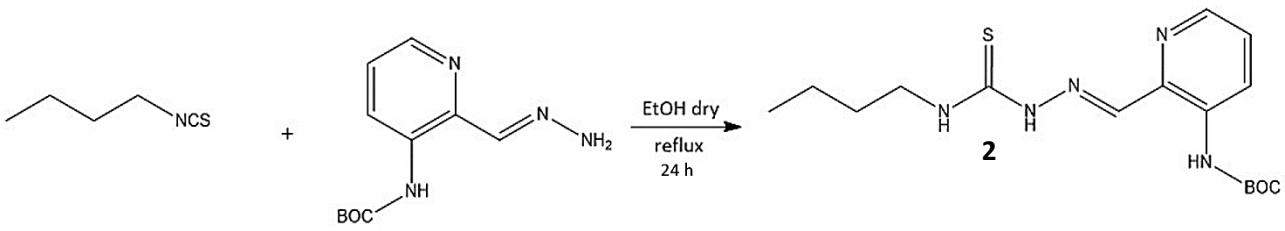


- **Model Reaction 2:**

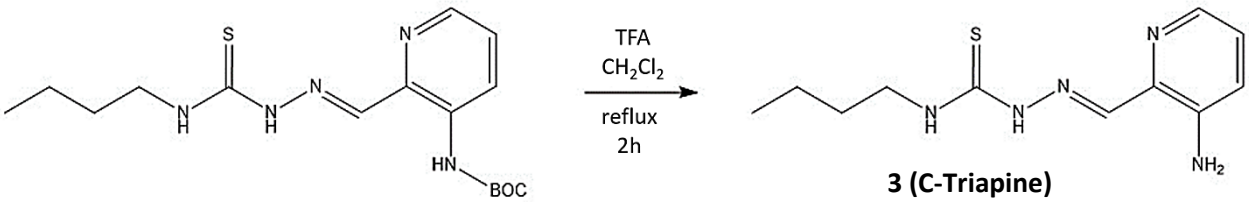

- **Model Reaction 3:**

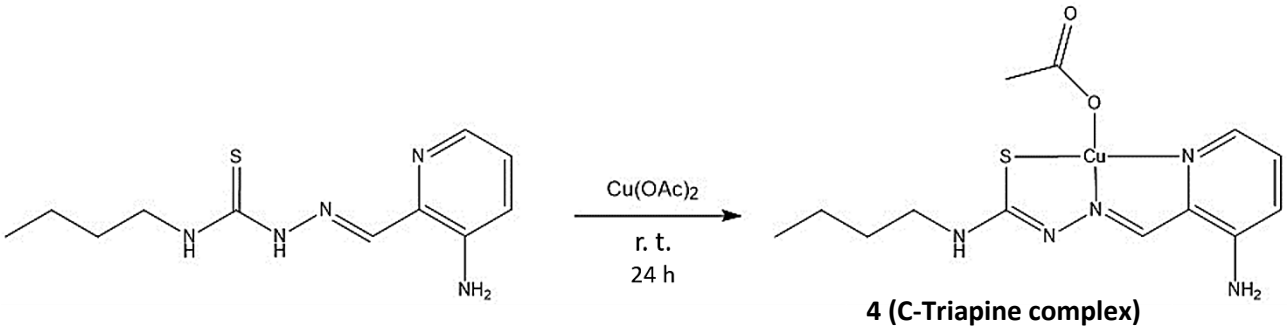


**4 (C-Triapine complex)**

Usually thiosemicarbazones are obtained from the reaction between an aldehyde and a thiosemicarbazide.[14,15,16]
Instead, this synthetic route is based on a condensation between an isothiocyanate and a hydrazone, obtained from the reaction of an aldehyde with hydrazine.

The C-Triapine synthesis reaction is very simple, and using an excess of hydrazine instead of a stoichiometric 1 : 1 ratio as reported in literature[17,18], the reaction yield has increased significantly (yield always > 97%). The final product was characterized with $^{1}$H-NMR spectroscopy.

Model Reaction 1 was carried out in dry ethanol to obtain compound **2**. Butylisothiocyanate was selected to simulate the Si-NCS linker that will be present on the NW surface. The yield was very good (about 96%) and the final product was characterized with $^{1}$H-NMR, FT-IR spectroscopies and ESI-MS.

The deprotection reaction of the BOC group (Model Reaction 2) is a standard reaction, with excellent yields. Compared to the reactions reported in the literature[19], the extraction of compound **3** did not occur in dichloromethane but in ethyl acetate because the compound was more soluble. Compound **3** was characterized with $^{1}$H-NMR, UV-Vis, FT-IR spectroscopies and ESI-MS spectrometry.

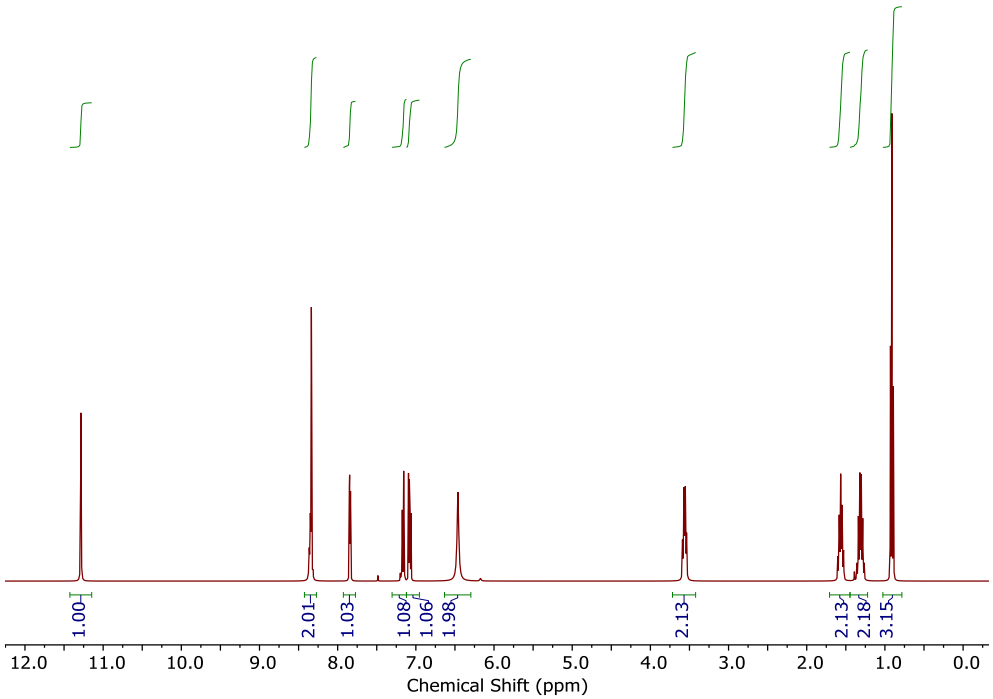


*Figure 5.3: $^{1}$H-NMR spectrum of compound **3** (C-Triapine) in DMSO-$d_6$.*

The $^{1}$H-NMR spectrum of C-Triapine in Figure 5.3 shows that the deprotection reaction occurred: the peak at about 1.6 ppm of the BOC protector group disappeared and the signal of the deprotected amine appears at 6.46 ppm.
The first peak at 11.28 ppm is the signal of the HN-N proton and is followed by the three peaks related to the aromatic protons (8.34ppm, 7.84 ppm and 7.16 ppm). Overlapping the first aromatic peak is the HC-N signal (at about 8.30 ppm), while the HN-C peak is at 7.08 ppm. In the aliphatic part of the spectrum are present the signals of the three $CH_2$ groups and the $CH_3$ group of the carbon chain.

For the complexation of the ligand **3** (Model Reaction 3), copper(II) acetate dihydrate was used.
To avoid the formation of the dimer with the stochiometric ratio ligand : metal = 2 : 1, the salt was dissolved in methanol and the solution containing the ligand (in methanol) was added drop by drop to the metal solution. The obtained dark powder was characterized with UV-Vis, FT-IR and ESI-MS.

Successful complexation can be seen for example in the UV-VIS spectrum in Figure 5.4 in which the free ligand **3** spectrum and the copper complex **4** spectrum are compared.

The main absorption bands (C-Triapine: 292 nm, 372 nm; C-Triapine complex: 296 nm, 446 nm) are assigned to n→π* transitions of the aminopyridine ring and the thiosemicarbazide moiety.[20] In the spectrum of the copper complex (in red) we observe a bathochromic shift at longer wavelengths, as reported in the literature for Triapine complexes.[21]

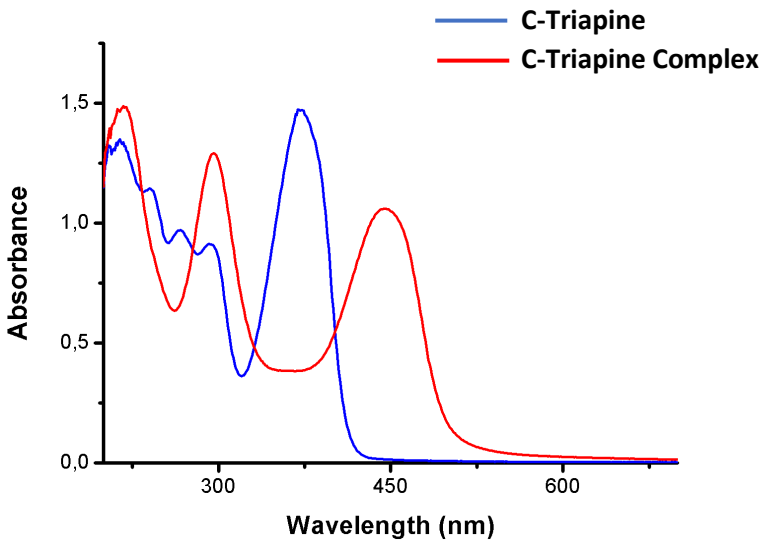


*Figure 5.4: Overlap of the two UV-Vis spectra of the free ligand C-Triapine (in blue) and of the C-Triapine copper complex (in red). Both spectra are recorded in ethanol, sample concentration: $1 \cdot 10^{-4}$ M.*

To test compounds in cancer cell lines it is essential that the synthesized molecules are stable in solution over a long period of time.

For this reason, compounds **2** and **3** (C-Triapine) were kept in the following conditions:

- as dry compounds,
- as compounds dissolved in a low donor number solvent ($CHCl_3$),
- as compounds dissolved in a high donor number solvent (DMSO),
- as compounds dissolved in water (plus a minimum amount of DMSO to dissolve the sample).

After 15 days the solvent was removed, and the dry compounds were study with $^{1}$H-NMR technique to verify if such molecules were still intact without presence of by-products in the spectrum.

Compounds **2** and C-Triapine (**3**) were extremely stable and do not exhibit by-products or impurities.
For example, in Figure 5.5 the spectra of compound **2** are shown.

The blue spectrum is the reference spectrum, recorded immediately after the synthesis of compound **2**. The dark green spectrum is the spectrum of compound **2** stored dry in the normal atmosphere for 15 days. The remaining spectra are the spectra of compound **2** dissolved in the various solvents for 15 days: in pink chloroform, in red dimethyl sulfoxide and in black water.

The last spectrum is probably the most important and diagnostic for assessing the stability of the compound in solution, in fact the cellular environment is rich in water. Therefore, it is essential that compounds **3** and **4** do not deteriorate in water to perform reliable *in vitro* tests.

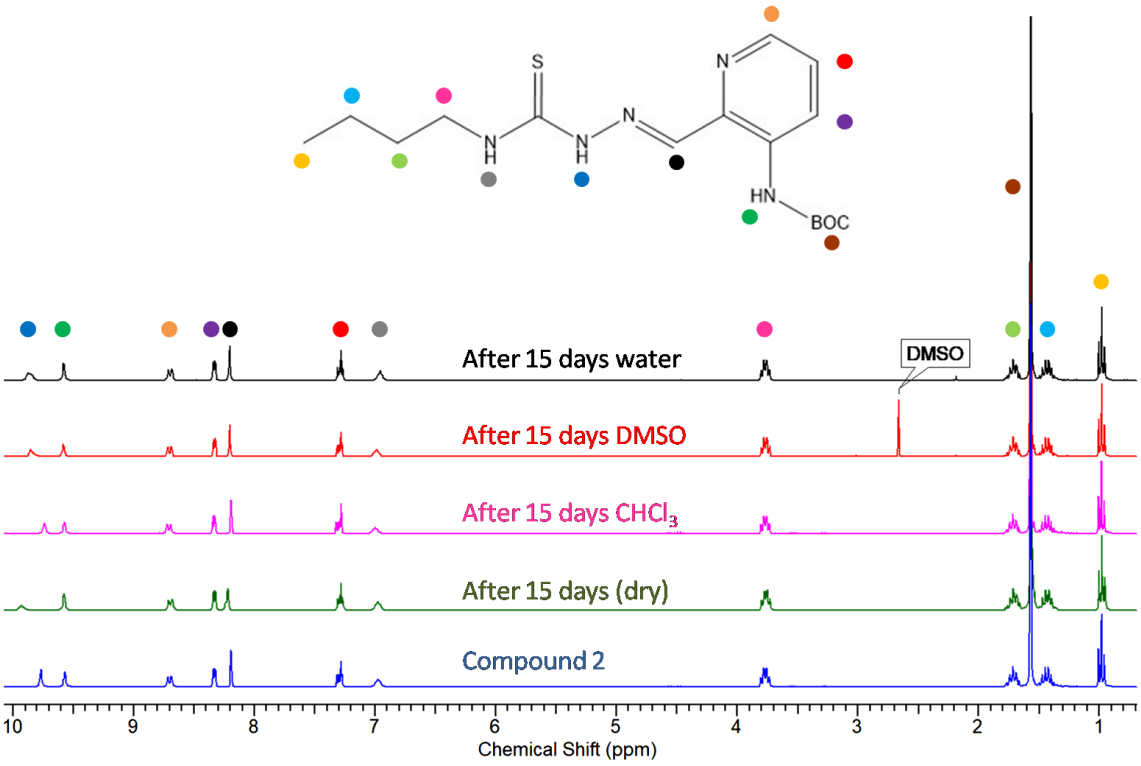


*Figure 5.5: $^{1}$H-NMR spectra of compound **2** in CDCl3: in blue the reference spectrum of compound **2** characterized immediately after the synthesis, in green compound **2** kept dry for 15 days, in pink compound **2** dissolved in $CHCl_3$ for 15 days, in red compound **2** dissolved in DMSO for 15 days (the DMSO label indicates the presence of residual solvent recorded in the spectrum), in black compound **2** dissolved in the minimum amount of DMSO and then added to water for 15 days (without DMSO compound **2** is insoluble in water).*

Figure 5.5 shows that all the spectra are clean with signals well defined.

The first two peaks are the signals of HN-N and of the protected aromatic amine (blue and dark green dots). Following the three aromatic protons (orange, purple and red dots) separated by the peak of HC=N at 8.21 ppm. At about 7 ppm the signal of the remaining NH near the C=S (gray dot).

The area between 4 and 0 ppm is characterized by the aliphatic signals of the three $CH_2$ groups and of the $CH_3$ group of the carbon chain (pink, light green, light blue and yellow dots). At 1.57 ppm the 9 H peak of the BOC protector group (brown dot).

To study the stability of complex **4**, the same approach was used: one sample stored dry for 15 days and other two samples dissolved one in DMSO and the other in water for the same period of time. The stability in chloroform was not checked because complex **4** is insoluble in this solvent.

Given the presence of copper ions, $^1$H-NMR spectra were not recorded, and the samples were studied using the ESI-MS technique.

The ESI-MS data reveal that copper complex **4** is stable over time and the metal remains bound to the ligand. Figure 5.6 shows the ESI-MS spectra of complex **4**.

The presence of the molecular peak at 313 m/z is clearly visible in the three spectra a, b and c. This value 313 represents the weight of the protonated C-Triapine molecule coordinated with one copper atom. Compared to complex **4**, the loss of the acetate group is highlighted.

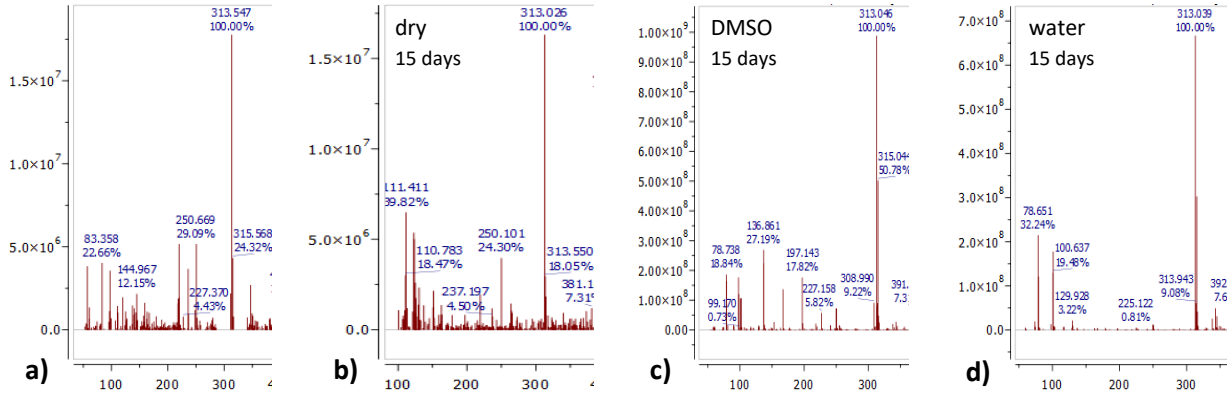


*Figure 5.6: Positive ESI-MS spectra of complex **4** in methanol: a) the reference spectrum of complex **4** characterized immediately after the synthesis, b) complex **4** kept dry for 15 days, c) complex **4** dissolved in DMSO for 15 days, d) complex **4** dissolved in the minimum amount of DMSO and then added to water for 15 days (complex **4** is insoluble in $CHCl_3$ and without DMSO is insoluble in water).*

## 5.3 Reactions on nanowires surface: C-Triapine and copper complex

The anchoring reactions of C-Triapine and its copper complex on the surface of NWs were carried out under the same conditions used for the Model Reactions in solution described above: same solvents, times and temperatures.

The various steps are shown below, and detailed descriptions of the reactions are in the Experimental Section at the end of the Chapter.

### 5.3.1 C-Triapine Precursor Synthesis

- **Reaction 0:**

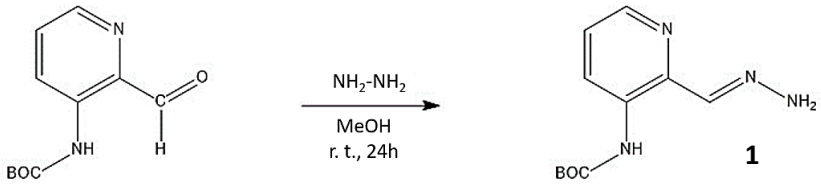


- **Reaction on NWs 1: (NWs surface activation)**

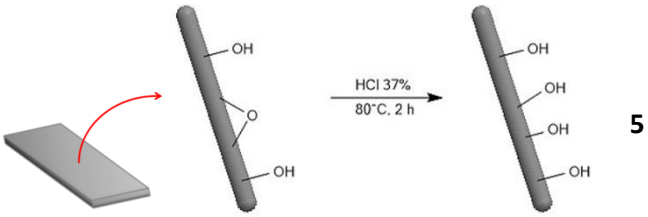


- **Reaction on NWs 2:**

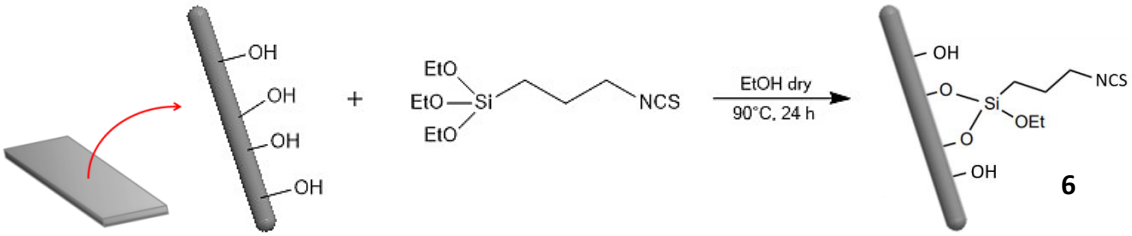


- **Reaction on NWs 3:**

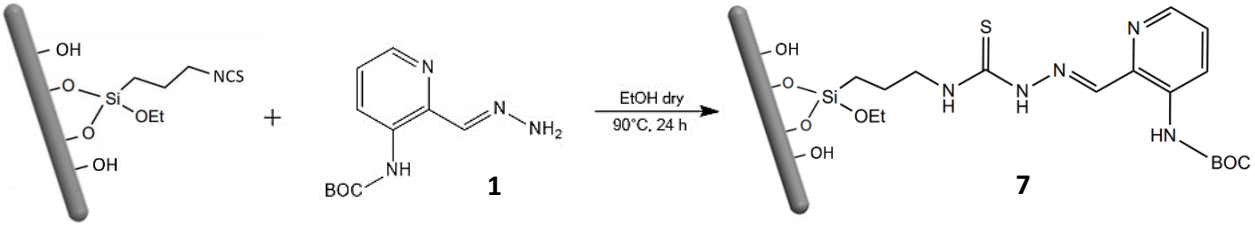

- **Reaction on NWs 4:**

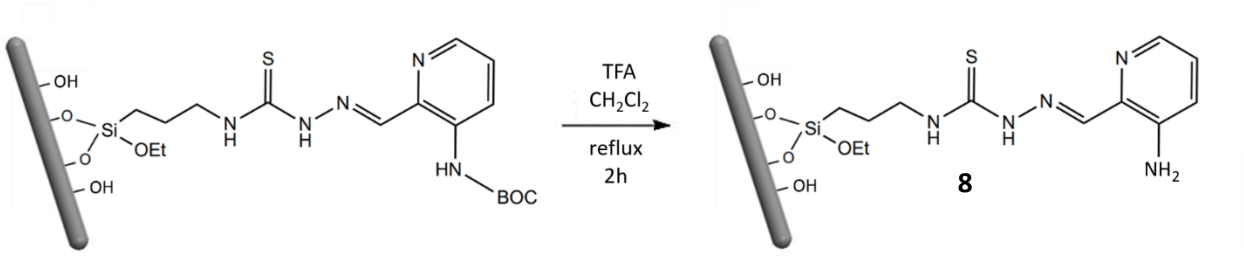


- **Reaction on NWs 5:**

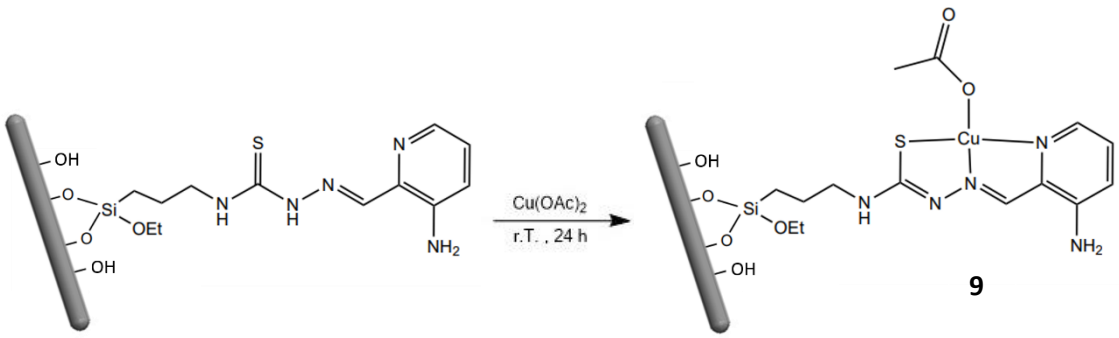


The first Reaction on NWs is the activation of NWs in concentrated hydrochloric acid. This step is necessary to activate the surface of nanowires (**5**) to make it more reactive to triethoxy(3-isothiocyanatopropyl)silane linker (Si-NCS). As shown in Figure 5.7, EDX-TEM analyses evidenced that the nanowires are well covered by the organic compound.

Once functionalized with the silane (**6**) (Figure 5.7), the isothiocyanate groups on the NWs surface are reacted with compound **1** freshly prepared.

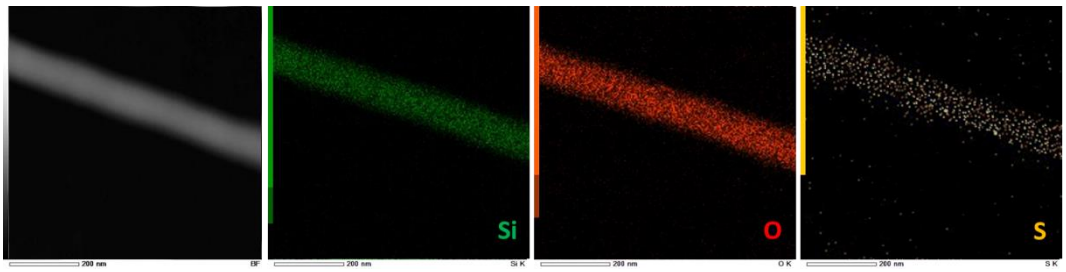


*Figure 5.7: EDX-TEM analysis of compound **6.** The elemental maps show the presence of silicon in green, oxygen in red and sulfur in yellow. The presence of S indicates that the NWs surface functionalization occurred.*

Reaction on NWs 3 occurs on nanowires detached from the growth substrate. In fact, in the scheme the nanowires are depicted without the platelet that is drawn on the left.
To detach the nanowires, the platelet is introduced into a falcon tube and covered with ethanol. The falcon is sonicated in an ultrasonic bath (59 MHz) for about an hour.

The bare platelet is removed and the ethanol containing the NWs is divided into several eppendorf tubes, which are centrifuged. The NWs that precipitate at the bottom of the eppendorfs are collected, joined together and dried.

The next step (Reaction on NWs 4) is the deprotection of the aromatic amine of compound **7** from the BOC protecting group.

Finally, copper(II) acetate dihydrate was added in order to obtain the complex anchored to the NWs (compound **9**)

Compound **9** was analyzed with EDX-TEM technique. Figure 5.8 shows the elemental superficial maps of functionalized NWs: in green silicon, in red sulfur and in blue copper. Copper covers perfectly the NWs and shows that the complexation of C-Triapine anchored on nanowires occurred.

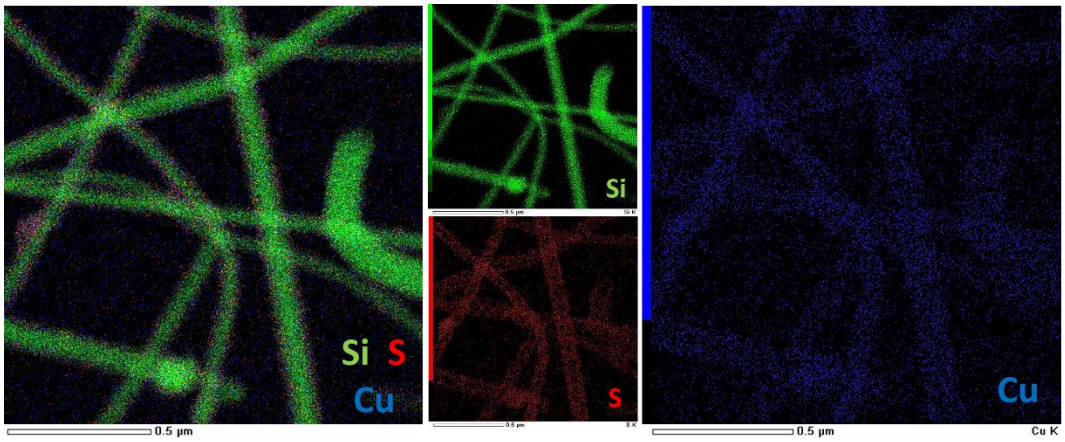


*Figure 5.8: EDX-TEM analysis of compound **9**. The elemental maps show the presence of silicon in green, sulfur in red and copper in blue. On the right, the overlap of Si, S and Cu maps on the NWs surface.*

### 5.3.2 Reaction on NWs platelet or on detached free NWs?

Model Reactions simulate the reactions occurring on the nanowires surface and allows obtaining useful chemical information regarding yields, level of purity of the compounds, any problems that arise during the reaction, etc.

However, Model Reactions cannot simulate how the reaction could be influenced by the presence of a nanomaterial in the reaction environment or if the presence of the silicon growth substrate goes to modify the reactivity.
Therefore, it is essential to understand if better results are obtained by making reactions on nanowires anchored to the silicon growth substrate or on nanowires detached from the platelets.

Particular attention was given to the first functionalization step between NWs and the linker triethoxy(3-isothiocyanatopropyl) silane Si-NCS (Reaction on NWs 2).
This reaction was selected as test reaction for two main reasons. First, previous experiments showed low EDX percentage of sulfur of compound **6** obtained with Reaction on NWs 2 (paragraph 4.3, 3$^{rd}$ Anchoring Method). Secondly, this step is the first reaction that takes place on the NWs and it is essential to obtain a good surface coating to have a good basis for subsequent reactions.

To evaluate the impact of the presence of the silicon substrate, experiments both on free detached nanowires and on nanowires anchored to the platelet were performed.

The first choice was to replace the previously used reaction reagent (toluene) with a less toxic and more biocompatible reagent: ethanol.

Below the various experiments, the reaction conditions used, and a brief evaluation of the results obtained.

*[Author's note: The reactions I previously drew in this paragraph are already the definitive reactions, with optimized reaction conditions and increased yields].*

- **Si-NCS functionalization on detached NWs**

  - **Experiment 1:**

After the activation with HCl, the platelet was sonicated to detach the NWs. Detached NWs reacted with 25 µL of Si-NCS in inert nitrogen atmosphere, at reflux for 48 h in 8 mL of dry ethanol.
At the end of the reaction, the ethanolic solution was slightly turbid and some suspended grey corpuscles could be observed in addition to NWs, similar to dust in water. (Figure 5.9 a, right)

In order to collect the NWs, the sample was centrifuged. Generally following the centrifugation NWs precipitate well, forming a compact body shaped like a curl at the bottom of the Eppendorf tube (Figure 5.9 b), but in this case the post-centifuged NWs did not precipitate and the surnatant remained turbid (Figure 5.9 c).

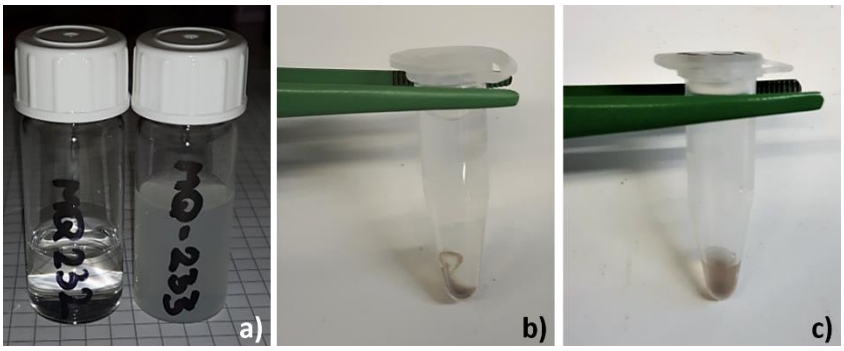


*Figure 5.9: a) Comparison of post-reaction ethanolic solutions of Si-NCS: on the left the solution obtained by the same reaction on the platelet (Experiment 3), on the right solution obtained by reaction on detached NWs in this experiment. b) Precipitation of functionalized NWs after centrifugation: on the bottom of the eppendorf tube there is dark grey curl of nanowires (Experiment 3). c) Absence of total precipitation of NWs functionalized after the detachment from the substrate: the solution is very turbid.*

Functionalized NWs were observed by TEM and mapped with EDX technique.
The TEM images show that the nanowires are poorly functionalized: the percentage of sulfur detected is very low, as shown in Figure 5.10 a. (2.3 keV is the characteristic lines in X-ray emission spectra correspond to sulfur).
In addition, the sample has a large amount of corpuscles trapped between the nanowires. (Figure 5.9 b and c)

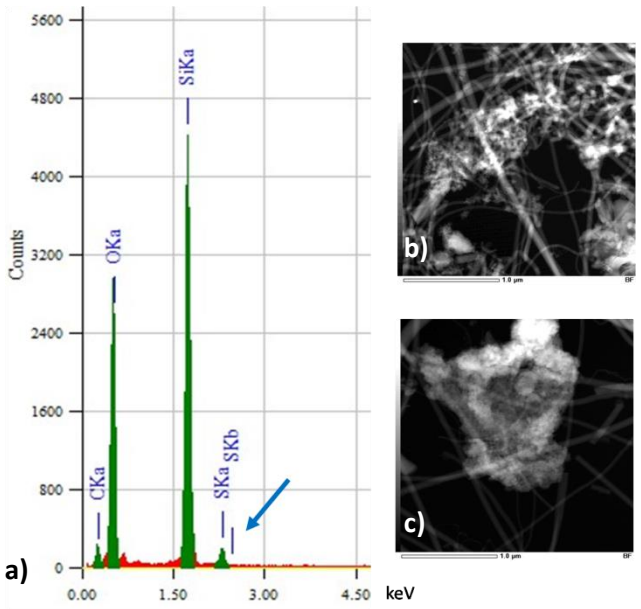


*Figure 5.10: a) EDX-TEM elemental analysis image of functionalized NWs. The amount of S, indicated by a blue arrow, is very low. b, c) TEM images of corpuscles trapped between the nanowires.*

Even after successive re-washing, sonication and centrifugation, these corpuscles remained attached to the nanowires. The EDX maps focused on the corpuscle showed the following elements: silicon and oxygen in large quantities and low presence of carbon and sulfur.

Probably Si-NCS polymerized in solution, forming these conglomerates that remain trapped between nanowires or bounded to nanowires surface.

Unfortunately, these corpuscles make it impossible to use the nanowires for future tests on tumor cells. In fact, the presence of these external bodies during *in vitro* tests could alter the results or induce a cell death rate higher than that obtained with the individual functionalized nanowires.

- **Experiment 2: Sonochemical approach**

The synthesis of nanomaterials[22,23] and their superficial functionalization[24,25] through sonochemical processes are two fairly common practices, with various examples reported in literature.
Sodipo and coworkers used a sonochemical approach to functionalize the surface of iron oxide nanoparticles with APTES.[26]
Therefore, a sonochemical process was adopted to functionalize the nanowires surface.

After the activation with HCl acid, the NWs were removed from the platelet by sonication and the solution containing NWS was deposited in a small schlenk.

The solvent was evaporated, and an inert atmosphere was created by fluxing nitrogen. Subsequently 8 ml of dry ethanol was injected, followed by 25 µL of Si-NCS.

The sealed Schlenk was sonicated for at least 3 h at room temperature. The final solution remained clear and Si-NCS did not polymerize. Finally, NWs were collected and analyzed.

The sonochemical approach allows to obtain nanowires with a great functionalization. The percentage of sulfur is high and in the EDX maps the presence of sulfur on the NWs surface is clearly observed. (Figure 5.11)

However, TEM images also revealed the presence of some corpuscles, even if in much lower quantities compared to Experiment 1.

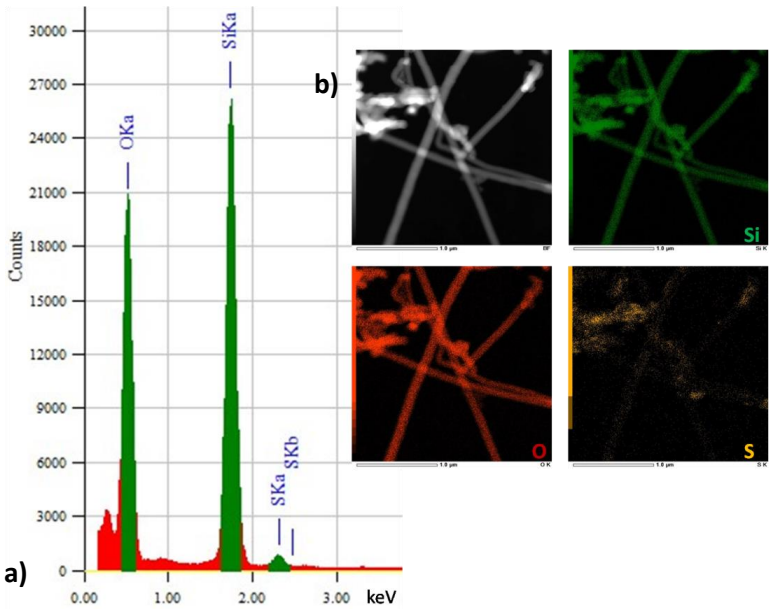


*Figure 5.11: a) EDX-TEM elemental analysis image of functionalized NWs. b) TEM EDX mapping of Si, O and S.*

This process can be considered good but still improvable.

Obviously, the corresponding experiment on anchored nanowires was not carried out. In fact, sonicating the platelet would cause the detachment of the nanowires from the substrate.

- **Si-NCS functionalization reaction on platelet**

- **Experiment 3:**

After the platelet activation with HCl, the reaction with Si-NCS (25 µl) was carried out in the same conditions described in Experiment 1.

In Figure 5.12, the amount of sulfur is low and the nanowires are poorly coated.
The percentage of sulfur obtained in Experiment 1 and that obtained in this experiment are comparable.

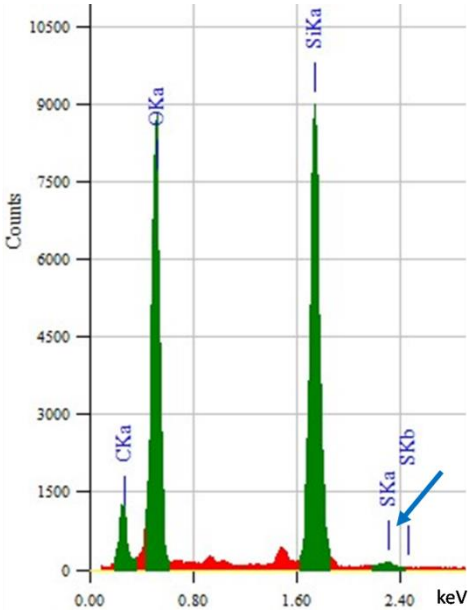


*Figure 5.12: EDX-TEM elemental analysis image of functionalized NWs. The amount of S, indicated by a blue arrow, is very low.*

However, unlike Experiment 1, at the end of the reaction the solvent was still transparent (as shown in Figure 5.8 a, left) and TEM images have shown that there are no corpuscles trapped between the nanowires.

This result can be explained by analyzing two main factors: i) Si-NCS did not polymerize probably because the reaction environment was more anhydrous, and therefore did not generate corpuscles.; ii) at the end of the reaction the platelet was carefully rinsed with ethanol to remove any possible by-products deposited on the surface, between the nanowires.

To improve the loading, the functionalization reaction was carried out twice consecutively and the amount of Si-NCS linker used was slightly increased.

- **Experiment 4: two consecutive reactions**

On the same platelet the reaction was repeated twice using 15 µL of Si-NCS. In place of 48 hours-reaction, the platelet reacted in two consecutive 24 hours-reactions.

In Figure 5.13, the yield of the functionalization is very high and the nanowires are well coated.

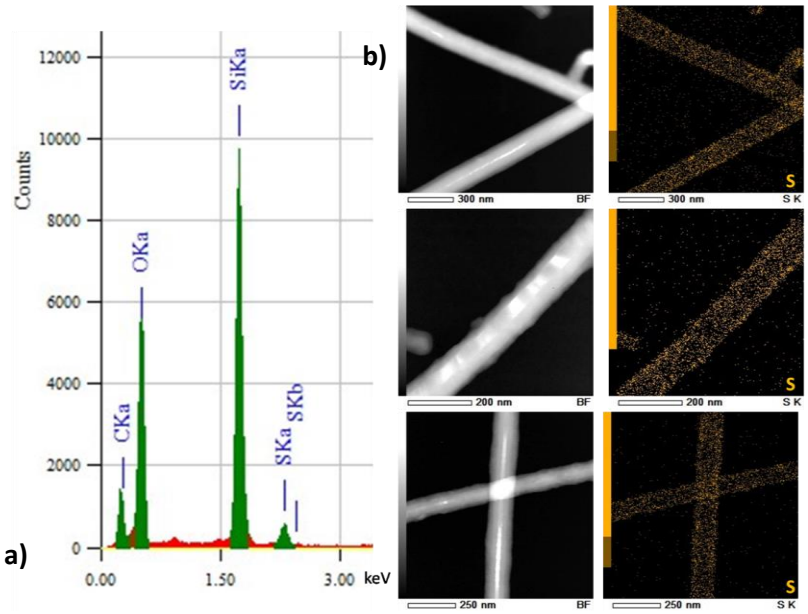


*Figure 5.13: a) EDX-TEM elemental analysis image of functionalized NWs. The amount of S is high. b) TEM EDX mapping of S in different random selected NWs.*

These two consecutive 24h-reactions protocol avoided the polymerization of Si-NCS, and in the final solution no corpuscles were found.

However, the addition of a further identical reaction to the previous two did not improve the loading.

## 5.4 Quantification of C-Triapine loading on NWs surface

The loading of C-Triapine or C-Triapine-metal complex bounded to core-shell NWs is an important issue to determine the success of the nanosystem in killing cancer cells.

In order to calculate the amount of drug to be administered during the *in vitro* tests to the cancer cells lines it is essential to know the exact amount of C-Triapine and its complex anchored to the nanowires.
In fact, a too high amount of anticancer drug would cause immediate cell death, whereas too low amount of drug would not give any effect on cell proliferation.
Further, it is important to compare the results obtained with the results relative to the "free" molecules of ligand and complex.

### 5.4.1 Experiment overview

The determination of C-Triapine loading on NWs surface was possible thanks to the possibility of quantifying the amount of copper released by C-Triapine-Cu complex: an indirect quantification of the metallated C-Triapine anchored on NWs was performed, exploiting the atomic absorption measure of the released free copper.
An acid treatment was used to remove copper ions from the C-Triapine complex. After the functionalization reactions, the NWs were dispersed in concentrated $H_2SO_4$, to remove Cu(II) from the C-Triapine anchored on NWs. The samples were centrifuged and washed with water and the resulting surnatant containing Cu(II) was collected and analyzed using atomic absorption.

This procedure was presented in a previous PhD thesis[27] where the supported complex was a copper porphyrin. In that thesis it was found that a higher degree of porphyrin loading was obtained carrying out the reaction using detached NWs after functionalization with the alkoxyaminopropylsilane (APTES).
Probably this result is due to the fact that detached NWs are more easily reached by the big molecules of porphyrin than when they are on the platelet.

### 5.4.2 The C-Triapine experiment

To determine the C-Triapine loading on the NWs, the protocol shown in figure 5.14 has been adopted.

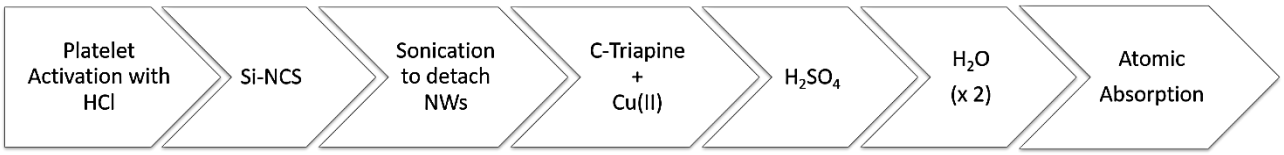


*Figure 5.14: Diagram representing the preparation steps of the C-Triapine-Cu(II) sample.*

After the platelet activation, the anchored NWs were functionalized with the linker Si-NCS and then detached from the silicon substrate. Free detached NWs were functionalized with C-Triapine and then, copper(II) acetate was used to obtain the C-Triapine complex anchored on NWs.

Subsequently, functionalized NWs were dispersed in a solution 5% *v/v* of concentrated $H_2SO_4$ (97%) in water. After the addition of acid, the NWs surnatant immediately turns green, an indication of the fact that copper is removed from the complexation with C-Triapine. (Figure 5.15 a-d)

This green surnatant was collected into volumetric flasks and the NWs were washed two times with distilled $H_2O$. This operation was repeated for four times, until the surnatant lost its green color. (Figure 5.16 e)

The photos in Figure 5.15 represent some phases of sample preparation for the atomic absorption measurements.

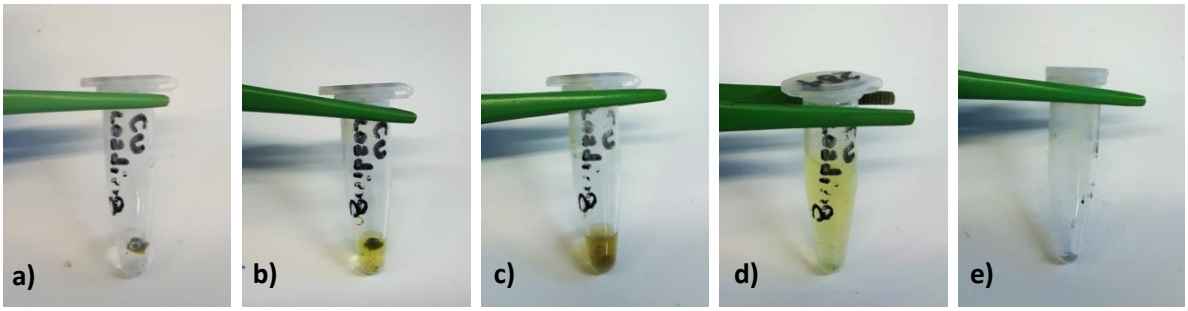


*Figure 5.15: Photos of sample preparation: a) NWs immediately after the addition of 100 µL of $H_2SO_4$. b) NWs in sulfuric acid. The solution is starting to turn green due to the presence of copper. c) NWs in sulfuric acid after sonication. The solution is intense green. d) NWs in sulfuric acid after the addition of 900 µL of distilled $H_2O$. e) NWs at the end of the copper removal process. They turned gray.*

By atomic absorption measurements, the amount of copper present is 22.8 ppm.

From the calculations made (described in detail in the Experimental Section) it was found that the weight percentage of C-Triapine covering the NWs surface is 17 % w/w of NWs.

## 5.5 *In vitro* test

Four samples, the free C-Triapine ligand, the free C-Triapine-Cu complex, the C-Triapine ligand anchored to NWs and the C-Triapine-Cu complex anchored to NWs, were tested on A549 human lung adenocarcinoma cell line. Data were collected after 24, 48 and 72 h.

### 5.5.1 Materials and method

- **Cell cultures**

A549 human lung adenocarcinoma cell line (Figure 5.16) was purchased from ATCC (VA, USA). Cells were grown in RPMI 1640 medium supplemented with 10% (v/v) heat-inactivated fetal bovine serum, 2 µM L-glutamine and antibiotics (100 U/ml penicillin and 100 µg/ml streptomycin) and maintained at 37 °C in a humidified and 5% $CO_2$ incubator. Exponentially growing cells were used for all assays.

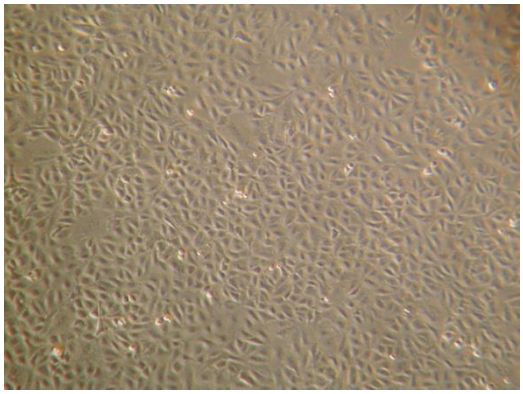

*Figure 5.16: A549 cells (Magnification: 100x)*

- **Cell proliferation/viability assays**

A549 cells in their logarithmic phase were allowed to adhere overnight at 37 °C, then increasing concentrations of compounds or NWs were added to the medium and the cells left exposed for 24, 48 or 72 h.

Cell morphology was monitored with an inverted phase contrast microscope (CK40, Olympus, Japan) and at the end of treatments viable cells were collected and counted in a Burker hemocytometer.

Viability was also assessed by MTT. The formazan crystals were solubilized, and the absorbance was measured using an automated microwell plate reader (Multiskan Ascent, Thermo Labsystems, Helsinki, Finland) at 550 nm. All experiments were performed at least in triplicate and cell viability was expressed as the percentage of controls (untreated cells). To exclude the interference or interaction of probe with the compounds or NWs, cell-free controls were included.

- **Cell cycle**

Cell phase distribution was assayed by determining the DNA content of the nuclei by means of flow cytometry. Briefly, after treatments, the cells were collected, washed in PBS, and fixed in ethanol (96%). They were then stained by propidium iodide-PI (20 µg/mL in PBS containing RNase-A) at 4 °C overnight. The

analysis was made using a FC500™ flow cytometer (Beckman Coulter, Brea, CA, USA), and cell cycle phase distribution was calculated as percentages using FlowJo software (Ashland, OR, USA).

### 5.5.2 Results and Discussion

The $IC_{50}$ values (the concentration of an inhibitor where the response or viability is reduced by half) for the free C-Triapine ligand (free ligand) and the free C-triapine-Cu complex (free complex) were obtained from the following dosage/viability% curves for A549 cells after 24, 48 and 72 h.

The curves are shown in Figure 5.17 and 5.18 and the $IC_{50}$ values obtained are collected in Table 5.1.

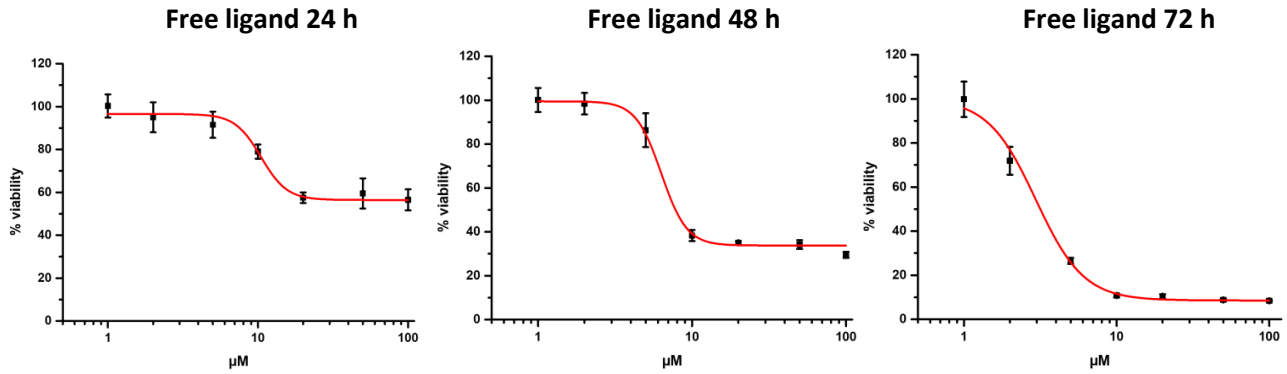


*Figure 5.17: Free C-Triapine ligand dose-response curves for A549 cells after: 24 h, 48 h and 72 h.*

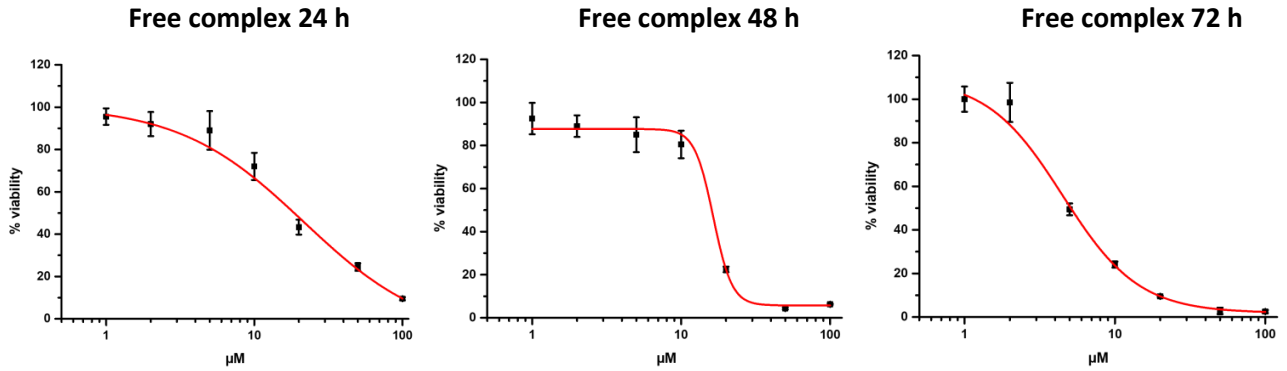


*Figure 5.18: Free C-Triapine complex dose-response curves for A549 cells after: 24 h, 48 h and 72 h.*

*Table 5.1: $IC_{50}$ values of the free ligand and the free complex after 24, 48 and 72 h in A549 cells.*

| | $IC_{50}$ (μM) | | |
|---|---|---|---|
| | **24 h** | **48 h** | **72 h** |
| **Free ligand** | > 100 | 6 ± 1 | 2.9 ± 0.4 |
| **Free complex** | 21 ± 4 | 16 ± 4 | 4.5 ± 0.4 |

Both the free ligand and the free complex reduce the viability of A549 cells.
However, the kinetics of action are different. The free complex is active already after 24 hours of treatment with $IC_{50}$ 24 h: 21 µM, while the effects of the free ligand on cell viability/proliferation occur in subsequent times ($IC_{50}$ 24 h: > 100 µM; $IC_{50}$ 48 h: 6 µM and $IC_{50}$ 72 h: 2.9 µM).

In both cases the most promising results are obtained over time: the $IC_{50}$ values after 72 h are better than the $IC_{50}$ values after 24 h. This phenomenon is not so rare in medicine: for example, cisplatin has a similar behavior, with good $IC_{50}$ values only after 48 h.[28]

The study of the cell cycle allows a better understanding of the mechanism of action of a drug.

The cell cycle is the series of events that take place in a cell that leads to its division and duplication of its DNA (DNA replication) to produce two daughter cells.
The cell cycle is characterized by five phases: phase $G_0$, phase $G_1$, phase S, phase $G_2$ and phase M (mitosis and cytokinesis). The letter G stands for Gap and S stands for Synthesis.
The genetic information must be correctly transmitted from the mother cell to the daughter cells, therefore the genome must first be duplicated during the period called S phase. Then the chromosomes are segregated in the two daughter cells during the M phase. The M phase is composed of two linked processes: mitosis (the nuclear division during which the chromosomes of the cell are divided between the two daughter cells) and the cytokinesis (in which the physical division of the cytoplasm of the cell takes place).
Between S and M phases, there are two periods of time called gap: $G_1$ between the end of mitosis/cytokinesis and the beginning of S phase and $G_2$ between the end of S phase and the beginning of M phase.
To avoid errors that could compromise cell viability, during the cell cycle there are control points (called checkpoints) located at the level of the $G_1$/S and $G_2$/M transitions.
When the cell has left the cycle and has stopped dividing, the rest phase (or quiescent phase) begins, called $G_0$.

Figure 5.19 shows the scheme of the cell cycle and its phases.

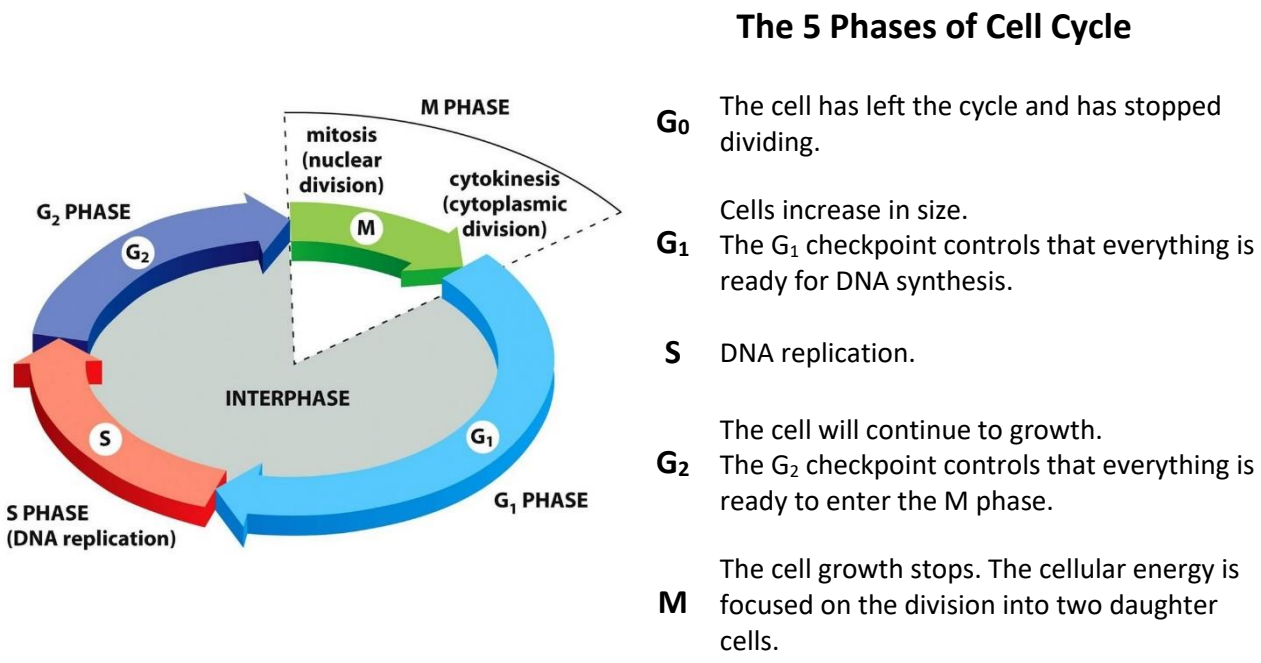


*Figure 5.19: The Cell Cycle and its phases: $G_0$, $G_1$, S, $G_2$ and M. Credit: https://mrrittner.weebly.com.*

The analysis of A549 cell cycle reveals that the mechanisms of action of the two free compounds are different. (Figure 5.20).

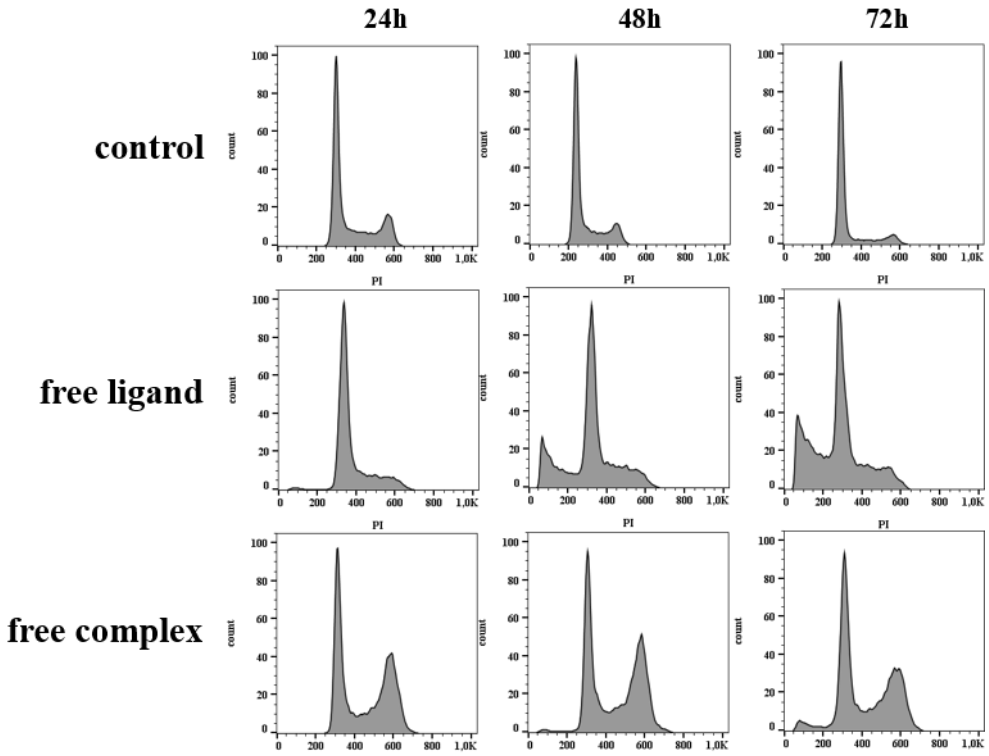


*Figure 5.20: A549 cell cycle distribution (after 24 h, 48 h and 72 h) for free ligand and free complex. The different peaks correspond to $G_0/G_1$, S and $G_2/M$ phases.*

The free complex causes a block in the $G_2$/M phase, while the free ligand activates processes of cell death (necrosis or apoptosis), highlighted by the presence of a high peak sub$G_0/G_1$.
In future studies it would be interesting to investigate the type of cell death occurred.

About the free complex, it is important to underline that all the cells blocked in phase $G_2$ and those blocked in phase M (mitosis or cytokinesis) are grouped together in the peak related to phase $G_2$/M.

The knowledge of the percentage progress of the blocked cells in each of these phases would be very useful to verify exactly which mechanism of action occurs. In fact, a net blockade in the $G_2$ phase could be indicative of an inhibition of the topoisomerase, while the block in phase M is typical of the antitubulinics, and the arrest in cytokinesis could reveal an inhibitory activity on actin.

Table 5.2 reports the percentage of the cells blocked in each phase of the cell cycle for the two free compounds, after 24, 48 and 72 h.

*Table 5.2: Percentage of the cells blocked in each phase of the cell cycle for the two free compounds, after 24, 48 and 72 h.*

| | | subG0/G1 | G0/G1 | S | G2/M |
|---|---|---|---|---|---|
| **24 h** | **Control** | | 49,80 | 34,70 | 15,50 |
| | **Free ligand** | | 67,00 | 18,80 | 14,20 |
| | **Free complex** | | 35,50 | 31,60 | 32,90 |
| **48 h** | **Control** | | 57,10 | 32,70 | 10,20 |
| | **Free ligand** | 24,20 | 51,40 | 12,50 | 11,90 |
| | **Free complex** | | 33,00 | 32,70 | 34,30 |
| **72 h** | **Control** | | 69,20 | 22,00 | 8,80 |
| | **Free ligand** | 32,80 | 44,20 | 11,80 | 11,20 |
| | **Free complex** | 5,70 | 44,20 | 12,00 | 38,10 |

Identical viability tests were carried out on the C-Triapine ligand anchored to the nanowires (NWs + ligand) and on the C-Triapine complex anchored to the nanowires (NWs + complex).

NWs were tested on the A549 cell line in two different concentrations (100 µg/mL and 50 µg/mL) for 24, 48 and 72 h. Non-functionalized nanowires (Bare NWs) were used as a reference.
The results obtained are shown in the histogram chart in Figure 5.21 where the reference Bare NWs are in blue, the NWs + ligand in yellow and the NWs + complex in pink.

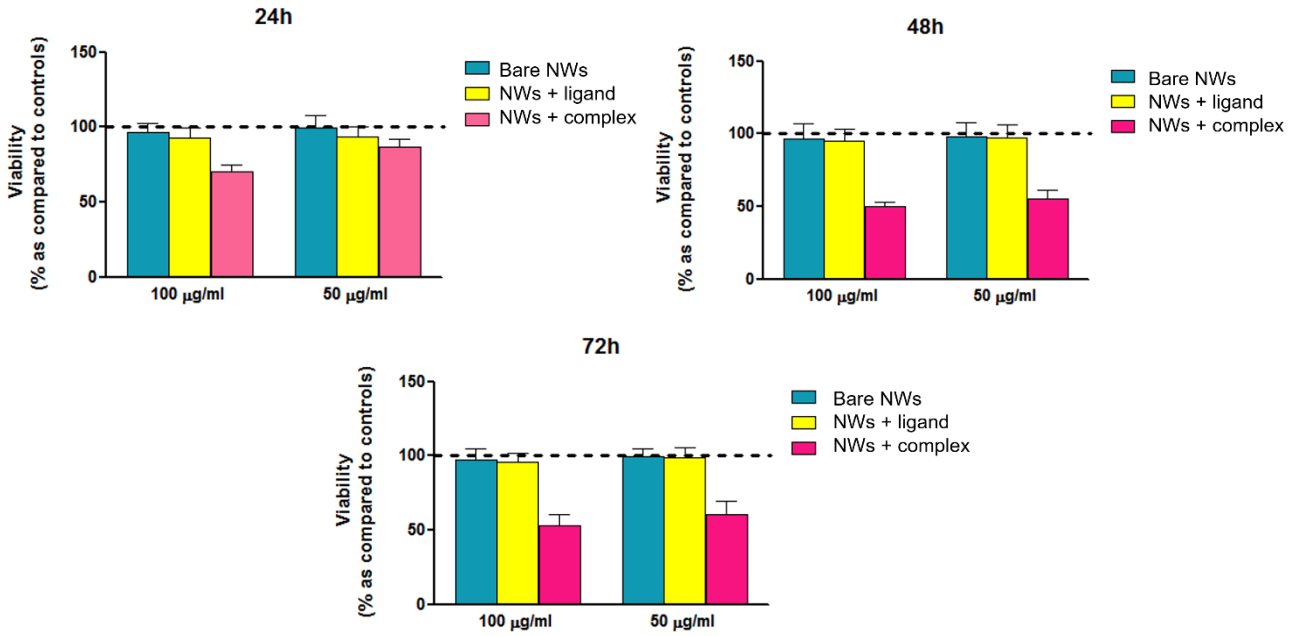


*Figure 5.21: Histograms of the viability test on A549 cell line of the functionalized NWs in two concentrations (100 µg/mL and 50 µg/mL) after 24, 48 and 72 h. The reference Bare NWs are in blue, the NWs + ligand in yellow and the NWs + complex in pink.*

From the experimental data, it can be stated that the NWs + complex cause a reduction in cell viability partially time-dependent only within the first 48 h. Between 48 h and 72 h there are no differences. Moreover, in the first 24 h there is a certain dose-dependence: 100 µg/mL of NWs + complex is more effective than 50 µg/mL.

Vice versa, the NWs + ligand are almost inactive, with values just slightly lower than the reference Bare NWs.

These results are the opposite of the results obtained for the free molecules: NWs + complex is more active than NWs + ligand, while the free ligand was more active than the free complex.
This difference cannot be attributed to the presence of extra-free copper ions trapped between the NWs, since the antitumor activity of copper salts has been shown to be ineffective *in vitro* at these concentrations. This behavior is widely documented in literature.[29]

Therefore, the only possible explanation is due to the presence of two different mechanisms of action between the free molecules and those anchored on NWs surface.

The study of the A549 cell cycle showed that only the NWs + complex is able to reduce the cells viability or proliferation, causing a significant increase in the cell population in the $G_2$/M phase (Figure 5.22 and Table 5.3). This behavior also occurred for the free complex.

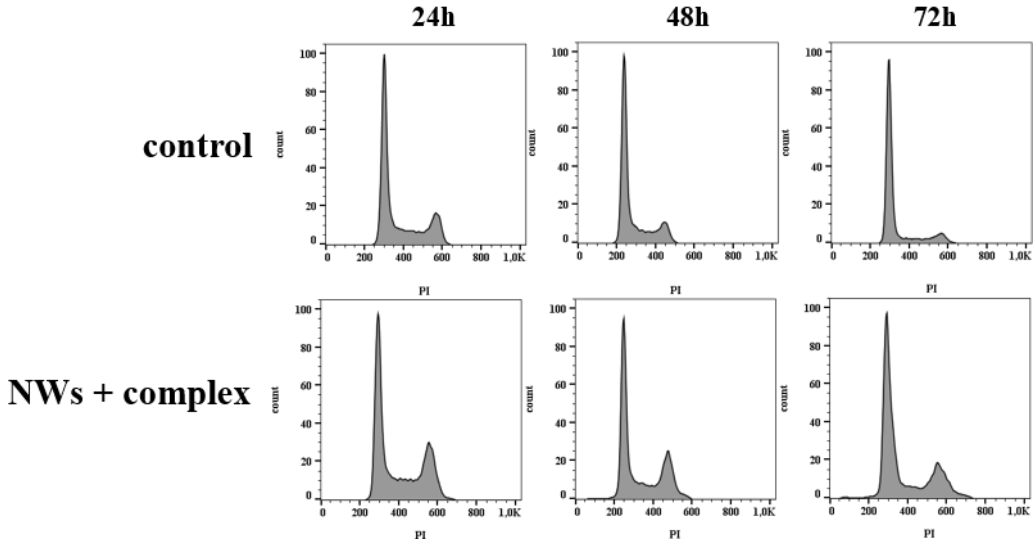


*Figure 5.22: A549 cell cycle distribution (after 24 h, 48 h and 72 h) for NWs + complex. The different peaks correspond to $G_0/G_1$, S and $G_2$/M phases.*

*Table 5.3: Percentage of the cells blocked in each phase of the cell cycle for the NWs + complex, after 24, 48 and 72 h.*

| | subG0/G1 | G0/G1 | S | G2/M |
|---|---|---|---|---|
| **24 h** | | 40,00 | 38,00 | 22,00 |
| **48 h** | | 46,50 | 31,50 | 22,00 |
| **72 h** | | 49,90 | 30,00 | 20,10 |

For visual convenience, the data in Tables 5.3 and Table 5.4 were combined and collected in the histogram chart shown in Figure 5.23.

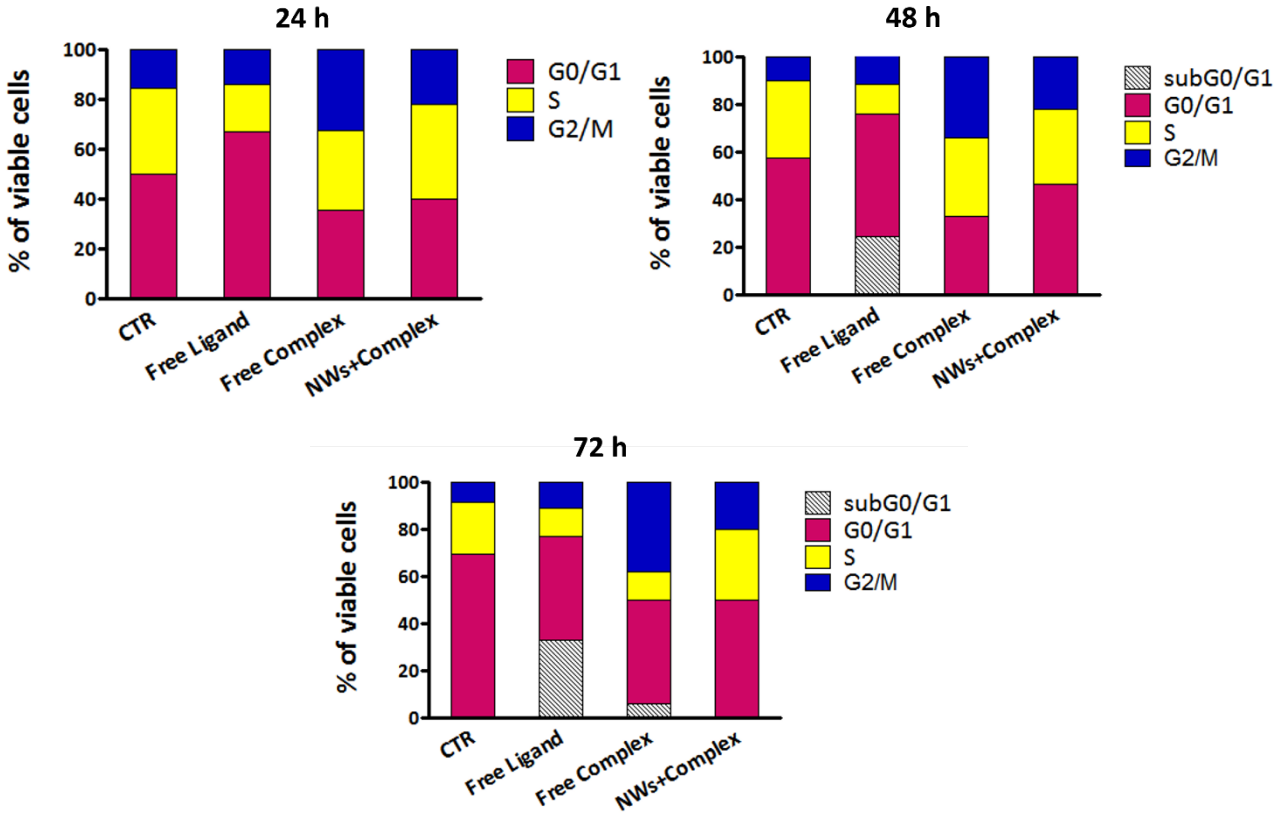


*Figure 5.23: Histograms showing the percentage of the A549cells blocked in each phase of the cell cycle (subG$_0$/G$_1$ in gray, G$_0$/G$_1$ in violet, S in yellow and G$_2$/M in blue) after 24, 48 and 72 h for the free ligand, the free complex, the NWs + complex and the control (CTR).*

## 5.6 Conclusions and future perspectives

Among all the thiosemicarbazones, Triapine has proved to be the molecule with the most promising anticancer properties. For this reason, Triapine was chosen as a study compound for this thesis oncology project.

The Model Reactions in solution allowed to optimize the steps of the reactions that would subsequently be tested on the nanowires surface, with the aim of anchoring the greater amount of C-Triapine on the NWs.

Following the appropriate characterizations (TEM, SEM and EDX techniques) and the quantification of the exact C-Triapine loading on the NWs it was possible to perform *in vitro* tests on A549 human lung adenocarcinoma cell line.

Initially the free C-Triapine ligand and the C-Triapine-Cu complex were tested without the presence of NWs. Both compounds showed good antitumor activity, especially after the first 48 h and 72 h, with good values of IC$_{50}$ (free ligand: IC$_{50}$ 48 h: 6 µM and IC$_{50}$ 72 h: 2.9 µM, free complex IC$_{50}$ 48 h: 16 µM and IC$_{50}$ 72 h: 4.5 µM).

The study of the cell cycle has allowed to understand that these two compounds have a different kinetics and mechanism of interaction with the cancer cells.

For the free ligand the peak sub$G_0/G_1$ that appears after 48 h and 72 h in the cell cycle distribution indicates that the free ligand induces in the cell a process of apoptosis or necrosis. Conversely, the free complex interferes with the cell cycle by blocking a subsequent cycle phase, as evidenced by the presence of a high peak relative to the $G_2$/M phase.

Subsequently, the same viability tests were carried out on the C-Triapine ligand anchored to the nanowires surface (NWs + ligand) and on the C-Triapine copper complex anchored to the nanowires surface (NWs + complex) in two different concentrations for 24, 48 and 72 h.

NWs + ligand was almost completely inactive throughout the *in vitro* test, even at different concentrations. On the contrary, NWs + complex was more active causing a reduction in cell viability partially time- and dose-dependent. As in the case of the free complex, the NWs + complex generate a block in the $G_2$/M phase.

The results obtained from *in vitro* tests of free molecules are the opposite of the results obtained by the molecules anchored on the NWs surface. Indeed, for the free molecules the ligand was found to be more active than the complex, while for the anchoring molecules the NWs + ligand was almost inactive, but the NWs + complex showed good activity against the cancer cell line.

This behavior is almost certainly attributable to the presence of two different mechanisms of action for the free molecules and for the molecules anchored on the NWs surface. The presence or the absence of the NW influences the way in which the molecules (free or anchored) interact with the cell and its cycle.

In any case, with the exception of the NWs + ligand, all the samples showed a good anti-tumor activity against the A549 cell line. Furthermore, it has been demonstrated that for the anchored molecules, this anticancer activity can not be caused only by the presence of the NWs since the same *in vitro* test was performed using as control non-functionalized NWs (bare NWs) that showed no signs of activity.

The results obtained are promising and open the way to the possibility of testing systems formed by NWs functionalized with different types of antitumor molecules on various cell lines. The anchoring of a drug to a nanomaterial used as a carrier would solve the problems related to the general hydrophobicity of these anticancer compounds and would be ideal for the treatment of solid tumors.

At the moment more detailed cell studies are still underway to better understand the two different mechanisms of action that have been revealed by the interaction between the tumor cell and the studied molecules.

Another interesting aspect that will surely be explored soon is the possibility of testing these compounds on different cell lines, to study how the anticancer activity and the mechanisms of action change in relation to the type of cells used.

Another option is to analyze how the complexation of the ligand with several different metal ions influences the activity of the complex (free and anchored on NWs) in the fight against cancer.

## 5.7 Experimental Section

### 5.7.1 Synthesis of *tert*-butyl (E)-(2-(hydrazineylidenemethyl)pyridin-3-yl)carbamate (1)

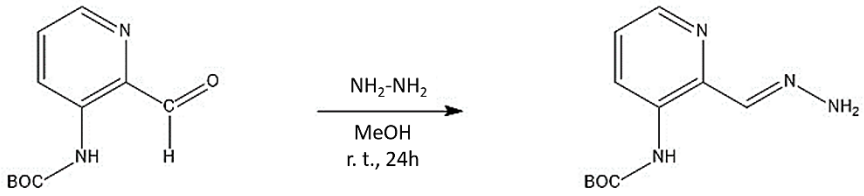


A cooled solution of *tert*-butyl (2-formylpyridin-3-yl)carbamate (200 mg, 0.90 mmol) in methanol (15 mL) was treated with an excess of hydrazine monohydrate (130 µL, 2.70 mmol). The solution was stirred for 24 h at room temperature. The reaction was monitored via TLC (80% AcOEt : 20% Hexane, $R_f$ = 0.37). After solvent removal under vacuum, product **1** was obtained as a light yellow solid. The yield is 98%.

**$^1$H NMR** (300 MHz, Chloroform-*d*) δ: 10.47 (1H, s, NH-BOC), 8.65 (1H, dd, *J* = 8.5, 1.4 Hz, H-arom), 8.17 (1H, dd, *J* = 4.5, 1.5 Hz, H-arom), 8.00 (1H, s, CH=N), 7.13 (1H, dd, *J* = 8.6, 4.6 Hz, H-arom), 5.81 (2H, s, $NH_2$), 1.51 (9H, s, $CH_3$ BOC).

### 5.7.2 Synthesis of *tert*-butyl (E)-(2-((2 (butylcarbamothioyl)hydrazineylidene)methyl)pyridin-3-yl)carbamate (2)

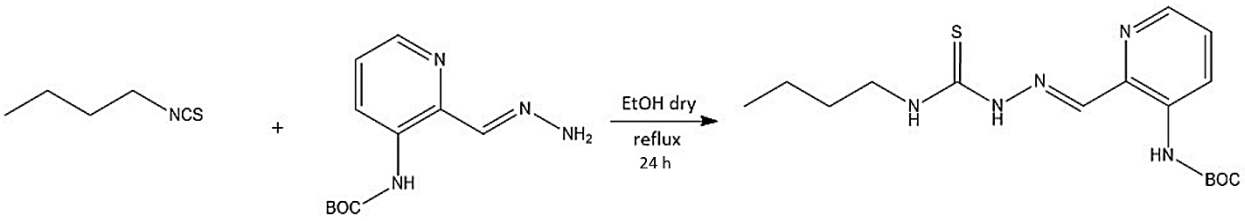


*Tert*-butyl (2-formylpyridin-3-yl)carbamate (**1**) (200 mg, 0.85 mmol) was introduced in a 25 mL round bottom flask, previously dried with three vacuum-nitrogen cycles, and dissolved in 8 mL of dry ethanol. An excess of 1-isothiocyanatobutane (307 µL, 2.54 mmol) was added and the reaction was stirred at reflux for 24 hours. The reaction was monitored via TLC (80% AcOEt : 20% Hexane, $R_f$ = 0.46). After solvent removal under vacuum, product **2** was obtained as a pale yellow solid. The final yield is 96%.

**$^1$H NMR** (300 MHz, Chloroform-*d*) δ: 9.88 (1H ,s, N-NH), 9.58 (1H, s, NH-BOC), 8.70 (1H, d, *J* = 8.6 Hz, H-arom), 8.33 (1H, dd, *J* = 4.5, 1.4 Hz, H-arom), 8.21 (1H, s, HC=N), 7.34 (1H, m, H-arom), 6.96 (1H , t, *J* = 6.1 Hz,NH-$CH_2$), 3.81 (2H, m, $CH_2$), 1.75 (2H ,m, $CH_2$), 1.57 (9H, s, $CH_3$ BOC), 1.43 (2H, dt, *J* = 14.8, 7.5 Hz, $CH_2$), 0.98 (3H, t, *J* = 7.3 Hz, $CH_3$).
**ESI-MS** in MeOH (negative): m/z 350 $[M-H]^-$, (positive): m/z 352 $[M+H]^+$, 374 $[M+Na]^+$.
**FT-IR** $cm^{-1}$ (selected bands): 3430 (w), 1718 (s), 1608 (m).

### 5.7.3 Deprotection of *tert*-butyl (E)-(2-((2-(butylcarbamothioyl)hydrazineylidene) methyl)pyridin-3-yl)carbamate (3)

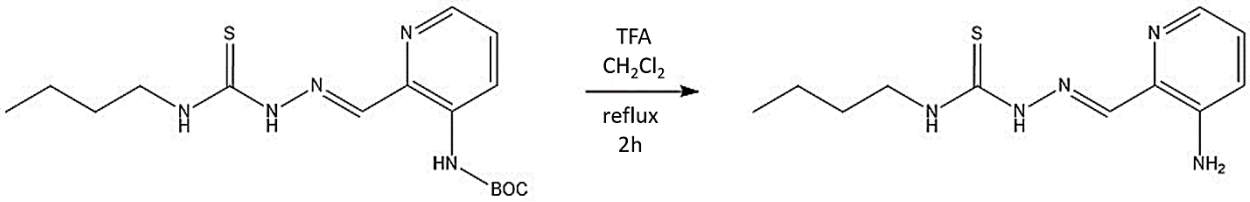


*Tert*-butyl(E)-(2-((2-(butylcarbamothioyl)hydrazineylidene)methyl)pyridin-3-yl)carbamate (**2**) (70 mg, 0.20 mmol) was introduced in a 25 mL round bottom flask and dissolved in 8 mL of DCM. TFA (2 mL) was added and the reaction was stirred at reflux for 2 hours. The solvent was removed under vacuum and the crude was dissolved in AcOEt. The solution was washed three times with an aqueous solution of $Na_2CO_3$ and with water to obtain a neutral pH.
The organic phase was dried on $Na_2SO_4$ and filtered. The white solid was dried and the final yield was 98%.

**$^1$H NMR** (400 MHz, DMSO-$d_6$) δ: 11.28 (1H ,s, HN-N), 8.34 (2H, overlap HC=N e H-arom), 7.84 (1H, dd, *J* = 4.3, 1.5 Hz, H-arom), 7.16 (1H, dd, *J* = 8.4, 1.5 Hz, H-arom), 7.08 (1H, dd, *J* = 8.3, 4.3 Hz, HN-C), 6.46 (2H , s, $NH_2$), 3.62 – 3.48 (2H, m, $CH_2$), 1.66 – 1.45 (2H ,m, $CH_2$), 1.31 (2H, h, *J* = 7.3 Hz, $CH_2$), 0.91 (3H, t, *J* = 7.3 Hz, $CH_3$).
**ESI-MS** in MeOH (negative): m/z 250 $[M-H]^-$, (positive): m/z 252 $[M+H]^+$
**UV-Vis** in EtOH, $\lambda_{max}$ nm (ε, $M^{-1}$ $cm^{-1}$): 217 (1.3373), 267 (0.9715), 292 (0.9140), 370 (1.4728).
**FT-IR** $cm^{-1}$ (selected bands): 3400 (w), 3310 (w), 1615 (s).

### 5.7.4 Complexation of (*E*)-2-((3-aminopyridin-2-yl)methylene)-*N*-buthylydrazine-1-carbothioamide (4)

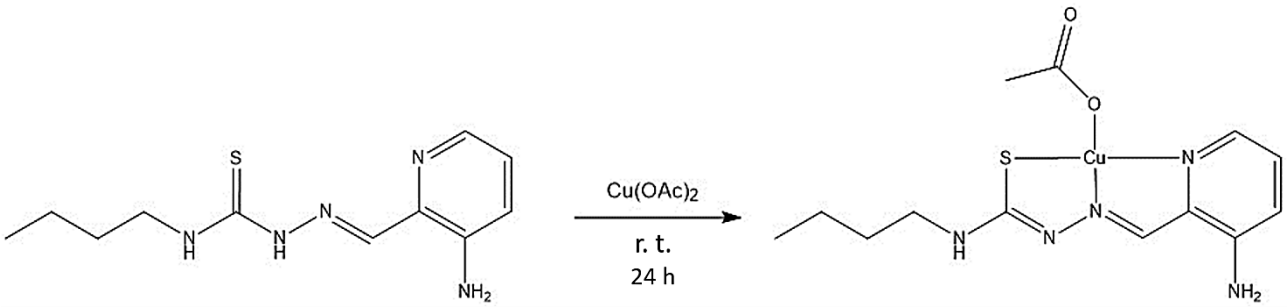


(*E*)-2-((3-aminopyridin-2-yl)methylene)-*N*-buthylydrazine-1-carbothioamide (**3**) (33 mg, 0.13 mmol) was dissolved in 6 mL of ethanol. The solution was slowly added to a solution of copper(II) acetate monohydrate (26 mg, 0.13 mol) in ethanol (6 mL) and the reaction immediately turns brown. The solution was stirred at room temperature for 24 hours. After solvent removal, the complex **4** was dried and isolated as dark green/brown solid in 88% yield.

**ESI-MS** in MeOH (positive): m/z 313 $[M-OAc]^+$
**UV-Vis** in EtOH, $\lambda_{max}$ nm (ε, $M^{-1}$ $cm^{-1}$): 221 (1.4836), 296 (1.2917), 446 (1.0602).
**FT-IR** $cm^{-1}$ (selected bands): 3350 (w), 1694 (m), 1602 (s).

### 5.7.5 Activation of NWs surface (5)

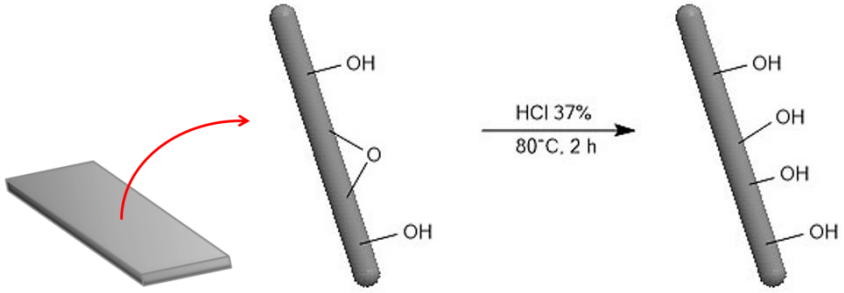


A platelet supporting $SiC/SiO_2$ nanowires was placed in a 25 mL round-bottom flask and covered with 8 mL of HCl 37 %. The system was heated to 80 °C for at least two hours.
On top of the refrigerant was placed a trap containing a solution of NaOH, to neutralize the HCl vapors. At terminated reaction the platelet was washed thoroughly with water and ethanol, making sure that the pH was returned to neutral.

### 5.7.6 Functionalization with triethoxy(3-isothiocyanatopropyl)silane (6)

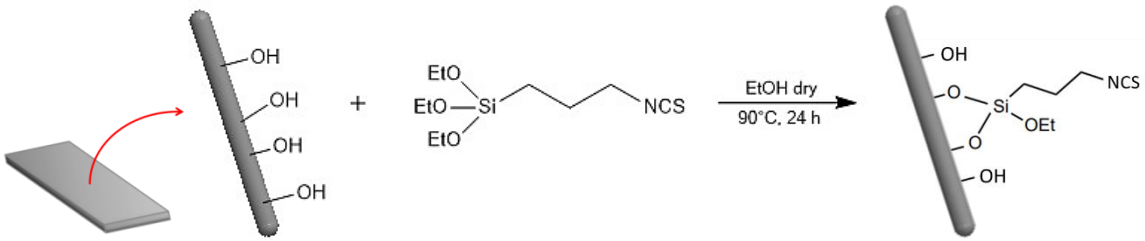


The activated platelet (**5**) was placed in a 25 mL two-neck round-bottom flask, after vacuum-nitrogen cycles to obtain an anhydrous environment. The platelet was covered with 8 mL of dry ethanol. 15 µL of triethoxy(3-isothiocyanatopropyl)silane (Si-NCS) was added to the round-bottom flask, under nitrogen flux. The reaction was stirred and heated at 90°C for 24 h. Once the solution has cooled, the platelet was washed with dry ethanol. This reaction is repeated twice, using new dry ethanol (8 mL) and fresh triethoxy(3-isothiocyanatopropyl)silane (15 µL).

### 5.7.7 Detachment of NWs from the silicon substrate

The platelet was placed in a falcon tube and covered with 20 mL of ethanol. The NWs were detached from the substrate using an ultrasound bath (59 MHz) for one hour. Then, the platelet was removed and the ethanol containing detached NWs was collected in several Eppendorf tubes and centrifuged for 15 minutes at 14.000 rpm. The precipitated NWs were united in one eppendorf and dried perfectly.

### 5.7.8 Synthesis of *tert*-butyl (E)-(2-((2-(butylcarbamothioyl)hydrazineylidene)methyl)pyridin-3-yl)carbamate ON NWs (7)

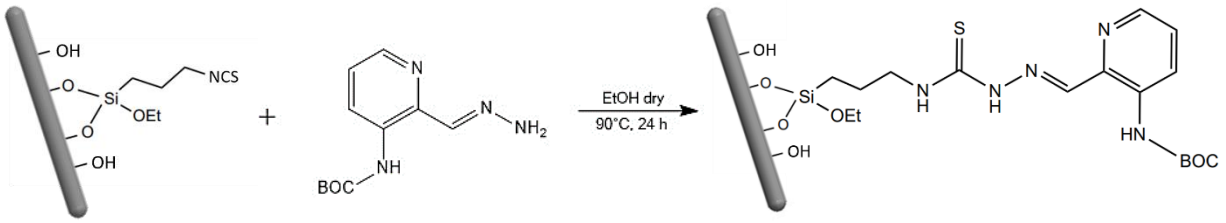


Detached functionalized NWs (**6**) were disperse in 3 mL of dry ethanol and introduced in a 25 mL round bottom flask, previously dried with vacuum-nitrogen cycles. Then 5 mL of dry ethanol was added.
*Tert*-butyl (2-formylpyridin-3-yl)carbamate (**2**) (25 mg, 0.11 mmol) was introduced and the reaction was heated at reflux for 24 hours. The functionalized NWs were centrifuged, washed several times with ethanol and collected in one Eppendorf tube.

### 5.7.9 Deprotection of *tert*-butyl (E)-(2-((2-(butylcarbamothioyl)hydrazineylidene)methyl) pyridin-3-yl)carbamate ON NWs (8)

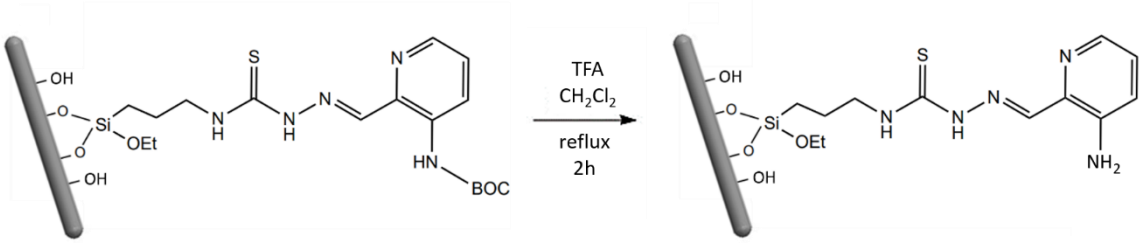


Detached functionalized NWs (**7**) were disperse in 5 mL of DCM in a 25 mL round bottom flask. 1.5 mL of trifluoroacetic acid (TFA) was added. The reaction was heated at 35 °C for 2 hours. Then the functionalized NWs were centrifuged, washed several times with DCM, ethanol and water and collected in one Eppendorf tube.

### 5.7.10 Complexation of (*E*)-2-((3-aminopyridin-2-yl)methylene)-*N*-buthylhydrazine-1-carbothioamide ON NWs (9)

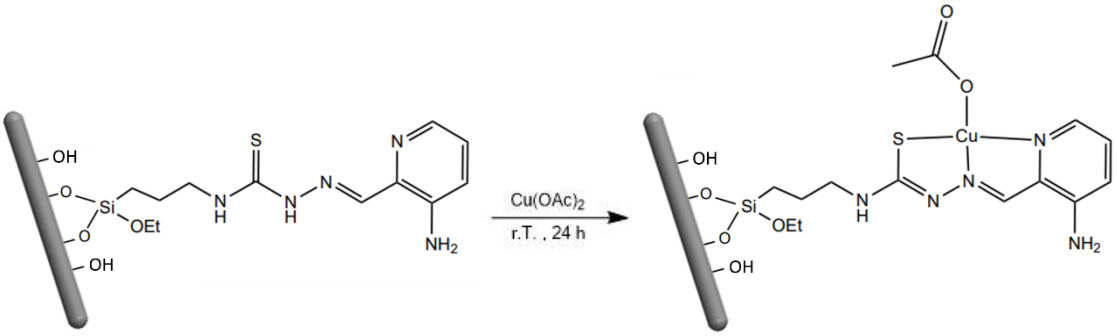


A $5 \cdot 10^{-3}$ M solution of copper(II) acetate in ethanol was prepared by dissolving 5 mg of copper(II) acetate monohydrate in 5 mL of ethanol.
Detached functionalized NWs (**9**) were disperse in 5 mL of ethanol and 87 µL of copper(II) solution was added. The suspension was slowly stirred at room temperature for 24 hours. Then the functionalized NWs were centrifuged, washed several times with ethanol and water and collected in one Eppendorf tube.

### 5.7.11 C-Triapine Loading

After the platelet activation with concentrated HCl, the anchored NWs were functionalized with the linker triethoxy(3-isothiocyanatopropyl)silane (Si-NCS).
NWs were detached from the substrate by sonication and functionalized with C-Triapine and then complexed with copper.
The NWs were collected in one Eppendorf tube and perfectly dried, obtaining a total weight of 1.42 mg.
Subsequently, NWs were dispersed by sonication in 100 µl of concentrated $H_2SO_4$ (97%) and brought to volume with 900 µl of distilled $H_2O$ to obtain a final solution 5% *v/v* of $H_2SO_4$ in water. The solution turned green.
After centrifugation, the green surnatant was collected into a 2 ml volumetric flask.
The NWs were washed two times with distilled $H_2O$ (500 µl per wash) and centrifuged each time.

The water of the two washes was added to the volumetric flask, obtaining a total volume of 2 ml. This operation was repeated for four times, until the surnatant lost its green color.

Following atomic absorption measurements, it was possible to determine the amount of copper present in the four flasks: (Table 5.4)

*Table 5.4: Copper concentration in each flask. Data obtained from atomic absorption measurements.*

| Flask | Cu concentration (mg/L) |
|---|---|
| 1 | 16.6 |
| 2 | 3.7 |
| 3 | 1.4 |
| 4 | 1.1 |

The total Cu concentration is 22.8 mg/L. Since each flask has a volume of 2 mL ($2 \cdot 10^{-3}$ L), the amount of Cu is $45.6 \cdot 10^{-3}$ mg.
Dividing the weight of Cu (II) found by the atomic weight of the copper the mmol of Cu (II): $0.718 \cdot 10^{-3}$ mmol were obtained.
Since there is a stoichiometric 1:1 ratio between copper and C-Triapine ligand, the number of copper moles corresponds to those of the C-Triapine.
The molecular weight of C-Triapine is 341.46 mg/mmol. Assuming that the ligand is anchored by two arms (as shown in Chapter 5.3), the amount of C-Triapine on NWs is: $0.718 \cdot 10^{-3}$ mmol x 341.46 mg/mmol = 0.245 mg.

Consequently, the weight percentage of C-Triapine covering the NWs surface is obtained by dividing the mg obtained by the weight of the sample: (0.245 mg / 1.42 mg) · 100 = 17 % w/w.

## References


1 A. C. Sartorelli, K. C. Agrawal, A. S. Tsiftsoglou and E. C. Moore, *Adv. Enzyme Regul.*, 1977, **15**, 117–139.

2 A. I. Matesanz and P. Souza, *Mini Rev. Med. Chem.*, 2009, **9**, 1389–1396.

3 J. Murren, M. Modiano, C. Clairmont, P. Lambert, N. Savaraj, T. Doyle and M. Sznol, *Clin. Cancer Res.*, 2003, **9**, 4092–4100.

4 R. A. Finch, M.-C. Liu, S. P. Grill, W. C. Rose, R. Loomis, K. M. Vasquez, Y.-C. Cheng and A. C. Sartorelli, *Biochem. Pharmacol.*, 2000, **59**, 983–991.

5 R. A. Finch, M.-C. Liu, A. H. Cory, J. G. Cory and A. C. Sartorelli, *Adv. Enzyme Regul.*, 1999, **39**, 3–12.

6 A. B. Miah, K. J. Harrington and C. M. Nutting, *European J. Clin. Med. Oncol.*, 2010, **2**, 1–6.

7 E. S. Ratner, Y. L. Zhu, P. G. Penketh, J. Berenblum, M. E. Whicker, P. H. Huang, Y. Lee, K. Ishiguro, R. Zhu, A. C. Sartorelli and Z. P. Lin, *Br. J. Cancer*, 2016, **114**, 777–786.

8 P. Heffeter, C. Pirker, C. R. Kowol, G. Herrman, R. Dornetshuber, W. Miklos, U. Jungwirth, G. Koellensperger, B. K. Keppler and W. Berger, *Biochem. Pharmacol.*, 2012, **83**, 1623–1633.

9 C. R. Kowol, R. Trondl, P. Heffeter, V. B. Arion, M. A. Jakupec, A. Roller, M. Galanski, W. Berger and B. K. Keppler, *J. Med. Chem.*, 2009, **52**, 5032–5043.

10 É. A. Enyedy, M. F. Primik, C. R. Kowol, V. B. Arion, T. Kiss and B. K. Keppler, *Dalt. Trans.*, 2011, **40**, 5895–5905.

11 C. R. Kowol, W. Miklos, S. Pfaff, S. Hager, S. Kallus, K. Pelivan, M. Kubanik, É. A. Enyedy, W. Berger, P. Heffeter and B. K. Keppler, *J. Med. Chem.*, 2016, **59**, 6739–6752.

12 R. Trondl, L. S. Flocke, C. R. Kowol, P. Heffeter, U. Jungwirth, G. E. Mair, R. Steinborn, E. A. Enyedy, M. A. Jakupec, W. Berger and B. K. Keppler, *Mol. Pharmacol.*, 2014, **85**, 451–459.

13 C. R. Kowol, P. Heffeter, W. Miklos, L. Gille, R. Trondl, L. Cappellacci, W. Berger and B. K. Keppler, *J. Biol. Inorg. Chem.*, 2012, **17**, 409–423.

14 C. Niu, J. Li, T. W. Doyle and S.-H. Chen, *Tetrahedron*, 1998, **54**, 6311–6318.

15 J. Li, L. M. Zheng, I. King, T. W. Doyle and S. H. Chen, *Curr. Med. Chem.*, 2001, **8**, 121–133.

16 M.-C. Liu, T.-S. Lin, A. C. Sartorelli and A. C. Potential Antitumor, *J. Med. Chem*, 1992, **35**, 20-27.

17 P. Singh, J. Jain, R. Sinha, A. Samad, R. Kumar and M. Malhotra, *Cent. Nerv. Syst. Agents Med. Chem.*, 2011, **11**, 60–65.

18 D. L. Klayman, J. F. Bartosevich, T. S. Griffin, C. J. Mason and J. P. Scovill, *J. Med. Chem.*, 1979, **22**, 855–862.

19 J. Eilstein, E. Giménez-Arnau, D. Duché, F. Rousset and J. P. Lepoittevin, *Chem. Res. Toxicol.*, 2006, **19**, 1248–1256.

20 É. A. Enyedy, N. V. Nagy, É. Zsigó, C. R. Kowol, V. B. Arion, B. K. Keppler and T. Kiss, *Eur. J. Inorg. Chem.*, 2010, 1717–1728.

21 A. Popović-Bijelić, C. R. Kowol, M. E. S. Lind, J. Luo, F. Himo, É. A. Enyedy, V. B. Arion and A. Gräslund, *J. Inorg. Biochem.*, 2011, **105**, 1422–1431.

22 B. T. Mayers, K. Liu, D. Sunderland and Y. Xia, *Chem. Mater.*, 2003, **15**, 3852–3558.

23 Y. Xia, B. Gates, B. Mayers and A. Grossman, *Adv. Mater.*, 2002, **14**, 1749–1752.

24 M. Moghaddari, F. Yousefi, M. Ghaedi and K. Dashtian, *Ultrason. Sonochem.*, 2018, **42**, 422–433.

25 Y. L. Zhong and S. L. Bernasek, *J. Am. Chem. Soc*, 2011, **133**, 8118–8121.

26 B. K. Sodipo and A. A. Aziz, *Beilstein J. Nanotechnol.*, 2014, **5**, 1472–1476.

27 C. Loffi, Synthesis of novel hybrid nanosystems composed by core-shell SiC/SiOx nanowires conjugated with porphyrins for X-ray-excited PDT, Università degli Studi di Parma, 2017.

28 S. Wesbuer, C. Lanvers-Kaminsky, I. Duran-Seuberth, T. Bölling, K.-L. Schäfer, Y. Braun, N. Willich and B. Greve, *Radiat. Oncol.*, 2010, **5**, 1–8.

29 B. M. Zeglis, V. Divilov and J. S. Lewis, *J. Med. Chem.*, 2011, **54**, 2391–2398.

# 6. The cardiology project: the epicardial interacting patch of SiC NWs

## 6.1 The human heart and its functioning

### 6.1.1 Anatomy of the human heart

The heart is the most important organ in the circulatory system and his task is to pump blood throughout the body. The human heart is approximately as big as a fist, its weight is about 250-300 g and usually beats from 60 to 100 times per minute. [1]

The heart is located in the chest between the lungs, behind the sternum, and above the diaphragm. The esophagus and the spine lie are behind the heart. Located above the heart are the great vessels: the superior and inferior vena cava, the pulmonary artery and the pulmonary veins, and the aorta. The aortic arch lies behind the heart. (Figure 6.1 a)

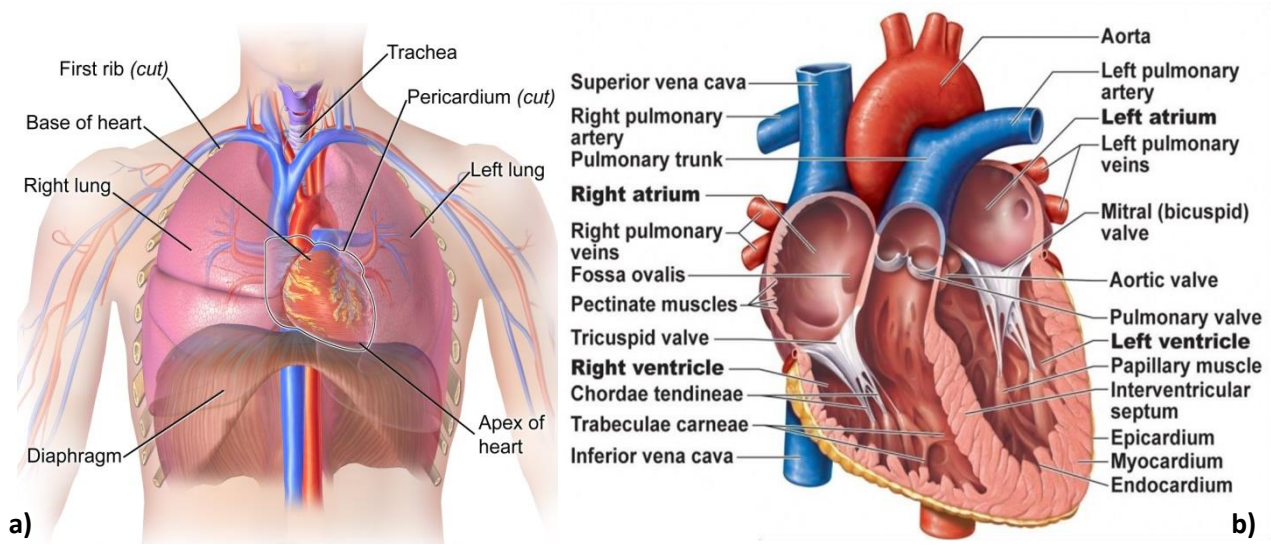


*Figure 6.1: a) Location of the heart in the thorax. b) The anatomy of the heart: atria, ventricles, valves, blood vessels and tissues.*[1]

The heart is divided in four chambers: the right atria, left atria, right ventricle and left ventricle.
The upper part of the heart is made up of the two atria, divided by a wall called the interatrial septum.
The lower part is formed by the two ventricles, divided by the interventricular septum.
Atria and ventricles are separated by two atrioventricular valves: the tricuspid valve separates the right atrium from the right ventricle, and the mitral valve separates the left atrium from the left ventricle.

In the heart there are two other important valves which connect the ventricles and the main blood vessels. The pulmonary valve lies between the right ventricle and the pulmonary artery (which leads to the lungs), and the aortic valve lies in the outflow tract of the left ventricle.
Blood vessels are divided into two species: arteries and veins. Arteries carry blood away from the heart, while veins carry blood back to the heart.

The right side of the heart (right atrium and right ventricle) receives deoxygenated blood and sends it to the pulmonary circuit, while the left side (left atrium and left ventricle) receives oxygenated blood and sends it to the systemic circuit.
The blood returns from the systemic circulation to the right atrium and from there goes through the tricuspid valve to the right ventricle. It is ejected from the right ventricle through the pulmonary valve to the lungs. Oxygenated blood returns from the lungs to the left atrium, and from there through the mitral valve to the left ventricle. Finally, blood is pumped through the aortic valve to the aorta and the systemic circulation. Two coronary arteries branch off at the beginning of the aorta and divide into a network of smaller arteries that provide oxygen and nourishment to the muscles of the heart. (Figure 6.1b)

The heart wall is composed of three layers of tissues.

1. The endocardium is the deepest tissue, made of a single layer of mesothelial cells, and delimits all the cavity of the heart.
2. The myocardium is the middle layer. It is made up of two types of tissue: smooth muscle tissue and connective tissue (in scarce quantities).
3. The pericardium is the most external tissue and adheres to the myocardium surrounding the heart. This structure, about 20 μm thick, consists of two distinct layers: the fibrous pericardium and the serous pericardium. The fibrous pericardium is the outer layer, made up of dense connective tissue; the serous pericardium is the inner layer formed by a parietal leaflet which adheres to the inner surface of the fibrous pericardium and a visceral leaflet which is applied to the myocardium. The upper part of the pericardium takes the name of epicardium.

These three layers have different thicknesses. In particular, the thickness of the myocardium is different in relation to the contractile force that each cavity has to exert for the thrust of the blood. The wall of the atrium is thin, while that of the ventricles is thicker. The left ventricular wall is three times thicker than the right ventricle, since it has to push the blood in aorta and in the large circulation.

As mentioned previously, the heart is the pump of the circulatory system and a pump needs electricity to work. The heart is able to create its own electrical impulses and control the route of these impulses via specialized conduction pathway. In detail, the heart conduction system is made up of:

1. The sino-atrial (SA) node
2. The atrio-ventricular (AV) node
3. The bundle of His
4. The left and right bundle branches
5. The Purkinje fibers

The human SA node, located in the posterior right atrium near the superior vena cava, is about 15 mm long and 5 mm wide. The SA nodal is made up of specialized muscle cells, called pacemaker cells. These cells are self-excitatory and they release electrical stimuli at a regular rate, by the needs of the body. Each stimulus passes through the myocardial cells of the atria creating a wave of contraction which spreads rapidly through both atria. (Figure 6.2, 1)

From the SA node, the activation propagates throughout the atria, but cannot propagate directly across the boundary between atria and ventricles, because they are electrically insulated. Indeed, the AV node, located near the tricuspid valve, is required to allow the conducting pulse to spread from the atria to the ventricles.

The electrical stimulus from the SA node reaches the AV node (Figure 6.2, 2) with a slight delay so that the contracting atria have enough time to pump all the blood into the ventricles.
Once the atria are empty of blood the valves between the atria and ventricles close. At this point the atria begin to refill and the electrical stimulus passes through the AV node and Bundle of His. (Figure 6.2, 3)
The Bundle of His descends into the interventricular septum and splits into two bundle branches propagating along each side of the septum, constituting the right and left bundle branches. (Figure 6.2, 4)
The bundles ramify into Purkinje fibers that diverge to the inner sides of the ventricular walls, in this way all the cells in the ventricles receive the electrical stimulus causing them to contract. (Figure 6.2, 5)

As the ventricles contract, the right ventricle pumps blood to the lungs where carbon dioxide is released, and oxygen is absorbed whilst the left ventricle pumps blood into the aorta from where it passes into the coronary and arterial circulation.
At this point the ventricles are empty, the atria are full and the valves between them are closed. The SA node is about to release another electrical stimulus and the process is repeated. Every time the SA and AV nodes release a stimulus they must recharge before they can do it again: the SA node recharges whilst the atria are refilling, and the AV node recharges when the ventricles are refilling. In this way there is no need for a pause in heart function. Again, this process takes less than one third of a second.

The term used for the release (discharge) of an electrical stimulus is depolarization, and the term for recharging is repolarization.

Therefore, the stages of a single heart beat are: atrial depolarization, ventricular depolarization, atrial and ventricular repolarization.

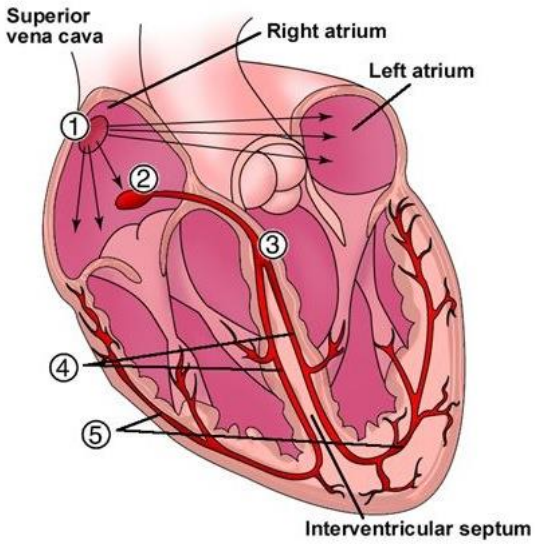


*Figure 6.2: Schematic representation of the heart conducting system 1) Sino-atrial node (SA node) 2) Atrio-ventricular node (AV node) 3) Bundle of His 4) Right and left bundle branches and 5) Terminal ramification with Purkinje fibers. Credits: Pinterest.com.*

### 6.1.2 Histology of the human heart and Cardiac Action Potential

Cardiac muscle, like skeletal muscle, appears striated due to the organization of muscle tissue into sarcomeres, the contractile basic units of muscle tissue.
Each sarcomere is composed of long fibrous proteins; in particular myosin, which forms a thick, flexible filament, and actin, which forms the thin, more rigid filament. Myosin and actin form together myofibrils.
Myosin has a long fibrous tail and a globular head which can bind to actin and also to ATP, the source of energy for muscle movement.
The mechanism of muscle contraction is based on the sliding of actin fibers on myosin, causing macroscopically the shortening of the muscle. When ATP binds to myosin, myosin is separated from the actin and can flow along the filament, causing a shortening of muscle fibers. In this way the contraction occurs. This is an extremely simplified description of the functioning of the cardiac contraction. In fact, this mechanism is a complex process regulated by calcium influx and several electrical stimuli.

Cardiac muscles are composed of tubular cardiomyocytes, also called cardiac muscle cells. The cardiomyocytes are composed of tubular myofibrils, which are the repeating units of sarcomeres.

Cardiomyocytes are cells approximately rod-shape, with an average length of 100 µm and 15-20 µm diameter. Cardiomyocytes are linked each other in a 3D cellular network. The contact areas are called intercalated disks and anatomically delimit each cardiomyocyte.
The union between the cells is both mechanical and electric. The mechanical union is guaranteed by the extroflexions of a first fiber that fit together in complementary extroflexions in the second fiber. Instead, the electrical connection is guaranteed by gap junctions, which allow the passage of ions. Being electrically connected by gap junctions, when a cell generates an impulse it propagates to the whole myocardium. (Figure 6.3 a)

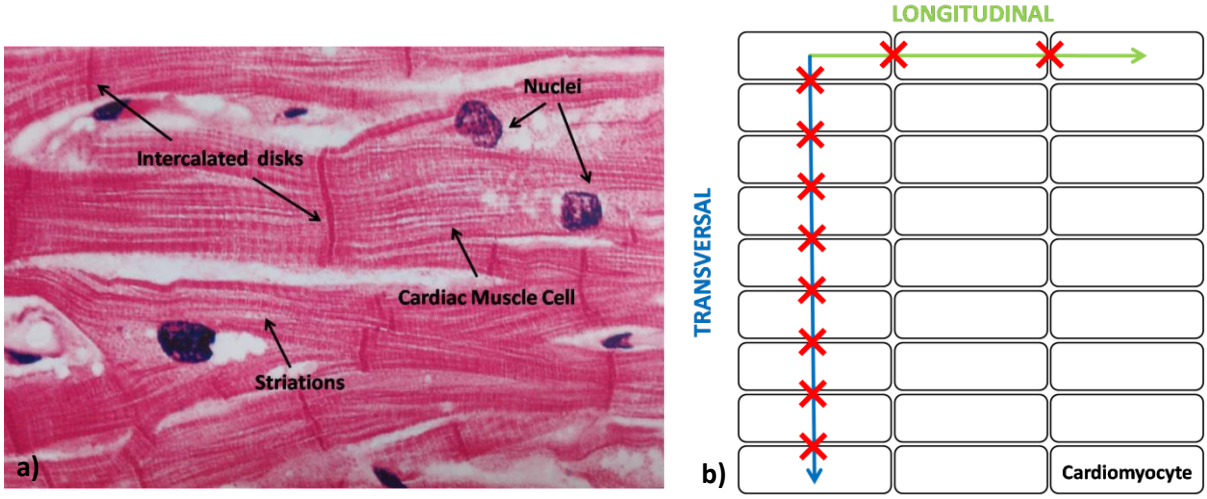


*Figure 6.3: a) Cardiomyocytes in human heart. In evidence: nuclei, striations and intercalated disks. Credits: Pinterest.co.ukb) Schematic representation of cardiomyocytes. At equal distance, the electrical propagation impulse encounters many more barriers (red crosses) in a transversal direction (blue arrow) with respect to the longitudinal direction (green arrow).*

The propagation of the electrical impulse through the cells is not random, in fact the shape of cardiomyocytes and their orientation create tissue anisotropy inside the heart.

Figure 6.3 b shows how the distribution of gap junctions and intercalated disks influence the electrical conduction. Longitudinally (green arrow) the resistance caused by these barriers (red crosses) is much lower than the transverse direction (blue arrow). Therefore, the electrical impulse propagates much faster longitudinally, thus the propagation is anisotropic.

The activation process of myocardium is called action potential (AP), and it is followed by the muscle contraction. The AP propagates in all directions through the heart cells, whose excitability depends on the balance of different ionic currents.[2]
Therefore, the AP is the result of the activated and inactivated cells due to movement of ions, which generate a current. Ions migrate passing through channels, placed inside the cell membrane, called ion channels.

Cell membranes are biological hydrophobic barriers made up of lipidic bilayers that separate the cytoplasm of the cell from the extracellular environment. The main function is to protect the cell from its surroundings. The cell membrane controls the movement of different substances in and out of cells thanks to different gates, such as membrane proteins of which ion channels belong.
Ion channels are hydrophilic pathway across the hydrophobic membrane that can be open or closed.
When the channel is open the ions can migrate through the membrane, when the channel is closed the current of ions is interrupted.
The switch from the active form (open channels) to the deactivated form (closed channels) and vice versa depends on various factors. In particular for channels called voltage-dependent the switch is determined by a change of membrane potential, while for channels called chemo-dependent the switch is due by the action of certain substances combining with specific active site of proteins constituting the channel.

In human heart, the most important ions channels are voltage-dependent and the AP is strongly influenced by $Na^+$, $Ca^{2+}$ and $K^+$ ions.

The AP in cardiomyocytes is made up of five phases, beginning and ending with Phase 4: (Figure 6.4)

1. Phase 4 (resting diastolic phase)
2. Phase 0 (depolarization)
3. Phase 1 (early repolarization)
4. Phase 2 (plateau)
5. Phase 3 (late repolarization)

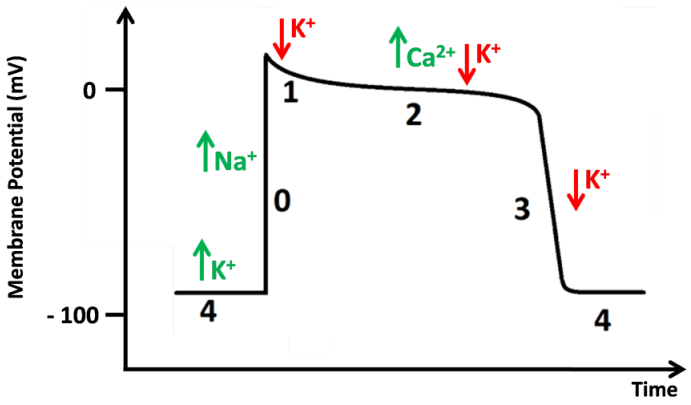


*Figure 6.4: The five phases of cardiac action potential: Phase 4, Phase 0, Phase 1, Phase 2, Phase 3. The green arrows indicate the ionic current entering the cell in a specific phase, the red arrows the ionic current coming out of the cell.*

1. Phase 4: The resting diastolic phase

Phase 4 is the resting potential in cardiomyocyte and the cell is not electrically excited. The cell remains in this situation until it is activated by an external electrical stimulus, which normally comes from an adjacent cardiac cell. This phase of action potential is associated with the diastole of the heart chamber. Diastole is the period of relaxation of the heart muscle after contraction (systole).

At the resting potential, the conductance for potassium ions is high in relation to the conductance for sodium and calcium ions. This means that during this phase the cell membrane is permeable to $K^+$, which can migrate across the ions channels. Vice versa, the sodium and calcium channels are closed.
Therefore, the resting membrane potential is mainly determined by $K^+$ equilibrium potential. The main ions found outside the cell are $Na^+$ and $Cl^-$, whereas inside the cell $K^+$.
The resting potential in a cardiomyocyte at rest is −90 mV, therefore the inside of the cell membrane is more negative than the outside.
When the membrane potential goes from -90 mV to -70 mV (due, for example, to the stimulus of an adjacent cell) Phase 0 starts.

2. Phase 0: Depolarization

Phase 0 is the depolarization phase, in which the voltage changes in positive. This process is due to the opening of the sodium channels, which generates a rapid entry of $Na^+$ ions inside the cell. At the same time, the concentration of $K^+$ decreases. In cardiomyocyte, the $Na^+$ channels are activated when a stimulus arrives from a nearby cell, through gap junctions. The voltage inside the cell increases slightly and at -70 mV (threshold potential) sodium channels are activated.
It generates an incoming current of $Na^+$ higher than the outgoing current of $K^+$ and these exchange of ions modify the membrane potential, moving away from the equilibrium potential of potassium (-90 mV) and approaching the equilibrium potential of sodium (+52 mV).
After reaching the peak, the $Na^+$ current starts to decline and the sodium channels are inactivated.

3. Phase 1: Early repolarization

Phase 1 is characterized by a slight decrease in the membrane potential. This behavior is caused by the closing of the sodium channels which block the flow of $Na^+$ ions and by the short opening of the potassium channels which allow the $K^+$ ions to migrate outside the cell. The opening and closing so immediate of the potassium channels make the membrane potential just a little more negative than in the previous phase.

4. Phase 2: Plateau

This phase is called the Plateau Phase because the membrane potential remains almost constant at 0-20 mV. This behavior is due to the formation of anionic equilibrium between the incoming and the outgoing currents, in fact the total charge of ions moving into and out of the cell is balanced.

During this phase, other potassium channels (called delayed rectifier channels) are open and allow $K^+$ ions to leave the cell. During Phase 0, the sodium current activated calcium channels and during this phase $Ca^{2+}$ ions start to enter inside the cells. Calcium is very important for the proper functioning of the heart, in fact it is responsible for the cardiac contraction.

Inside the cells, calcium activates chloride channels, which allow $Cl^-$ to migrate into the cells.
The membrane potential remains relatively constant because the voltage change caused by the output of $K^+$ ions is balanced by the entry of $Ca^{2+}$ and $Cl^-$.

The Plateau Phase is the phase of the AP that lasts longer (about 200 ms).

5. Phase 3: Late repolarization

During Phase 3 the calcium channels are closed, while the delayed rectifier potassium channels remain open. This situation causes a strong outward ions current, which drastically reduces the membrane potential to negative values. The lowering of the membrane potential involves the opening of new fast-exchange potassium channels.

For the cell, this outward $K^+$ current corresponds to the loss of positive charges and causes the cellular repolarization. The potassium delayed rectifier channels are closed when the membrane potential reaches the value of about -80 mV, while fast-exchange potassium channels remain working during Phase 4, helping to maintain the resting membrane potential.

### 6.1.3 Electrocardiogram (ECG)

The electrocardiogram (ECG) is a recording of the electrical impulses, generated by the activity of the cardiomyocytes.

As mentioned before, the cardiac cells produce an action potential which spread through the heart. These impulses can be detected by ECG machine through electrodes placed in contact with the skin of the thorax. Therefore, the ECG is the graphic record of the direction and magnitude of the depolarization and repolarization of atria and ventricles.[3]
The machine detects and amplifies the electrical activity that occurs at each heartbeat: single electrical impulse takes the form of a wave and the recorded ECG is composed of a succession of connected waves, interspersed with linear segments.
The combination of waves and segments gives rise to intervals. (Figure 6.5)

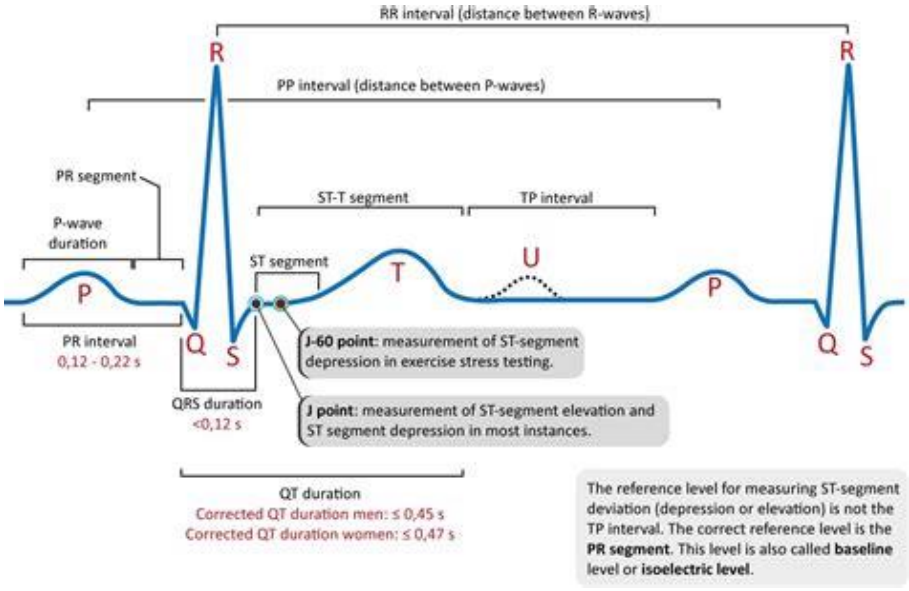


*Figure 6.5: Human electrocardiogram (ECG). Waves, segments and intervals are highlighted.*

ECG starts with P wave. The P wave is a small, positive, smooth wave caused by the depolarization of the atria (activation of atria in yellow in Figure 6.6 a below). During this phase the depolarization spreads from the SA node towards the AV node and from the right atrium to the left atrium. Usually in humans the P wave has a duration of about 120 ms.

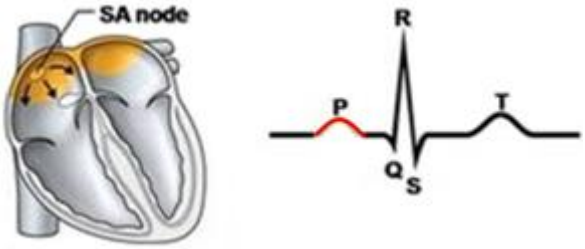


*Figure 6.6 a: Atria depolarization and corresponding P wave in ECG.*

Afterwards you meet the PR segment or PQ segment, which connects the end of P wave and QRS complex. PR segment serves as baseline for measuring the amplitudes of all ECG waves. The PR interval starts from the onset of the P wave and ends with the QRS complex. PR interval represents the time between the beginning of atria depolarization and the beginning of ventricular polarization. This segment lasts on average from 120 ms to 220 ms.


*Figure 6.6 b: Atria depolarization (in yellow) and beginning of ventricular polarization. The electrical impulse passes through the AV node. On the right, the corresponding PR segment and PR interval in ECG.*

The QRS complex reflects the ventricles depolarization (activation of ventricles in yellow) and consists of the sum of three waves: small negative Q wave, tight positive R wave and small negative S wave. The QRS duration is short (less than 120 ms) as in a healthy individual the depolarization of the ventricles occurs very rapidly. In fact, a wide QRS complex can mean serious dysfunctions or problems in the cardiac system. The QRS complex amplitude is higher than the P wave amplitude because the ventricles have a larger muscle mass in comparison to the atria (involved for the P wave and in this phase totally repolarized, red area).

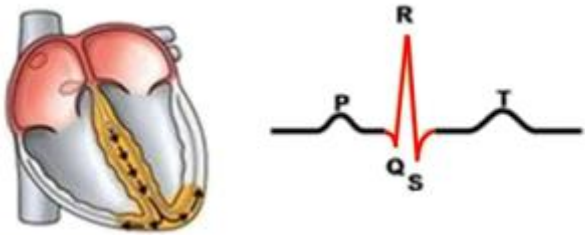


*Figure 6.6 c: Ventricular depolarization in yellow and atria repolarization in red. The corresponding ECG signal is the QRS complex.*

The QRS complex is followed by the ST segment that starts at the end of QRS complex and ends at the onset of the T wave. The ST segment corresponds the Plateau Phase of the action potential and lasts 5-150 ms. During this phase all the ventricular cardiomyocytes are depolarized.

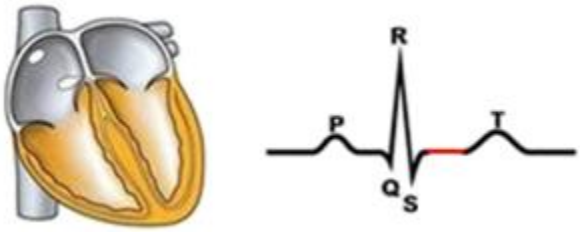


*Figure 6.6 d: Total depolarization of the ventricles in yellow and corresponding ST segment in ECG.*

The T wave is an asymmetric wave with a slow upstroke and a rapid down stroke and represents the ventricular repolarization. The first part of the T wave is due to the decline of the action potential plateau, while the maximum peak represents the total repolarization of the cardiomyocytes.

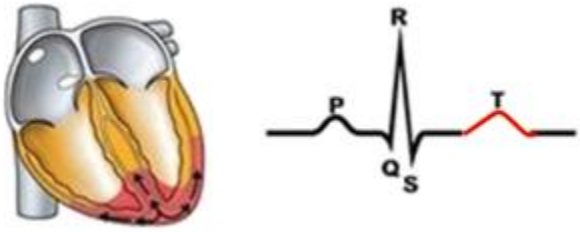


*Figure 6.6 e: The ventricular repolarization begins at the apex of the heart (red area). The T wave is the corresponding signal in ECG.*

The QT duration is measured from the beginning of QRS complex to the end of T wave and reflects the total duration of depolarization and repolarization of ventricles. The QT duration is inversely related to the heart rate: the faster the heart beats, the more the QT segment will be short and vice versa.

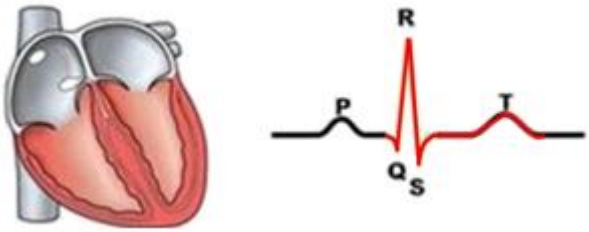


*Figure 6.6 f: Total repolarization of ventricles in red and corresponding QT duration in ECG.*

U wave is the last wave, represented by a dashed line (Figure 6.5) as it is not always visible in the ECG due to its small size. U waves are the result of the repolarization of the Purkinje fibers.

PP interval and RR interval provide us useful information on heart rate. The heart rate is the number of heart contractions over a specific period of time, usually beats per minute (bpm). The PP interval is measured from the onset of the first P wave and the onset of the second P wave. Since the P wave is due to the depolarization of the atria, the PP interval represents atria rate. RR interval is the distance between two consecutive R waves and it is used to calculate the ventricular rate.

In sinus rhythm, the normal rhythm of the heart where electrical stimuli are initiated in the SA node, then conducted through the AV node, bundle of His, bundle branches and Purkinje fibers, the PP interval and RR interval have the same duration.

Electrocardiography is commonly used in veterinary practices to record the heartbeats of several types of animals. For small animals, like rats, the ECG interpretation can be difficult because some parameters, such as certain waves or segments, are very small and the average values deviate a lot from the human ECG.

In particular in rat ECG the Q wave is very small and the QRS complex is basically formed only by R and S waves. In rat ECG the ST segment is absent, and the T wave tends to overlap the S wave. For this reason, the QT duration is very short compared to human QT. Another aspect to consider is the drastic reduction of the PR segment, used in the human ECG as a baseline for the other waves. On average, in the rat the PP interval measures a few hundred ms, while in humans it varies from 600 ms to about 1 s.[4] (Figure 6.7)

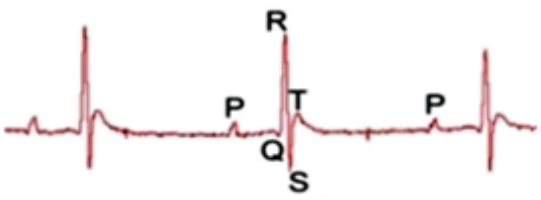


*Figure 6.7: Example of rat ECG.*

## 6.2 Cardiac irregularities and Infarction

As stated previously, the ECG is a very effective tool to verify the correct functioning of the heart. Any problems or cardiac irregularities are immediately visible to an expert eye.
Among the main disorders, arrhythmias are the most common.

Arrhythmia is a clinical condition in which the rhythm, the frequency of the heartbeat and the electrical stimulus propagation are altered from the normal standard condition. The most common symptoms in the case of arrhythmia are palpitations, irregular heartbeat, dizziness, chest pain and dyspnea (lack or irregular breathing).[5]

Arrhythmias may be classified as:

- Extrasystole: the electrical stimulus does not originate from the SA node in the atria, but from different areas.

- Tachycardia: a severe acceleration of the heart rhythm with frequencies at 150-250 bpm (normally at rest a healthy heart beats at about 60-70 bpm). Tachycardia may be supra-ventricular or ventricular, depending on the area of the heart in which they are formed.

- Fibrillations: extreme form of tachycardia in which the heart muscle loses its ability to contract. The fibrillation can be atrial or ventricular: the ventricular arrhythmia is the most dangerous between these two disorders and causes an immediate cardiac arrest.

- Bradycardia: arrhythmia that causes a slow heartbeat, less than 50 bpm. The most common bradycardias are the dysfunction of the SA node, the slowing down or blocking of the electrical impulse of the AV node or the slowing down or blocking of the bundle branches.

Therefore, the most common cause of cardiac disorders is an erroneous propagation of the electrical impulse. Generally, the cardiac stimulus is slowed down or blocked during its normal cycle and the main obstacles it encounters may be an anatomical interruption (e.g. a cellular damage to a certain area of the heart) or a refractoriness of the cardiomyocytes to respond to impulses (prolonged refractoriness). Refractoriness is a short-term decrease in the excitability of muscle tissue occurring immediately after the manifestation of action potential.

Figure 6.8 a shows the map of the world highlighting the diseases that caused most of the deaths, while figure 6.8 b is related to European nations.
As can be seen, the pink area, which represents death from heart disease, is the most prevalent. For instance, among cardiovascular diseases heart attack is one of the leading causes of death in many countries in the world and in Europe.

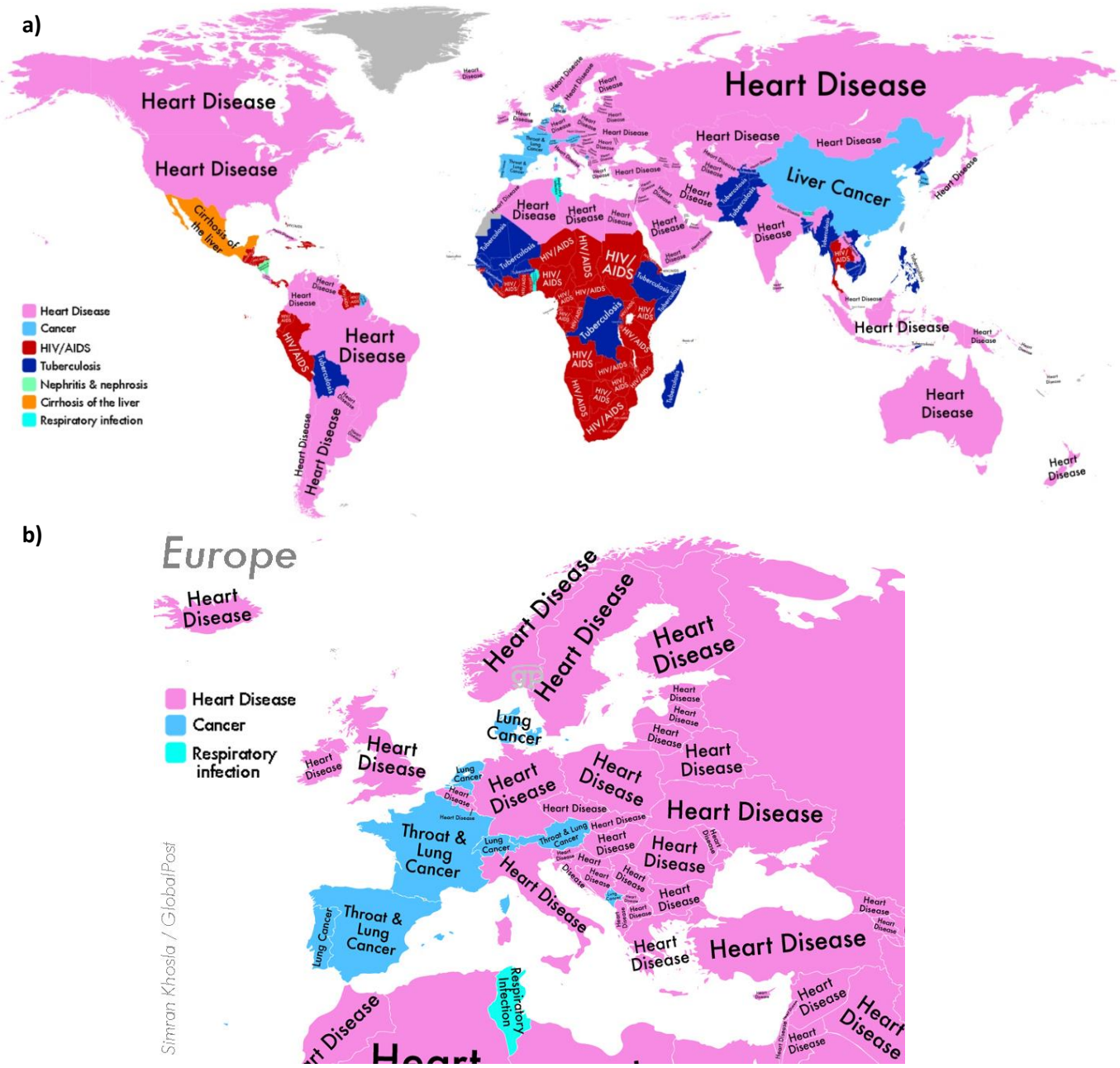


*Figure 6.8: a) World map indicating the disease that caused the most deaths within the nation. b) Map of European countries. Credit: Simran Khosla/GlobalPost, courtesy PRI®* [6]

Infarction is the death (necrosis) of the heart muscle tissue (myocardium) due to the lack of adequate oxygenation by the arterial blood flow (ischemia). At its origin there is the partial or total occlusion of the coronary arteries due to an accumulation of lipid material (atherosclerotic plaques), which hinders the normal flow of blood.
Another possible cause is the formation of blood clots, due to the detachment of a part of the plaque present in a blood vessel, which obstructs the artery.

The severity of the infarction depends on both its location in the heart and the extent of the damage.
If the coronary obstruction is not rapidly treated and normal blood flow restored, the heart muscle begins to die and is replaced by scar tissue.

Generally, almost all infarctions affect the left ventricle and may be classified into two classes:

- Transmural myocardial infarction: the ischemic necrosis affects the entire thickness of the ventricular wall.
- Subendocardial infarction: the ischemic necrosis affects the innermost layers of the ventricular wall.

After the infarction, the affected area is no longer able to contract.
The damaged cardiomyocytes died, and the organism removes these dead tissues without regenerating new cardiac cells, forming in that area a scar of fibrous connective tissue (composed of collagen fibers).
Fibrous connective tissue is a rigid functionless tissue. Therefore, the heart definitely loses part of its functionality and serious complications from a point of view of the cardiac impulse propagation arise.

The main problem encountered after an infarction is arrhythmia induction: with the damaged cardiac tissue new incorrect pathways develop, through which the cardiac pulse can propagate faster than the standard conditions.
Another possibility is that the fibrous connective tissue excessively slows down the electrical wave propagation or even block it. Moreover, myofibroblasts can depolarized cardiomyocytes creating a source for arrhythmogenesis.
Other disorders may be heart failure (the healthy part of the muscle cannot pump enough blood to the heart and the rest of the body), damage to the valves and tearing of the cardiac tissues (fatal).

The ECG is a tool that allows to evaluate the normal functioning of the heart and its possible dysfunctions.
In the case of infarction, the death of cardiomyocytes irreversibly damages a certain area of the heart and the myocardium tissue loses the capacity of depolarization and repolarization, therefore becomes electrically silent.
The alteration of normal cardiac propagation generates ECG signals that deviate from those of a healthy individual. In particular, the most marked changes are the elevation of the ST segment, the change of the T wave shape and the prolongation and amplitude increase of the Q wave.
The ST segment represents the time between the depolarization of the ventricles and their repolarization.
The elevation of the ST segment is caused by the lesion wave in a transmural infarction (STEMI, ST segment elevation myocardial infarction, Figure 6.9).
The T wave changes its shape because in the case of ischemia the repolarization of the myocardium is altered and occurs in a different way compared to the normal situation.
The altered Q wave is a wave that confirms myocardial necrosis.

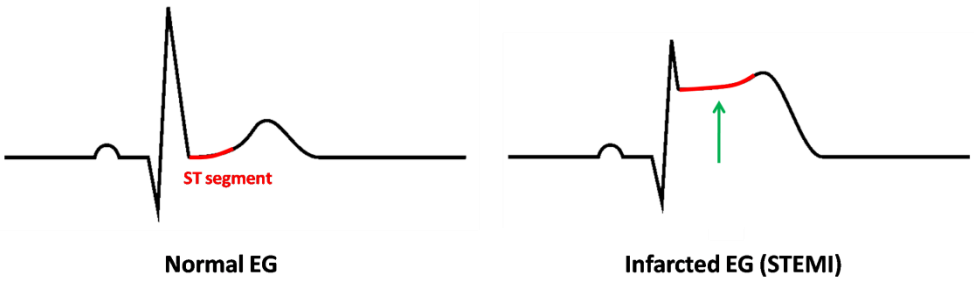


*Figure 6.9: Schematic representation of normal ECG with ST segment in red and STEMI ECG with elevation of ST segment (green arrow).*

## 6.3 SiC NWs: *In vitro* experiment

As mentioned in the previous paragraph, after an infarction the heart tissue is deeply damaged and the cardiomyocytes involved lose the ability to propagate the electrical impulse. Therefore, one could imagine this situation as the presence of isolated cardiac cells, no longer able to interact.

In a previous *in vitro* experiment[7], this situation of isolation was simulated by positioning two HL-1 cells (cardiac muscle cell line: cardiomyocytes) very distant from each other. In this way they were not able to interact and propagate any type of physiological impulse.
In order to connect these two isolated cells again, a bridge SiC NW was positioned. (Figure 6.10)
What was observed was the creation of electrical synchronism between the two cells.

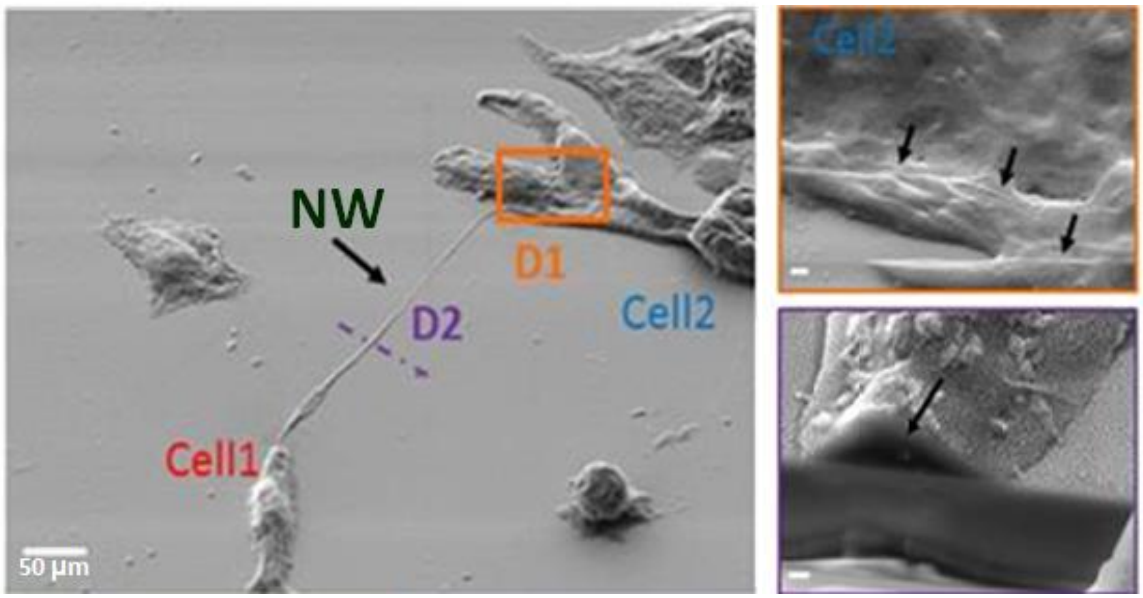


*Figure 6.10: SEM images of SiC NWs that connects two cardiomyocytes. Orange framed picture: SEM zoom image of the orange rectangular area showing that the SiC NWs are coated by cell membrane (black arrows). Purple framed picture: focused ion beam microscopy shows the sagittal section of SiC NWs. The cut was made along the purple dotted line D2.*

In this experiment, 300 µg of SiC NWs were suspended in 100 µL of a solution containing 0.5 µg of collagen (Human Placenta IV). This suspension was deposited in 22 mm coverslips with a central area of 4 mm. Over it, $1.5x10^3$ $mm^2$ of HL-1 cells were seeded. After 48 hours the cells were stained with a voltage-sensitive dye (Di-8-ANEPPS) and the electrical pulse propagation was measured (with temporal resolution 2 KHz, at 36 °C)

It was observed that the separated cells, thanks to the presence of SiC NWs, were able to propagate the electrical impulse over a distance of 410 µm.
In Figure 6.11 we can see the propagation of the action potential from activated Cell 1 (in red) to Cell 2 at rest (in blue) with a minimal delay of 1.2 ms. Following the activation, it can be noted that Cell 1 is illuminated while Cell 2 (which has not undergone activation) is turned off. The action potential is propagated through the SiC NWs from Cell 1 to Cell 2 almost instantaneously: Cell 2 activates and illuminates, while Cell 1 starts to switch off.

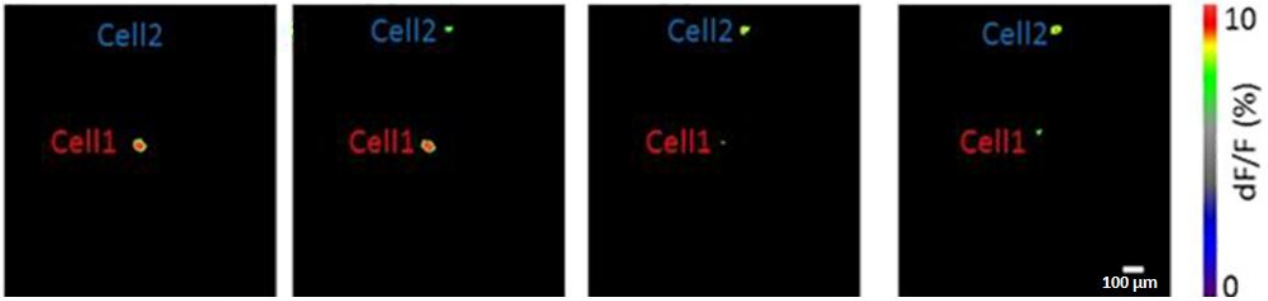


*Figure 6.11: Fluorescence recording the transmission via SiC NWs of cardiac bioelectricity from Cell 1 to Cell 2 with a delay of 1.2 ms over a distance of 410 µm.*

Figure 6.12 a shows the intracellular optical action potential of the two cells highlighted: Cell 1 in red and in Cell 2 in blue.

These two traces recorded are superimposed. This behavior indicates that there is a physiological propagation between the two cells.

In particular, SiC NWs can synchronize the action potential with almost the same gap junctional conductance typical for the cardiac tissue.

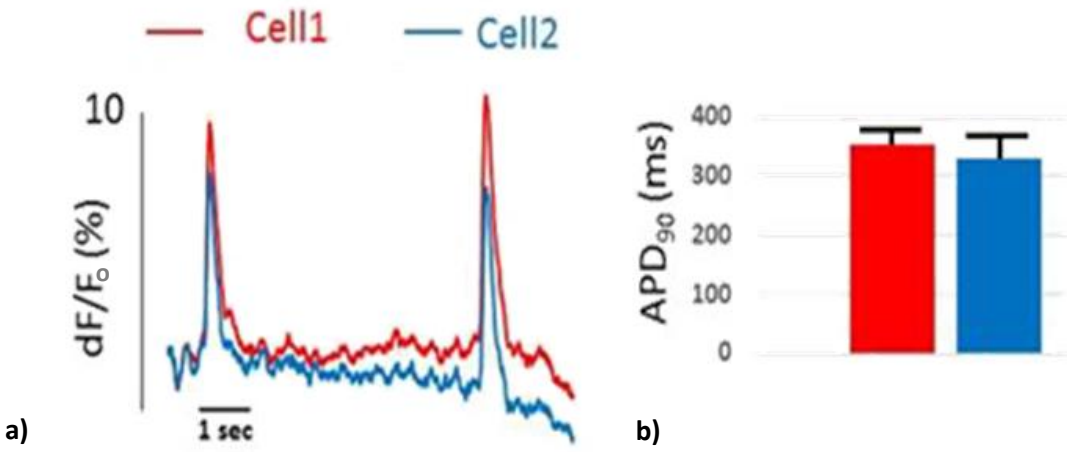


*Figure 6.12: a) Superimposed intracellular optical action potential ($F/F_0$) recorded in Cell 1 and in Cell 2. b) Action potential duration calculate at 90% of repolarization time ($APD_{90}$) for propagated action potentials between the two cells (Cell 1 in red, Cell 2 in blue).*

## 6.4 SiC NWs: *In vivo* experiment

From *in vitro* experiment it has been observed that SiC NWs are able to electrically connect two distant cardiomyocytes, synchronizing their action potentials, with a minimum delay of 1.2 ms.
The *in vivo* tests described in this part of the thesis had the task of analyzing this behavior on three-dimensional samples: the rat heart.

The aim of this project is to evaluate the electrophysiological alterations that occur during and after a cardiac infarction, to estimate the tendency to form of arrhythmias and to verify if the use of SiC NWs (placed in the ischemic region by injection) goes to restore normal electrical cardiac function.

A sensor, consisting of an electrode grid placed in direct contact with the epicardial surface of the rat's heart, was used to monitor electrical cardiac functioning. During the experiment the EGs (electrograms recorded directly on the epicardial surface) were recorded before, during and after the infarction in order to compare the variations of the sinus rhythms in these three different conditions. The infarction was physically induced by three different processes: intramyocardial injection of formaldehyde, formaldehyde deposition and cryoinjury caused by liquid nitrogen.

### 6.4.1 The electronic equipment

A high spatial resolution electrode grid was used to monitor the rat heart electrical activity.
The sensor consists of an 8x8 or 11x11 electrode matrix constructed on a surgical gauze substrate. The resolution of the mesh is 1x1 or 0.5x0.5 mm. Externally to the array, four independent electrodes which inject constant current are used as reference (fiducial marks). (Figure 6.13 a, b)

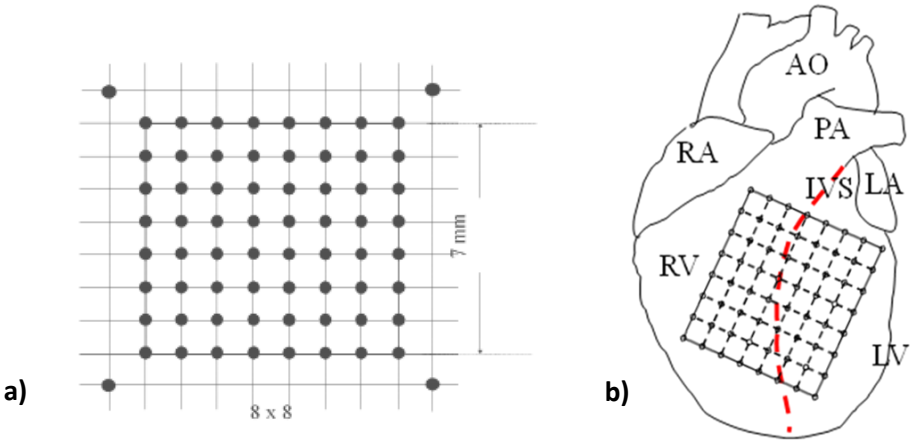


*Figure 6.13: a) Schematic representation of 8x8 electrode grid. The resolution is 1x1mm. Externally the four reference electrodes. b) Schematic representation of 8x8 electrode grid on the heart surface.*

The electrodes are rings with a diameter of 250 µm, obtained by knotting a 60 µm diameter silver wire around the intersection between the weft and the warp of the gauze. To close the knot, the end of the short wire has been twisted to the end of the long wire, and cut close to the circuit. (Figure 6.14)
To perform these operations, the use of a stereomicroscope (Cobra, Vision Engineering, Send U.K.) was necessary.

a) 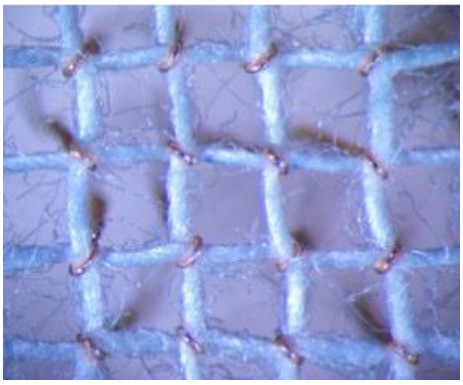 b) 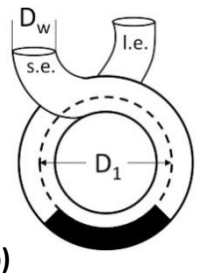


*Figure 6.14: a) Picture of the electrodes grid fastened on the gauze. b) Schematic electrode design: the electrode is a silver wire knot with a short end (s.e.) and a long end (l.e.). $D_1$ is the knot diameter (250 µm); $D_w$ is the silver wire diameter (60 µm). The black area is the estimated electrode contact surface area.*

Since the silver electrodes are polarizable, they have been coated with a thin layer of chloride in order to obtain uniform impedance values and more accurate cellular potential data. The chlorination of the electrodes was conducted with electrical method.[8,9]

The electrodes were immersed in a 0.9% NaCl solution and positively charged applying a 2.5 mA current through the silver wire for 2 minutes. In this way, the electrode assumed the behavior of an anode attracting to itself the chloride ions. To remove the excess of chloride ions not adhered to the wire surface, an inverted polarity current (respect to the previous one) was made to flow into the electrodes for 30 s. This mechanism has modified the charge of the electrode transforming it into a cathode able to repel chloride ions.

One of the two ends of the knotted wire was connected to a 50 pins connector coupled to a differential gain amplifier with AC coupling of a 256-channel mapping system. For measurements, the reference electrode was placed on the left hind leg of the animal, the ground electrode on the right hind leg and the return electrode on the chest near the heart.

Data were recorded at a bandwidth of 0.03–500 Hz, input impedance of 1012 Ω, sampling rate of 1 or 16 kHz/channel. The continuous flow of data (overall rate of 256 kHz with 12 or 16-bit resolution) was handled by a double buffering technique.

During the recording session, all EG data were visible in real time on the oscilloscope display.

The equipment consists of the following instruments, visible in Figure 6.15:

- 128-channel switch box and Multiplexer (a)
- Display Module Monitor (Lbo-51ma X-y CRT, Leader Electronics Corp., Yokohama, Japan) (b)
- 4-channel stimulus generator (model STG4004-1.6 mA, multi-channel system, Reutlingen, BW, Germany) (c)
- Small animal ventilator (RoVent, Kent Scientific Corporation, Connecticut, U.S.A.) (d)

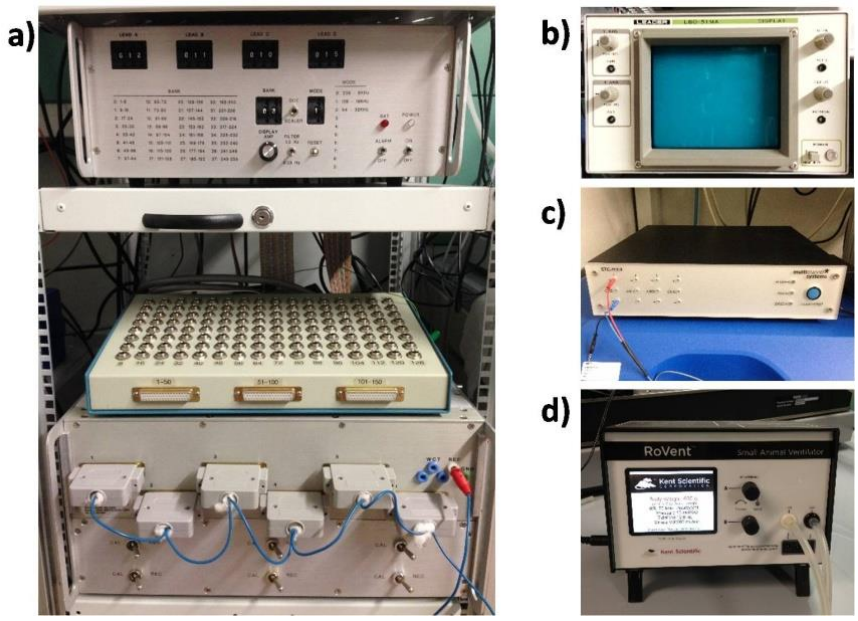


*Figure 6.15: a) 128 channels switch box and Multiplexer. b) Display Module Monitor. c) 4-channel stimulus generator. d) Small animal ventilator.*

### 6.4.2 Procedure and protocol

*In vivo* tests were conducted on ten rats.
The rats were anaesthetized with an intraperitoneal injection of Domitor (a muscle relaxant) and Zoletil (an anesthetic):

- DOMITOR: 0.015 ml / 100 g of body weight
- ZOLETIL: 0.02 ml / 100 g of body weight

Once sedated, the animals were placed on the surgical table in the supine position, with immobilized legs. To prevent the collapse of the lungs during measurements, the animals were attached to an artificial ventilator via a Y-tube inserted into the trachea. The respiratory volume was calibrated from 8 to 2.5 ml/min with a frequency of about 1.3 Hz.

Thereafter, a thoracotomy with pericardial incision was performed to open the thoracic cavity, making the heart visible.
The electrode grid sensor was placed on the surface of the pulsing heart. To reduce the pressure on the heart tissues, the electric cables connecting the electrodes to the computer were suspended. Rats' body temperature was kept constant at 37 °C thanks to an infrared lamp and the thorax of the rats was kept covered by a plastic surgical towel. (Figure 6.16)

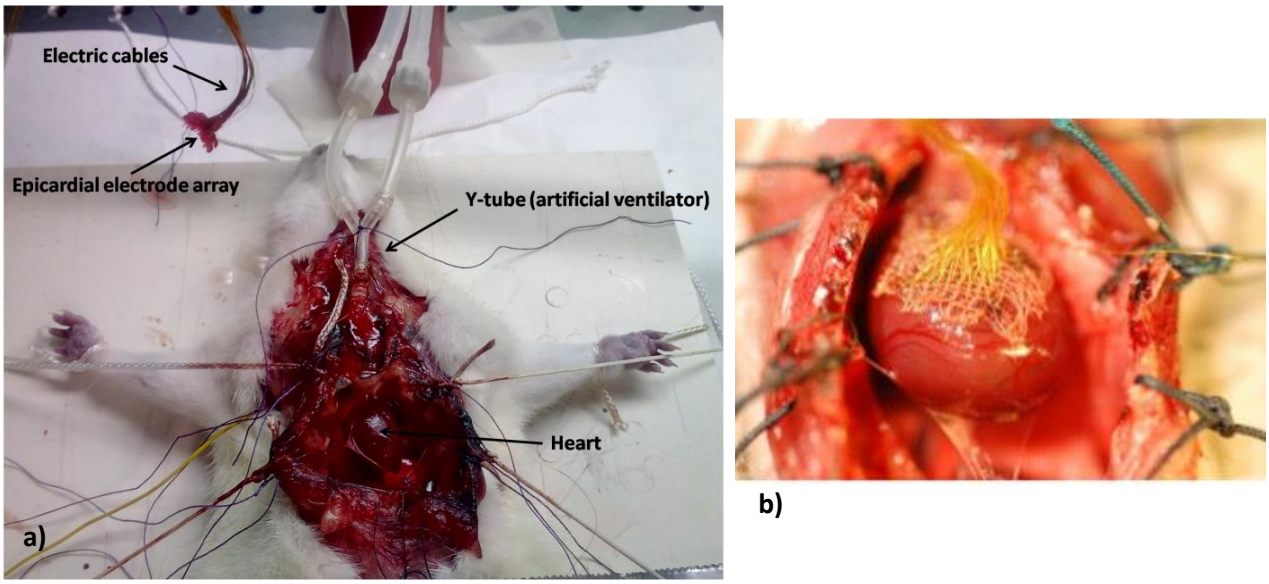


*Figure 6.16: a) Rat during the open-heart experiment attached to the artificial ventilator. b) Epicardial electrode array on the heart surface.*

At the beginning of the experiment, 30 seconds of sinus rhythm were recorded to obtain data on the correct functioning of the animal healthy heart (control conditions).
The infarction was induced in three different ways: by the injection of 300 µl of formaldehyde solution (4% and 38%) into the midwall region of the left ventricle, by deposition of a drop of formaldehyde 38% solution on the epicardial surface with a micropipette or by cryoinjury with liquid nitrogen.
The values of damaged cardiac electrical propagation were recorded immediately after the infarct and 1 hour later.

A negative control was performed by injecting a saline solution into the ischemic zone. This control was done to make sure that the induced infarction was stable over time and was not washed away by the addition of an aqueous solution able to dilute the formaldehyde concentration.

The SiC NWs (0.2 mg/100 g of body weight) dispersed in saline solution by sonication (30 minutes at 37 °C) were injected onto the rats. The NWs data were recorded after 1 hour from the injection of SiC NWs and after 5 hours.

At the end of the experiment, the animals were sacrificed and their hearts removed. The hearts were washed for 1 minute in phosphate buffered saline solution and the small area containing the ischemia was OCT (Optimal Cutting Temperature compound) included and stored in liquid nitrogen.

The data that have been collected concern the main electrophysiological parameters of sinus rhythm. In particular the most important parameters to analyze are: the RR interval, the P wave (atrial depolarization), the PQ segment, the QRS complex (ventricular activation), the QRS amplitude (index of cardiac excitability), the QT duration, the QTc interval (the heart rate corrected QT interval), the AT duration (the time interval between the beginning of QRS complex and the R wave), the RT duration and the T wave duration.

In order to determine the alteration in cardiac propagation, isochrone maps have been recorded.

Isochrone maps are visual representations of the depolarization wavefront propagation during specific progressive time intervals and show the areas of the heart that are activated in the same period of time.
In fact, these maps combine points that are activated simultaneously: the blue zones are the areas that are electrically activated first, while the red zones are those that are activated last.

The isochrone maps allow to see if there are any alterations in the conduction of the electric excitation.
After an ischemia there is a reduction in the speed at a specific point which can lead to a conduction block (possible starting point of an arrhythmia).

The distance between the lines gives an indication of the speed of propagation of the electrical impulse in the area under the electrode array sensor. The closer the lines are to each other, the lower the speed will be. Contrary, the more distance there is between the lines, the greater the speed will be.

The isochrone maps have allowed to obtain the longitudinal conduction velocity ($CV_L$) and the transverse conduction velocity ($CV_T$) with respect to the orientation of the fibers. $CV_L$/ $CV_T$ gives the anisotropic ratio. These velocity vectors provide information on the velocity and direction of the propagating electrical wavefront. (Figure 6.17)

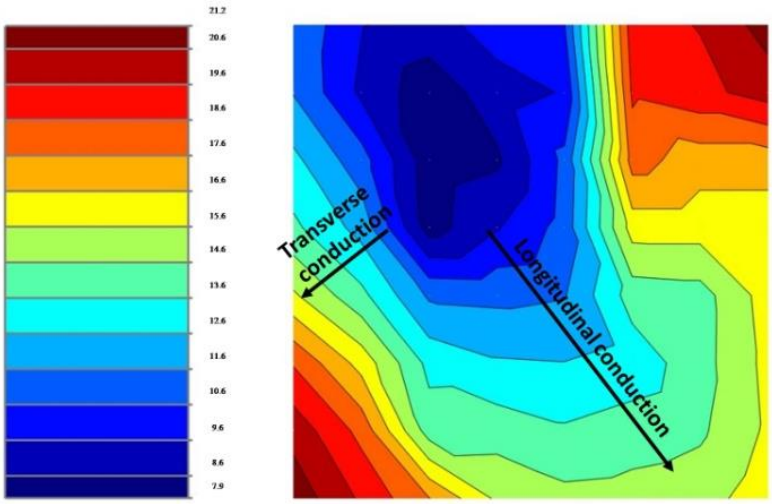


*Figure 6.17: Example of an isochrone map in which the early activation heart area is colored in blue and the late activation area in red. The two arrows indicate the longitudinal conduction and the transverse conduction. The numbers in the color scale (left) are the activation time: the milliseconds that pass from the beginning of the QRS complex.*

### 6.4.3 Results

The ten rats were treated with the following protocols:

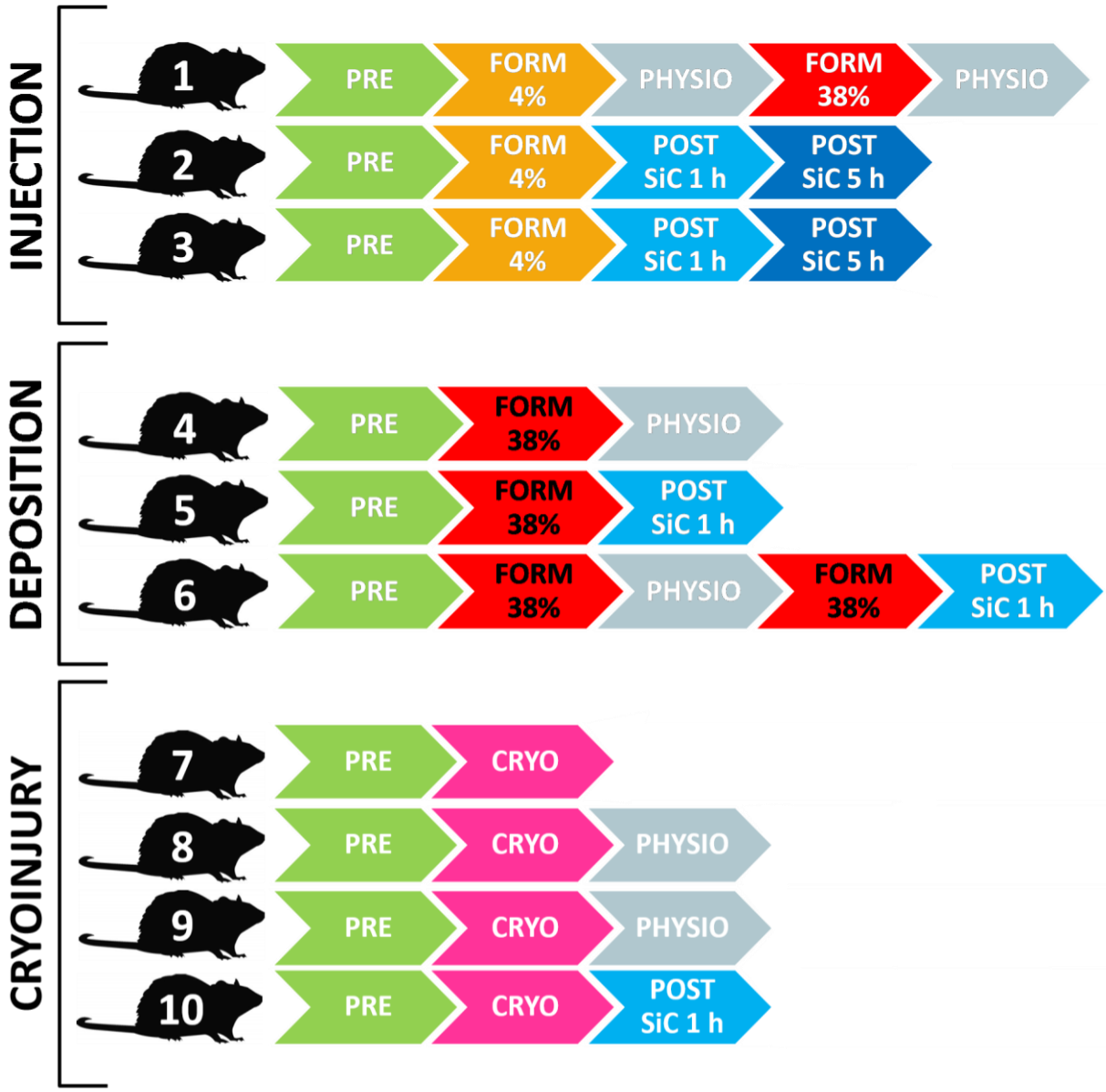


The abbreviations in the graph:

- PRE: situation of cardiac normality (pre-infarction).
- FORM 4% (in white): situation monitored 1h after the injection of 4% formaldehyde solution (infarction).
- FORM 38% (in white): situation monitored 1h after the injection of 38% formaldehyde solution (infarction).
- FORM 4% (in black): situation monitored 1h after the deposition of 4% formaldehyde solution (infarction).
- FORM 38% (in black): situation monitored 1h after the deposition of 38% formaldehyde solution (infarction).
- CRYO: situation monitored 1h after the cryoinjury caused by liquid nitrogen (infarction).
- PHYSIO: situation monitored 1h after the injection of saline solution.
- POST SiC 1h: situation monitored 1h after the injection of SiC NWs dispersed in saline solution.
- POST SiC 5h: situation monitored 5 h after the injection of SiC NWs dispersed in saline solution.

After recording the values relating to normal cardiac conduction of the healthy heart, a cardiac tissue damage was performed in one of the three ways provided by the three protocols.

In the first experiment (INJECTION, rats 1, 2 and 3) the infarction was caused by an injection of formaldehyde[10] on the free wall of the left ventricle, generating an ischemic zone visible to the naked eye (white area in Figure 6.18 a).

In the second experiment (DEPOSITION, rats 4, 5 and 6) the infarction was caused by a deposition of a small drop of formaldehyde 38% solution on the left ventricular epicardial surface (small drop in Figure 6.18b).

In the third experiment (CRYOINJURY, rats 7, 8, 9 and 10) the infarction was caused by cryoinjury[11,12,13,14] with a thin tip cooled with liquid nitrogen which burned a small area of the ventricular tissue (the cooled tip in Figure 6.18 c and the burned area in Figure 6.18 d).

Saline and SiC NWs saline injections (0.2 mg / 100 g body weight) were made in the same point where the infarction was induced. The area with injected SiC NWs can be seen in Figure 6.18 e (dark area).
At the end of the experiment, after the animal's sacrifice, the ischemic area containing the SiC NWs was withdrawn from the heart and incorporated into OCT (Optimal Cutting Temperature) compound[15] for further histological analysis.(Figure 6.18 f, g)

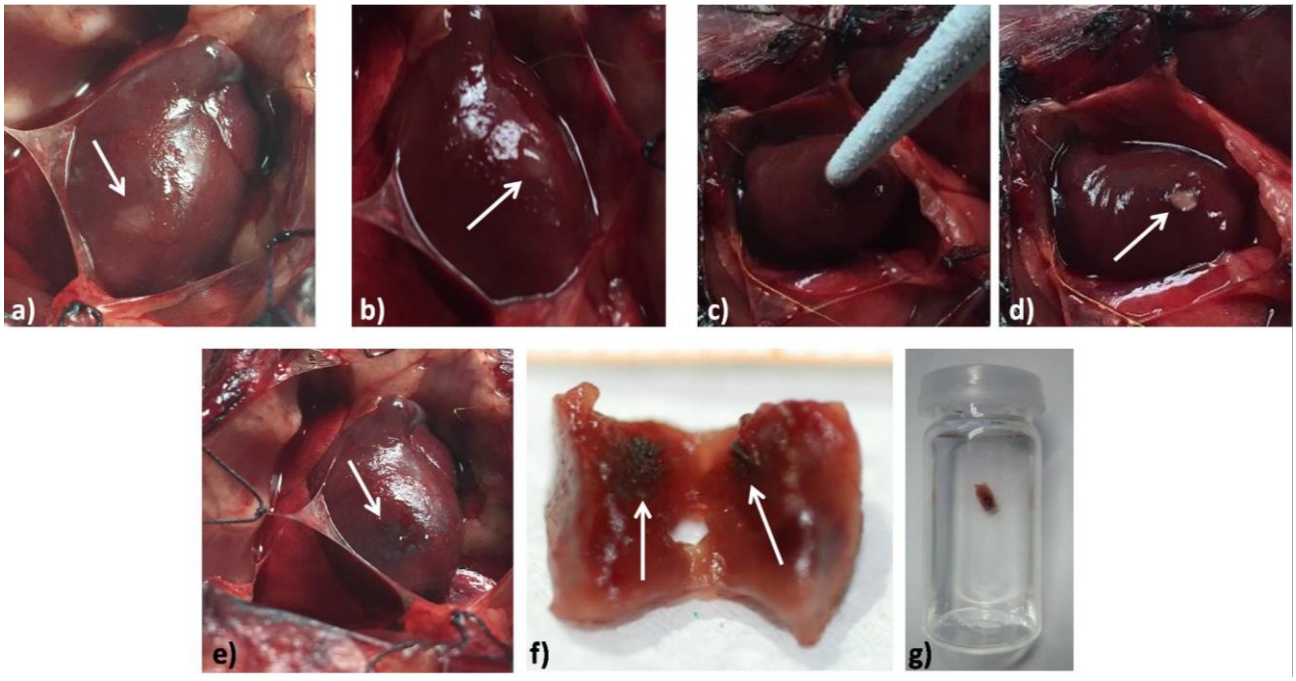


*Figure 6.18: a) Anterior view of rat heart after formaldehyde injection (white region). b) Formaldehyde drop deposition on left ventricular free wall epicardium. c) Anterior view of rat heart during the induction of cryoinjury. d) Left ventricular free wall epicardium after local cryoinjury (white region). e) Anterior view of rat heart after the SiC NWs injection in a saline solution (black region). f) Free wall region cut transversally with the view of ischemic region with SiC NWs (dark area). g) The small area containing the ischemia, OCT (Optimal Cutting Temperature compound) included.*

Before introducing the individual experiments, it is necessary to explain the symbology that will be used.

In the figures relating to the collected EGs, the colors of the frames surrounding the individual EG refer to the specific phases of the experiment: green is the standard pre-infarction condition, orange is post-formaldehyde 4%, red is post-formaldehyde 38%, pink is post-cryoinjury, gray is the condition after the saline solution injection, light blue is the situation after 1 h from the injection of nanowires, and dark blue is the situation after 5 h from the injection of nanowires.

This combination "phase of the experiment - specific color" is also used in the histograms.
Furthermore, four symbols are used in the histogram charts: *, #, §, ●.

The symbol * means that a comparison is made between the "X data in analysis" and the standard pre-infarction situation (vs Pre), the symbol ● indicates the comparison with the post-infarction formaldehyde 4% condition (vs Post form 4%), the symbol § indicates the comparison with the post-infarction formaldehyde 38% condition (vs Post form 38%), and the symbol # the comparison with the post-saline solution injection (vs Physio).

The symbols also indicate the significance (the number p) obtained from the statistical analysis when comparing two quantities: 1 symbol is used if $p<0.05$ (there is significant difference, but not striking), 2 symbols if $p < 0.01$, 3 symbols if $p <0.001$ (big difference). As these statistical tests are made by comparing pairs of quantities, each symbol (*, #, §, ●) explains with what the bar of the histogram has been compared and the magnitude of the statistical difference.

All data were expressed as means ± SEM. Normal distribution of variables was checked by means of the Kolmogorov-Smirnov test. Statistics of variables included paired Student's t-test, two-way ANOVA (post hoc analyses: Bonferroni test or Games-Howell test, when appropriate) and Kruskal-Wallis (post hoc analyses: Dunn's multiple comparison). Prism 5.0 software (GraphPad Software) was used to assess the normality of the data and for statistical calculation. Statistical significance was set at $p < 0.05$.

The individual experiments on the ten rats will be discussed below.

- **INJECTION EXPERIMENTS**

  - **RAT 1**

In the EG recorded during the control conditions (surrounded by a green frame) it is possible to observe a completely positive QRS interval and a heart rate (HR) of about 210 bpm (Figure 6.19).
After the injection of formaldehyde 4% (orange-framed EG), a decrease in heart rate occurs (HR at 130 bpm) and two ventricular extrasystoles (indicated by red arrows) appear with a negative QRS complex.
After 1 hour from the saline injection, the gray EG is similar to the post-formaldehyde 4% EG, but with a slight increase of the S wave compared to the S waves of the EG under both control conditions (green) and after injection of formaldehyde 4% (orange-framed EG). Heart rate increases slightly to 150 bpm.
After 1 hour from the formaldehyde 38% injection the heart rate does not change significantly (HR = 135 bpm). In the red EG, it can be seen that the T wave becomes slightly negative and a ventricular extrasystole (red arrow) develops at the beginning of the recording with a negative QRS complex.

After 1 hour from the second injection of saline solution, no particular differences are observedin the EG (in gray).

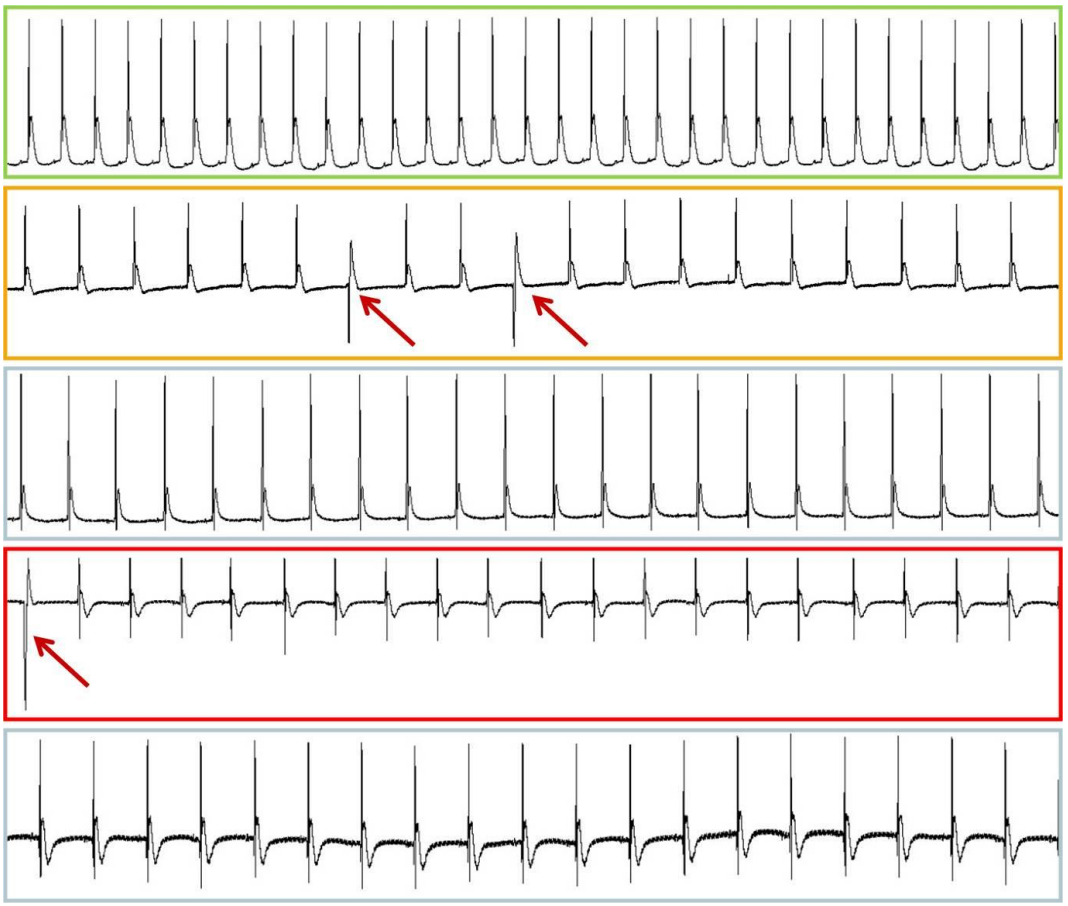

*Figure 6.19: EGs recorded (9 seconds long) in control condition (green), after formaldehyde 4% injection (orange), after 1h of saline solution injection (gray), after 1h of formaldehyde 38% injection (red), after 1h of saline solution injection (gray). Red arrows point out specific behavior (see text for details).*

The isochrone maps recorded during the experiment are shown in Figure 6.20.
Due to the change in the grid position during recording, isochrone maps may show slight differences that are not dependent on the treatment.
During the control phase, sinus rhythm activation is present with two breakthroughs (blue area) on the left ventricle (LV) and right ventricle (RV) free wall and a delayed collision area near the interventricular septum (red area).
The formaldehyde 4% injection (black circle) creates a large area of delayed activation and the RV breakthrough disappears.
After the saline solution injection, there is a partial restoration of the normal activation of the sinus rhythm.
A second formaldehyde 38% injection (black circle) in a different cardiac area, creates a region of discontinuous activation (isochrones lines gradient) and the RV breakthrough disappears again.
After the last injection of saline solution, there is an alteration of the global activation.

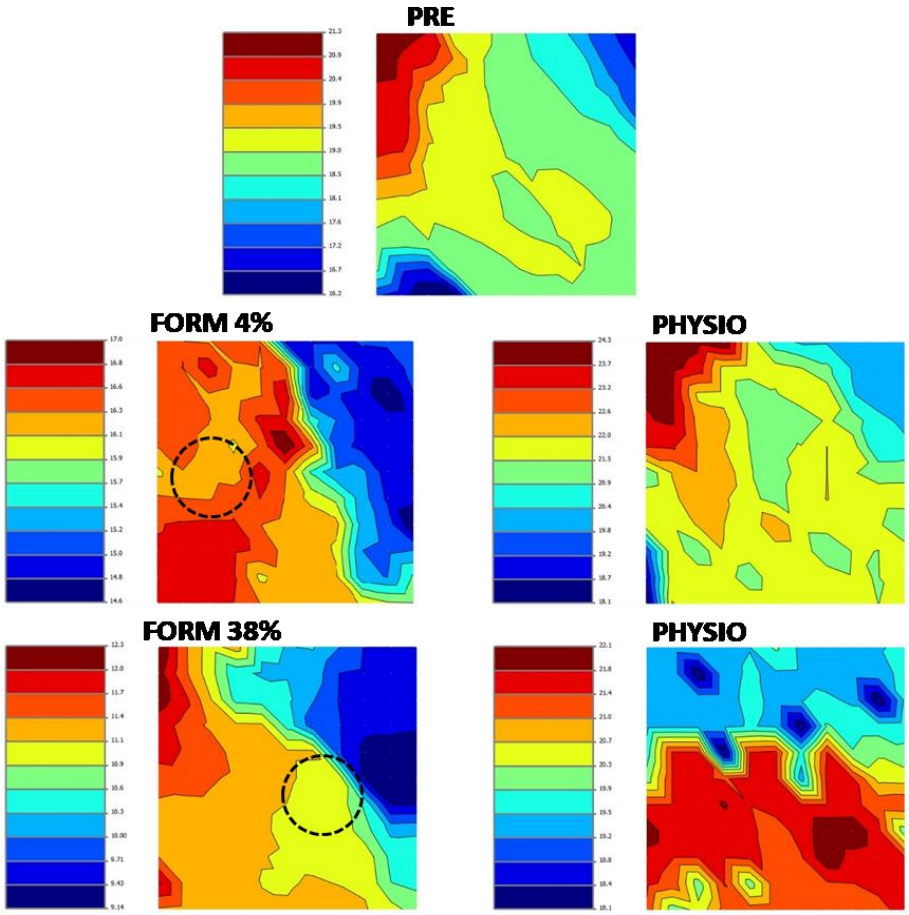


*Figure 6.20: Isochrone maps recorded in control condition (PRE), after formaldehyde 4% injection (FORM 4%), after 1h of saline solution (PHYSIO), after formaldehyde 38% injection (FORM 38%) and after 1h of saline solution (PHYSIO). The number in the scale bar are milliseconds from QRS onset. The black circles represent the area of the injections.*

Figure 6.21 shows the main electrophysiological parameters extracted from the EGs.

In two graphs, the post-formaldehyde 4% and post-second injection physio values are not displayed because the end of the P wave was very noisy and difficult to evaluate.
After injection of formaldehyde 4%, the durations of the RT interval and the RR interval increase. Vice versa, the PQ interval, the AT interval, the QRS complex, the QRS amplitude, the QTc interval and the T wave decrease.
After 1 hour from the injection of saline solution there is a reduction of all the parameters with respect to the control conditions, while the RT interval is increased. Furthermore, there is an increase in amplitude of the QRS complex compared to the post-formaldehyde 4% situation.
After formaldehyde 38% injection, the duration of the QRS complex and the T wave increase while a decrease in amplitude of the QRS complex is observed.
After the last injection of the saline solution there is a decrease in amplitude of the QRS complex with respect to the first saline injection while the PQ interval, the AT interval, the QRS complex, the RT interval and the RR interval increase.
Compared to the post-formaldehyde 38% condition, the increase in the RT interval and a decrease in amplitude of the QRS complex occur.

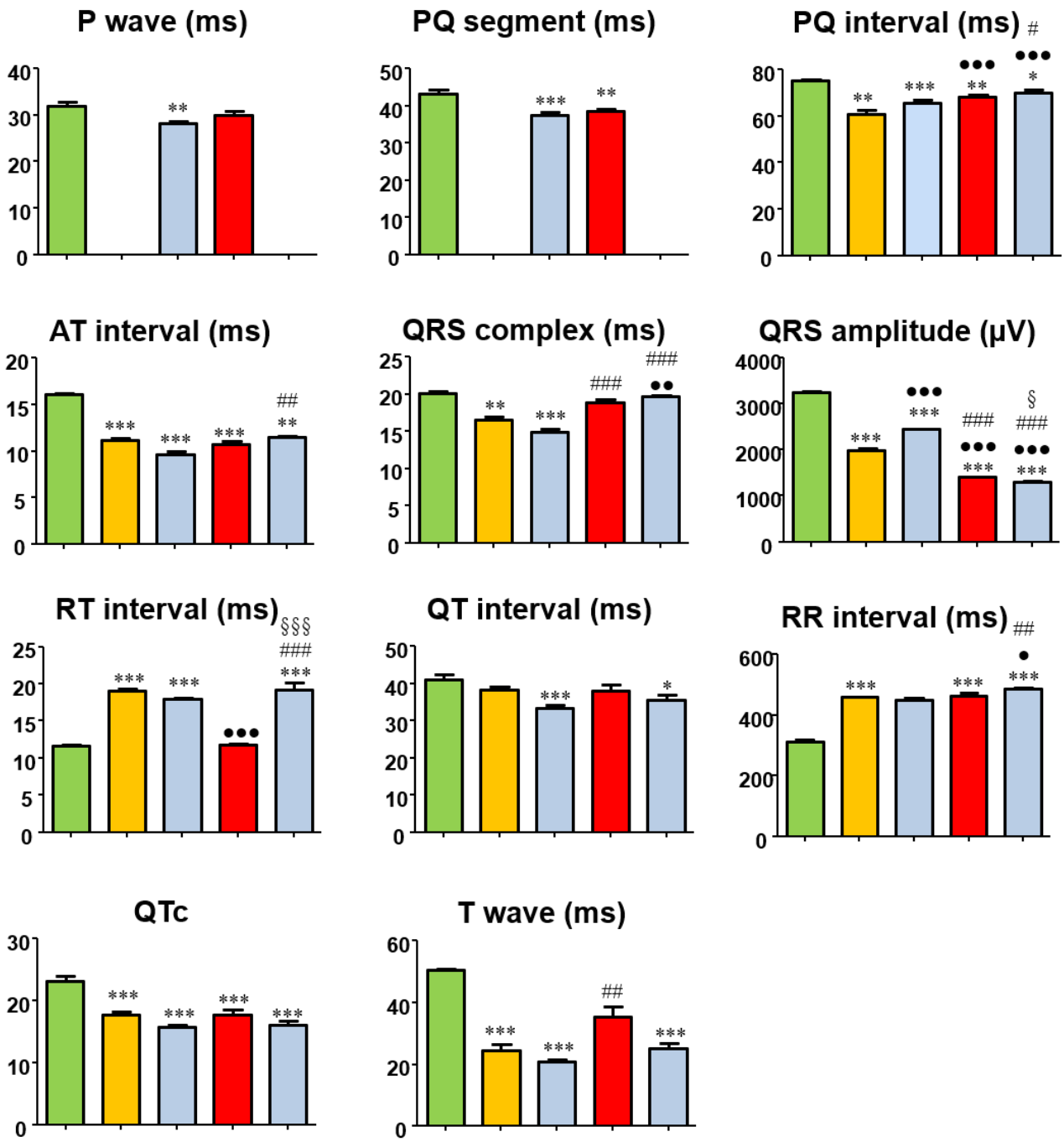


*Figure 6.21: Histograms displaying the EG wave and interval durations in control condition (Pre, green), after formaldehyde 4% injection (Post form 4%, orange), after 1h of saline solution (Post Physio, gray) and 1h after formaldehyde 38% injection (Post form 38%, red).*
** vs Pre; ● vs Post form 4%; # vs Post Physio; § vs Post form 38%*

- **RAT 2**

Figure 6.22 shows the experimental recorded EGs. The EG during the control conditions (in green) shows a sinus arrhythmia (red square). The QRS complex interval is completely positive and the heart rate is around 270 bpm.
After the formaldehyde 4% injection (orange frame), the QRS complex has a positive and negative trend. An increase in peak Q indicates the presence of ischemia. An increase in frequency occurs with HR at 390 bpm.
One hour after the injection of SiC NWs, the EG in light blue shows a similar pattern to the previous EG post-infarction with an increase in the S wave (compared to the control conditions). The heart rate is 210 bpm. The T wave becomes more pronounced. With this mild bradycardia, sinus arrhythmia appears again, highlighted by the red square.
After 5 hours from the injection of SiC NWs, the duration of the QT interval increases. The dark blue EG shows an increase in the duration and amplitude of the T wave. Bradycardia is present (HR = 120 bpm). As already observed after 1 hour, the sinus arrhythmia is confirmed as evidenced by the red square.

*Figure 6.22: EGs recorded (7 seconds long) in control condition (green), after formaldehyde 4% injection (orange), after 1 h of SiC NWs in a saline solution injection (0.2mg/100g of body weight) (POST SiC 1h) (light blue) and after 5h of SiC NWs in a saline solution injection (0.2mg/100g of body weight) (POST SiC 5h) (dark blue). Red square points out specific behavior (see text for details).*

Figure 6.23 shows the isochrone maps. During the control phase, normal sinus rhythm activation is present with a breakthrough (blue area) on the left wall of the left ventricle and a delayed collision area near the interventricular septum (red area).
After the injection of formaldehyde 4% (black circle) no particular differences occur.
After 1 h from the injection of SiC NWs, the wavefront coming from the right ventricle is more evident at the bottom of each isochrone map.
No change occurs after 5 hours from SiC NWs injection.

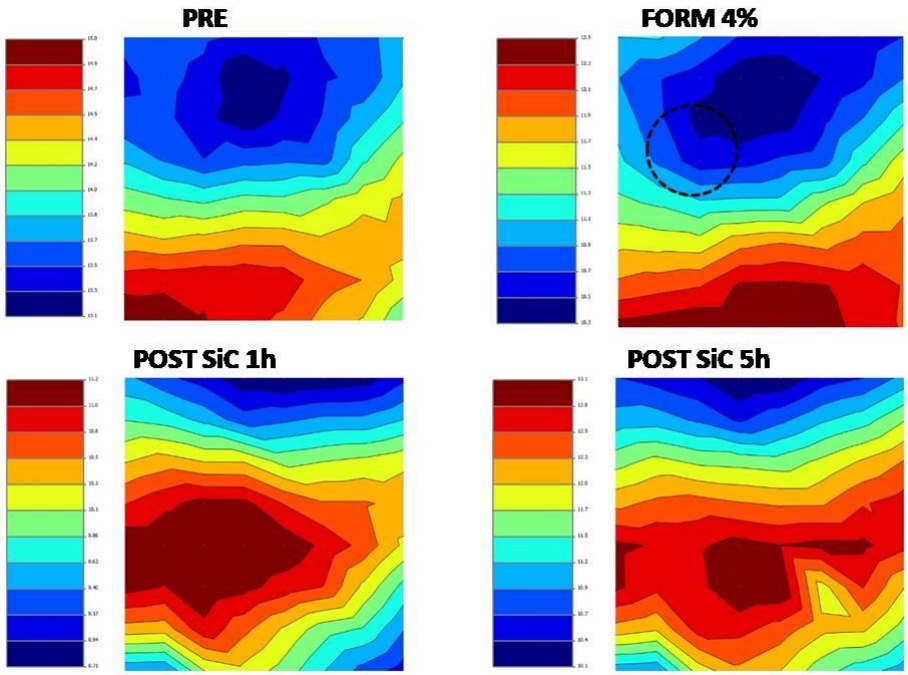


*Figure 6.23: Isochrone maps recorded in control condition (PRE), after formaldehyde 4% injection (FORM 4%), after 1 h of SiC NWs in a saline solution injection (0.2mg/100g of body weight) (POST SiC 1h) (light blue) and after 5h of SiC NWs in a saline solution injection (0.2mg/100g of body weight) (POST SiC 5h). The number in the scale bar are milliseconds from QRS onset. The black circle represents the area of injections.*

Figure 6.24 shows the main electrophysiological parameters extracted from the EGs. After the injection of formaldehyde 4% the durations of QTc, the RT interval and the QRS complex increase.
After 1 hour from the injection of the SiC NWs, there is a reduction of the P wave, the AT interval and the QTc with respect to the control conditions. Instead, the durations of the PQ segment, the RT interval, and the T wave have increased. Furthermore, there is a reduction of the P wave, the AT interval, the QRS complex, the QT interval, QTc and the heart rate compared to the post-formaldehyde 4% conditions.
After 5 hours from the injection of SiC NWs an increase of the P wave, the QRS complex, the RT interval and the QT interval occurs, with respect to the condition relating to the first hour after injection of SiC NWs.

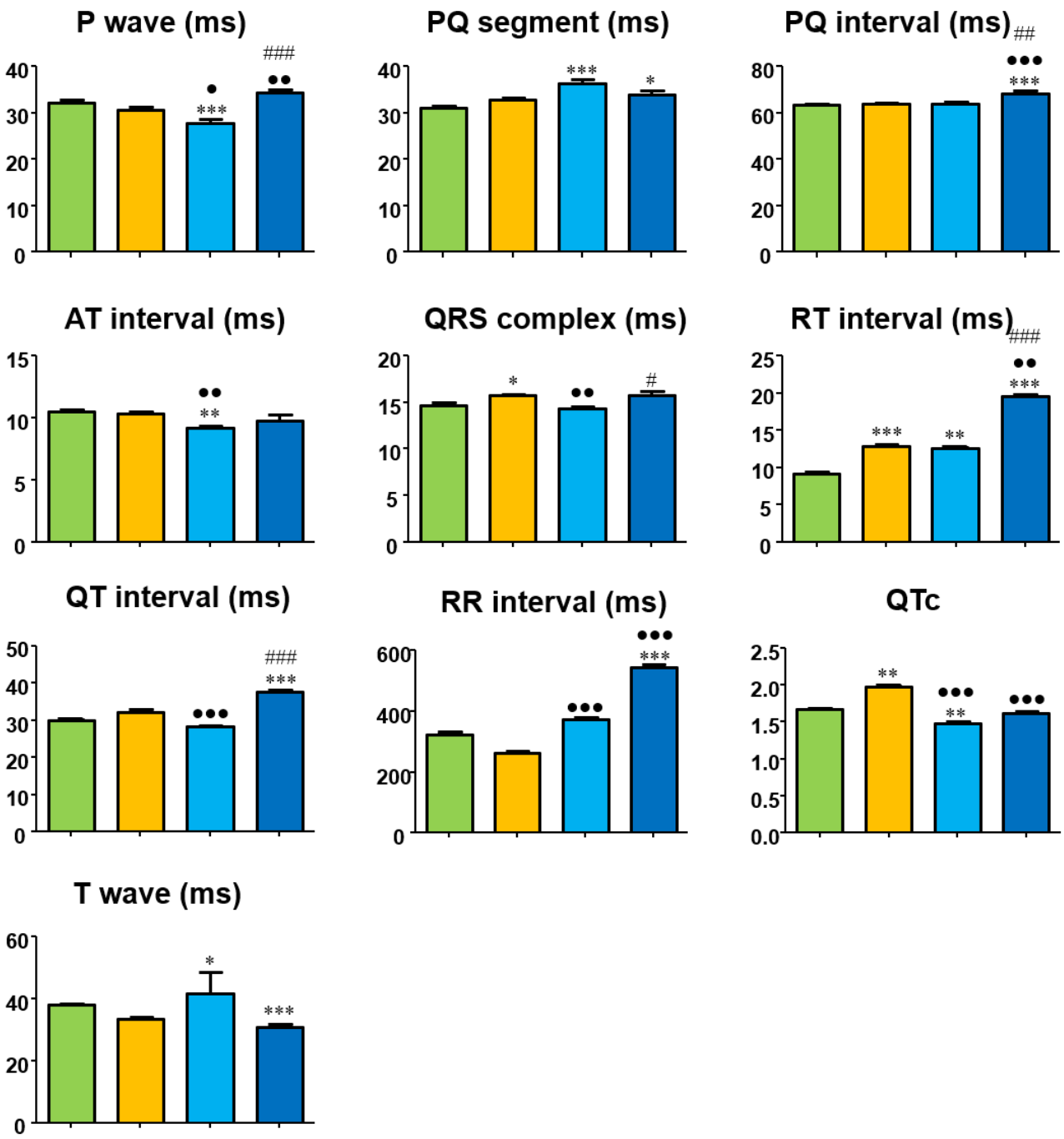


*Figure 6.24: Histograms displaying EG wave and interval durations of control condition (Pre, green), after formaldehyde 4% injection (Post form 4%, orange), after 1 h of SiC NWs in a saline solution injection (0.2mg/100g of body weight) (POST SiC 1h, light blue) and after 5h of SiC NWs in a saline solution injection (0.2mg/100g of body weight) (POST SiC 5h, dark blue).*

** vs Pre; ● vs Post form 4%; # vs Post SiC 1h*

- **RAT 3**

The EG during the control conditions (Figure 6.25, green frame) shows a sinus arrhythmia (red square). The QRS complex interval is completely positive and the heart rate is about 120 bpm.
After the injection of formaldehyde 4% the QRS complex has a completely negative trend, due to a complete AV dissociation (orange EG). AV dissociation is a problem of cardiac mechanics in which the ventricles are electrically activated independently of the atria and therefore the activation is not synchronous. Cardiac frequency is about 162 bpm.
After 1 hour from the injection of SiC NWs, the EG (in light blue) shows a shape similar to the previous EG, with an increase of the S wave (compared to the control conditions). The heart rate is 120 bpm. The T wave becomes more pronounced. With this mild bradycardia, sinus arrhythmia appears again, highlighted by the red square.
After 5 hours from the injection of SiC NW, the duration of the QT interval increases. The EG (in dark blue) shows an increase in the duration of the T wave. The heart rate rises to 156 bpm.

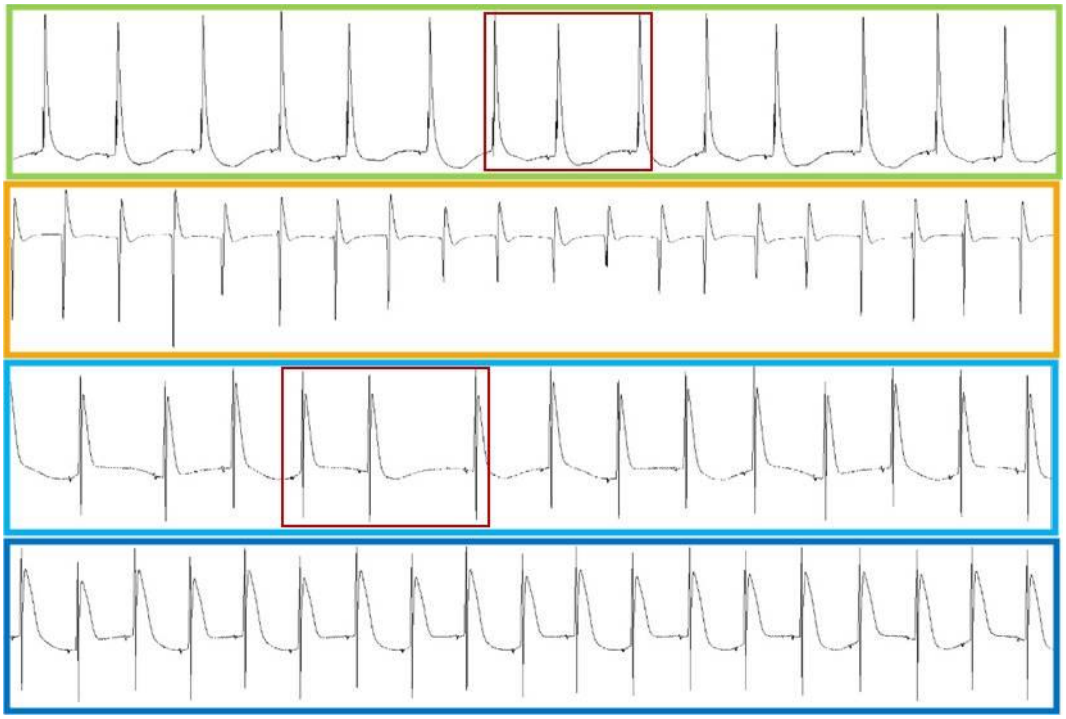

*Figure 6.25: EGs recorded (7 seconds long) in control condition (green), after formaldehyde 4% injection (orange), after 1 h of SiC NWs in a saline solution injection (0.2mg/100g of body weight) (POST SiC 1h) (light blue) and after 5h of SiC NWs in a saline solution injection (0.2mg/100g of body weight) (POST SiC 5h) (dark blue). Red square points out specific behavior (see text for details).*

The isochrone map (Figure 6.26) during the control shows that a normal sinus rhythm activation is present with a breakthrough (blue area) on the free RV wall and a delayed collision area near the interventricular septum (red area).
After injection of formaldehyde 4% (black circle) the sinus pattern changes completely and becomes specular to that of the control condition. Therefore, following the injection of formaldehyde, the first area activated during normal sinus rhythm becomes the last.

At 1 h from the injection of SiC NWs, isochrone maps show the first activation in the RV free wall (as during normal sinus rhythm) with an early activation near the injection area.
After 5 hours from the injection of SiC NWs the situation remains almost unchanged.

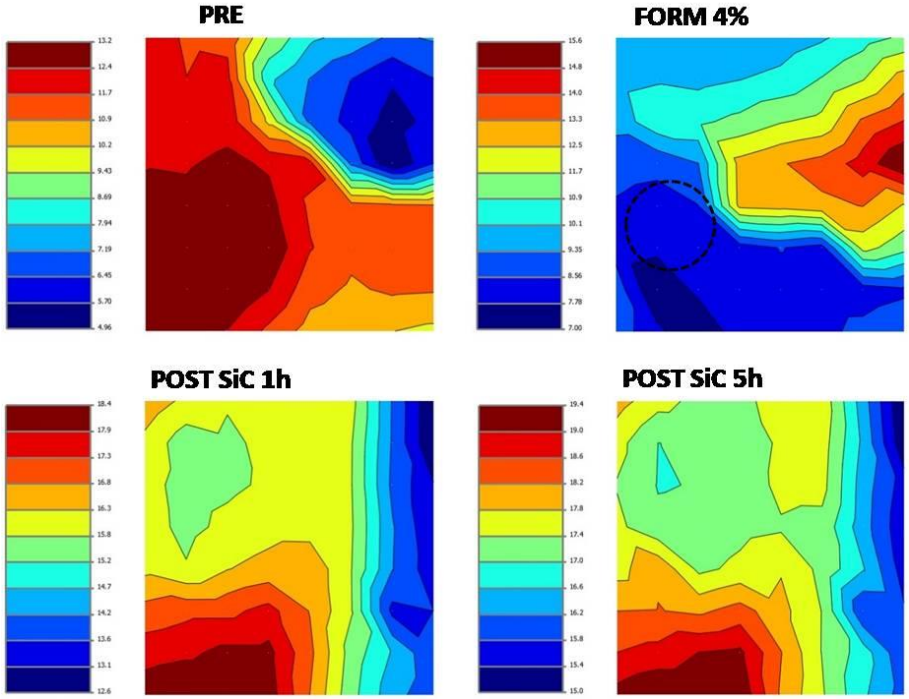


*Figure 6.26: Isochrone maps recorded in control condition (PRE), after formaldehyde 4% injection (FORM 4%), after 1 h of SiC NWs in a saline solution injection (0.2mg/100g of body weight) (POST SiC 1h) (light blue) and after 5h of SiC NWs in a saline solution injection (0.2mg/100g of body weight) (POST SiC 5h). The number in the scale bar are milliseconds from QRS onset. The black circle represents the area of injections.*

Figure 6.27 shows the main electrophysiological parameters extracted from the EGs. In the first three graphs, the post-formaldehyde 4% value is not displayed due to AV dissociation.
After the formaldehyde 4% injection, there is an increase in the duration of the AT interval, the QRS complex, the RT interval and the QTc interval. Vice versa the RR interval decreases.
After 1 hour from the injection of SiC NWs, all parameters are increased with respect to the control conditions, except for the decreasing RR interval. Furthermore, there is an increase in the RR interval and the T wave compared to the post-formaldehyde 4% conditions.
After 5 hours from the injection of SiC NWs the duration of the RT interval and the QTc interval increases (compared to the post 1h SiC injection condition).

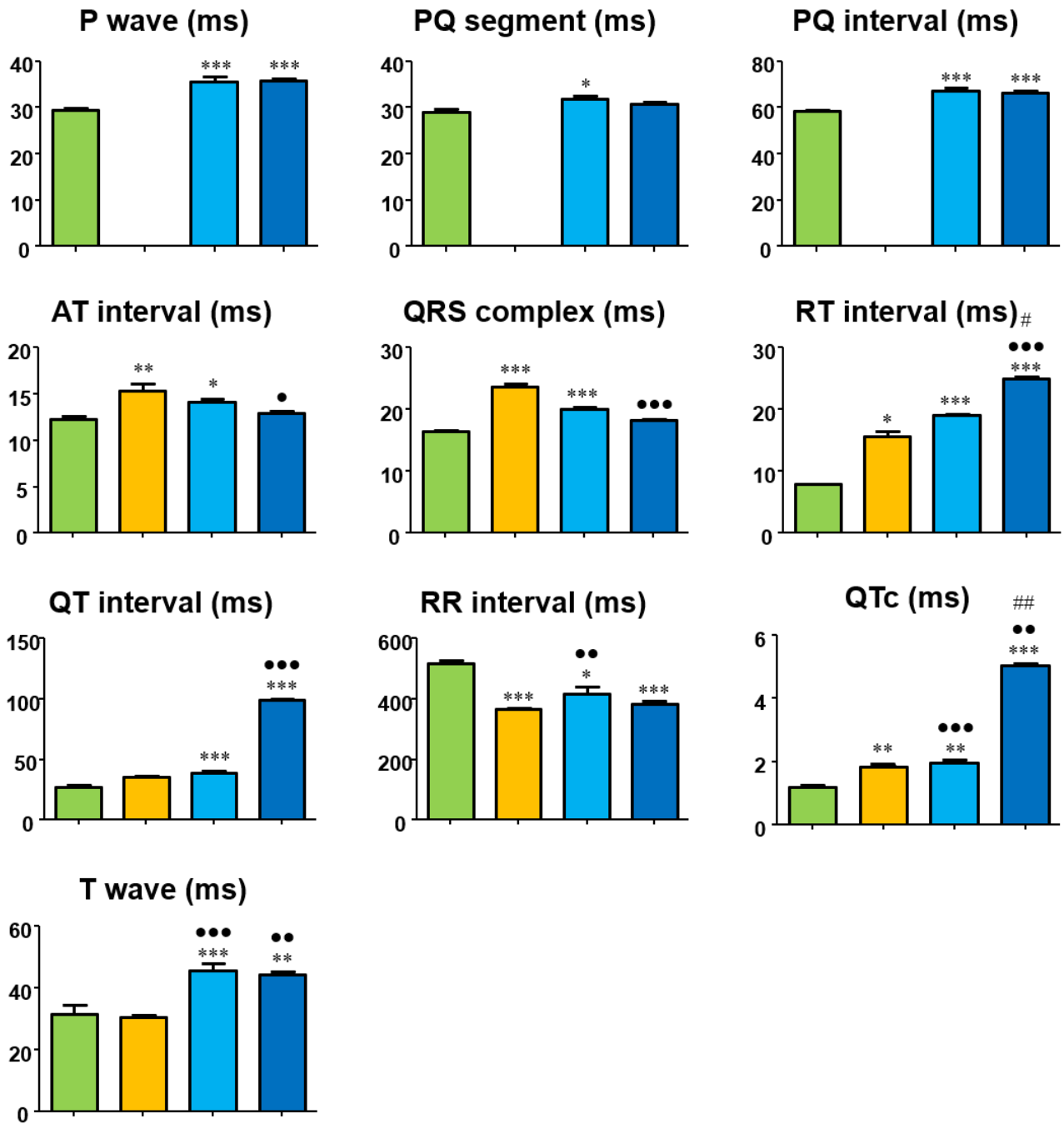


*Figure 6.27: Histograms displaying EG wave and interval durations of control condition (Pre, green), after formaldehyde 4% injection (Post form 4%, orange), after 1 h of SiC NWs in a saline solution injection (0.2mg/100g of body weight) (POST SiC 1h, light blue) and after 5h of SiC NWs in a saline solution injection (0.2mg/100g of body weight) (POST SiC 5h, dark blue).*
** vs Pre; ● vs Post form 4%; # vs Post SiC 1h*

✓ **DEPOSITION EXPERIMENTS**

✓ **RAT 4**

During the control conditions (EG with green frame in Figure 6.28) a positive QRS complex is observed with a small negative S wave and a frequency of about 140 bpm. The sinus arrhythmia present is highlighted by a red square.
After formaldehyde 38% deposition, the QRS complex in the red EG has a completely positive trend, the heart rate does not change. Sinus arrhythmia (red squares) is still present.
After 1 hour from the saline injection, the EG (gray) has a behavior similar to the EG post-formaldehyde, but the shape of the S wave is more pronounced negatively (compared to the control conditions). Since in the rats the wave T is attached to the S wave, variations of the T wave can affect the wave S. Variations of the T wave are synonymous of altered tissue repolarization and therefore of appearance of ischemia. HR is 130 bpm. Even the T wave becomes more pronounced. With this mild bradycardia, sinus arrhythmia remains as evidenced by the red square in the EG.

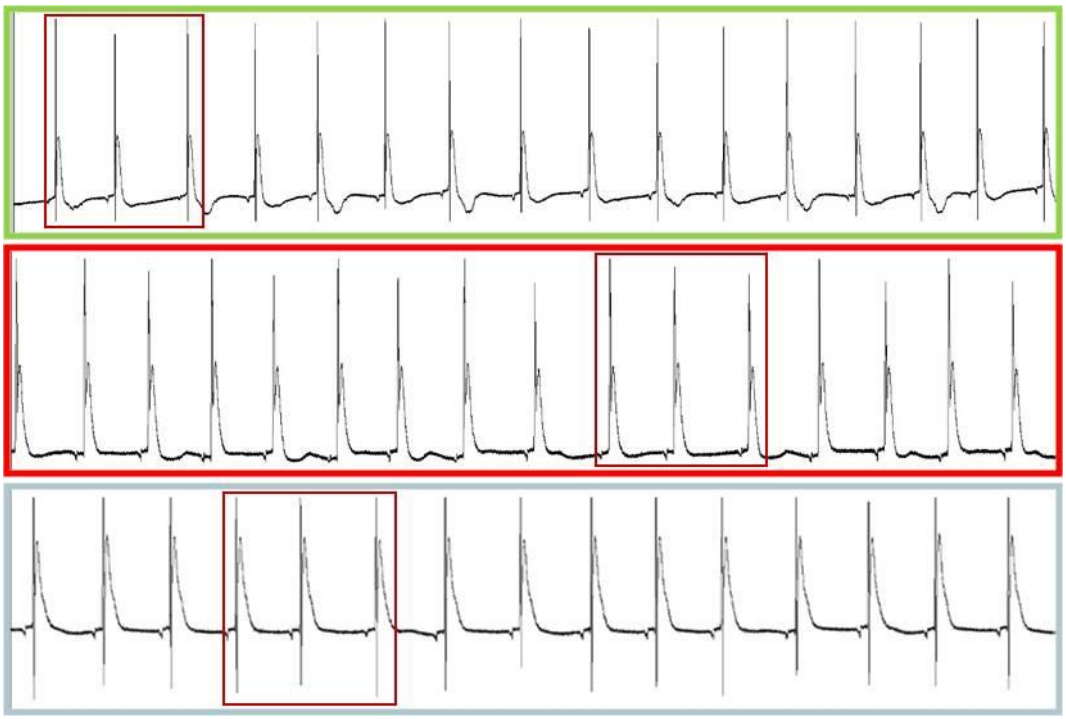

*Figure 6.28: EGs recorded (7 seconds long) in control condition (green), after formaldehyde 38% deposition (red), after 1h of saline solution injection (gray). Red squares point out specific behavior (see text for details).*

The isochrone map (Figure 6.29) of the control situation (PRE) shows an activation of the normal sinus rhythm with two breakthroughs (blue area) on the LV and RV free wall and a delayed collision area near the interventricular septum (red area).
After the deposition of formaldehyde 38% (black circle) the sinus rhythm activation does not change while a slowing of the conduction speed near the injection area occurs. During sinus rhythm activation there is a

ventricular extrasystole (red arrow) with an activation coming from the apex of the heart and a turn near the injection area.
After injection of the saline solution the isochrone map remains the same as the post-infarction condition.

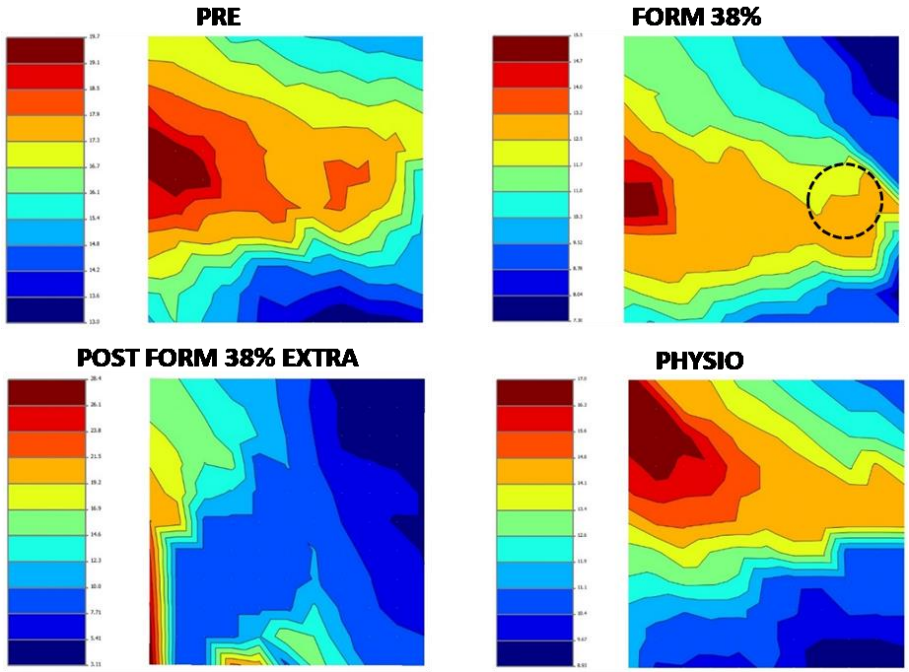


*Figure 6.29: Isochrone maps recorded in control condition (PRE), after formaldehyde 38% deposition (FORM 38%) and after 1h of saline solution (PHYSIO). Ventricular extrasystole was recorded after formaldehyde 38% deposition (POST FORM 38% EXTRA). The number in the scale bar are milliseconds from QRS onset. The black circle represents the area of deposition.*

Figure 6.30 shows the main electrophysiological parameters extracted from the EGs. After the formaldehyde 38% deposition, the durations of the P wave, the PQ segment, the PQ interval, the QRS complex and the RT interval increase, but the width of the QRS complex decreases.
After 1 hour from saline injection there is an increase of all parameters with respect to the control conditions, except for the width of the QRS amplitude which decreases. In addition, there is an increase in the P wave, the PQ segment, the PQ interval, the AT interval, the RT interval, the QT interval and QTc compared to post-formaldehyde 38% conditions.

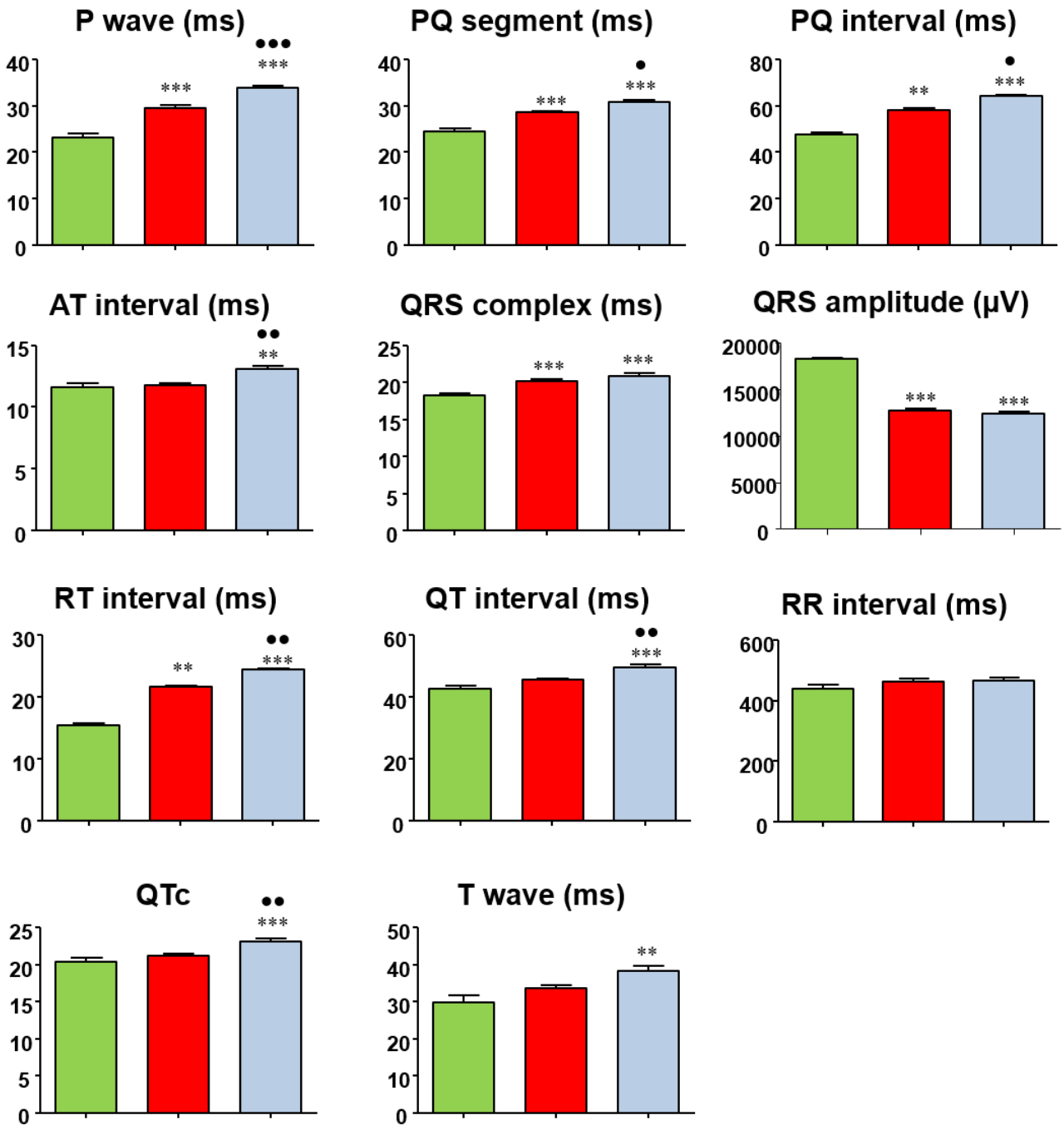


*Figure 6.30: Histograms displaying EG wave and interval durations in control condition (Pre, green), after formaldehyde 38% deposition (Post form 38%, red) and after 1h of saline injection (Post physio 1h, gray). * vs Pre; ● vs Post form 38%*

✓ **RAT 5**

The EG during the control conditions (Figure 6.31, green frame) shows the completely positive QRS complexes and a heart rate of about 130 bpm. In addition, there is a negative terminal part of the T wave, index of ischemic presence.
After formaldehyde 38% deposition, there is a decrease in heart rate at 90 bpm. In the red EG the QRS interval is completely positive, the T wave becomes more pronounced and a sinus arrhythmia (red squares) occurs.
After 1 hour from the injection of SiC NWs, the EG in light blue has a similar shape compared to the post-formaldehyde 38% EG, but the S wave is more pronounced. In addition, a small change in heart rate occurs (HR = 85bpm) and sinus arrhythmia (red squares) remains.

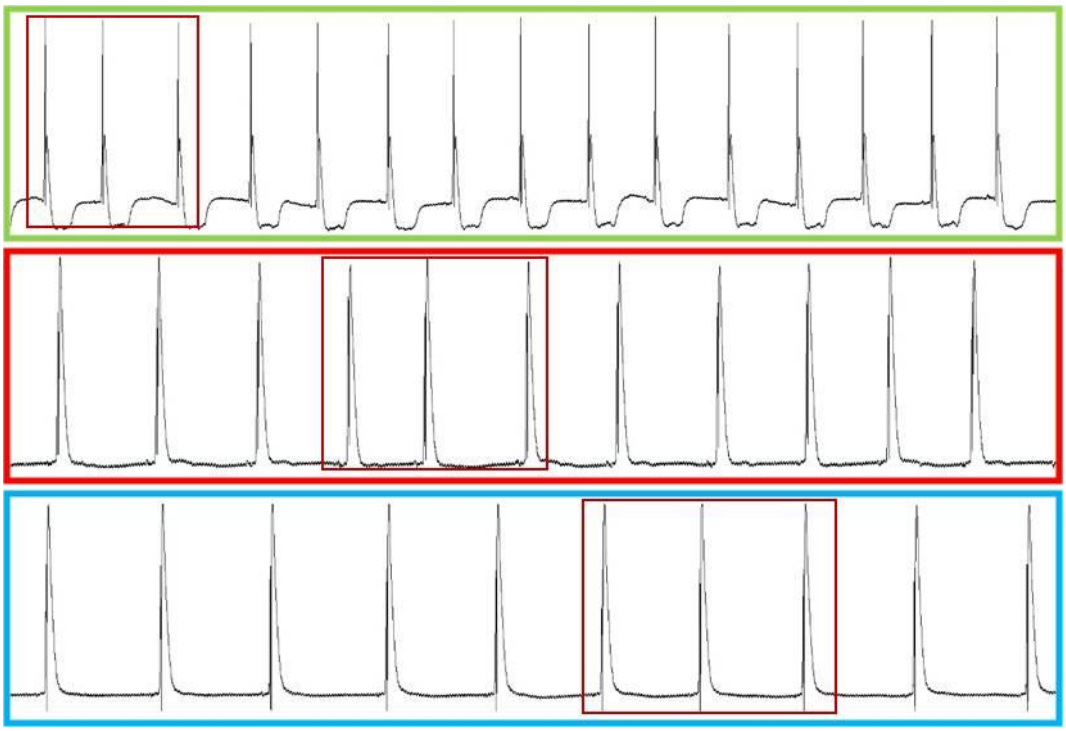

*Figure 6.31: EGs recorded (7 seconds long) in control condition (green), after formaldehyde 38% deposition (red) and after 1h from the SiC NWs in a saline solution (0.2mg/100g of body weight) injection (light blue). Red square points out specific behavior (see text for details).*

In the isochrone map (Figure 6.32) of the control condition, normal sinus rhythm activation is present with a breakthrough (blue area) on the free RV wall and a delayed collision area near the interventricular septum (red area).
After the deposition of formaldehyde 38% (black circle) the activation of sinus rhythm shows some little differences, in particular there is a slight slowing of the conduction velocity near the injection area. Furthermore, during the activation of the sinus rhythm, a ventricular extrasystole is recorded with an activation coming from the LV and a breakthrough near the injection area.
After 1 hour from the injection of SiC in a saline solution (0.2 mg / 100 g of body weight), the activation of sinus rhythm does not change with respect to the control conditions.

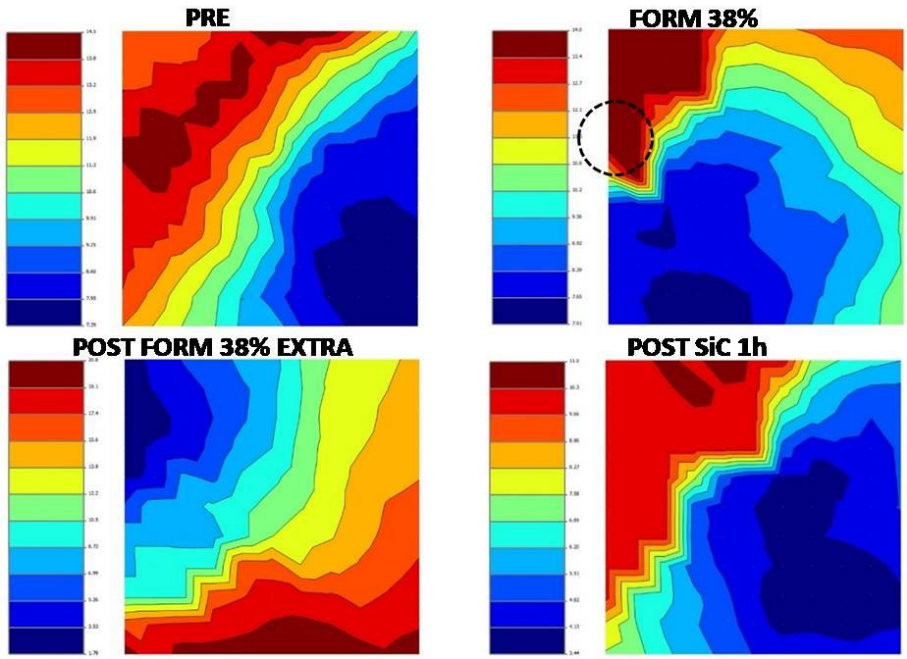


*Figure 6.32: Isochrone maps recorded in control condition (PRE), after formaldehyde 38% deposition (FORM 38%) and after 1 h of SiC NWs in a saline solution injection (0.2mg/100g of body weight) (POST SiC 1h). Ventricular extrasystole was recorded after formaldehyde 38% deposition (POST FORM 38% EXTRA). The number in the scale bar are milliseconds from QRS onset. The black circle represents area of deposition.*

Figure 6.33 shows the main electrophysiological parameters extracted from the EGs. After the formaldehyde 38% deposition, the durations of the AT interval, the QRS complex, QRS complex amplitude, the QT interval and QTc decrease, while the RR interval increases.

After 1 hour from the injection of the SiC NWs there is an increase in the RR interval and the RT interval with respect to the control conditions. Conversely, the AT interval, QRS complex amplitude and QTc decrease. Moreover, an increase of the QRS complex, of the RT interval, of the QT interval, of the RR interval and of the wave T wave with respect to the post-formaldehyde 38% conditions is observed. Instead the QRS complex amplitude decreases.

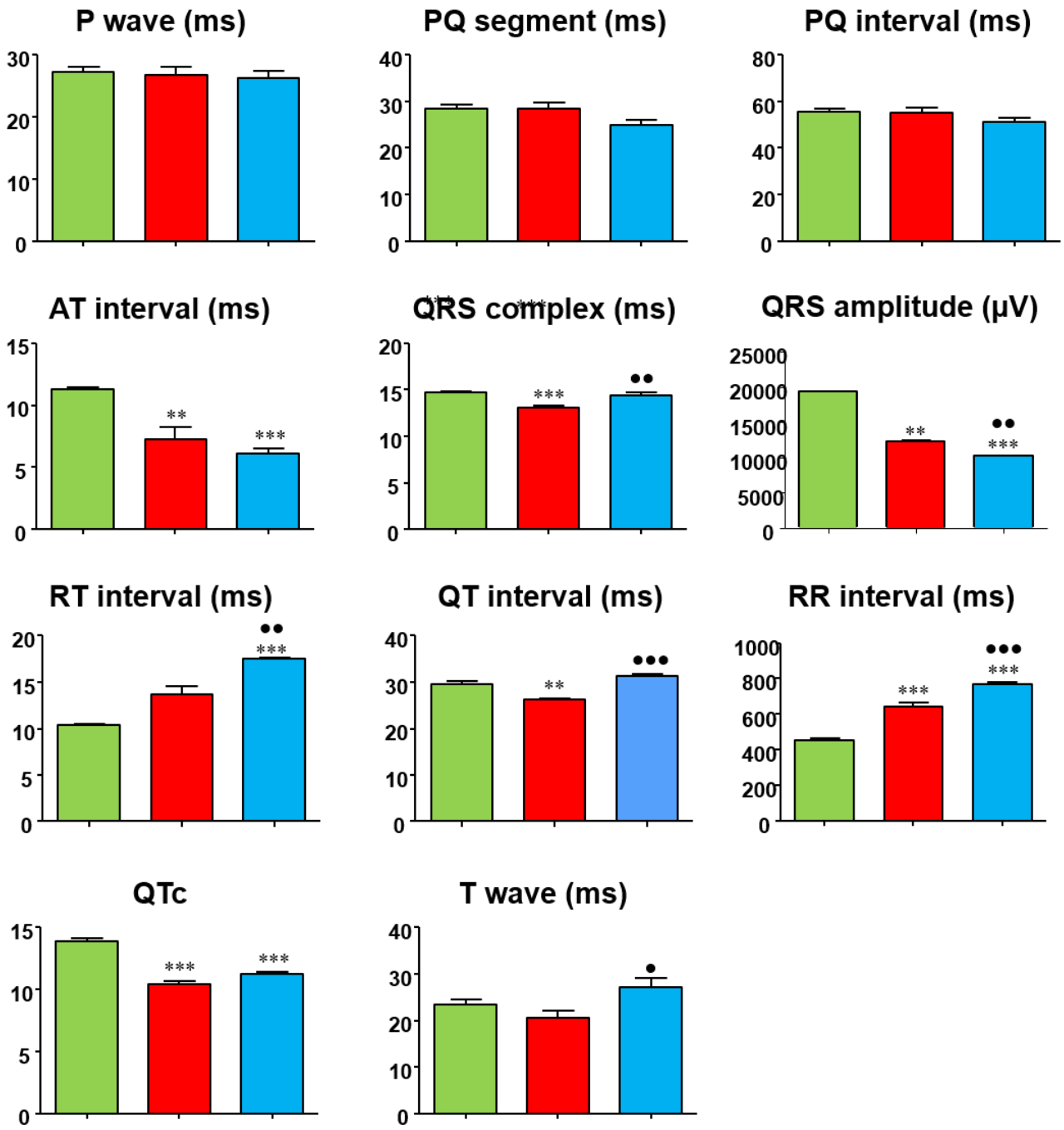


*Figure 6.33: Histograms displaying EG wave and interval durations in control condition (Pre, green), after formaldehyde 38% deposition (Post form 38%, red) and after 1h of saline solution (0.2mg/100g of body weight) of SiC NWs injection (Post SiC 1h, light blue).*

** vs Pre; ● vs Post form 38%*

✓ **RAT 6**

The EG during the control condition (Figure 6.34, in green) shows the completely positive QRS complex and a heart rate of about 320 bpm.
After formaldehyde deposition 38%, there is a decrease in heart rate at 150 bpm and the appearance of sinus arrhythmia (red square).
After 1 hour from the saline injection, the EG in gray shows a similar pattern to the post-infarct clinical condition, but with a slight increase in heart rate to 160 bpm.
After the second 38% formaldehyde deposition the heart rate does not change (HR = 150 bpm) and also the shape of the QRS complex remains the same (EG in red).
After 1 hour from the injection of SiC NWs in a saline solution (0.2mg / 100g of body weight), a more pronounced T wave is evident in the light blue EG.

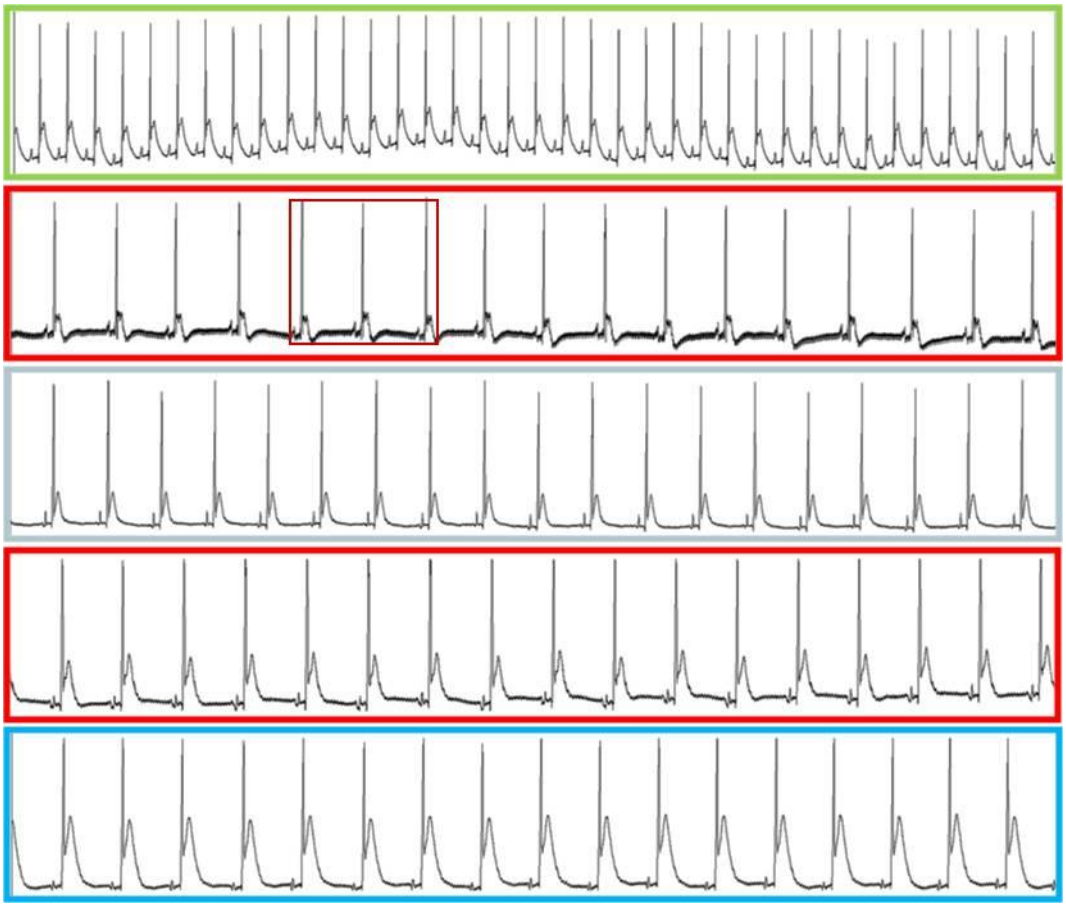

*Figure 6.34: EGs recorded (7 seconds long) in control condition (green), after formaldehyde 38% deposition (red), after 1h of saline solution injection (gray), after formaldehyde 38% deposition (red) and after 1h of SiC NWs in a saline solution injection (0.2mg/100g of body weight) (Post SiC 1h, light blue). Red square points out specific behavior (see text for details).*

The isochrone map (Figure 6.35) during the control phase shows a normal activation of the sinus rhythm with a breakthrough (blue area) on the free wall of the left ventricle and a delayed collision area near the interventricular septum (red area).
After the deposition of formaldehyde 38% (black circle) the activation of sinus rhythm remains constant.

Following the saline injection, the pattern remains conserved while a slowing of the conduction velocity is evident.
After the second formaldehyde 38% deposition (black circle) the sinus rhythm activation does not change as well as after the injection of SiC NWs.

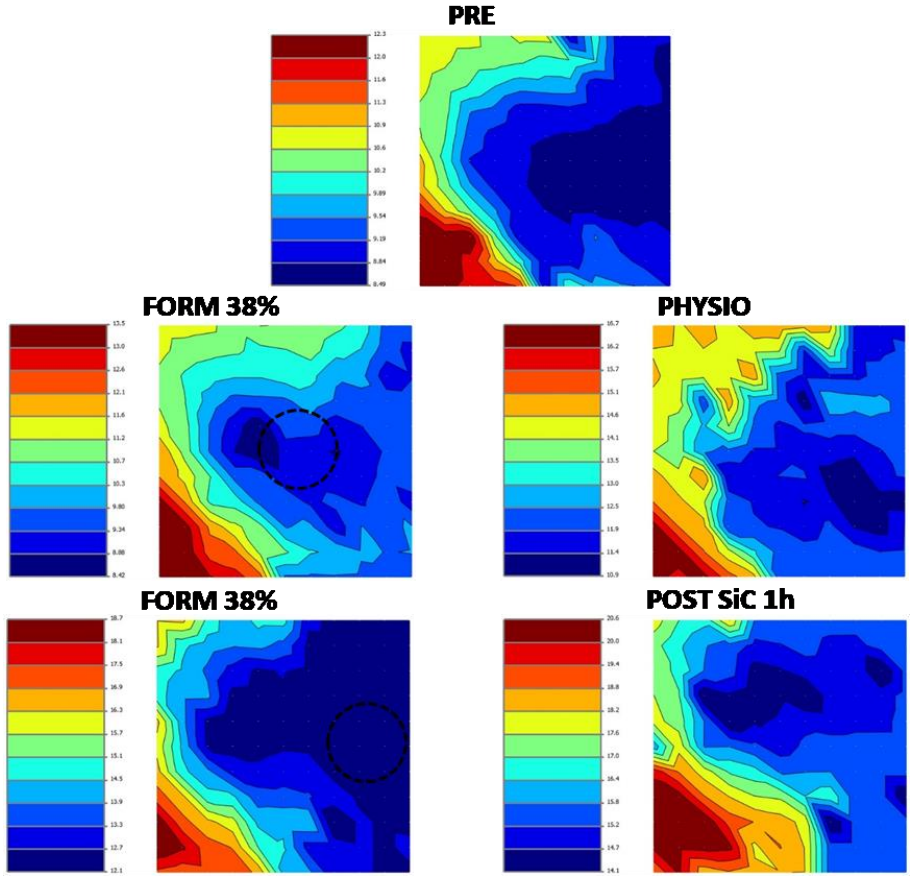


*Figure 6.35: Isochrone maps recorded in control condition (PRE), after formaldehyde 38% deposition (FORM 38%), after 1h of saline solution (PHYSIO), after a second deposition of formaldehyde 38% (FORM 38%) and after 1 h of SiC NWs in a saline solution injection (0.2mg/100g of body weight) (POST SiC 1h). The number in the scale bar are milliseconds from QRS onset. The black circle represents area of deposition.*

Figure 6.36 shows the main electrophysiological parameters extracted from the EGs. After formaldehyde 38% deposition, the AT interval and the QTc duration decrease. There is also an increase in RR compared to control conditions. After 1 hour from the saline injection, a decrease in the AT interval and an increase in the RT interval (with respect to the control conditions) are noted. Furthermore, there is an increase in P wave, PQ interval, QT interval, RR interval and T wave. Vice versa, the QRS complex amplitude decreases compared to the post-formaldehyde 38% condition.
After the second 38% formaldehyde deposition, the duration of the QRS complex and the duration of the RR interval increase while there is a decrease in the QRS complex amplitude compared to the post-physio situation. After 1 hour from the injection of SiC NWs in a saline solution (0.2 mg/100g of bodyweight) is visible an increase in the PQ segment, the PQ interval, the AT interval, the QRS complex, the RT interval, the QT

interval, QTc and the wave T (with respect to saline injection). Furthermore, the P wave, the PQ interval, the T wave and the width of the QRS complex increase with respect to the second formaldehyde 38% deposition.

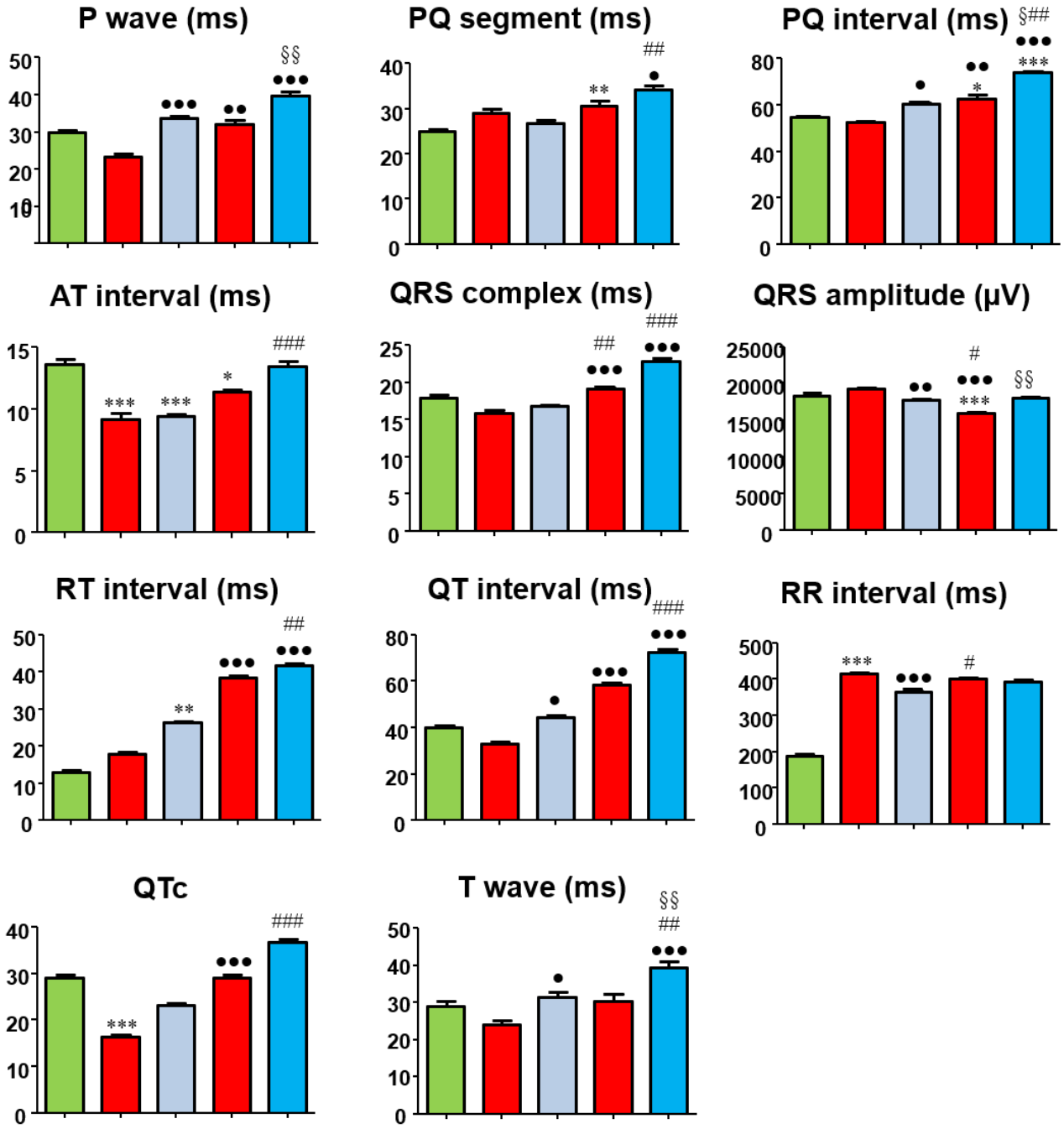


*Figure 6.36: Histograms displaying EG wave and interval durations in control condition (Pre, green), after formaldehyde 38% deposition (Post form 38%, red), after 1h of saline solution (Post physio, gray) and at the final stage after 1h of saline solution (0.2mg/100g of body weight) of SiC NWs injection (Post SiC 1h, light blue).*

** vs Pre; ● vs Post form 38%; # vs Post physio; § vs Post form 38% second injection.*

## ❖ CRYOINJURY EXPERIMENTS

### ❖ RAT 7

The EG after cryoinjury (Figure 6.37, in pink) shows the completely positive QRS complex as well as positive shift of the T wave and a heart rate of about 130 bpm. Moreover, sinus arrhythmia (red square) were recorded.

*Figure 6.37: EG recorded (5 seconds long) after the cryoinjury infarction caused by liquid nitrogen.*

The isochrone map (Figure 6.38) after cryoinjury shows a normal activation of the sinus rhythm with a breakthrough (blue area) on the free wall of the right ventricle and a delayed collision area near the interventricular septum (red area).

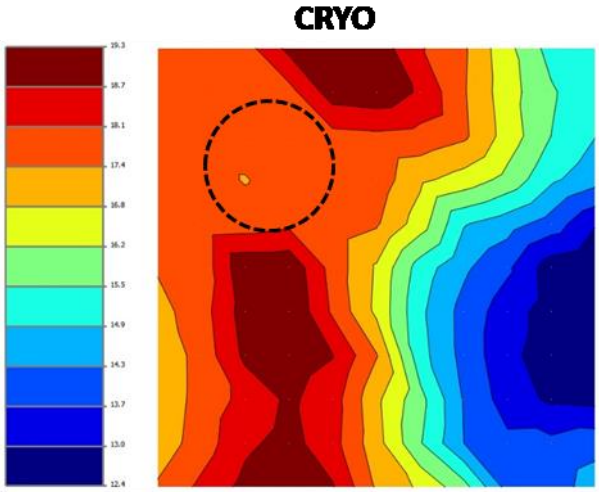


*Figure 6.38: Isochrone map recorded after cryoinjury. The number in the scale bar are milliseconds from QRS onset. The black circle represents area of deposition.*

### ❖ RAT 8

The EG during the control conditions (Figure 6.31, green frame) shows the completely positive QRS complexes and a heart rate of about 130 bpm. In addition, there is a negative terminal part of the T wave. After cryoinjury, there is an increase in heart rate at 180 bpm. In the pink EG we see that the QRS interval is bifasic, the T wave becomes less pronounced and a sinus arrhythmia (red squares) occurs.

After saline solution injection, the EG in gray has a similar shape compared to the post-cryoinjury. In addition, a small change in heart rate occurs (HR = 200 bpm) while an increase in T wave amplitude is present.

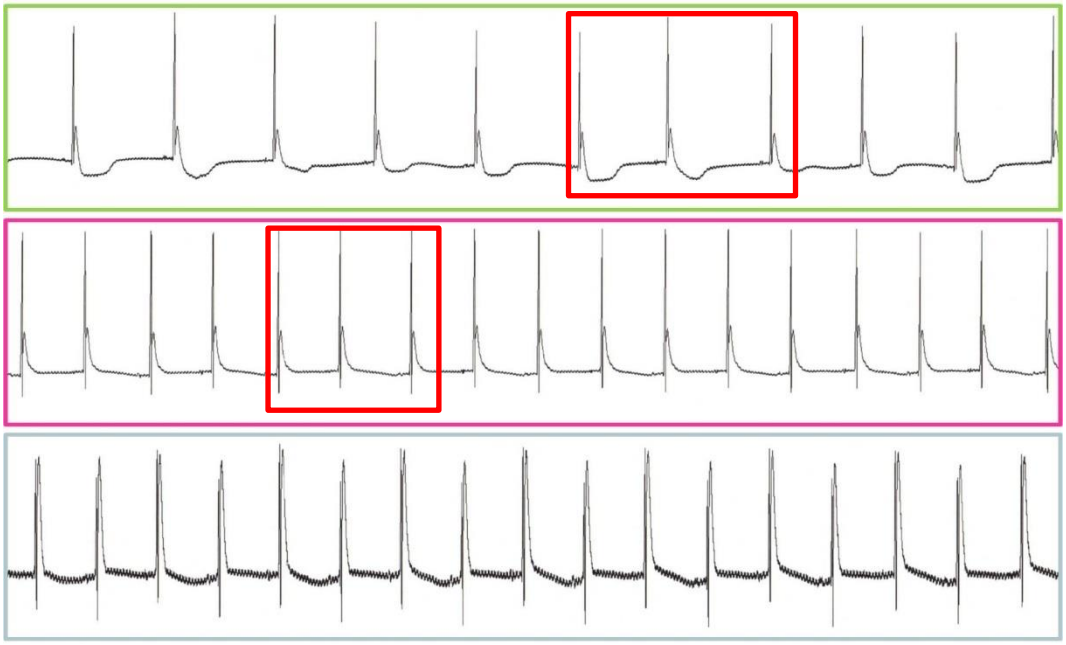

*Figure 6.39: EGs recorded (5 seconds long) in control condition (green), after cryoinjury infarction (pink) and after 1h of saline solution injection (gray). Red squares point out specific behavior (see text for details).*

In the isochrone map (Figure 6.40) of the control condition, normal sinus rhythm activation is present with a breakthrough (blue area) on the LV apex and a delayed collision area near the interventricular septum (red area). After cryoinjury (black circle) the activation of sinus rhythm shows some little differences, in particular there is a slight slowing of the conduction velocity near the injection area and an appearance of the RV activation is present. After saline solution injection the activation of sinus rhythm does not change with respect to the CRYO condition and little differences are present due to different location of electrode array.

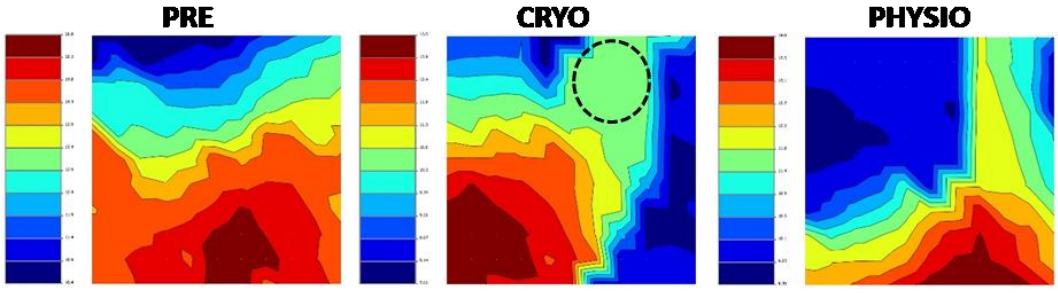


*Figure 6.40: Isochrone maps recorded in control condition (PRE), after cryoinjury (CRYO) and after 1 h of saline solution injection (PHYSIO). The number in the scale bar are milliseconds from QRS onset. The black circle represents area of deposition.*

After the cryoinjury infarction, a decrease in the value of almost all the parameters studied (Figure 6.41) compared to the standard pre-infarct conditions can be observed. Following the injection of saline solution,

AT interval, QRS complex amplitude, QT interval, RR interval and T wave parameters decrease with respect to the standard conditions.
Vice versa, QRS complex, RT interval, QT interval, and QTc increase when compared to the post-infarction condition. However, QRS complex amplitude decreases compared to the post-cryo situation.

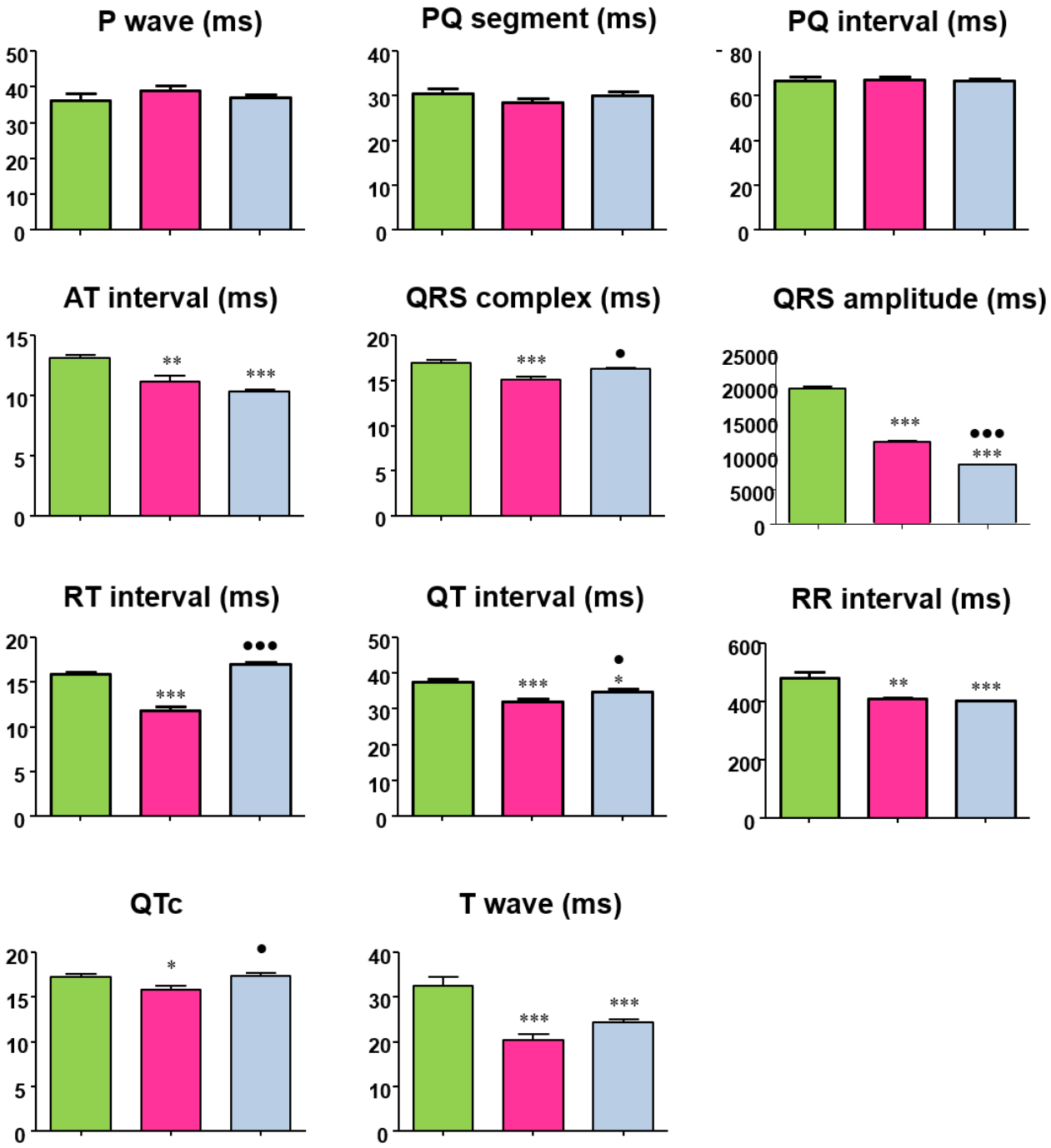


*Figure 6.41: Histograms displaying EG wave and interval durations in control condition (Pre, green), after cryoinjury infarction (pink) and after 1h of saline solution (Post physio, gray).*
** vs Pre; ● vs Post cryo*

❖ **RAT 9**

The EG during the control conditions (Figure 6.42, green frame) shows the completely positive QRS complexes and a heart rate of about 130 bpm. In addition, there is a negative terminal part of the T wave.
After cryoinjury, there is an increase in heart rate at 140 bpm. In the pink EG we see that the QRS interval is bifasic, the T wave becomes more pronounced as well as the negative terminal part.
After saline solution injection, the EG in gray differs compared to the post-cryoinjury. In addition, a small change in heart rate occurs (HR = 150 bpm) while a small decrease in T wave amplitude is present and the negative terminal part disappears.

*Figure 6.42: EGs recorded (5 seconds long) in control condition (green), after cryoinjury infarction (pink) and after 1h of saline solution injection (gray).*

In the isochrone map (Figure 6.43) of the control condition, normal sinus rhythm activation is present with two breakthroughs (blue area) on the RV and a delayed collision area near the interventricular septum (red area). After cryoinjury (black circle) the activation of sinus rhythm shows some little differences, in particular there is a slight slowing of the conduction velocity near the injection. After saline solution injection the activation of sinus rhythm does not change with respect to the CRYO condition and little differences are present due to different location of electrode array.

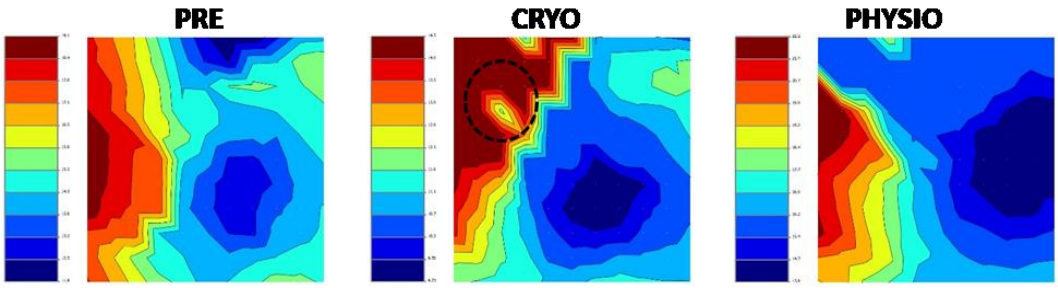


*Figure 6.43: Isochrone maps recorded in control condition (PRE), after cryoinjury (CRYO) and after 1 h of saline solution injection (PHYSIO). The number in the scale bar are milliseconds from QRS onset. The black circle represents area of deposition.*

Figure 6.44 shows the main electrophysiological parameters extracted from the EGs. After the cryoinjury infarction, the following parameters increase with respect to the control conditions: the duration of P wave and T wave, PQ segment, PQ interval, RT interval, QT interval and QTc.
Vice versa, QRS complex amplitude decreases.
After the injection of saline solution, almost all parameters increase with respect to standard pre-infarction conditions, except for AT interval and QRS complex amplitude which decrease. RR interval remains almost constant.
When compared to post-cryo parameters, P wave, QRS complex, RT interval, QT interval and QTc increase. Instead, the values of QRS complex amplitude and RR interval remain almost the same.

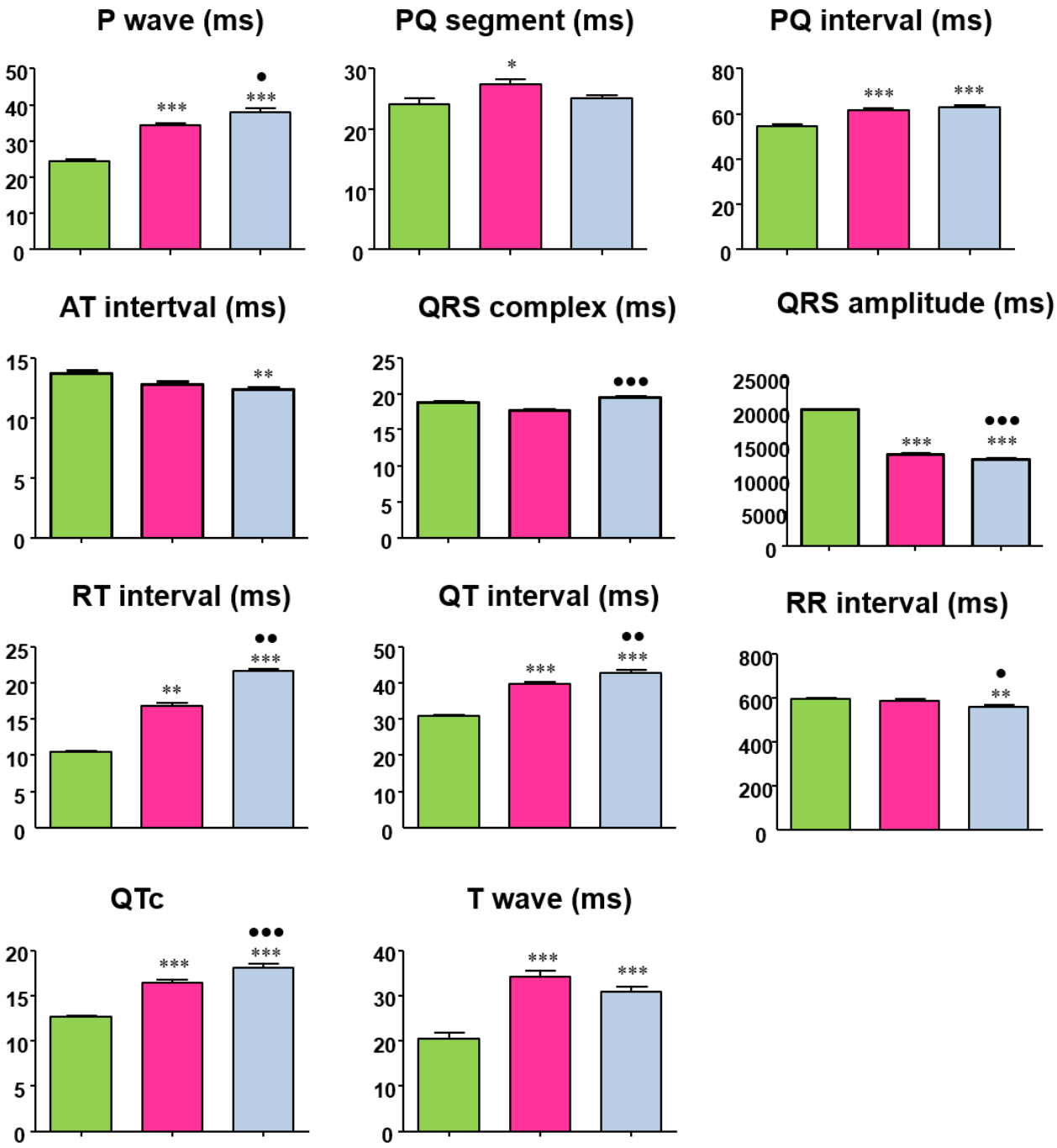


*Figure 6.44: Histograms displaying EG wave and interval durations in control condition (Pre, green), after cryoinjury infarction (pink) and after 1h of saline solution (Post physio, gray).*
** vs Pre; ● vs Post cryo*

❖ **RAT 10**

The EG during the control conditions (Figure 6.45, green frame) shows the completely positive QRS complexes. After cryoinjury, there is a slight increase in heart rate and the T wave becomes more pronounced with a negative terminal part.
After the SiC NWs injection, the EG in light blue shows a more pronounced R wave and the negative part of the T wave is reduced.

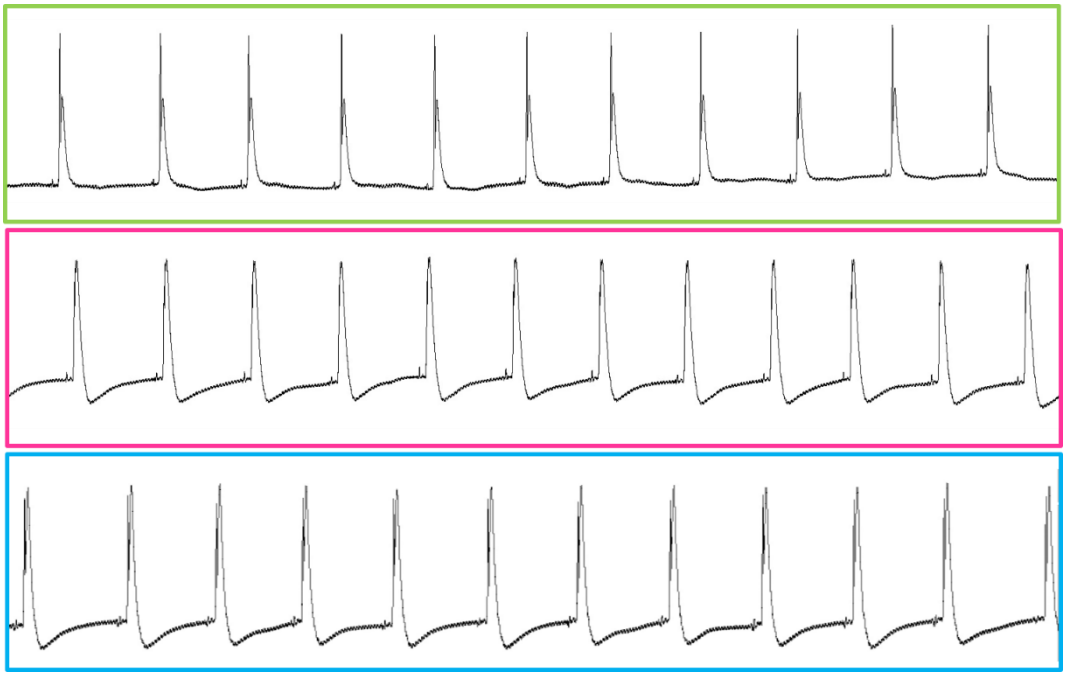

*Figure 6.45: EGs recorded (5 seconds long) in control condition (green), after cryoinjury infarction (pink) and 1h of SiC NWs in a saline solution injection (0.2mg/100g of body weight) (Post SiC 1h, light blue).*

In the isochrone map (Figure 6.46) of the control condition, epicardial point stimulation generates a point of early activation with elliptical shape (blue area) with the major axis along epicardial fibers direction and a delayed activation (red area) across the direction of the fibers.
After cryoinjury (black circle), at the same point of stimulation the early activation of elliptical shape disappears presenting a delay zone in the low area of the electrode array (in red) towards the base of the heart.
After the SiC NWs injection the isochrone map presents an activation similar to that of the pre-cryoinjury conditions, with an early activation under the stimulating electrode with an elliptical activation wavefront with the major axis parallel to the epicardial fibers direction.

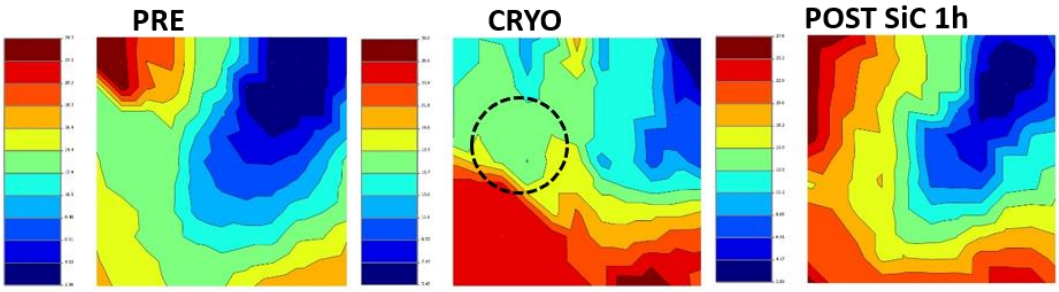


*Figure 6.46: Isochrone maps recorded in control condition (PRE), after cryoinjury (CRYO) and after 1 h of SiC NWs in a saline solution injection (0.2mg/100g of body weight) (POST SiC 1h). The number in the scale bar are milliseconds from QRS onset. The black circle represents area of deposition.*

The parameters related to ventricular activation (AT interval and QRS complex) increase after the cryoinjury, but after the injection of SiC NWs get lower (Figure 6.47). In particular QRS complex returns very similar to the initial control values. Repolarization (visible in the RT interval and T wave) decreases after cryoinjury but returns similar to initial pre-infarction values after injection of SiC NWs.

The frequency (calculated as the inverse of the RR interval) increases after the infarction (as already highlighted above in the EG) and following the injection of SiC NWs returns to the same frequency as the pre-cryoinjury phase.

The QRS amplitude parameter decreases after the injection of SiC NWs. Probably this behavior is due to the formation of a thin layer of physiological saline solution during the injection of SiC NWs. This thin layer creates a slight short-circuit effect on the electrodes and this generates a lowering of the detected signal.

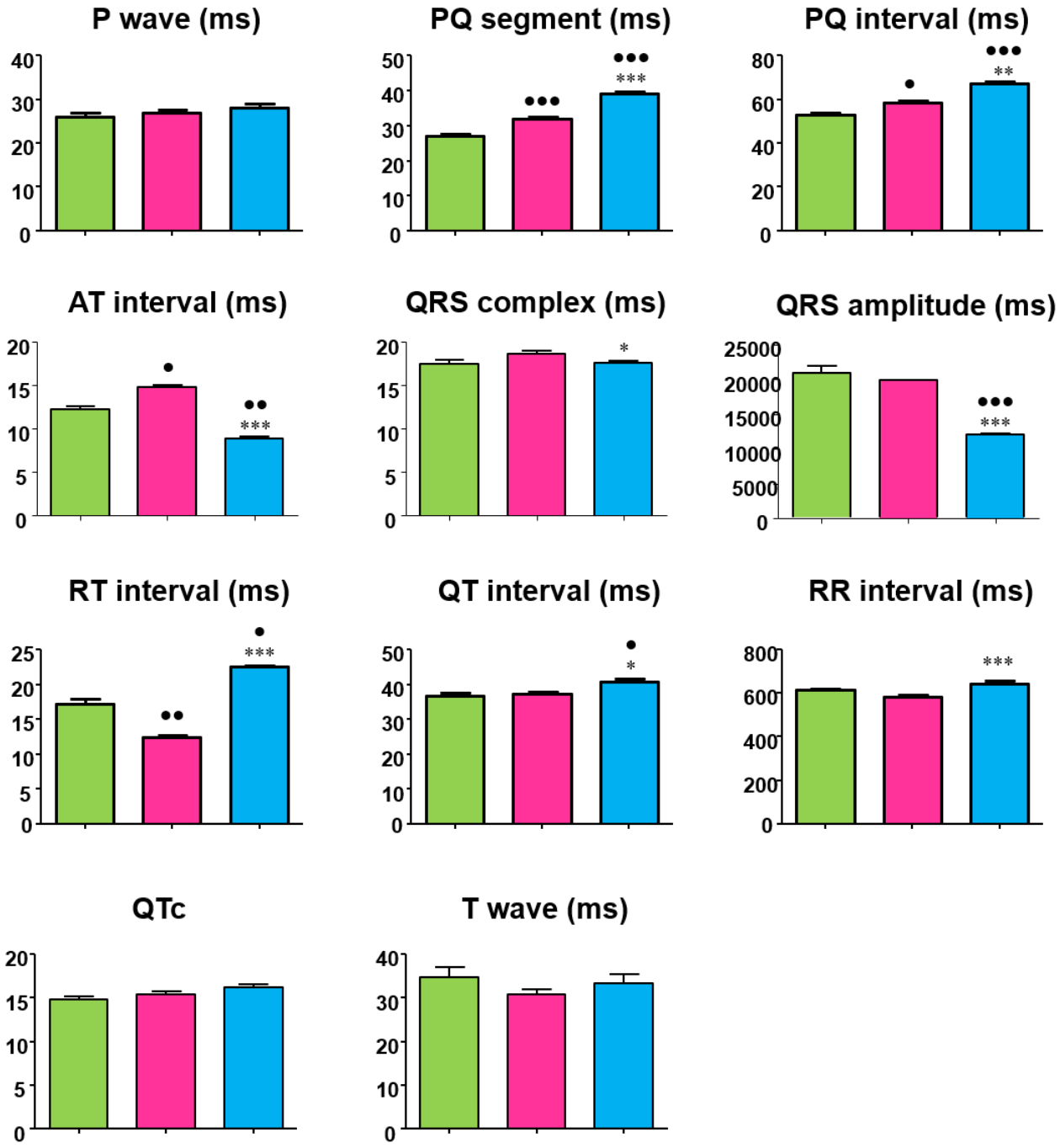


*Figure 6.47: Histograms displaying EG wave and interval durations in control condition (Pre, green), after cryoinjury infarction (pink) and after 1h of saline solution (0.2mg/100g of body weight) of SiC NWs injection (Post SiC 1h, light blue).*
** vs Pre; ● vs Post cryo*

### 6.4.3 Discussion and Conclusion

The ten rats were treated with three different protocols. The infarction was produced with three different methodologies to evaluate its short and long-term effectiveness, its reproducibility on other samples and to verify if external factors (for example the injection of physiological solution) modify or not the post-infarction situation.

To study the cardiac behavior, the various EGs obtained before, during and after the various phases of the experiments were analyzed.
From the EGs parameters it is possible to determine the functioning and the electrical duration of a specific part of the heart that is involved during the experiment. The parameters that are expected to be the most influenced by the variations that occur after an ischemia are the QRS complex (which indicates the ventricular activation), the T wave and related RT and QT intervals. In particular, following the infarction, the QRS complex should change significantly in shape and also, but not always, in duration. In fact, an infarction generates a zone of necrosis and the death of the cardiac cells in that area produces a decrease in the conductive ionic current of the electrical pulse. This damage is manifested macroscopically by the reduction of the QRS complex amplitude compared to the standard health reference condition.

Conversely, the P wave (which identifies atrial activation) and the PQ value (which represents the duration of the atrio-ventricular physiological delay) should not change much during the various phases of the experiment. In fact, the surgical protocols used in these experiments provide an invasive intervention only in the ventricular area, therefore the values of the P wave should be almost similar in all phases of the experiment. Possible variations of the P wave parameter could be attributed to the diffusion of the formaldehyde in areas of the heart adjacent to the zone of infarction creation. This would mean that formaldehyde may have also partially reached the atria.

The results of INJECTION experiments show that after injection of formaldehyde 4% in all rats, pronounced and easily visible ventricular arrhythmias are observed in EGs. Conversely, after the injection of formaldehyde 38%, a sharp decrease in the amount of ventricular extrasystoles are recorded. Given the greater concentration of formaldehyde present in the 38% solution compared to that of 4% an opposite behavior would have been expected: a much larger arrhythmic effect following the 38% intramural injection compared to the 4% one.

The possible explanation of this anomalous behavior could be attributed to issues intrinsic to the injection approach.
Performing an intramural injection into the free wall of the left ventricle in a beating heart at the time of injection is indeed a difficult task. Despite the high skill of the surgeon, the very small dimensions of the heart make this operation easily wrong or affected by several injection errors: position, depth, pressure of the liquid exiting the syringe, extraction of the needle without damaging other tissues, etc.
Another aspect to take into consideration is the possibility that the injected solution can spread through the bloodstream, diluting the concentration of formaldehyde present in the ischemic zone created. Therefore, post-injection arrhythmic behavior may have been caused not so much by a local response of the ischemic zone (in which the heart is affected by the death of some selected tissues), but by a global response due to the dilution of formaldehyde in other nearby cardiac tissues.

Nevertheless, in all three rats after a formaldehyde 4% injection it is possible to see a high increase in the value of the RT interval. The increase in this parameter indicates an increase in the duration between the activation peaks and the repolarization peaks, so this phenomenon is a symptom of serious global alteration

of cardiac electrical activity. This result confirms that the injection, even if of formaldehyde 4%, has caused serious damage to the heart.

In rat 1, after the formaldehyde 38% injection, the QRS complex amplitude decreases significantly due to the reduction in the number of live cells below the area explored by the electrode grid.
Therefore, it can be said that to create a good ischemic zone, a formaldehyde 38% injection is more effective in cell killing than a formaldehyde 4% injection.
For this reason, the more diluted formaldehyde solution was abandoned and only 38% solution was used in all the next deposition protocols.

After injection of SiC NWs, isochrone maps were recorded after 1 h from the injection and after 5 h. In fact, from previous *in vitro* experiments[16] it was observed that SiC NWs were internalized in cells after about 3 hours from their placement.

Conversely, *in vivo*, both EGs and isochrone maps do not change over time and the data collected after 1 hour are similar to those collected after 5 hours. This behavior shows a stable heart condition for a long-time interval and suggests that the SiC NWs do not disperse in other nearby tissues but remain localized exclusively in the injection area.

Since the data collected after 1 h from the injection of SiC NWs and those collected after 5 h are almost identical, in future experiments only data after 1 h from the injection will be collected. This decision was also taken for other reasons: to be sure of working in a fresh ischemic zone, to obtain data less affected by possible errors (both human and physiological) and to avoid unnecessary suffering to animals.

In the three rats treated with the DEPOSITION protocol (rat 4, 5 and 6) the ischemic zone is obtained by depositing on the left ventricular free wall epicardium a drop of formaldehyde 38% solution using a micropipette.

The isochrone maps confirm that the infarction caused by deposition is more effective compared to that induced by injection of formaldehyde. The maps highlight a local velocity conduction slowdown, shown by the high line gradient observed near the drop deposition area. Another important fact to observe is that the ventricular ectopic activity (ventricular extrasystole) originates at the boundary of the deposition area of the formaldehyde, where lesion currents can generate ectopic activity. The fatal arrhythmias that arise post-infarction are the ventricular ones (ventricular extrasystole) and are usually born near discontinuities such as those in the border zone of the infarcted area.
Here again, after the deposition of the formaldehyde drop, it is possible to see an increase in the RT interval parameter and a decrease in the QRS complex amplitude value. These data highlight that a good ischemic zone has been created and the cardiac conduction at that point has been seriously damaged.
Both after the injection of saline solution (rat 4 and 6) and after the injection of SiC NWs (rat 5 and 6) the ventricular extrasystoles disappear and there is an improvement in the cardiac conduction due to a partial restoration of the functionality of ischemic tissue.

In order to obtain an even more reproducible and stable infarct over time it was decided to use protocol three on rats 7, 8, 9 and 10: CRYOINJURY.

The first element that can be seen visually is that the infarction caused by the cryoinjury has much clearer and more defined edges than the infarctions caused by injection or by deposition of formaldehyde. Moreover, the procedure for causing infarction with this technique is simpler than the previous ones.
In fact, with CRYOINJURY a metal tip cooled by liquid nitrogen is simply placed on the surface of the beating heart exerting a slight pressure.

Conversely, with the INJECTION, the needle of the syringe must be insert in the exact spot and the liquid must be injected while the heart continues to beat. This procedure inevitably requires more time. The greatest risks are to miss the injection point by penetrating too deeply with the needle or staying too much on the surface, exerting too much pressure or damaging other tissues during the extraction of the needle.
Instead, with the DEPOSITION there is the problem that the drop of formaldehyde could slide away from the surface of the heart due to the beats. In this way, the drop could expand too much by wetting many more tissues than necessary, or the infarction could stop at a too superficial level without penetrating deeper tissues.

Therefore, to conclude, the infarction obtained by injection is less experimentally reproducible and the less lasting in time. As reported in the experiment on rat 1, definitely the best results were obtained after injection of formaldehyde 38% and not using formaldehyde 4%. The shape of the T wave in the EG of post-formaldehyde injection and the sharp decrease of the QRS complex amplitude parameter are proof of this.

The infarction obtained by deposition of a drop of formaldehyde 38% gave good results, highlighted by the decrease of the QRS complex amplitude and by the variation of the T wave, RT and QT parameters.

However, the most stable and lasting infarction is obtained with the cryoinjury technique.
The EGs and isochrone maps of rats 7-10 are proof of this. In particular the isochrone maps show a narrower gap between the lines, which is an index of poor electrical conduction and guarantees the effectiveness of the cryoinjury technique in causing infarctions. Another parameter to be highlighted is the great decrease of the QRS complex amplitude following the infarction. This value does not increase after the injection of saline solution; therefore, the infarction is stable over time.

The data obtained following the injection of nanowires are a bit fluctuating. Regardless of the protocols used to cause the infarction, some positive effects have been observed, with a post-nanowires condition that returned similar to the initial pre-infarction situation. For instance, an increase of the T wave and of the QT parameter are observed in all the treated rats (2, 3, 5, 6 and 10). Another element to underline is the disappearance of ventricular extrasystoles after the injection of SiC NWs. However, not all the parameters showed such a recovery, and it is difficult to unveil the specific contribution of the NWs by the isochrone maps at our disposal. This could be partly due to the mismatch between the area of the infarction and the area in which the SiC NWs were injected.

Experiments similar to that of rat 10 were scheduled for the end of December 2018 (on 5 other rats).

Among all, the cryoinjury experiments followed by the SiC NWs injection are the experiments that have shown the greatest potential to offer promising results in the treatment of infarction.

## 6.5 Future works

Future studies will be focused on the realization of a conductive epicardial patch designed for a rapid and direct application on the damaged epicardial area of the heart following the infarction.

The idea is to incorporate the SiC NWs inside a Teflon surgical gauze (polytetrafluoroethylene). These gauzes are already used in the cardiovascular field as stents or grafts and are easily applicable on the human heart. The presence of SiC NWs inside would make the patch conductive and restore the normal cardiac propagation.
The patch would be sewn on the surface of the heart, with SiC -NWs in direct contact with the cardiac tissue. In this way, the nanowires may propagate the wavefront between the healthy areas of the heart, bypassing the insulating scar area created after the infarction. (Figure 6.48)

The design and creation of a conductive cardiac patch is of course a very complex task and requires time and great skills and experience in the chemical, biological and anatomical fields.

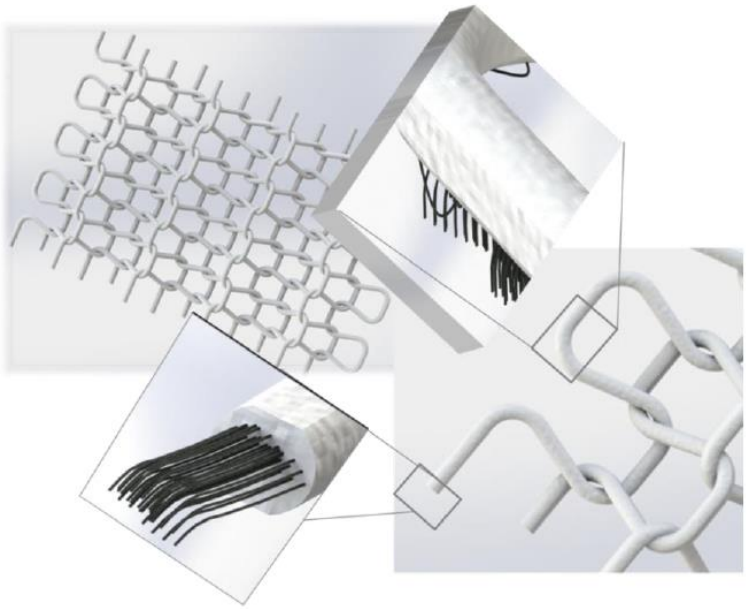

*Figure 6.48: Hypothetical model of a conductive cardiac patch: SiC NWs (in black) are present inside the Teflon wires (in white).*

A prototype of this device has already been developed at CNR-IMEM[7], but never tested *in vitro* or *in vivo*.

The NWs were grown from normal procedure (see Chapter 2) and etched to remove the oxide layer. (Figure 6.49 A)
A polymethylmethacrylate (PMMA) solution 15% weight was dropped onto the substrate. (Average $M_W$: 350000). (Figure 6.49 B)
PMMA has been chosen as polymer because it has a high electrical resistivity (1019 Ω) and is totally biocompatible. In fact it is already widely used in ophthalmology for orthopedic prostheses and for intraocular lenses for the treatment of cataracts.[17]
A GORE-TEX® support has been anchored to the surface. (Figure 6.49 C)
To peel the nanowires from the silicon platelet, a peeling was performed, making the patch free. (Figure 6.49 D)

Since the nanowires were still embedded in the polymer, the PMMA was etched by plasma oxygen to expose the heads of the NWs. (90 seconds at 60.4 mTorr and 50 mW) (Figure 6.49 E)
The result of the plasma etching was analyzed with SEM. (Figure 6.49 1 and 2)

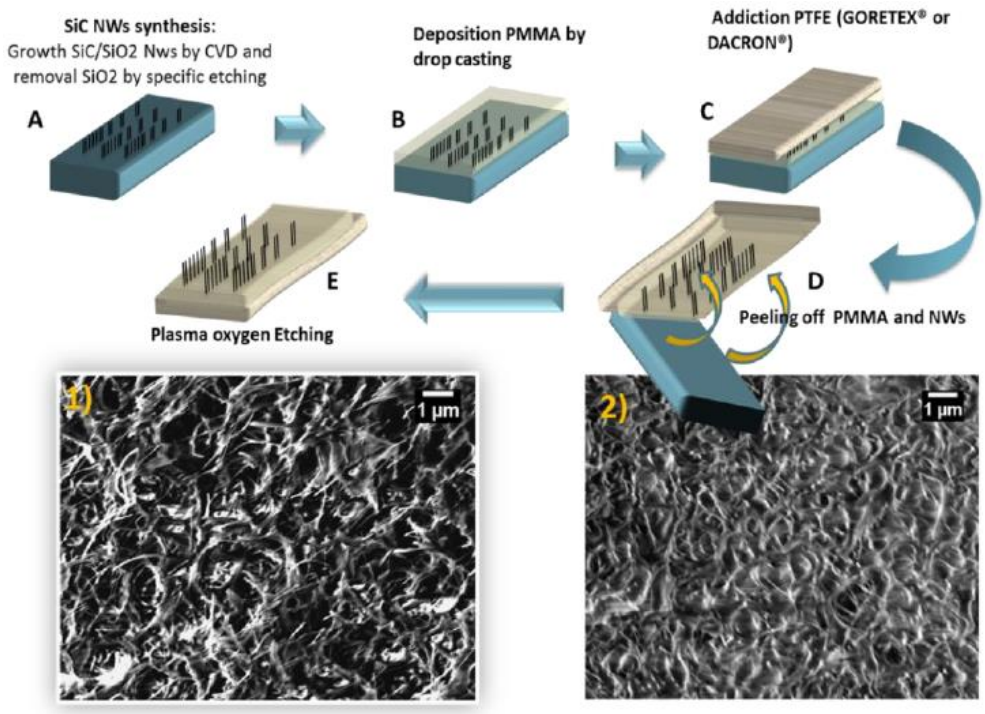


*Figure 6.49: Schematic process for the creation of SiC NWs epicardial patch. A) SiC NWs on silicon platelet (in blue) grown by CVD technique. B) PMMA (in transparent gray) deposition on SiC NWs platelet. C) Anchoring of GORE-TEX substrate (in dark gray). D) The peeling to remove the silicon substrate from the epicardial patch. E) PMMA etching by Plasma Oxygen. The NWs heads are now visible. 1) SEM image after the plasma etching. 2) SEM image before the plasma etching.*

Based on this prototype, another possible solution that would make the heart patch even more conductive and efficient could be designed. The idea behind this future project is described below.

A careful bibliographic research has shown the existence of similar projects from the point of view of the possible design and material construction of this epicardial conductive patch. [18,19, 20]
Among all these projects I found particularly interesting the works that dealt with the use of polydopamine (PDA) as a biocompatible adhesive polymer for attaching nanowires of different materials to flexible surfaces of different composition.

Yu and coworkers fabricated a silver NWs-polydopamine nanocomposite cloth via dip-coating technique.
The cloth surface was modified by soaking it into a polydopamine solution and subsequently was dip-coated with a dispersion of silver nanowires in a polydopamine solution. Once dry the cloth was covered uniformly and permanently by the crosslinked nanowires.[21]

Akter and Kim described in their paper the deposition of a stretchable, transparent and conductive coating of silver NWs on polydopamine-modified polydimethylsiloxane substrate (PDMS). The nanowires were

homogeneously distributed on the substrate using a spray-deposition technique exploiting the adhesive properties of PDA present on the PDMS surface.[22]

Even in the work of Miao and coworkers the PDA plays a fundamental role in the functionalization of surfaces making them sticky and thus capable of adhering permanently to the nanowires. Specifically, Miao et al. prepared a hybrid nanomaterial made of polydopamine-functionalized graphene with silver nanowires.[23]

For the development of the conductive epicardial patch for this cardiology project the best candidate to use as a substrate to be functionalized with polydopamine is definitely GORE-TEX®.
Indeed, GORE-TEX® is biocompatible, porous, inert and can be surgically sewed on the heart. Once it adheres to the external heart tissue, its extreme flexibility allows it to perfectly follow the movements of contraction and relaxation of the heart without hindering its beats.
To anchor the nanowires to the support of GORE-TEX®, polydopamine could be used. As mentioned before, PDA is a biocompatible adhesive, able to adhere perfectly to any type of surface, while maintaining a good flexibility.[24,25] Furthermore its synthesis does not require high costs.

On a surgical gauze of GORE-TEX® a thin layer of PDA could be deposited by dropping or by spin coating. Before the PDA is dry the SiC NWs could be placed on the adhesive surface by spray coating or by dispersing them in solution and depositing them drop by drop. (Figure 6.50)
Of course, preliminary studies should be carried out to understand the best coating technique with PDA and with the nanowires. Furthermore, it should be analyzed if the solvent in which nanowires are dispersed interacts or not with the PDA or reduces its adhesive power.

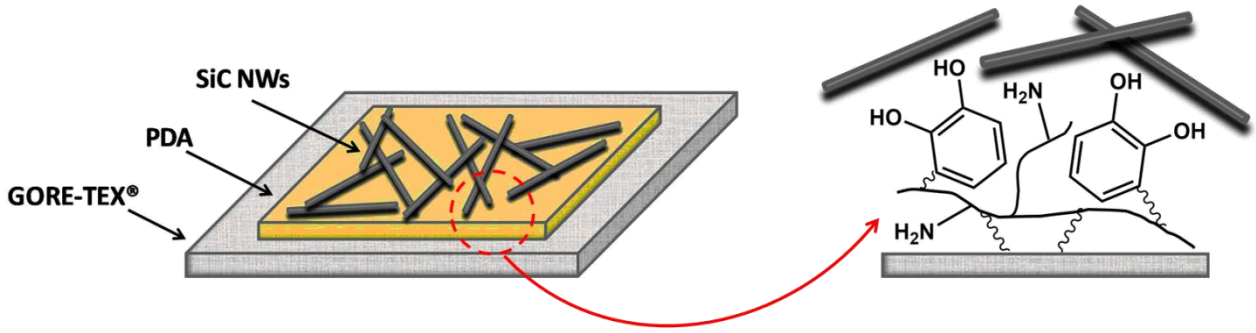


*Figure 6.50: Schematic representation of GORE-TEX® epicardial patch with SiC NWs and PDA. In gray the GORE-TEX® support, in yellow the PDA. On the left the magnification of the area circled in red. In gray the GORE-TEX® layer, above the molecules that form the layer of PDA and on top the SiC NWs.*

Currently the design and construction of this cardiac patch are at a very preliminary stage, but soon it could be realized and tested.

## References


1 P. A. Iaizzo, *Handbook of Cardiac Anatomy, Physiology, and Devices*, Springer International Publishing AG, Third Edit., 2015.

2 M. R. Franz, C. Schmitt and B. Zrenner, *Monophasic Action Potentials : Basics and Clinical Application*, Springer Berlin Heidelberg, 1997.

3 J. H. O'Keefe, S. C. Hammill and M. Freed, *The complete guide to ECGs : a comprehensive study guide to improve ECG interpretation skills*, Physicians' Press, fourth edi., 2017.

4 P. Konopelski and M. Ufnal, Electrocardiography in rats: a comparison to human. Medical University of Warsaw.

5 S. Saksena, *Electrophysiological disorders of the heart*, Elsevier Churchill Livingstone, 2005.

6 S. Khosla, Global Illness map charts countries' most fatal diseases, Simon Khosla, GlobalPost.

7 P. Lagonegro, *Study of interaction between Si(O,C) nanowires and biological systems*, Università degli Studi di Parma, 2016.

8 Warner Instrument, Chloriding Ag/AgCl Electrodes Disk, Pellet, or Wire.

9 L. A. Geddes, L. E. Baker and A. G. Moore, *Med. Biol. Eng.*, 1969, **7**, 49–56.

10 S. Watabe, B. Taccardi, R. L. Lux and P. R. Ershler, *Circulation*, 1990, **82**, 2115–2127.

11 M. M. Ciulla, R. Paliotti, S. Ferrero, P. Braidotti, A. Esposito, U. Gianelli, G. Busca, U. Cioffi, G. Bulfamante and F. Magrini, *J. Surg. Res.*, 2004, **116**, 91–97.

12 J. A. Jensen, J. C. Kosek, T. K. Hunt, W. H. Goodson and D. C. Miller, *Ann. Surg.*, 1987, **206**, 798–803.

13 T. Misaki, S. P. Allwork and H. H. Bentall, *Cardiovasc. Res.*, 1983, **17**, 61–69.

14 E. G. Strungs, E. L. Ongstad, M. P. O'Quinn, J. A. Palatinus, L. J. Jourdan and R. G. Gourdie, Humana Press, Totowa, NJ, 2013, 343–353.

15 Agar scientific, Optimal Cutting Temperature OCT compound, http://www.agarscientific.com/oct-compound.html.

16 A. Cacchioli, F. Ravanetti, R. Alinovi, S. Pinelli, F. Rossi, M. Negri, E. Bedogni, M. Campanini, M. Galetti, M. Goldoni, P. Lagonegro, R. Alfieri, F. Bigi and G. Salviati, *Nano Lett.*, 2014, **14**, 4368–4375.

17 M. R. Ophthalmic Research Center., M. Dānishgāh-i 'Ulūm-i Pizishkī va Khadamāt-i Bihdāshtī-Darmānī-i Shahīd Bihishtī. and B. Abazar, *Journal of ophthalmic & vision research.*, 2008, vol. 4.

18 B. Shen, B. Xiong and H. Wu, *Biomicrofluidics*, 2015, **9**, 1–11.

19 S. Ye, A. R. Rathmell, Z. Chen, I. E. Stewart and B. J. Wiley, *Adv. Mater.*, 2014, **26**, 6670–6687.

20 B. G. Nair, K. Hagiwara, M. Ueda, H. H. Yu, H. R. Tseng and Y. Ito, *ACS Appl. Mater. Interfaces*, 2016, **8**, 18693–18700.

21 Z. Yu, Y. Gao, X. Di and H. Luo, *RSC Adv.*, 2016, **6**, 67771–67777.

22 T. Akter and W. S. Kim, *ACS Appl. Mater. Interfaces*, 2012, 1–3.

23 J. Miao, H. Liu, W. Li and X. Zhang, *Langmuir*, 2016, **32**, 5365–5372.

24 M. E. Lynge, R. Van Der Westen, A. Postma and B. Städler, *Nanoscale*, 2011, **3**, 4916–4928.

25 V. Ball, D. Del Frari, M. Michel, M. J. Buehler, V. Toniazzo, M. K. Singh, J. Gracio and D. Ruch, *Bionanoscience*, 2012, **2**, 16–34.

## Acknowledgments